MODELLING SEASONAL AND LONG-TERM CHANGES OF WATER MASSES AND CIRCULATION IN THE SOUTHEAST ASIA REGION

Thesis submitted in accordance with the requirements
of the University of Liverpool for the degree of
Doctor in Philosophy

by

Binh Trong Do

March, 2009

Acknowledgements

I would like to express my special thanks and profound gratitude to my supervisor Dr Harry Leach for his kindness and all the continuous supervision, fundamental scientific input, patient explanations and advice throughout the development of this work. To my second supervisor Dr Jason Holt for his help with POLCOMS model and the computer resources.

I would like to express my special thanks to Dr Vassil Roussenov who kindly supported and provided invaluable help with the data assimilation and all aspects of the modelling work. I also would like to thank Prof. Ric Williams for reading Chapter 4, and his comments and advice on interpreting the model results. I would like to extend my sincere thanks to all of my colleagues in the physical oceanography postgraduate research group at the University of Liverpool, especially Susan, Gualtiero, Phil and Angela for their help and encouragement throughout the whole of my PhD work.

I also would like to thank my examiners, Dr David Stevens and Dr Miguel Angel Morales Maqueda, for constructive suggestions for improvements to the thesis.

Finally, I especially wish to thank my family in Vietnam and my wife for their patience and enormous support throughout this work.

This work was funded by the Vietnamese Overseas Scholarship Program (VOSP), and was carried out at the Department of Earth and Ocean Sciences (DEOS) in the University of Liverpool, and the Proudman Oceanographic Laboratory (POL), in the United Kingdom.

Abstract

In the global thermohaline circulation, the North Atlantic Deep Water which spreads throughout the global ocean requires a return flow in the upper waters and the Indonesian throughflow forms an important pathway for this return flow by providing a connection between the Pacific and Indian Oceans. In this study the MICOM model was tailored to the geography of the Southeast Asian region which enabled prediction of flow and transport on seasonal and inter-annual time scales. The focus of the study was to answer the questions: What are the main driving forces of the Indonesian Throughflow (ITF)? What is the magnitude and variability of the ITF? Is there a link between the ITF transport and ENSO, and what might happen under idealised global warming scenarios?

A series of numerical model experiments with the idealised geometries and wind forcing were carried out in order to learn about the model, the possible flow regime, the volume transport and their responses to changes of forcing and topography. The model has successfully reproduced the physical phenomena such as the basin scale gyres, the boundary currents, and the equatorial currents. The model results show that the volume transport is sensitive to the changes of topography, the applied wind stress regime and the strength of wind stress.

The model experiments with the realistic geometry and forcing have pointed out that wind stress can produce a rather high seasonal variation of the ITF transport, but it produced a relatively small volume transport compared to the recent observation and numerical studies. The model experiments clearly indicate that the main driving forces of the ITF are the wind stress and thermal forcing. Among them the thermal forcing is certainly dominant. The total annual-mean ITF transport produced by the model is about 16.25 Sv, with 62% of the transport appears in the upper layers. There is a strong seasonal variability of the ITF transport with the minimum of about 12.26 Sv in December, and the maximum of about 20.28 Sv in July. During a certain period of the year the ITF's source is from the northern hemisphere only and at other time it is from both northern and southern hemispheres. The result also shows that the South China Sea plays a significant role in the variability of the ITF.

The model results show a clear linkage between the ITF and ENSO with the annual-mean ITF transport reduced in the El Niños and enhanced during the La Niñas. The correlation coefficient between the annual-mean ITF transport produced by the MICOM and OCCAM 1/12° global models and the ONI index is 0.63 (with 97.5 % confidence) and 0.89 (99% confidence) respectively. There was a very significant correlation between the ITF transport and the 6 strongest ENSO events from 1982-2001 with the correlation coefficient of about 0.89 (97.5% confidence). In addition the model experiment with idealised global warming suggesting that global warming seems makes little difference to the ITF transport.

TABLE OF CONTENTS

LIST OF TABLES

LIST OF FIGURES

LIST OF ABBREVIATIONS

ACC	Antarctic Circumpolar Current
ACIA	Arctic Climate Impact Assessment
ADCP	Acoustic Doppler Current Profiler
AOGCM	Atmosphere Ocean General Circulation Model
ARGO	Global Array of Temperature/Salinity Profiling Floats
ARLINDO	Arus Lintas Indonesia
BBL	Bottom Boundary Layer
CLIVAR	Climate Variability and Predictability
CSIRO	Commonwealth Scientific and Industrial Research Organisation
CTD	Conductivity Temperature Depth
ECMWF	European Centre for Medium range Weather Forecasts
EIC	Equatorial Intermediate Current
ENSO	El Niño Southern Oscillation
ETOPO5	Earth Topography Five Minute Grid
EUC	Equatorial Undercurrent
GCM	General Circulation Model
GCOS	Global Climate Observing System
GODAE	Global Ocean Data Assimilation Experiment
GOOS	Global Ocean Observing System
HE	Halmahera Eddy
HIM	Hallberg Isopycnal Model
HOPE	Hamburg Ocean Primitive Equation Model
HYCOM	HYbrid Coordinate Ocean Model
INSTANT	International Nusantara Stratification And Transport Program
IPCC	Intergovernmental Panel on Climate Change
ITF	Indonesian Throughflow
JAXA	Japan Aerospace Exploration Agency
MC	Mindanao Current
MICOM	Miami Isopycnal Circulation Ocean Model
MITgcm	Massachusetts Institute of Technology General Circulation Model
MOM	Modular Ocean Model
MOMA	Modular Ocean Model - Array processor Version
NAS	National Academy of Sciences
NASA	National Aeronautics and Space Administration
NCEP	National Centres for Environmental Prediction

NEC	North Equatorial Current
NECC	North Equatorial Counter Current
NOAA	National Oceanic and Atmospheric Administration
OCCAM	Ocean Circulation and Climate Advanced Modelling
OGCM	Ocean General Circulation Model
ONI	Oceanic Niño Index
POL	Proudman Oceanographic Laboratory
POL3DB	Proudman Oceanographic Laboratory Three-Dimension Baroclinic B-Grid Model
POLCOMS	Proudman Oceanographic Laboratory Circulation Ocean Model System
POM	Princeton Ocean Model
POSEIDON	Poseidon Ocean General Circulation Model
POSUM	Parallel Oregon State University Model
PPM	Piecewise Parabolic Method
ROMS	Regional Ocean Modelling System
SC	Somali Current
SCS	South China Sea
SEA	Southampton-East Anglia
SEC	South Equatorial Current
SECC	South Equatorial Counter Current
SPEM	S-coordinate Primitive Equation Model
SST	Sea Surface Temperature
Sv	Sverdrup ($1\ Sv = 10^6\ m^3/s$)
TAO	Tropical Atmosphere Ocean project
THC	Thermohaline Circulation
U.S.	United States
WCRP	World Climate Research Programme
WOCE	World Ocean Circulation Experiment
WPWP	West Pacific Warm Pool
WW	Weather World

Chapter 1

INTRODUCTION

The Southeast Asian region forms a crucial part of the global ocean by providing a connection between the Pacific and Indian Oceans. However, most of the region between the Asian mainland and Australia consists of shelf seas shallower than 200 metres depth. Only a few deeper channels connect the deep waters of the Pacific and Indian Oceans particularly through the Molucca, Banda, Savu and Timor Seas. In the global thermohaline circulation, the North Atlantic Deep Water which spreads throughout the global ocean requires a return flow in the upper waters and the Indonesia Throughflow (ITF) forms an important pathway for this return flow. The ITF therefore is the low latitude tropical current system that transfers mass, heat and fresh water from the western tropical Pacific into the south-eastern tropical Indian Ocean through the Indonesian seas, through which it transfers the climate signals and their anomalies around the world's oceans. Understanding the seasonal and inter-annual variability of the flow of ocean currents through the S.E Asian region will help to resolve some of the complexities surrounding global and regional climate. On other hand, as a major global population centre, there are major economic interests in the shelf seas of the region, so understanding the ITF will also provide a valuable insight for governments and industry in their management of ocean and land-based resources. For example, one third of Australia's gross domestic product is sourced on the North West Shelf, which is flooded by Throughflow waters and influenced by its variability (CSIRO, 2004).

In his early works, based on hydrographic observations, sea level records, drifts and climatological wind patterns, Wyrtki (1961; 1987) first estimated the ITF magnitude and proposed the mechanism of transferring water from the Pacific Ocean to the Indian Ocean. He suggested that the ITF is driven by a pressure gradient between the Pacific and Indian Ocean. Godfrey (1989) invented the so-called "island rule" based on a Sverdrup model to estimate the mean ITF magnitude. Wajsowicz (1993a,b;

1994) further modified Godfrey's "island rule" to account for the complex geometry of the Indonesian Gateways by including the bottom topography, frictional effects and multiple straits. In agreement with the modified "island rule", the ocean general circulation model (OGCM) experiments of Wajsowicz (1995; 1996) confirm that inter-annual variability in the depth-integrated Throughflow is generated by wind stress variations over the Pacific. However, comparison of the inter-annual variations in depth-integrated transport predicted by the theory and simulated by the coupled OGCM shows disagreement with observation in both magnitude and phasing of the Throughflow (Wajsowicz and Schneider, 2001). A different approach was suggested by Andersson and Stigebrandt (2005) where only the density gradient between the Pacific and the Indian Ocean is considered to drive the Throughflow. This estimate crucially depends on the width and depth of the downstream buoyant pool formed in the North Australian Basin as well as on the reference temperature and salinity used in the calculation. In terms of volume transport, the actual magnitude of the ITF and the annual variation still remains controversial, despite many efforts in recent years to measure it. The numerical value of the ITF volume transport ranges from near zero to 30.0 Sv (Siedler et al, 2001) depending on the method, location, time and data used in calculating it.

The early theoretical work of Wyrtki (1987) and Clarke and Liu (1994) hinted at a relationship between the ITF and the ENSO, and suggested that the volume transport of the ITF would be reduced (enhanced) during El Niño (La Niña) events. The hypothesis was based on the change in the Pacific trade winds during ENSO events and the associated responses of Pacific and Indian Ocean sea level and the ITF. Other work (Meyer, 1996) showed that the depth integrated transport from Australia to Java, computed from observational data (temperature and salinity) was enhanced during the La Niña event of 1988/1989 and reduced during the El Niño of the early 1990s. However in more recent studies (England and Huang, 2005; Sprintall et al, 2004) a major part of the inter-annual variation in the ITF appears to be independent of ENSO, and there are several years in which the ITF transport does not appear to match ENSO variation.

The existing theories and research on the ITF therefore still leave the unanswered question of how to approach the Throughflow dynamics in order to predict the

volume transport magnitude and variability, the relationship between ITF and the ENSO events? Therefore being able to use numerical ocean models to predicting currents and understand water mass transport in the region is important.

The first aim of this research project was to establish a numerical ocean model of the Southeast Asia region which would enable prediction of flow and transport on seasonal and inter-annual time scales. To achieve this aim the high-resolution Proudman Oceanographic Laboratory Circulation Ocean Model System (POLCOMS) model and the Miami Isopycnal Circulation Ocean Model (MICOM) were tailored to the geography of S.E. Asia. The models were driven by using realistic wind stress and other surface forcing in order to investigate the changing currents and water mass structure under different climatic conditions. A sensitivity test was also carried out to explore the sensitivity of the ITF to changes in forcing (strength of wind and variability in time) resulting from climate change. The second aim of the study (the main goal) was to conduct model experiments to address the questions: What are the main driving forces of the ITF? What is the magnitude and variability of the ITF? Is there a link between the ITF transport and ENSO, and what might happen under idealised global warming scenarios?

In Chapter 2 a review of the general ocean circulations, the Southeast Asian Water and its circulation, the Asian monsoon and the ITF and its transport and variability are presented. In Chapter 3 the main model equations and parameters are introduced. A series of model experiments with the different idealised geometry and wind forcing in order to learn about the models, the possible flow regimes, volume transports and their responses to changes of forcing and topography are presented in Chapter 4. The model experiments using realistic topography and forcing to simulate the circulation and volume transport of the throughflow between the Pacific and Indian Oceans through the Southeast Asia region are presented in Chapter 5. Throughout the model experiments the magnitude and variability of the ITF transport, the main driving forces of the ITF and the main characteristics of the ITF will be discussed and compared with the observations and other studies where possible. In Chapter 6 the model experiments of the ENSO events and the model result for the longterm variation of the ITF will be presented. The correlation between the ITF transport and ENSO events, and global warming will be described in this chapter too. The main conclusions of the study are summarised in Chapter 7.

Chapter 2

LITERATURE REVIEW

2.1. The General Ocean Circulation

The oceans and their circulation (Figure 2.1) are an important part of the global climate system by influencing wind, air temperature and the hydrological cycle (van Aken, 2007). However, there is no official or unique definition of the general ocean circulation. In text books on geophysical fluid dynamics and physical oceanography (Warren and Wunsch 1981; Gill, 1982; Abarbanel and Young, 1987; Pickard and Emery, 1990; Pedlosky, 1987, 1996; Knauss, 1997; Tomczak and Godfrey, 2001; Siedler et al, 2001) the general circulation of the ocean is the term used to describe the movement of waters on large spatial and temporal scales in the ocean basins.

The winds blowing over the ocean's surface will transfer energy to the upper layer of the oceans through friction to produce surface circulation (wind-driven circulation), while the deep circulation is driven by the density difference between water-masses which is caused by the cooling and sinking of waters in the polar regions (thermohaline circulation).

The surface circulation carries the upper warm waters poleward from the tropics (except in the South Atlantic, where the flow is to the North Atlantic). Heat is disbursed along the way from the waters to the atmosphere. At the high latitudes, the water is further cooled during winter, and sinks to the deep ocean. This is especially true in the North Atlantic (where the North Atlantic Deep Water is formed) and around Antarctica (where the Antarctic Bottom Water is formed). Deep ocean water gradually returns to the surface at various places around the globe. Once at the surface it joins the return flow to the North Atlantic, and the cycle begins again.

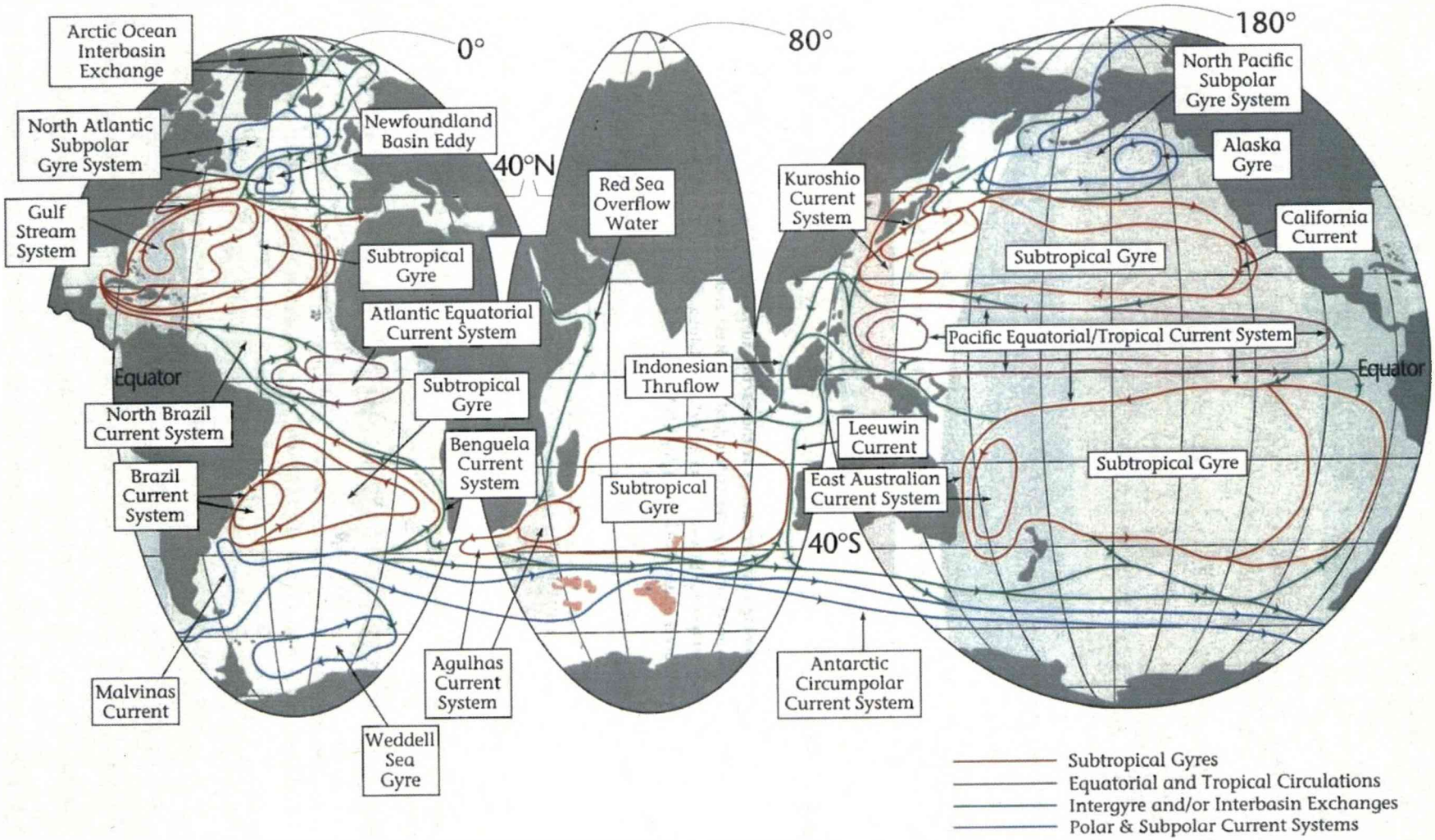

Figure 2.1: Schematic of the major upper ocean current system and the connection between these flows (from Schmitz, 1996a) (Siedler et al, 2001).

Variations in the ocean's circulation can lead to variations in heat transport and to variations in weather patterns. One important variation in the circulation is the change in the equatorial circulation known as El Niño which occurs with an irregular period of about 4 years. The period between the appearance of an El Niño event is different between different authors such as 2-5 years; 2-7 years; 3-7 years (Open University, 2002; NOAA, 2005; WW2010, 1998).

The instrumental observations of ocean currents on a global scale began in 1872, during the voyage of *HMS Challenger*, starting from Portsmouth, England. This ocean expedition was to navigate the globe in three and a half years, with measurements of the state of the ocean taken at 354 stations (Siedler et al., 2001). The most ambitious oceanographic experiment undertaken to date is the World Ocean Circulation Experiment (WOCE), 1990-2002 with about 30 nations participating. It was a component of the World Climate Research Program (WCRP). The aims of the programme were to establish the role of the oceans in the Earth's climate and to obtain a baseline dataset against which future change could be assessed. Besides the observational programme, using ships for employing moored and drifting instrumentation to make physical and chemical observations, and observations from satellites, a number of sophisticated numerical ocean models were also developed to provide a framework for the interpretation of the observations and for the prediction of the future ocean state. On the completion of WOCE other large-scale projects which involve the ocean and climate are being actively pursued. Among them are: CLIVAR - a Global Study of the Earth's Climate Variability and Predictability; GODAE - the Global Ocean Data Assimilation Experiment; and ARGO - a global array of temperature/salinity profiling floats (Sparrow et al., 2005). The ARGO array is part of the Global Climate Observing System/Global Ocean Observing System GCOS/ GOOS). Up to the present (21 June, 2007) there are 2856 floats which have been deployed over the global ocean (Figure 2.2)

2.1.1. Wind-driven circulation

The wind-driven circulation is principally concentrated in the upper few hundred metres of the ocean and therefore is principally a horizontal circulation in contrast to the thermohaline one (Pickard and Emery, 1990) that will be mentioned in the next section.

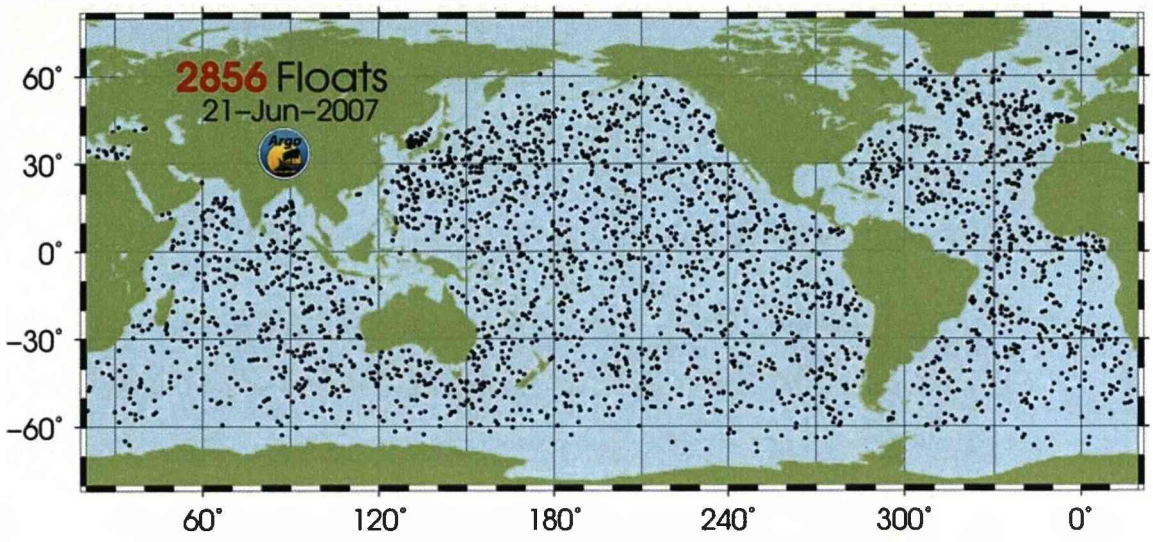

Figure 2.2: The positions of the Argo's floats on 21 June 2007 (Argo, 2007).

In texts on physical oceanography the mechanism of the wind driven circulation is widely accepted as the mechanism by which wind (caused ultimately by the solar energy) blowing over the sea surface transfers its energy to surface water to cause the surface layer to move horizontally (the main gyre circulations of the oceans are formed as consequence) and this motion in coupling with water friction will in turn cause the deeper layers to move (vertical effect).

The very first of a remarkable series of studies (Table 2.1) conducted during the first half of the twentieth century that led to an understanding of how winds drive the ocean's circulation, as stated by Stewart (2006), were the works of Fridtjof Nansen and Vagn Walfrid Ekman. However the theory for wind-driven, geostrophic currents was first outlined in a series of papers by Sverdrup (1947), Stommel (1948), and Munk (1950) (Abarbanel, 1987; Stewart, 2006). Sverdrup showed that the curl of the wind stress ($\beta v = \text{curl}\tau$) drives water masses equator-ward in the sub-tropical and pole-ward in the sub-polar areas, and that this can be used to calculate currents in the ocean away from western boundary currents. Stommel showed that western boundary currents are required for flow to circulate around an ocean basin when the Coriolis parameter varies with latitude. Finally, Munk showed how to combine the two solutions to calculate the wind-driven geostrophic circulation in an ocean basin. In all cases, the current is driven by the curl of the wind stress (Stewart, 2006).

Table 2.1: Contributions to the Theory of the Wind-Driven Circulation (Stewart, 2006)

Fridtjof Nansen	1898	Qualitative theory, currents transport water at an angle to the wind
Vagn Walfrid Ekman	1902	Quantitative theory for wind-driven transport at the sea surface
Harald Sverdrup	1947	Theory for wind-driven circulation in the eastern Pacific
Henry Stommel	1948	Theory for westward intensification of wind-driven circulation (western boundary currents).
Walter Munk	1950	Quantitative theory for main features of the wind-driven circulation
Kirk Bryan	1963	Numerical models of the oceanic circulation
Bert Semtner and Robert Chervin	1988	Global, eddy-resolving, realistic model of the ocean's circulation

The western boundary currents, equatorial current systems, anticyclonic subtropical gyres, cyclonic subpolar gyres and circumpolar current systems are typical currents of the wind-driven system. Figure 2.3 is an illustration of the global surface wind-driven circulation.

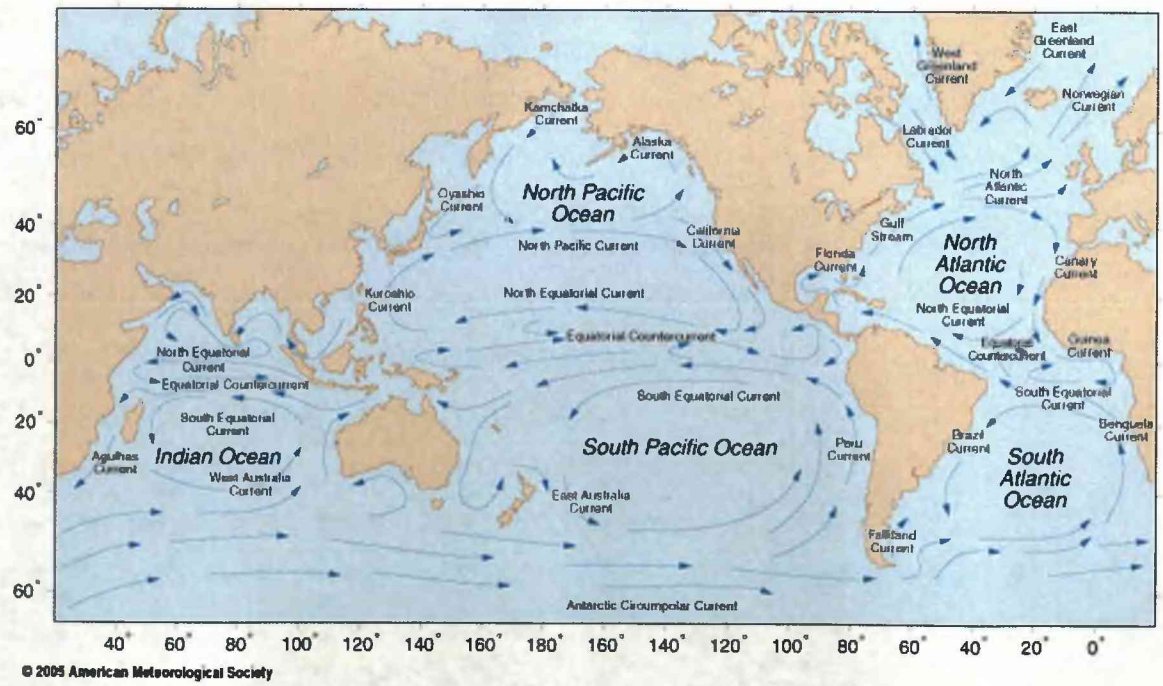

Figure 2.3: The global surface wind-driven circulation. (American Meteorological Society) (NASA, 2007).

2.1.2. The thermohaline circulation

2.1.2.1. Definition and mechanism of the THC

The term thermohaline circulation (THC) is often used in climatological and oceanographic publications to describe the deep circulation in the ocean basins. However the definition of THC is not unique, many terms have been used to describe the circulation. Pickard and Emery (1990) defined THC as the movement of waters that takes place when its density is changed by a change of temperature or of salinity in a suitable part of its bulk. Wunsch (2002), before defining the deep circulation as the circulation of mass, listed from the literature seven different, sometimes inconsistent and incomplete definitions of the concept of the global THC as following: *1-The circulation of mass, heat, and salt; 2-The abyssal circulation; 3-The meridional overturning circulation of mass; 4-The global conveyor, that is, the diffusely defined gross property movements in the ocean that together carry heat and moisture from low to high latitudes; 5-The circulation driven by surface buoyancy forcing; 6-The circulation driven by density and/or pressure differences in the deep ocean; 7-The net export, by the North Atlantic, of a chemical substance such as the element protactinium.* Stewart (2006) gave four definitions of THC such as *1-Abyssal circulation; 2-Thermohaline circulation; 3-Meridional overturning circulation; and 4-Global conveyor.* Therefore THC seems to be the most widely used but the concept has not been clearly defined, and the term is widely misused (Wunsch, 2002; Stewart, 2006).

Despite many different definitions of the THC having been given as mentioned above, the mechanism by which the THC is formed is widely agreed. The THC starts from high latitude North Atlantic and Southern Ocean where intense ocean heat loss to the atmosphere combined with salt rejection from the formation of sea ice produces cold, dense surface waters (Siedler et al., 2001) which are convectively unstable (Wunsch, 2002). When these waters become dense enough they sink down to form the deep and bottom waters. These waters then spread out to fill up the deep global ocean. As a consequence of mass conservation the surface waters from low latitude will then flow poleward into these regions to replace this spreading deep water.

Wallace Broecker in order to make an illustration for an article about the Younger Dryas event that was published in the November 1987 issue of Natural History has expressed the global THC by the simplified diagram named 'The great ocean conveyor' (Figure 2.4) (Broecker, 1991). This diagram is not intend to be a realistic picture of warm and cold currents (even wrongly interpreted sometimes), but is a representation of the overall effect of warm and cold currents on the vertical circulation within ocean (Open University, 2002). As mentioned by Siedler et al., (2001) although this diagram oversimplifies a complex but vital component of the climate system it still has captured the public's and politicians' imagination.

2.1.2.2. Some important aspects of the THC

Stewart (2006) suggested that the THC carries heat, salinity, oxygen, CO_2, and other properties from high latitudes (in winter) to lower latitudes throughout the world. This has very important consequences such as:

- The contrast between the cold-deep water and the warm-surface waters determines the stratification of the ocean which strongly influences ocean dynamics.
- The volume of deep water is far larger than the volume of surface water. Therefore although currents in the deep ocean are relatively weak, they have transports comparable to the surface transports.
- The fluxes of heat and other variables carried by the deep circulation influences the Earth's heat budget and climate. The fluxes vary from decades to centuries to millennia, and this variability is thought to modulate climate over such time intervals. The ocean may be the primary cause of variability over times ranging from years to decades, and it may have helped modulate ice-age climate.

Two aspects of the THC are especially important for understanding the Earth's climate and its possible response to increased carbon dioxide CO_2 in the atmosphere: i) the ability of cold water to store CO_2 absorbed from the atmosphere, and ii) the ability of deep currents to modulate the heat transported from the tropics to high latitudes (Stewart, 2006).

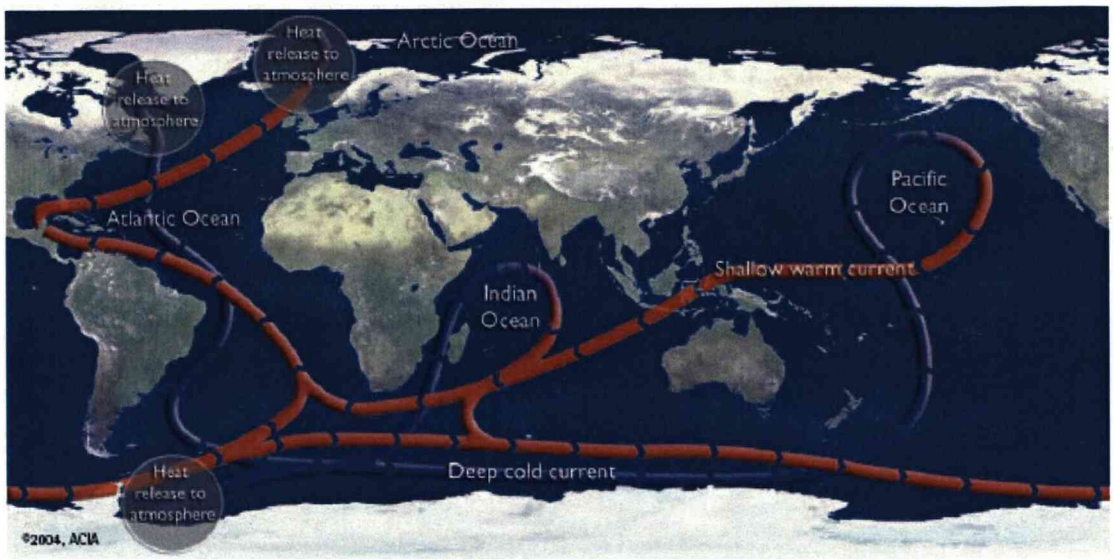

Figure 2.4: The global thermohaline circulation proposed by Wallace Broecker (ACIA, 2007).

2.1.3 Circulation system in the Pacific Ocean

2.1.3.1. Western boundary currents

Western boundary currents (poleward are warm and equatorward are cold) are deep-reaching, narrow, and fast flowing surface currents that occur on the west side of the ocean basins. All western boundary currents have a number of features in common: They flow as swift narrow streams along the western continent of ocean basins; They are the deepest-reaching ocean surface flows, extending up to 1000 metres below the ocean surface (PhysicalGeography.net, 2007), well below the thermocline; they separate at some point and continue into the open ocean as narrow jets, developing instabilities along their paths. These features result from general hydrodynamic principles and reflect the balance of forces in the western boundary regions of the subtropical and subpolar gyres. Additional characteristics are imposed by the topography that gives each boundary current its own individuality (Tomczak and Godfrey, 2001).

The well-known western boundary current in the Pacific Ocean is the Kuroshio Current, also called the Japan Current (Figure 2.5). It is the second strongest western boundary current in the world after the Gulf Stream and is famous for being strong and fast flowing. The Kuroshio Current is part of a large, warm current circulating in the North Pacific Ocean. The current begins where the North Equatorial Current approaches the Philippines and continues northward east of Taiwan. It crosses the

ridge that connects Taiwan with the Okinawa Islands and Kyushu and continues along the continental rise east of the East China Sea. The current separates into two branches near 30°N: the Tsushima branch (east of Kyushu) and the South of Kyushu branch. The South of Kyushu branch passes through Tokara Strait and comes along the continental rise of Japan to the Izu Ridge (south of Honshu). After passing the ridge the current reaches to the separation point (near 35°N) where it leaves the Japanese coast to define the transition from the Kuroshio proper current into the Kuroshio Extension which basically is a strong eastward jet flow. The Kuroshio Extension continues into open water as a free inertial jet before ending up near 170°E (Pickard and Emery, 1990; Tomczak and Godfrey, 2001). During its pathway as the consequence of the injection of a strong jet into the relatively open water environment (the Pacific Ocean) the current becomes strongly unstable. Such jets create instabilities along their paths which develope into eddies or rings. Therefore the Kuroshio Extension also stands out as one of the regions with very high eddy energy (Tomczak and Godfrey, 2001).

As with other western boundary currents, the volume transport of the Kuroshio Current system increases along its path (Tomczak and Godfrey, 2001). The volume transport of the Kuroshio Current itself is about 40Sv (Pickard and Emery, 1990) and of the Kuroshio Extension varies between 57Sv (Tomczak and Godfrey, 2001) to 65 Sv (Pickard and Emery, 1990).

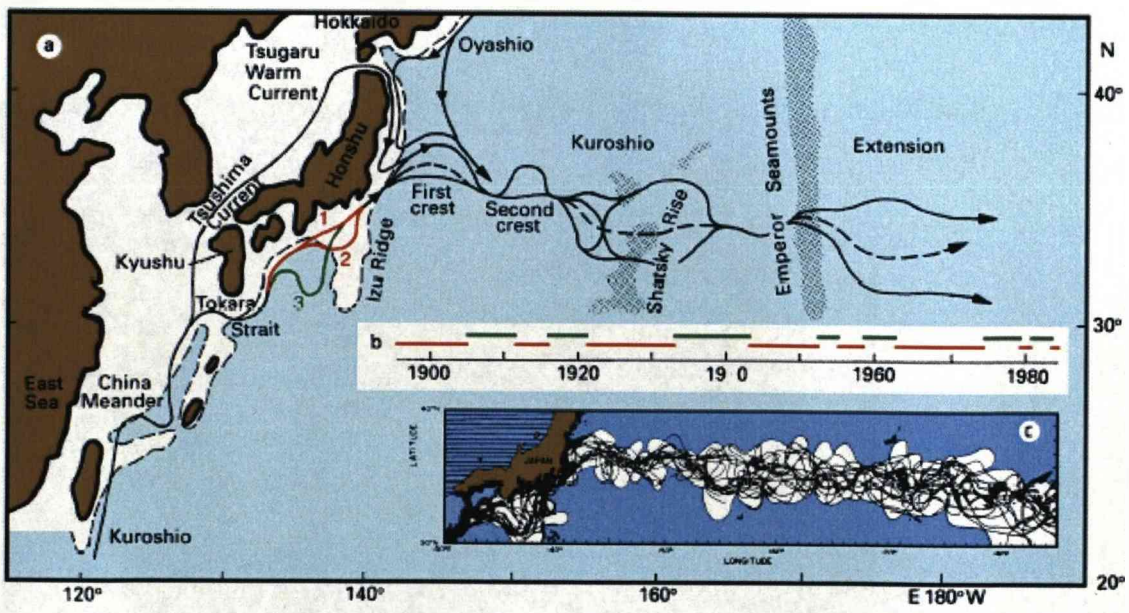

Figure 2.5: The Kuroshio Current. Adapted from Kawai (1972) and Mizuno and White (1983) (source: Tomczak and Godfrey, 2001).

2.1.3.2. The equatorial current system

The Pacific equatorial current system is recognised to include at least four major currents, three of which extend to the surface and one of which is below the surface. The three major upper-layer currents are the westward-flowing *North Equatorial Current* (NEC) between about 20°N to 8°N, the westward-flowing *South Equatorial Current* (SEC) from about 3°N to 10°S, and the narrower *North Equatorial Counter Current* (NECC) flowing to the east between them, and the fourth current is the *Equatorial Undercurrent* (EUC) (Pickard and Emery, 1990). In addition to above four major current are the weak, eastward surface *South Equatorial Counter Current* (SECC) and the weak westward-flowing *Equatorial Intermediate Current* (EIC) (Tomczak and Godfrey, 2001).

The major westward components of the equatorial current system (the NEC and the SEC) are directly wind-driven and respond quickly to variations in the wind field. They are therefore strongly seasonal and reach their greatest strength during the winter of their respective hemispheres when the trade wind is strongest. The NEC carries about 45 Sv with speeds of 0.3 m/s or less; it is strongest in February. The SEC is strongest in August when it reaches speeds of 0.6 m/s. Its transport at the longitude of Hawaii (155°W) is then about 27 Sv; this decreases to 7 Sv in February (Tomczak and Godfrey, 2001).

The *EUC* is a swift flowing ribbon of water extending over a distance of about 14,000 km along the Equator with a thickness of only 200 m and a width of at most 400 km (Tomczak and Godfrey, 2001; Stewart, 2006). The current core is found at 200 m depth in the west, rises to 40 m or less in the east and shows typical speeds of up to 1.5 m/s. Surface flow above the EUC is usually to the west, and the EUC does not appear in reports of ship drift. Although it is the swiftest of all equatorial currents its existence remained unknown to oceanographers until 1952 when it was discovered by Townsend Cromwell and Ray Montgomery (Tomczak and Godfrey, 2001; Stewart, 2006).

The second most important eastward flow in the equatorial current system is the NECC. It is prominent in the integrated flow which shows it being fed by western boundary currents both from the south and the north. In its formation region the

NECC participates in the Mindanao Eddy. At its other end it turns north on approaching the central American shelf, creating cyclonic flow close to the continent. The NECC varies seasonally in strength and position. During February - April when the Northwest Monsoon prevents the South Equatorial Current from feeding the NECC it is fed only from the north. It is then restricted to 4-6°N with a volume transport of 15 Sv and maximum speeds below 0.2 m/s; east of 110°W it disappears altogether. During May - January the NECC is then fed from both hemispheres and flows between 5°N and 10°N with surface speeds of 0.4 - 0.6 m/s (Tomczak and Godfrey, 2001).

2.1.3.3. El Niño/Southern Oscillation (ENSO) and La Niña

One important phenomenon that could not avoid being mentioned when discussing the Pacific Ocean is El Niño, an abnormal warming of the surface ocean waters in the eastern tropical Pacific, which is one part of the Southern Oscillation.

Originally, the name El Niño meaning the 'Christ Child' or 'The Boy' (Open University, 2002) was coined in the late 1800s by fishermen along the coast of Peru to refer to a seasonal invasion of warm southward ocean current that displaced the north-flowing cold current in which they normally fished; typically this would happen around Christmas. Today, the term no longer refers to the local seasonal current shift but to part of a phenomenon known as El Niño-Southern Oscillation (ENSO), a continual but irregular cycle of shifts in ocean and atmospheric conditions that affect the globe. Its counterpart--effects associated with colder-than-usual sea surface temperatures in the region--was labelled "La Niña" (or "little girl") as recently as 1985 (NAS, 2000).

As described by the Open University (2002); NOAA (2007); TAO (2007) El Niño events are perturbations or disruption of the ocean-atmosphere system resulting from interaction between the surface layers of the ocean and the overlying atmosphere in the tropical Pacific. It is the internal dynamics of the coupled ocean-atmosphere system that determine the onset and termination of El Niño events. The physical processes are complicated, but they involve unstable air-sea interaction and planetary scale oceanic waves. Up to now it is not yet known whether the perturbations originate in the atmosphere or the ocean (Open University, 2002) or in other words

we do not know why El Niño events begin (TAO, 2007). The most obvious sign that an El Nino event is underway is the appearance of unusually warm surface water off the coast of Ecuador and Peru, occurring irregularly, approximately every two to seven years (Open University, 2002; NOAA, 2005) within a few months of Christmas (Open University, 2002).

El Niño has important consequences for weather and climate around the globe. Among these consequences is increasing rainfall across the southern tier of the United States and in Peru, which has caused destructive flooding, and drought in the West Pacific, sometimes associated with devastating bush fires in Australia. Observations of conditions in the tropical Pacific are considered essential for the prediction of short term (a few months to 1 year) climate variations (TAO, 2007).

La Niña is sometimes called El Viejo (the old one), anti-El Niño, or simply "a cold event" or "a cold episode". It is characterized by unusually cold ocean temperatures in the Equatorial Pacific, compared to El Niño, which is characterized by unusually warm ocean temperatures in the Equatorial Pacific. La Niña occurs almost as often as El Niño, but has been lesser known. The impacts of La Niña to the global climate tend to be opposite to those of El Niño impacts (TAO, 2007).

To provide necessary data for improving detection, understanding and prediction of El Niño and La Niña, NOAA operates a network of buoys which measure temperature, currents and winds in the equatorial band. The TAO (the Tropical Atmosphere Ocean project) array (which took 10 years to build from 1984 to 1994, has been functioning since 1994, and was renamed as the TAO/TRITON array on 1 January 2000) consists of approximately 70 moorings in the Tropical Pacific Ocean, telemetering oceanographic and meteorological data to shore in real-time via the Argos satellite system. These daily real-time data and graphic displays from the TAO/TRITON array are freely available to the research community, operational forecasting community, and the general public (TAO, 2007).

Figure 2.6 below shows the mean and anomalies of sea surface temperature from 1986 to present, showing El Niño events 1986-1987, 1991-1992, 1993, 1994 and 1997 and La Niña events in 1985 and 1995

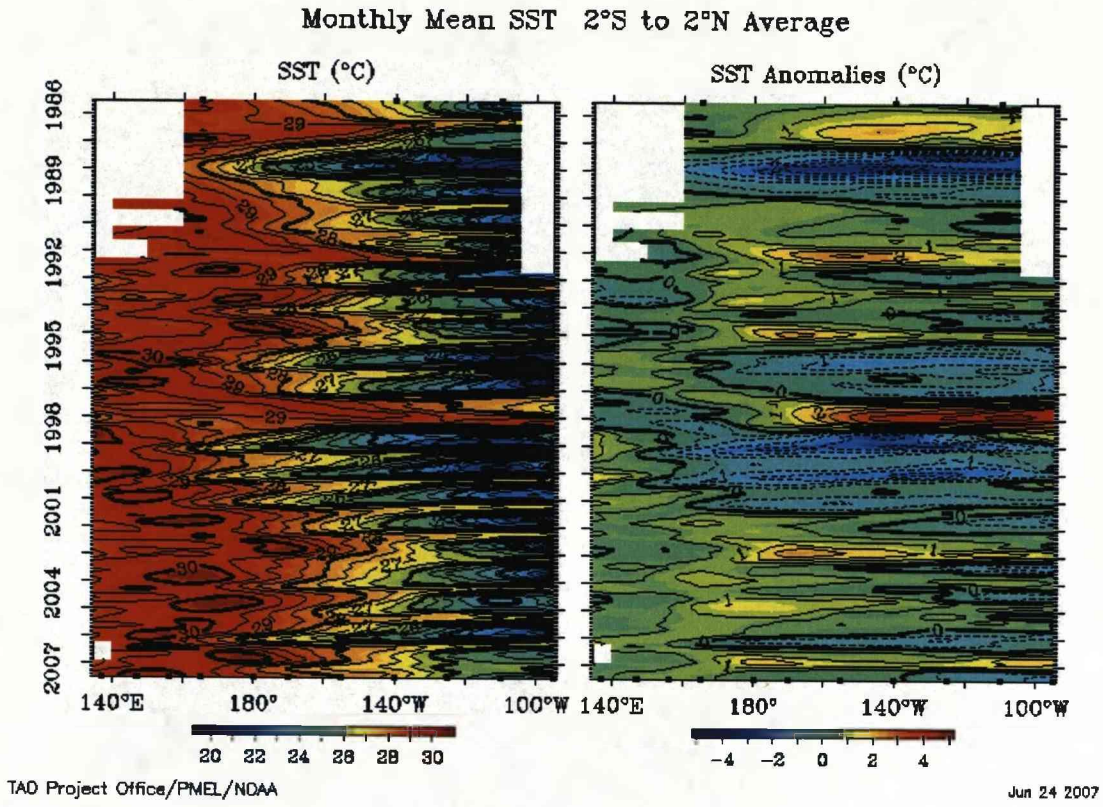

Figure 2.6: Recent El Niño & La Niña events (mean and anomalies of sea surface temperature) (TAO, 2007).

2.1.4 Circulation system in the Indian Ocean

In comparison with others the Indian Ocean is the smallest of all oceans (Tomczak and Godfrey, 2001). The circulation and transport of heat in the Indian Ocean is unique because the Asian landmass blocks the ocean in the north so currents cannot carry tropical heat to a higher northern latitude as in the Atlantic and Pacific Oceans. Otherwise, the Indian Ocean receives extra heat from Pacific Ocean through Indonesian throughflow. The other difference is the seasonal reversal of the monsoon winds and its effects on the ocean currents in the northern hemisphere to make the surface currents change seasonally in response to the monsoon. Figure 2.7 shows a summary of the monsoon system and the major currents that develop in response to the wind in the Indian Ocean. The surface current system in the Indian Ocean is illustrated in the Figure 2.8.

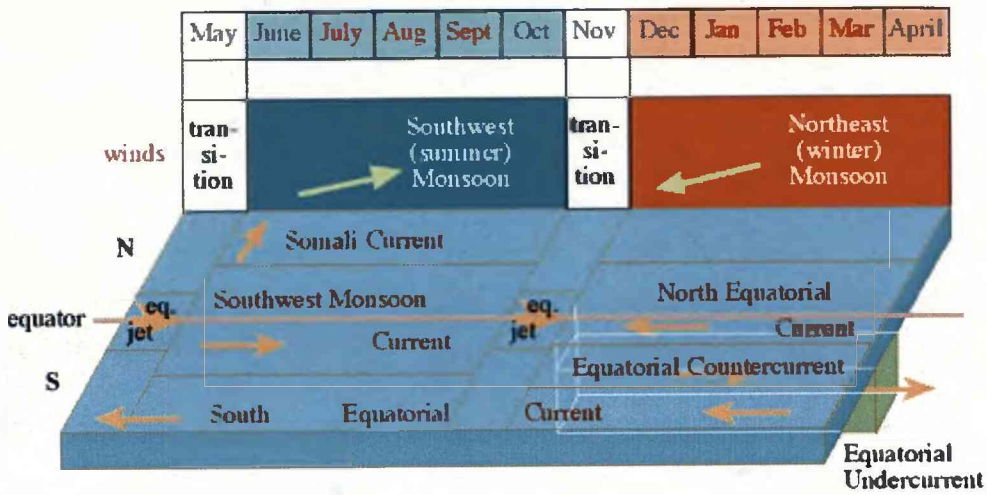

Figure 2.7: The Monsoon system and major currents that develop in respond to monsoon wind (Tomczak and Godfrey, 2001).

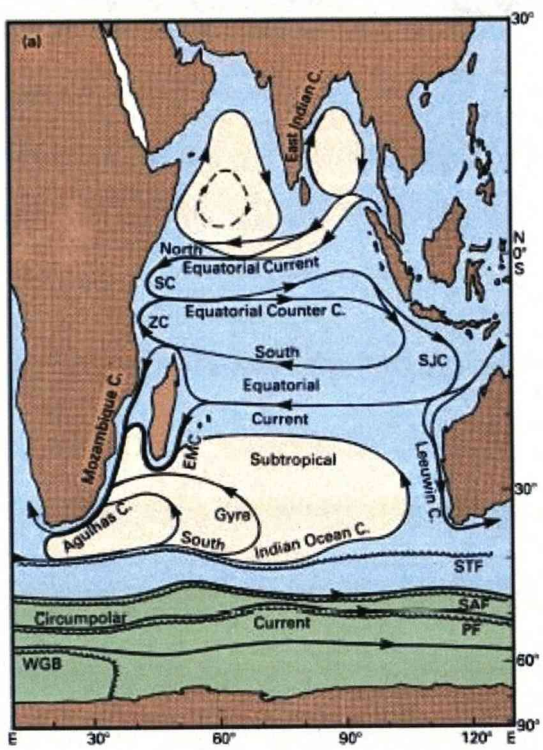

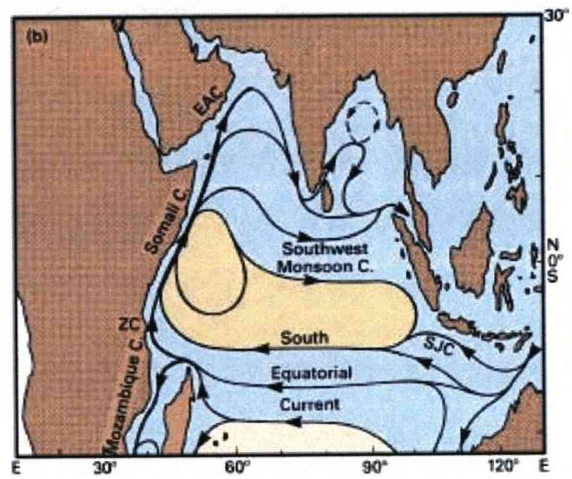

Figure 2.8: Surface currents in the Indian Ocean.

a) Northeast monsoon season
b) Late Southwest monsoon season (the circulation south of 20°S remains unchanged)

(source: Tomczak and Godfrey, 2001)

2.1.4.1. The western boundary current system

In the Indian Ocean the western boundary current system includes four main currents. The two major ones are the Somali Current (SC) and the Agulhas current, and the other two are the Mozambique and East Madagascar currents on a smaller scale (Open University, 2002). These western boundary currents begin east of

Madagascar, where the South Equatorial Current separates into the northern and southern branches. The southern branch feeds the East Madagascar Current. The contribution of the northern branch to the circulation in the southern hemisphere is the Mozambique Current which is maintained throughout the year, and the contribution to the circulation in the northern hemisphere ceases during the Northeast Monsoon season (Tomczak and Godfrey, 2001).

The most spectacular seasonal change is the reversal of the Somali Current (SC). It first occurs in early December near the Equator and expands rapidly north in January with velocities of 0.7-1.0 m/s. During the Northeast Monsoon the current flows to the southwest but for the rest of the year it flows to the northeast. The surface flow reverses in April, during the inter-monsoon period. During the Southwest Monsoon, the SC develops into an intense jet with extreme velocities of 2.0 m/s for mid-May and 3.5 m/s and more for June (observed during the Indian Ocean Experiment - INDEX, 1976-1979). During the southwest monsoon it becomes a major western boundary current with volume transport of the upper 200m reaching 60Sv (Open University, 2002).

The Agulhas Current is formed from the Mozambique current and east Madagascar current, although the contribution of the Mozambique Current is comparatively small (Tomczak and Godfrey, 2001). The Agulhas current flows poleward along the coast of Africa to the tip of South Africa to form a feature known as the "Agulhas retroflection" which is source of "Ring-like" eddies. Most of the eddies are injected into the Benguela current and are carried away north-westward into the Atlantic Ocean (Open University, 2002).

2.1.4.2. The equatorial current system

The evolution of surface currents in the Indian Ocean through the seasons is shown in Figure 2.9. During the northeast monsoon there is a westward-flowing North Equatorial Current from 8°N to the Equator (Pickard and Emery, 1990). The Current is prominent in January and March when the Northeast Monsoon is fully established. It runs as a narrow current of about 0.3 m/s from Malacca Strait to southern Sri Lanka, where it bends southward and accelerates to reach 0.5 - 0.8 m/s between 2°S

and 5°N in the region between 60°E and 75°E (Tomczak and Godfrey, 2001). The South Equatorial Current occupies the region south of 8°S to between 15 and 20°S (Pickard and Emery, 1990) with velocities rarely exceeding 0.3 m/s. Between these westward flows is the eastward-flowing Equatorial Countercurrent from the Equator to 8°S (Pickard and Emery, 1990) with 0.5 - 0.8 m/s in the west but getting weaker in the east; in January it does not reach beyond 70°E, being opposed in the east by weak westward flow (Figure 2.9a) (Tomczak and Godfrey, 2001).

The transition from Northeast to Southwest Monsoon (from early April until late June) is characterized by the intense Indian Equatorial Jet (Figure 2.9c; Figure 2.10a), first described by Wyrtki (1973), with velocities of 0.7 m/s or more. It is possible that in any particular year the jet appears within the three-month window April - June as a feature of shorter (one month) duration with higher peak velocities. The jet converges at the Equator, away from the Equator the current speed falls off to less than 0.2 m/s at 3°S or 3°N (Tomczak and Godfrey, 2001).

During the southwest monsoon the flow north of the Equator is reversed. When the Southwest Monsoon is fully established during July and September the entire region north of 5°S (Tomczak and Godfrey, 2001) or 7°S (Pickard and Emery, 1990) is dominated by the eastward-flowing Southwest Monsoon Current. Velocities in the Southwest Monsoon Current are generally close to 0.2 - 0.3 m/s, but the acceleration in velocity from 0.5-1.0 m/s occurs south and southeast of Sri Lanka. The South Equatorial Current expands slightly towards the north, reaching 6°S (Tomczak and Godfrey, 2001) in September. The SEC continues to the west south of 7°S but is stronger than during the north-east monsoon (Tomczak and Godfrey, 2001).

The transition before the onset of the Northeast Monsoon (Figure 2.9e; Figure 2.10b) is again characterized by the Equatorial Jet. Concentrating all eastward flow in a 600 km wide band along the Equator it reaches its peak in November with velocities of 1.0-1.3 m/s and disappears in early January, when the annual cycle is repeated (Tomczak and Godfrey, 2001).

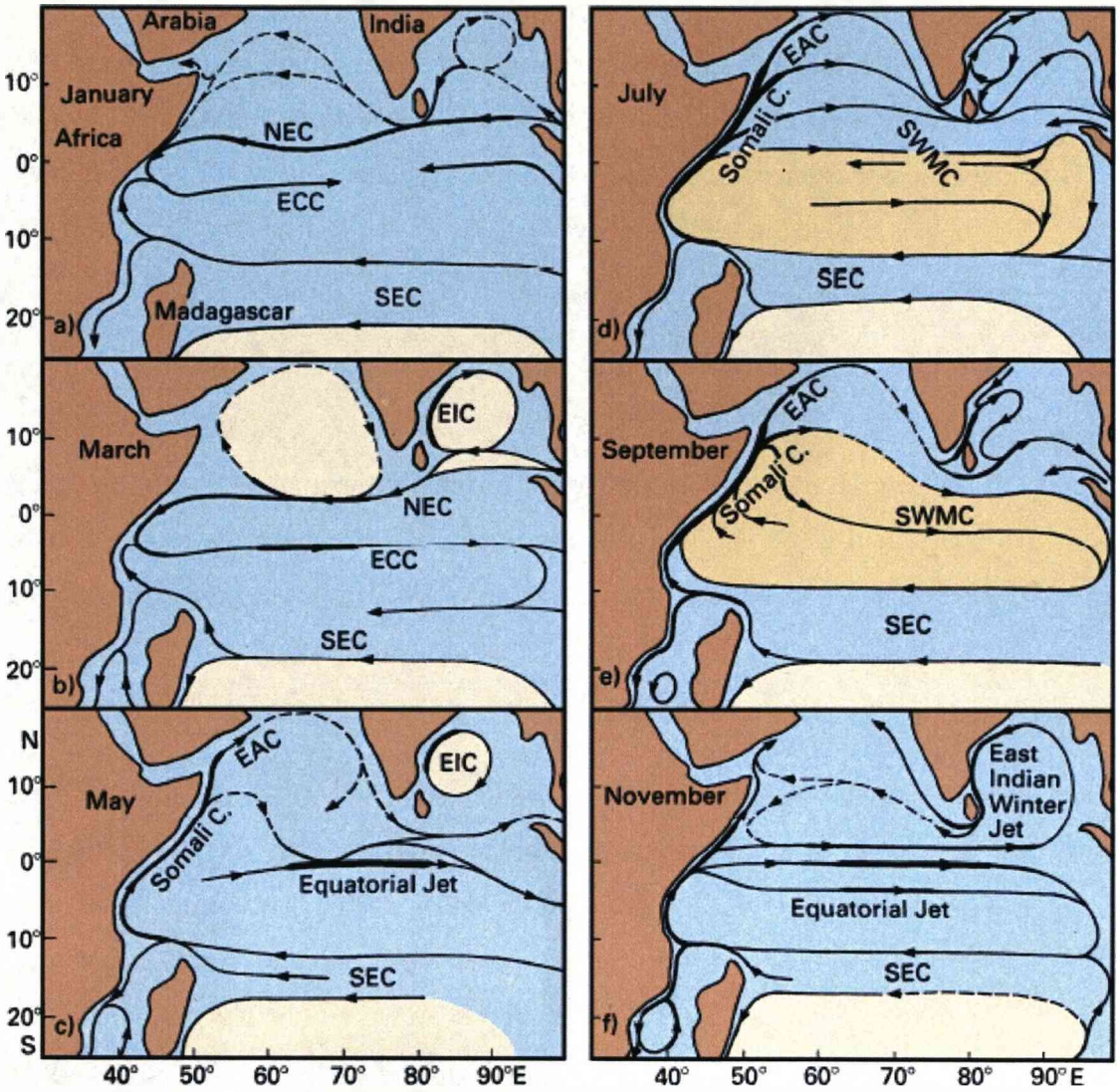

Figure 2.9: Surface currents in the northern Indian Ocean as derived from ship drift data. Adapted from Cutler and Swallow (1984). (source: Tomczak and Godfrey, 2001).

The Equatorial undercurrent is found in the thermocline during the north-east monsoon period. It is weaker than those in the Pacific Ocean and Atlantic Ocean (Pickard and Godfrey, 1990). The first direct observations of the undercurrent were made during the International Indian Ocean Expedition (1959-1965). At that time it was seen to be an ocean-wide feature, but later observations showed that this may not have been typical. In general, in the Indian Ocean, the undercurrent seems to be a stronger, more long-live flow in the western part of the ocean than in the central or eastern parts. The undercurrent is usually associated with the persistent trade winds from the east. This westward stress at the surface, and corresponding elevation of the

sea surface in the west creates a zonal pressure gradient between the boundaries. In the Indian Ocean such a zonal pressure gradient (similar to those in the Pacific or the Atlantic), can only be established during the northeast monsoon. Thus, the presence of the undercurrent is related to the seasonal change of wind stress. In the southwest monsoon with the general flow to the east at the Equator the undercurrent finally disappears (Pickard and Godfrey, 1990; Tomczak and Godfrey, 2001).

2.1.4.3. The eastern boundary current

The well-known eastern boundary current in the Indian Ocean, along the western Australian coast, is known as the Leeuwin Current. However the dynamics of the Leeuwin Current are very unusual. It is a warm ocean current that flows strongly southwards along the Western Australian coast, before turning eastwards at Cape Leeuwin and continuing into the Great Australian Bight where its influence extends as far as Tasmania.

The strength of the Leeuwin Current varies through the year, with the weakest southwards flow occurring from November to March when the winds tend to blow strongly northwards. The time of greatest flow is in the autumn and winter when the opposing winds are weakest. The current frequently breaks out to sea, forming both clockwise and anti-clockwise eddies. Typical current speeds in the Leeuwin Current and its eddies are about 0.5 m/s, although speeds of 1 m/s are common. The annual mean transport of the Leeuwin Current is estimated at 5 Sv (Tomczak and Godfrey, 2001).

The Leeuwin Current is about 300 m deep and beneath it is a northwards countercurrent called the Leeuwin Undercurrent. The 'core' of the Leeuwin Current can generally be detected as a peak in the surface temperature with a strong temperature decrease further offshore. The surface temperature difference across the Current is about 1K at North West Cape, 2-3K at Fremantle and can be over 4K off Albany in the Great Australian Bight (CSIRO, 2001).

The Leeuwin Current is also known to be influenced by El Niño conditions, with slightly lower sea levels along the Western Australian coast and a weaker Leeuwin Current (CSIRO, 2001).

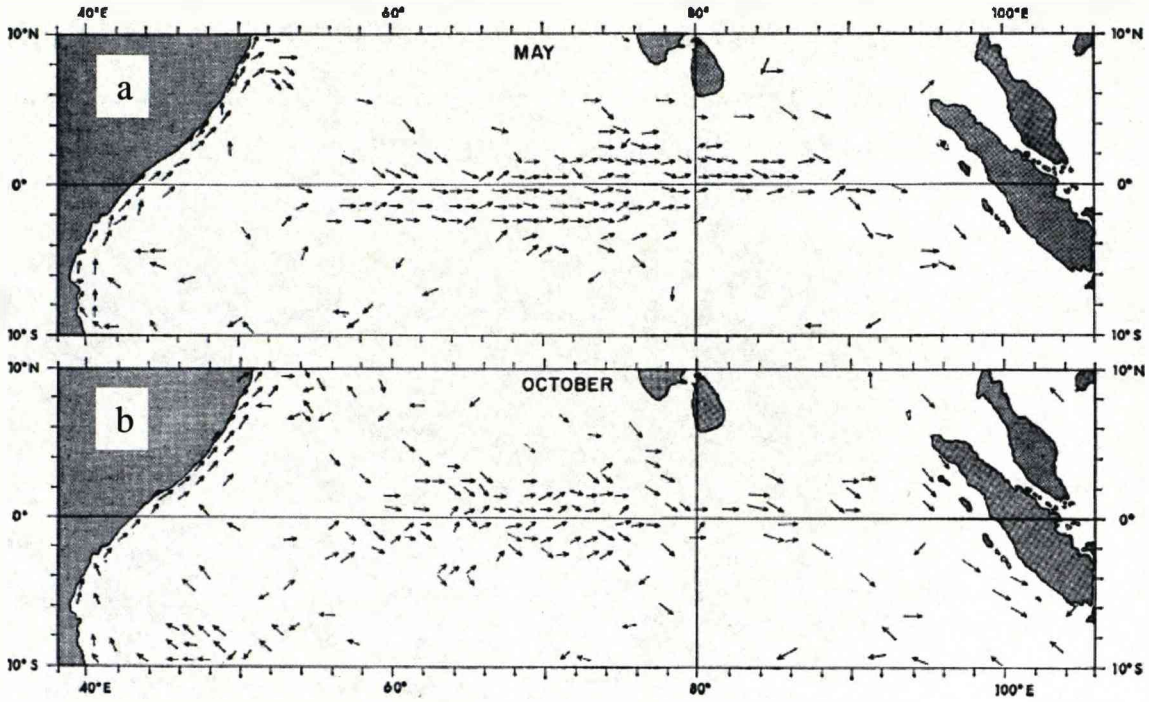

Figure 2.10: The equatorial jet in the Indian Ocean in the transition period (May and October) (Wyrtki, 1973).

2.2. The Southeast Asian waters

2.2.1 Definition and configuration of the Southeast Asian waters

The Southeast Asian region consists of the waters and highly fragmented land and islands lying in between Asia and Australia, and between the Pacific and the Indian Oceans. Physically, the region is divided into the continental part of mainland Asia, which consists of Myanmar, Thailand, Laos, Cambodia and Vietnam; and the rest of the region, regarded as the archipelago of South-East Asia including the Malaysian peninsular, Java, Sumatra, Borneo, Timor and the Philippines (Figure 2.11).

In oceanographic terms, the S.E. Asian waters are part of the Pacific Ocean, and are separated from the Indian Ocean by the islands of Sumatra, Java and the Lesser Sunda. As described by Wyrtki [1961] *"The South East Asian waters consist of the South China Sea, the Java sea, the Sulu sea, the Philippine waters, the Celebes sea, the Banda sea, the Flores sea, the Arafura sea, the Timor sea, and the Andaman sea. The whole region comprises an area of 8.94 million square kilometres which is 2.5 percent of the surface of all oceans"*

In the SE Asian wasters, practically all types of topographical features are to be found such as shelves, deep sea basin, troughs, trenches, sills, and continental slope of various shapes, volcanic and coral islands (Wyrtki, 1961).

Figure 2.11: The Southeast Asian Region.
(http://www.lib.utexas.edu/maps/middle_east_and_asia/southeastasia_ref01.pdf).

2.2.2. Water circulation in the region

Wyrtki (1961) constructed the surface current charts for the region based on the available current atlases of the U.S Navy Hydrographic Office (1944, 1950), Netherlands Meteorological Institute (1936, 1949, 1952), U.S. Weather Bureau (1938), etc. In his works the region has been divided into three main parts as following: the North-eastern Indian Ocean, the Western North Pacific Ocean and the Southeast Asian Waters. In the framework of this research project we put most of the attention in the circulation in the Southeast Asian Waters.

2.2.2.1. Surface current of the Southeast Asian Waters

2.2.2.1.1. The South China Sea

The South China Sea (SCS), located between the Asian landmass to the north and west, the Philippine Islands to the east, Borneo to the southeast, and Sumatra to the south, is the largest marginal sea in the Southeast Asian Waters. It connects in the south with the Sulu and Java Seas through a number of shallow passages and in the north with the Pacific Ocean through the deep Luzon Strait. The circulation in the SCS is mainly driven by the Asian monsoons (north-easterly in winter and south-westerly in summer), the Kuroshio intrusion and surface heat flux (Wyrtki, 1961, Bogdanov and Moroz, 1995, Wu, 1998; Fang, 1998; Qu, 2000; Wang G. et al, 2003; Wang H. et al, 2004; Gan et al, 2006).

The early studies on the SCS's circulation were mostly based on the observational drift current data. Dale (1956) presented monthly schematic surface current charts for the SCS. Though the data used were very old, the basic patterns do not differ from the recently published atlas (Fang, 1998). Wyrtki (1961) made a comprehensive study of the physical oceanography of Southeast Asian Waters. He presented bimonthly charts for surface currents and volume transports (Plates 1 to 6 - Appendix). The circulation pattern in the SCS has recently attracted many oceanographers' interest (Shaw and Chao, 1994; Chao, 1996, Metzger and Hurlburt, 1996; Wu, 1998; Fang, 1998; Chu, 1999; Qu, 2000; Wang G. et al, 2003; Wang H. et al, 2004, Fang, 2005; Gan et al, 2006; etc.), and a number of new findings and concepts have been presented.

Fang (1998) reviewed the studies (both observational and models) on the SCS Upper Ocean Circulation to propose a schematic diagram (Figure 2.12) of the SCS circulation pattern in both winter and summer. In the Fang's diagram the main SCS circulation patterns in summer (winter) from north to south is presented as follows: the SCS north-eastward (south-westward) coastal current, the SCS warm current, the Dongsha current, the Luzon cold ring, the south eastern Dongsha cyclone, the southern SCS anticyclonic gyre (cyclonic gyre) (Wang et al, 2003).

In general, on a seasonal time scale, the surface circulation of the SCS is cyclonic in winter and anticyclonic in summer. In winter, when the Northeast Monsoon is fully developed over the SCS, the northern part of the SCS is intruded by Kuroshio Current through Luzon strait (Dale, 1956; Wyrtki, 1961). The current is southward along the continental margin from China to southern Vietnam (Shaw and Chao, 1994). During this season most of the southern SCS is occupied by the SCS Southern Cyclonic Gyre. A weaker anti-cyclonic gyre may exist near the main gyre, then along the border of these two gyres there exists a strong upwind current called the Natuna Off-Shelf Current flowing north-eastward (Fang, 1998). In summer, when the monsoon reverses its direction the southern part of the SCS is occupied by the SCS Southern Anti-Cyclonic Gyre (Fang, 1998), while in the north the current reverses its direction from south-westward to north-eastward (Dale, 1956; Wyrtki, 1961).

In both seasons, the western edge of the main gyres in the SCS intensify along the western boundary of the basin called the Southeast Vietnam Off-Shore Current and located at latitude of about 11° N. In winter, this current follows the western boundary throughout with velocity often exceeding 100cm/s (Wyrtki, 1961), but in summer the northward boundary current separates it from the coast east of central Vietnam between 11°N to 14°N (Wyrtki, 1961; Shaw and Chao, 1994).

The circulation in the central SCS is also governed by monsoon winds and the interaction between the circulation systems in northern and southern SCS. However the basic features of the circulation in the central SCS are not yet well understood, though some results based on dynamic calculation and numerical simulation have been presented (Fang, 1998).

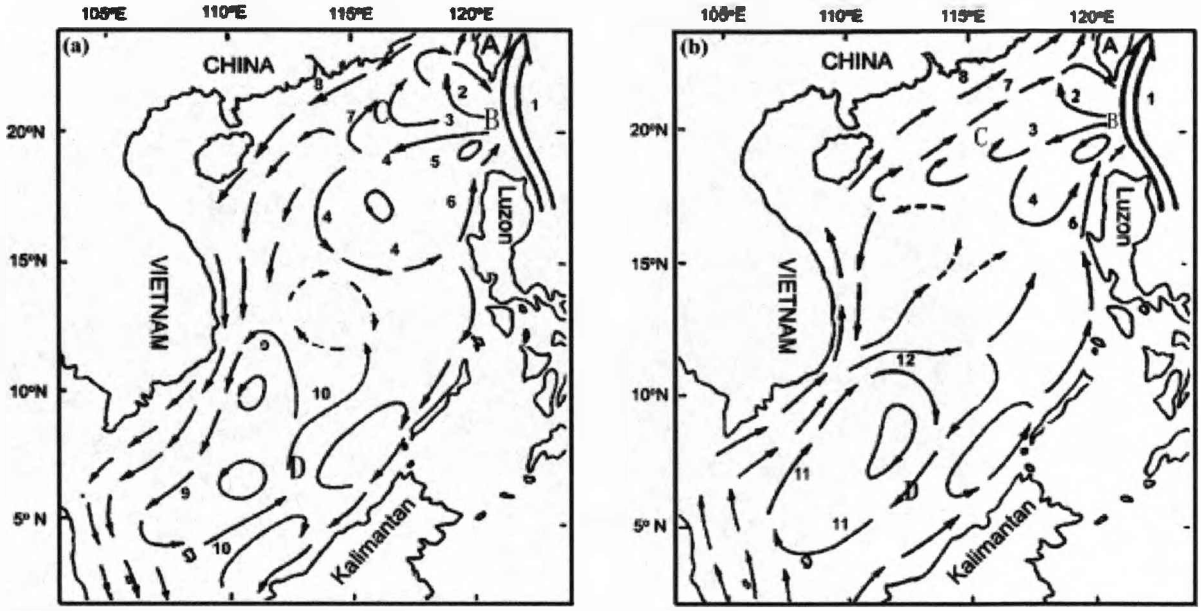

Figure 2.12. Schematic diagrams of the South China Sea circulation patterns in (a) winter; (b) summer. 1. Kuroshio current, 2. loop current, 3. SCS branch of Kuroshio or Dongsha current, 4. NW Luzon cyclonic gyre, 5. NW Luzon cyclonic eddy, 6. NW Luzon coastal current, 7. SCS warm current, 8. Guangdong coastal current, 9. SCS southern cyclonic gyres, 10. Natuna off-shelf current, 11. SCS southern anticyclonic gyre, 12. SE Vietnam offshore current. A. Taiwan Island, B. Bashi Channel, C. Dongsha Archipelago, D. Spratly Archipelago (Fang et al., 1998).

2.2.2.1.2. The Java Sea

The Java Sea is essentially smaller than the SCS, and the current may occupy its full width without development of larger eddies and counter current (Wyrtki, 1961). The circulation and hydrography are determined by the annual cycle of monsoon winds, with currents flowing westward from June to August and eastward during the rest of the year (Tomczak and Godfrey, 2001) or slightly differently as urged by Wyrtki (1961) westward from May to September and eastward from November to March.

In the transition time (April and October) the direction of the flow changes and eddies occur. Normally in these months a current towards the east prevails off the coast of Java and a current towards the west off the coast of Borneo (Wyrtki, 1961).

In the small passages between Borneo and Sumatra in the Karimata and Gaspar straits, when the winds are fresh the velocity of the currents reach often 100cm/s, especially during the full north monsoon (Wyrtki, 1961).

2.2.2.1.3. The Makassar Strait

As described by Wyrtki (1961) the flow in the Makassar Strait is directed to the south during the whole year and the velocities are normally small with minimal velocities appearing in December/January and May. The strongest current occurs in February and March and from July to September. The water masses leaving the strait in the south flow during the southeast monsoon into the Java Sea and during the northeast monsoon into the Flores Sea.

The current mooring results of the INSTANT (2003-2006) and ARLINDO (1993-1994; 1996-1998; 1998-2007) projects are the main recent research on currents in the region. Figure 2.13 show a time series of velocity of current mooring at the Makassar Strait from 1996 to 1998 of the ARLINDO project.

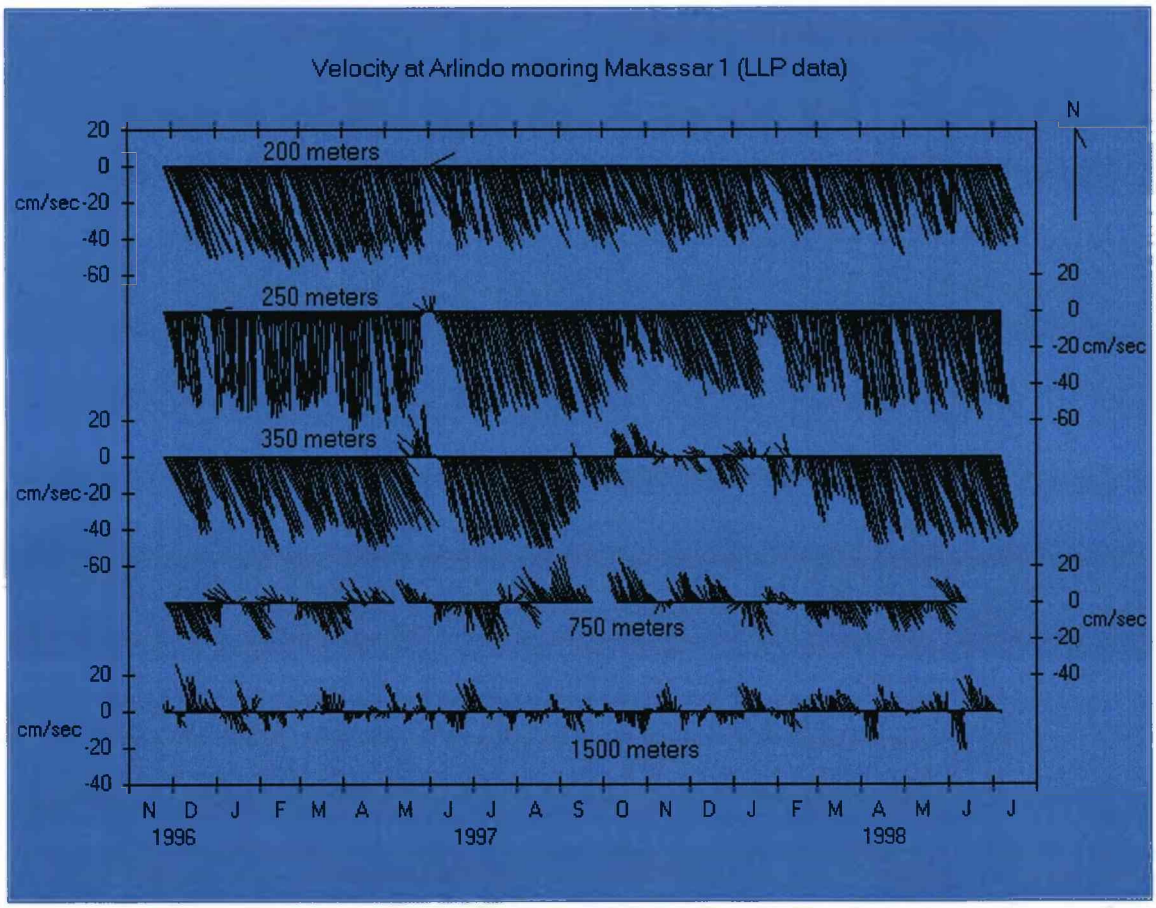

Figure 2.13: The velocity at different depths at Makassar Strait (ARLINDO current mooring).
(Source: http://cmdac.oce.orst.edu/data/datarpt/makassar/mak1/m1aa_gif.htm)

2.2.2.1.4. The Flores Sea

Over the Flores Sea west wind prevails from December to March and southeast wind in other months. Therefore from December to March a uniform current to the east exists, being remarkably intensified along the north coast of the Lesser Sunda Island. With the disappearance of the west winds in April, a weak westwards current forms under the coast of Celebes, while north of the Lesser Sunda Islands the strong current to the east is still present. Even during the full southeast monsoon in July and August this coastal current remains, but is considerably weakened. During this period the west-going drift current in the north part of the Flores Sea occupies most of its width, and in August has velocity of about 75cm/s. With the decrease of the southwest monsoon the coastal current north of Lesser Sunda Island is again intensified and in October only a weak drift is to be noted south of Celebes (Wyrtki, 1961).

2.2.2.1.5. The Banda Sea

The largest and deepest Sea in the region is the Banda Sea which has depths in excess of 4500 m in the southeast (also known as the South Banda Sea) and in the northwest (the North Banda Sea), separated by a ridge of less than 3000 m depth; largest depths are near 7440 m in the south and 5800 m in the north (Tomczak and Godfrey, 2001). The Banda Sea is entered during the northwest monsoon by water masses out of the Flores Sea. A part of this water flows north of Buru into the Ceram Sea and from there through the Halmahera Sea into the Pacific Ocean. Another part moves as a wide drift south of Ceram into the Arafura Sea. At the time of the changing of the monsoon in April the currents are so variable, that a general currents pattern can not be derived. The coastal current north of the Lesser Sunda Island turns east of Timor sharply to the south. During the southeast monsoon water masses out of the Pacific Ocean flow through the Halmahera and Ceram Seas at both sides of the island Buru into the Banda Sea and pass in a southwest direction into the Flores Sea (Wyrtki, 1961).

2.2.2.1.6. The Timor Sea

In the Timor Sea a current to the southwest prevails during the whole year, its axis runs close to the coast of Timor. From April to September the current reaches to the Australian coast, although its velocity decreases in that direction. From October to

March a weak current towards the northeast is formed off the Australian coast under the influence of winds from the southwest. The Timor Current takes its water from October to April out of the current flowing along the north coast of the Lesser Sunda Island to the east, which turns around the eastern end of Timor. Only at the time of the full development of the southeast monsoon is the Timor Current supplied by water out of the upwelling region in the Arafura and eastern Banda Seas (Wyrtki, 1961).

2.2.2.1.7. The Celebes Sea

The Celebes Sea is wide open to the Pacific Ocean and its currents enter this region. A branch of the Mindanao Current flows south of Mindanao southwestwards into the Celebes Sea. Its water is deflected to the south and later to the east in the central parts of the sea and flows back to the east along the north coast of Celebes. In the region northwest of Halmahera this coastal current joints again with the branch of the Mindanao Current coming directly from the north between the islands Sangihe and Talaut, and it receives water coming out of the Molucca Sea, all forming the root of the Counter Current. This system of circulation is maintained during the whole year, even though its extension to the west may vary. The current in the Makassar Strait is supported from February to September almost exclusively by water from this current system. But from October to January, when north winds prevail over the Celebes Sea, the eddy in which the Mindanao Current turns back to the east, it displaced to the east, and water from the Sulu Sea flows through the western part of the Celebes Sea into the Makassar Strait. In the northern part of the Celebes Sea the water movements are normally weak and irregular but movements into the Sulu Sea prevail from March to July and in the other months movements are towards the southwest (Wyrtki, 1961).

2.3. The Asian Monsoon

The Asian monsoon is a special weather phenomenon which plays a key role in affecting the livelihood of the Asian and Australian region where more than 60% of the world's population lives. The word "monsoon" is derived from an early Arabic word called "Mausin", meaning 'winds that change seasonally' (Irwin, 1968; Open University, 2002). The distinguishing feature of the monsoon is that it blows one

direction for part of the year and from the opposite direction in the other part of the year. The monsoons were known and used by Arabian, Indian and Chinese traders in their trading voyages before the Christian era (Irwin, 1968).

Whilst the seasonal pattern of the monsoon has been known to farmer and sailor through thousands of years, it is only in recent years that meteorologists have been able to explain why the monsoon occurs. Understanding of the monsoon is now possible because scientists have developed instruments which enable them to observe what is happening in the atmosphere not only at the earth's surface but also at heights miles above the earth (Irwin, 1968).

2.3.1. What causes the Monsoon?

For centuries, people have tried to understand what causes the Monsoon. Generally speaking the monsoon is basically caused by land-sea temperature differences due to heating by the solar radiation. The mechanism of the Monsoons could be briefly described by as follows:

- Because of the inclination or tilting of the earth's axis, the Sun appears to move north and south of the Equator. The Sun is directly overhead at the Equator on or about 21 March and 21 September. This is the *equinox* which literally means equal night; that is the day and night are of equal length. On or about 21 December, the sun's apparent movement has brought it directly over the Tropic of Capricorn. This is the southern hemisphere summer. On or about 21 June, the Sun is directly over the Tropic of Cancer and this is the northern hemisphere summer. The movement is referred to as the apparent movement of the Sun because, in fact, it is the Earth which changes inclination relative to the Sun; it is not the Sun which moves (Irwin, 1968).
- In the northern hemisphere winter, when the Sun moves over the southern hemisphere, the air over Asian landmass is cooler and denser than air over the ocean, and so the surface atmospheric pressure is greater over the continent than over the ocean. It creates low temperatures over central Asia. As temperature drops, atmospheric pressure rises and an intense high pressure system (anticyclone) develops over Siberia. This resulting pressure gradient leads to a cold air flowing out of Siberia as a north-westerly wind and turns into

north-easterly on reaching India and the coastal waters of China before heading towards Southeast Asia. This flow of air is the Northeast Monsoon. It flows from the Asian landmass crossing the Equator to the south where the air flow is turned to the left by the Coriolis force and converges with the south-east trades at about 10-20°S (Open University, 2002).

- In the northern hemisphere summer, when the Sun moves north over the Asian landmass, the land is heated more rapidly than the surrounding seas. The intense solar heating leads to scorching temperatures over the Asian landmass. As hot air expands and rises upwards, a low-pressure area develops. The south-easterly air-flow originating from the southern Indian Ocean and the Indonesian-Australian region transforms into south-westerly on crossing the Equator and flow across India, Southeast Asia before converging towards Indochina, China and Northwest Pacific to create the Southwest Monsoon.

A monsoon seasonal change is characterized by a variety of physical mechanisms which produce strong seasonal winds, a wet summer and a dry winter. All monsoons share three basic physical mechanisms: differential heating between the land and oceans; Coriolis forces due to the rotation of the Earth; and the role of water which stores and releases energy as it changes from liquid to vapour and back (latent heat). The combined effect of these three mechanisms produces the monsoon's characteristic reversals of high winds and precipitation. Scientists say that the two key ingredients needed to make a monsoon are a hot land mass and a cooler ocean.

In India, for instance, the land absorbs heat faster from the Sun than the surrounding Indian Ocean does. This causes air masses over the land to heat up, expand, and rise. As the air rises, cooler, moister, and heavier air from over the ocean will replace it. Over India, this damp, cool layer can be up to three miles (~ 5km) thick. As the cool air arrives, the winds also shift. During the dry season, the winds blow offshore, from land to sea. Then, as the monsoon begins, the winds blow onshore, from sea to land. In the case of the Indian Ocean Monsoon the first and third mechanisms produce more intense effects than in any other place in the world.

2.3.2. The Southeast Asian winter monsoon

In the Southeast Asian region, the north-eastern winter monsoon (Figure 2.14) takes place from November to March. The characteristics of the Monsoon are described by Wyrtki (1961) as follows: In October the equatorial trough begins to move rapidly southwards, and by the middle of the month, lies along a line from the centre of the Bay of Bengal to the north coast of New Guinea. North of this line northeast winds prevail, south of it still the southeast monsoon. In the Indian Ocean between the Equator and 10°N the southwest monsoon has turned so far, that it comes almost from the west. In November the equatorial trough runs clearly south of the Equator. The northeast monsoon has intensified especially over the China Sea and normally exceeds wind force 4. Over the Indian Ocean the system of the southeast monsoon has collapsed, and the southeast trades are confined to south of about 5°S. By December the equatorial trough moves further to the south and lies at about 5°S. The northeast monsoon reaches its maximal force over the China Sea, crosses the Equator as a north wind and temporarily reaches Java and the Lesser Sunda Islands. Over the Java Sea west winds prevail. The southeast trades of the Indian Ocean have retreated further to the south and reach just up to 10°S, and near the Australian northwest coast, south winds prevail. In January the north monsoon is fully developed. Over Asia a high is formed and the equatorial trough lies just north of Australia. Over the whole China Sea and over the Andaman Sea the northeast monsoon blows, and continues towards the Pacific Ocean as the northeast trades. In the China Sea wind force 5 is often exceeded. The monsoon passes the Equator as a north wind and south of it turns to the east, where it appears as the northwest monsoon. The equatorial trough lies over the Indian Ocean at about 10°S, south of which the southeast trades are found. Off the northwest coast of Australia the trades are deflected and blow almost parallel to the coast towards the northeast with only a small force. In February the equatorial trough moves northwards and lies over Java and the Lesser Sunda Islands. Over the whole region between Java and Australia southwest winds now prevail branching off from the southeast trades. North of the Equator conditions have not changed, but the strength of the monsoon has decreased. In March the southeast trades of the Indian Ocean extend further northwards and eastwards, while over the Timor and Arafura Seas northwest winds still prevail. Over the China Sea the northeast monsoon has weakened.

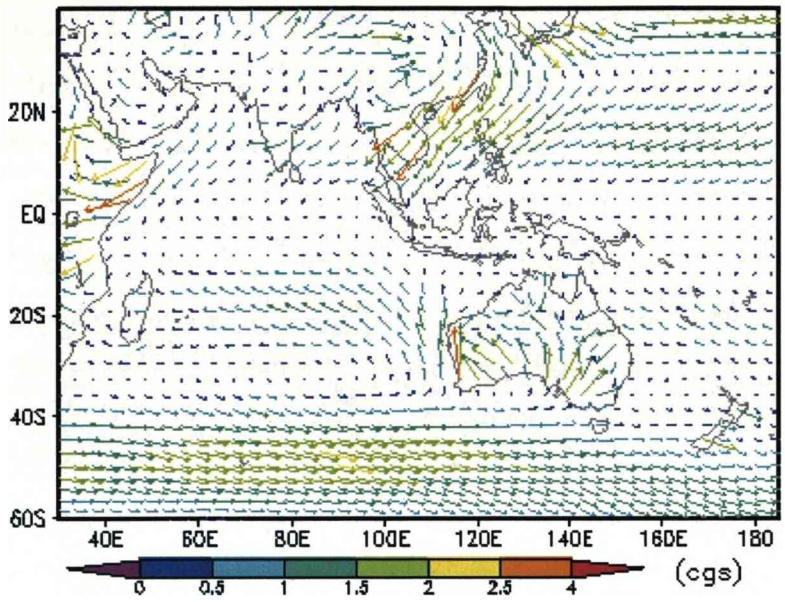

Figure 2.14: NCEP's monthly mean wind stress in December (Winter monsoon).

2.3.3. The Southeast Asian summer monsoon

The south-western summer monsoon (Figure 2.15), the stronger of the two monsoons (Open University, 2002), occurs from May to September. The Southeast Asian summer monsoon is described by Wyrtki (1961) as follows: In May, the system of the northeast winds over the China Sea and the Philippines collapses, and the south monsoon succeeds over the whole of Southeast Asia. South of the Equator the southeast monsoon blows, continuing to the Indian Ocean as the southeast trades. At the Equator south winds prevail, and north of it the southwest monsoon. In the area of the Philippines and of the Celebes Sea the winds are still weak and unsteady. In June the distribution changes slightly; the winds become stronger, and reach force 4 and more over the Arafura Sea, over the Indian Ocean, and especially over the Bay of Bengal. In July and August the south monsoon reaches its full development. In these months the low over Asia and the high over Australia are strongest and the circulation reaches its greatest strength. Over the open sea wind force 4 is often exceeded, but over the Indonesian Archipelago and over the Philippines the wind remains on the average below force 4. In September over the waters around Formosa (once called Taiwan) and Hong Kong the first northeast winds occur, indicating a weakening of the Asian low. In the other parts of the region the south monsoon only slightly loses strength.

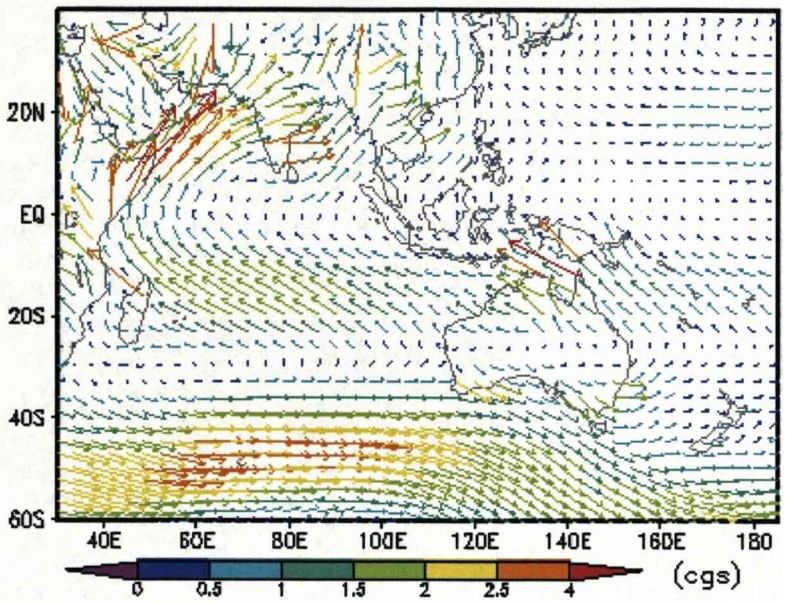

Figure 2.15: NCEP's monthly mean wind stress in July (Summer monsoon).

2.4. The Indonesian Throughflow

The Indonesian Throughflow (ITF) is an important pathway of the global thermohaline circulation. The ITF is the only low latitude tropical current system that transfers mass, heat and fresh water from one ocean basin to another and through that it transfers climate signals and their anomalies around the world's oceans. Figure 2.16 is the illustration of the surface currents in the Indonesian seas.

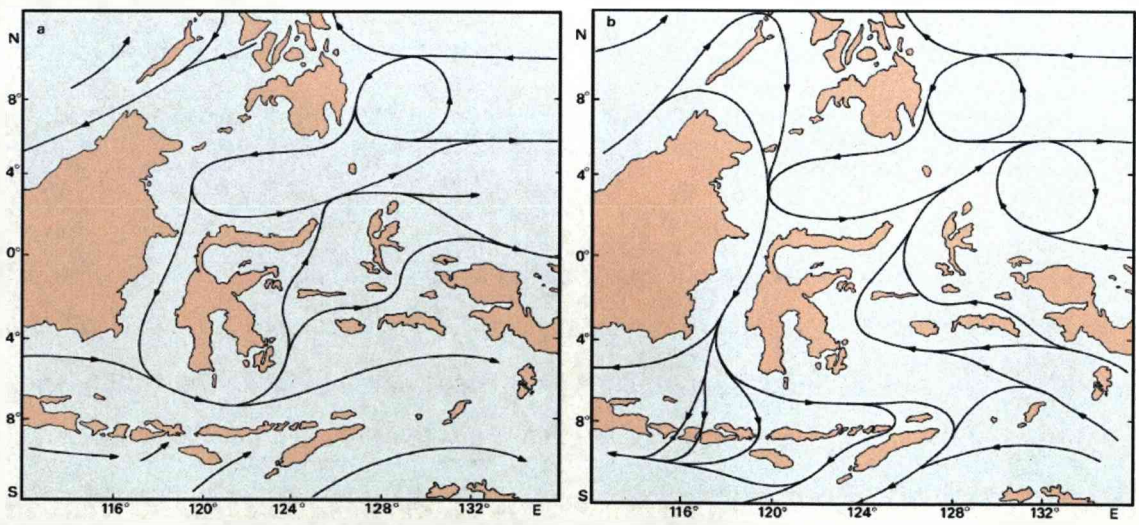

Figure 2.16 : Surface currents in the Indonesian Seas. (a) in February (north monsoon, minimum throughflow), (b) in August (south monsoon, maximum throughflow). (M. Tomczak and J. S. Godfrey, 2001).

2.4.1. Origin of the ITF

The ITF is formed within the complex equatorial current system in the western Pacific region, where part of the South Equatorial Current turns, via the Halmahera eddy, to join the North Equatorial Counter-current and where the southward branch of the Mindanao Current (MC) turns eastward to joint into the North Equatorial Counter-current.

In the western Pacific Ocean the most powerful branch of circulation is the North Equatorial Current that flows steadily during the whole year towards the Philippines. After approaching the Philippine coast the North Equatorial Current bifurcates. The large branch turns northwards to form the root of the Kuroshio Current. The other one flows south-eastwards, feeding the MC. At the entrance of the Indonesian Seas, the MC splits, one branch enter the Celebes Sea to become the main source of the ITF, the other branch continues in the direction of the main current to the south, forming the Mindanao Eddy (ME) (Wyrtki, 1961). The other powerful circulation in the western Pacific Ocean is the South Equatorial Current which flows along the coast of New Guinea island with high velocities as far as Halmahera. Here it separates into two parts, one part enters the Indonesian seas near the Halmahera Island to form another source of the ITF, the other deflected to the north, part of them then creating the Halmahera Eddy (HE), the rest joins the current returning from the Celebes Sea, then combining with the Mindanao Current to form the root of the North Equatorial Countercurrent (NECC) (Wyrtki, 1961; Godfrey, 1996; Gordon and Fine, 1996; Gordon, 2001).

The observations based on hydrography (Wyrtki, 1987; Gordon, 1986; Ffield and Gordon, 1992; Bingham and Lukas, 1994; Ilahude and Gordon, 1996; Gordon and Fine, 1996; Sprintall et al, 2004), drifters (Lukas et al., 1991), tritium content (Fine, 1985) and the numerical ocean models results (Semtner and Chervin, 1992; Hirst and Godfrey, 1993; Nof 1996) suggest that the water in the upper 500m of the ITF originates mainly from the North Pacific thermocline and intermediate waters, while the lower thermocline and deeper water masses at the eastern entrance to the Indonesian archipelago are fed from South Pacific water arriving through the eastern Maluku and Helmahera Seas with a dense water overflow at Lifamatola Passage (van

Aken et al., 1988; Ilahude and Gordon, 1996; Gordon and Fine, 1996; Hautala et al., 1996; Gordon and McClean, 1999; Gordon et al, 2003).

Inside the Indonesian Seas, the main path of the ITF is through the westernmost Celebes Sea and Makassar Strait (Ffield and Gordon, 1992). While part of the flow enters the Indian Ocean through Lombok Strait (Murray and Arief, 1998; Murray et al., 1989; Meyers et al., 1995; Arief and Murray, 1996), the bulk of the flow turns eastward via the Flores Sea towards the Banda Sea. Then finally, the flow exits into the Indian Ocean through the Ombai Strait and Timor Passage to join the SEC (Fieux et al., 1994; Hautala et al., 1996; Gordon and Fine; 1996, Hautala et al., 2001; Potemra et al., 2003).

2.4.2. Which physical processes drive the ITF?

In his early work, based on hydrographic observations, sea level records, drifts and climatological wind patterns, Wyrtki (1961; 1987) first estimated the ITF magnitude and proposed the mechanism of transferring water from the Pacific Ocean to the Indian Ocean; the ITF is driven by a pressure gradient between the Pacific and Indian Ocean. His assumption was that the ITF magnitude can be correlated with the sea-level difference between the Davao (Philippines, West Pacific) and the Darwin (Australia, East Indian Ocean) stations. However, the Davao record was found to be a poor indicator of sea-level variability in the western Pacific, as the signal was influenced by the fluctuations of the unstable Mindanao Current and other off-equatorial signals. The Darwin station is located within the downstream buoyant pool of the North Australian Basin and hence the sea-level variation here must mainly be of Pacific Ocean origin therefore Darwin is also a poor choice to use when studying sea level differences between the Indian and Pacific Oceans (Clarke and Liu, 1994; Andersson and Stigebrandt, 2005). These left an open question on what controls the pressure head between the Pacific and Indian Ocean on the long-term mean and how to asses the variability of the Throughflow.

Godfrey (1989) invented the so-called "island rule" based on a Sverdrup model to estimate the mean ITF magnitude. The "island rule" is derived by integrating the depth-averaged, linear, horizontal momentum equations for the stratified ocean,

subjected to a wind forcing. In the simplest formulation, the "island rule" states that the long-term (inter-annual or longer time-scales) depth-integrated transport of the ITF can be obtained by the wind stress line integral across the Pacific and around Australia and New Guinea (see Section 4.5, p.85). The prevailing winds cause an increase in sea level on the western side of the oceans and a lowering on the eastern side. Additional components to the "island rule" include topographic and frictional effects as well as the pressure difference between the northern and southern entrances to the Indonesian Seas that balances the alongshore wind stress. Godfrey's "island rule" which using annual mean wind stress gives an estimation of the net mean depth-integrated transport of 16 ± 4 Sv (Sv = 10^6 m^3/s). The value is higher than that in comparison with the observational estimates of the mean ITF transport of approximately 10 - 12 Sv (Godfrey and Golding, 1981; Fu, 1986; Murray and Arief, 1988; Meyers et al., 1995; Gordon et al., 1999; Wajsowicz et al., 2003). This implies that frictional and topographic effects might play a significant role in reducing the net Pacific to Indian Ocean transport.

Wajsowicz (1993a, b; 1994) further modified the Godfrey's "island rule" to account for the complex geometry of the Indonesian Gateways by including the bottom topography, frictional effects and multiple straits. The resulting analytical model showed that the narrow channels in the Indonesian archipelago could indeed reduce the net transport due to the frictional effects. However, estimations of frictional contribution are dependent on the parameterization and boundary conditions adopted in the model.

In agreement with the modified "island rule", the ocean general circulation model (OGCM) experiments of Wajsowicz (1995; 1996) confirm that inter-annual variability in the depth-integrated throughflow is generated by wind stress variations over the Pacific. However, a simple estimate of the magnitude and variability of the ITF using the analytical model still seems to be problematic when topographic effects and density driven flow are considered. Moreover, comparison of the inter-annual variations in depth-integrated transport predicted by the theory and simulated by the coupled OGCM shows disagreement in both magnitude and phasing of the Throughflow (Wajsowicz and Schneider, 2001).

A different approach was suggested by Andersson and Stigebrandt (2005) where only the density gradient between the Pacific and the Indian Ocean is considered to drive the Throughflow. The Indonesian Seas are taken as part of the North Pacific water masses assuming that the hydrographic properties do not change significantly within the Gateways. A downstream buoyant pool is formed in the North Australian Basin, which drives the upper flow from the Pacific towards the Indian Ocean due to the difference in sea level. The ITF is then predicted from the simple geostrophic transport taking into account the density difference and depth of the pool. However, these estimates crucially depend on the width and depth of the pool as well as on the reference temperature and salinity used in calculation.

The given theories of the Throughflow forcing therefore still leave the unanswered question of how to approach the Throughflow dynamics in order to predict the transport magnitude and variability. A possible simplified description of the ITF that would also incorporate accurate estimates of the transport would be an useful tool in studying long-term climate changes.

2.4.3. Magnitude of the ITF

The Indonesian Seas represent the only tropical inter-ocean link between the western Pacific and the eastern Indian Ocean and take responsibility for transferring a large amount of water mass from the upper Pacific Ocean to the Indian Ocean. While the heat and relatively fresh water carried by the ITF are known to affect the basin budgets of both the Pacific and Indian Oceans, the magnitude, vertical distribution and variability of the ITF are not well known (Sprintall et al, 2004). The estimation of the ITF transport magnitude and variability has been a challenging task for both observational and numerical ocean model due to the complicated topography of the Indonesian Seas and the complex equatorial ocean dynamics.

Because of difficulties in calculation as well as difference in methods used for calculation of the ITF, the actual magnitude of the ITF and the annual variation still remains controversial, despite of many efforts in recent years. The numerical value of the ITF volume transport ranges from near zero to 30.0 Sv (Siedler et al, 2001) depending on the method, location, time and data used in calculation (Wyrtki, 1961;

Godfrey and Golding, 1981; Wunsch et al, 1983; Piola and Gordon, 1984; Fine, 1985; Fu, 1986; Gordon, 1986; Semtner and Chervin, 1988; Murray and Arief, 1988; Toole et al, 1988; Kindle et al., 1989; Godfrey, 1989; Wijffels et al, 1992; Toole and Warren, 1993; Fieux et al., 1994, 1996; Meyers et al., 1995; Potemra, 1999; Gordon et al., 1999; Hautala et al., 2001; Molcard et al., 2001; Susanto and Gordon, 2004; Li Wei, 2006; Potemra and Schneider, 2007).

Since the 1960s, there have been several attempts to estimate the transport of the Throughflow by using a variety of direct and indirect methods. The first attempt to estimate the strength of the ITF was the works of Wyrtki in 1961. In his research, Wyrtki provided a general picture of the complex, and varying flow pattern inside and surrounding water of the Indonesian Seas.

The direct measurement of the ITF through the Lombok Strait conducted by Muray and Arief (1988) from January 1985 to January 1986 showed an annual mean transport of about 1.7 Sv with a maximum of 4.0 Sv towards the Indian Ocean during July and August, and less than 1 Sv from December 1985 to January 1986. The recently observational programmes monitoring of the ITF exist such as INSTANT (2003-2006) and ARLINDO (1993-1994; 1996-1998; 1998-2007). The initial result of the ARLINDO has shown an average southwards transport in 1997 within Makassar Strait of 9.3 Sv, with a range of about ± 2.5 Sv depending on how the surface flow is taken into account (Gordon et al., 1999). Based on the recent mooring measurements in Makassar Strait (*Gordon et al.*, 1999; *Wajsowicz et al.*, 2003; *Susanto and Gordon*, 2004), as the main passage of the Throughflow and estimates of the transport in the outflow passages (*Murray and Arief*, 1988; *Creswell et al.*, 1993; *Molcard et al.*, 1994; 1996; 2001; *Hautala et al.*, 2001) a general picture of the ITF is depicted in the Figure 2.17, with the total ITF transport is about 10.5 Sv and the transports of Makassar Strait, Lombok Strait, Ombai Strait, and Timor Strait are 9.0 Sv, 1.7 Sv, 4.5 Sv, and 4.3 Sv respectively (Gordon, 2001). Although direct current measurements of the ITF are of limited duration, none are long enough to properly describe greater than annual variability of the ITF, observations indicate that the bulk of the ITF passes through the Makassar Strait (Vranes and Gordon,

2005). The total net throughflow and the transport through the main Indonesian passages are shown in the Table 2.2 and Table 2.3.

The reason of the uncertainly about the numerical value of the ITF lies in a number of special difficulties. Firstly the ITF passes from the equatorial Pacific to the Indian Ocean through a highly complex system of channels. These channels span the Equator, and internal tides are very active within them, which can cause severe aliasing in the estimation of steric heights from single measurement; Secondly the ITF originates near the region where part of the SEC turns its direction to join the NECC, and where the Mindanao current turns eastward into the NECC; Thirdly, when calculating the ITF, the long-term mean flow through the South China Sea is often ignored (Godfrey, 1996), even through the South China Sea could contribute approximately 3.9 Sv to the ITF (Fang, 2005); and finally the given values of the ITF were calculated based on differences in method, location, time and data.

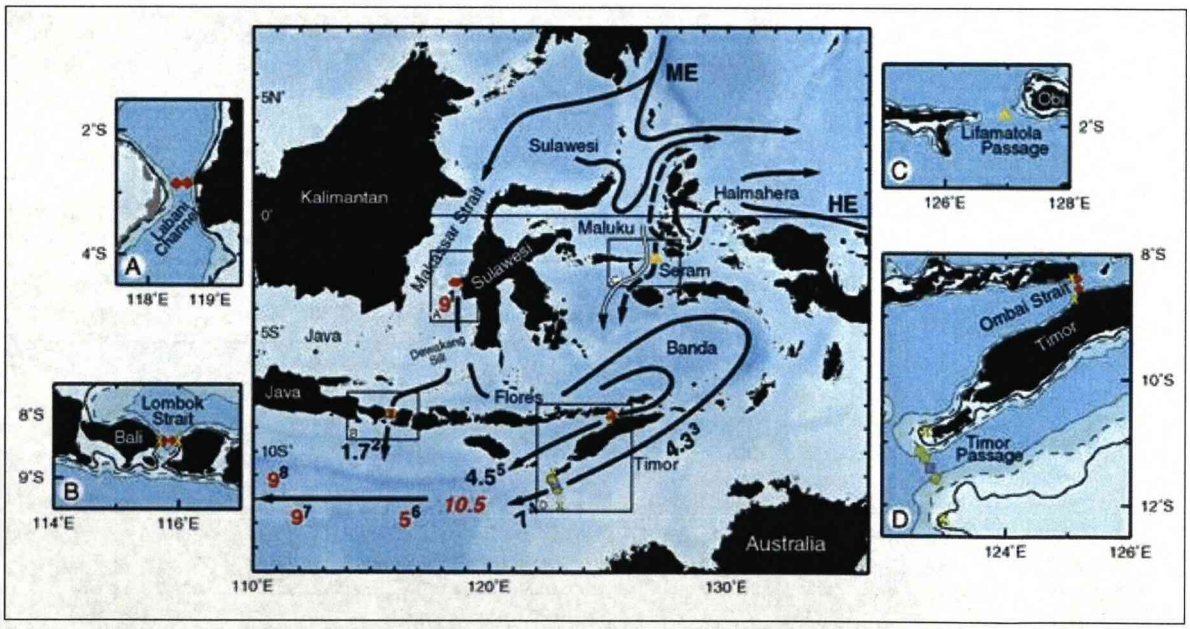

Figure 2.17: Schematic of Indonesian Throughflow pathways (Gordon, 2001). The solid arrows represent North Pacific thermocline water; the dashed arrows represent South Pacific lower thermocline water. Inserts A-D show positions of INSTANT' moorings. Insert A: 2 Makassar Strait Inflow moorings within Labani Channel. Insert C: Netherland's mooring within the main channel of Lifamatola Passage. Insert B, D: Sunda moorings in Ombai Strait, Lombok Strait, and Timor Passage.

Table 2.2: The mean transport of the ITF

No	Reference	Method	Results (Sv)	Note
1	Wyrtki, 1961	Geostrophy	1.7	Top 200m
2	Godfrey and Golding, 1981	Geostrophy, 11 Indian Ocean sections	10	Sections unclosed, 32°S
3	Wunsch et al, 1983	Inverse calculation, 43°S and 28°S Pacific sections	<<10	
4	Piola and Gordon, 1984	Freshwater budget, Pacific and Indian Oceans	14	
5	Fine, 1985	Tritium budget, West Pacific	5	Top 300m
6	Fu, 1986	Inverse calculation, Australian-Timor	7	Timor Strait only
7	Toole et al, 1988	Salinity budget, West Pacific	< 5	Sensitive to Indonesian salinity
8	Murray and Arief, 1988	Current meter survey	1.5	Lombok Strait only
9	Godfrey, 1989	Geostrophy, Australia-Sumatra, Levitus annual mean data	12	Boundary currents unresolved
10	Toole and Warren, 1993	Inverse estimate, Indian Ocean 32°S	7	
11	Wijffels et al, 1992	Heat budget, closed box, 14°S-165°E-10°N	0-8	
12	Fieux et al, 1994	Geostrophy, Australia-Bali, plus current meter	18.6±7	August 1989 snapshot
13	Fieux et al, 1996	Geostrophy, Australia-Bali, plus current meter	-2.6±7	February-March 1992 snapshot
14	Meyers et al, 1995	Time series from expendable bathythermograph sections	5	Top 400m
15	Semtner and Chervin, 1988	Global Ocean GCM	16.0	
16	Hirst and Godfrey, 1993	Global Ocean GCM	17.0	
17	Inoue and Welsh, 1993	Regional ocean model	9.8	
18	Kindle et al., 1989	Numerical ocean model	7.5	
19	Masumoto and Yamagata, 1996	General circulation model	9.5	
20	Potemra, 1999	Numerical ocean model	> 8.0	
21	Molcard et al., 2001	Current mooring	4 – 6	Ombai Strait only
22	Li Wei, 2006	General circulation model	15.68	The major transport occurs in the upper 300 m

Note: 1 - 14 is from the summary of Godfrey, 1996.

Table 2.3: Volume transport (Sv) through the main Indonesian passages.

Passages	Observations
Makassar Strait	9.3 ± 2.5 *Gordon et al., 1999* 8.1 ± 1.5 *Susanto and Gordon, 2004*
Sulawesi–New Guinea	~ 1-2 *Gordon et al., 2000*
Lombok Strait	1.7 ± 1.2 *Murray and Arief, 1988* 2.6 ± 0.8 *Hautala et al., 2001*
Ombai Strait	5.0 ± 1.0 *Molcard et al., 2001*
Timor Passage	7.0 *Creswell et al., 1993* 4.5 ± 1.5 *Molcard et al., 1994* 4.3 ± 1.0 *Molcard et al., 1996*

Note: Positive values indicate southward transport towards the Indian Ocean.

2.4.4. Seasonal and Inter-annual variation of the ITF

The Indonesia Seas lies in the region that forms a crucial pathway of return water from the Pacific Ocean into the Indian Ocean. In this region the tropical monsoon causes a very clear seasonal variation of climate and ocean circulation. The annual fluctuations of sea level of the western coast of Thailand and Indonesian are forced predominantly by the coastal alongshore monsoon wind. For the six months from the April to September this monsoon wind has a south-easterly component towards Indian, raising coastal sea level in the Northern Hemisphere and lowering it in the Southern Hemisphere; during the other six months winds and sea level reverse (Clarke and Liu, 1993).

The ITF transport shows high variability on both seasonal and inter-annual timescales. The seasonal cycle is characterized by the monsoonal wind change. The transport within Makassar Strait is strongest in the boreal summer monsoon. The flow is weakest in the boreal winter monsoon (*Gordon et al.*, 1999, 2003). The transport time series based on the shallow pressure gauge and ADCP data in the main outflow passages (Lombok Strait, Sumba Strait, Ombai Strait, and Timor Passage) show a similar mean annual cycle as in the Makassar Strait (*Hautala et al.*, 2001). However, possible differences in timing of the outflow transport relative to the transport from the inflow passages point to convergence in the Indonesian Seas (*Gordon and Susanto*, 2001; *Potemra et al.*, 2003).

Wyrtki (1987) and Clarke and Liu (1994) suggested that ITF transport, normally from the Pacific Ocean to the Indian Ocean would be reduced during an El Niño event or enhanced during a La Niña event. The hypotheses were based on the change in the Pacific trade wind during ENSO events and the associated responses of Pacific and Indian sea level and the ITF. For example, during an El Niño event, easterly trades relax and the pressure force maintaining the ITF is reduced (Potemra and Schneider, 2007). The hypothesis was supported by the work of Meyer (1996). The depth integrated transport computed from the observation of temperature and salinity along the repeat XBT line IX-1 (from Java to Australia) was indeed enhanced during the La Niña event of 1988/1989 and reduced during the El Niño of the early 1990s. However in more recent studies (England and Huang, 2005; Sprintall et al., 2002) a major part of the inter-annual variance in ITF appears to be independent of ENSO, and there are several years when the ITF transport does not appear to match ENSO variation.

According to Potemra and Schneider (2007), the apparent discrepancy between ENSO and the ITF variability may be explained in several ways: firstly, the observed estimates are based on a geostrophic calculation, and the actual flow maybe ageostrophic; secondly, the geostrophic calculation relies on a level of no motion that may not be accurate; the third reason why the ITF does not show coherent variability with ENSO is that inter-annual forcing may act differently on different vertical layers of the ITF, and the result may not have a clear signal in the depth integrated transport value; and finally, it may be the case that inter-annual variations of the ITF are caused by something other than, or in combination with, ENSO.

2.4.5. The effect of the ITF to regional and global circulation and climate

Due to its geographical position the ITF plays an important role in the world ocean circulation. It is also an integral part of the tropical climate system, playing an important role in the tropical ocean-atmosphere coupling by influencing the position and extent of the West Pacific Warm Pool (WPWP).

Numerical ocean modelling studies have provided some guidance to the effects that are likely to occur as result of natural, seasonal and inter-annual fluctuation of the ITF (Godfrey, 1996). According to numerical models, changes in ocean circulation

associated with the throughflow are likely to affect patterns of heat exchanges with the atmosphere in widely separated regions of the world ocean. In particular, an increased ITF will result in more heat loss to the atmosphere in the subtropical Indian Ocean and less in the Pacific Ocean (Godfrey, 1996).

Results from the coupled ocean-atmosphere general circulation model (AOGCM) (Schneider and Barnett, 1997; Schneider, 1998) show that the open ITF increases surface temperatures in the eastern Indian Ocean, reduces temperatures in the equatorial Pacific, and shifts the warm pool and centres of deep convection in the atmospheric pressure in the entire Tropics and, via atmospheric teleconnections, in the mid-latitude. As result, the atmospheric pressure in the entire tropics and the related surface wind stress is changed. Table 2.4 shows some of the possible effects of the ITF to the Oceans as suggested by Godfrey (1996).

Blocking of the ITF results in an ENSO-like signal in the Pacific and a pattern similar to the Indian Dipole Mode over the Indian Ocean (*Wajsowicz and Schneider*, 2002). In the Indian Ocean, blocking of the ITF is associated with colder SSTs in the eastern Indian Ocean and warmer temperatures in the western basin. The resulting wind signal is an increase in southeast trades over the Indian Ocean. Accompanying precipitation anomalies show a northward shift in rainfall from Indonesia and small increase of rainfall over East Africa. The response of the Pacific Ocean is an enhanced warming in the eastern equatorial Pacific associated with increased westerly anomalies in wind stress and rise in precipitation along the Equator.

Table 2.4: The possible effects of the ITF to the Oceans (Godfrey, 1996).

The Indian Ocean	**The Pacific Ocean**	**The Atlantic Ocean**
Warming of the Agulhas out flow; Strengthening of the Leeuwin Current system; Ocean-wide thermocline deepening; Warm water in the Indonesian upwelling region; Observed ENSO-related variability of the Leeuwin Current; Change of SST in the Indian Ocean.	Altering the strength of the East Australian Current; The East Australian Current and ENSO; Climatic effects of the throughflow on other parts of the Pacific Ocean.	Effect of the ITF to the Atlantic is very weak.

Chapter 3

MODEL DESCRIPTION

3.1 Some advantages and disadvantages of numerical ocean models

Oceanography is a relatively young field, barely a century old. Numerical ocean modelling is even younger. The very early comprehensive numerical global baroclinic ocean model was formulated by Kirk Bryan (1969) in the late sixties and programmed by Michel Cox. However, the advent of high performance computers has led to a phenomenal growth in the field, especially in the last decade (Kantha and Clayson, 2000). A fairly complete overview of the models currently in use, with links to the websites where these models are available, is given at: http://stommel.tamu.edu/~baum/ocean_models.html. In the review of Griffies et al., (2000), some advantages and disadvantages of several numerical ocean models have been pointed out as following:

The z-coordinate models: The advantages of the depth or z-coordinate models (e.g. MOM, MOMA. OCCAM, SEA, HOPE, MIT…) are they can provide the simplest and most established framework for ocean climate modelling; In general a z-coordinate system provides a useful framework for representing diabatic processes; well-suited for situations with strong vertical/diapycnal mixing and/or low stratification. For a Boussinesq fluid the horizontal pressure gradient can be easily represented; the highly nonlinear equation of state for ocean water can be accurately represented; the surface mixed layer is naturally parameterised. The disadvantages are that the representation of tracer advection and diffusion along inclined density surfaces in the ocean interior is cumbersome, representation and parameterization of the bottom boundary layer is unnatural, and representation and parameterization bottom topography is difficult.

The ρ-coordinate models: The isopycnic or density coordinate models (e.g. MICOM, HIM, POSUM, HYCOM, POSEIDON…) are less well established for climate modelling application, but they have strong foundation in idealised configurations. They are well-suited to modelling the observed tendency for tracer transport to be along density surfaces (or isopycnals). The topographic interactions are better represented in comparison to z-coordinate models (there is no restriction related to Δz). For a diabatic fluid, the horizontal pressure gradient can be easily represented; the volume or mass between isopycnals is conserved. The disadvantages are that the representation of the effect of a realistic equation of state is cumbersome; isopycnic coordinate models are an inappropriate framework for representing the surface layer or bottom boundary layer, since these boundary layers are mostly unstratified.

The σ-coordinate models: The sigma coordinate models (e.g. POM, SPEM, ROMS, POLCOMS…) provide suitable a framework in situations where capturing the dynamical and/or boundary layer effect associated with topography is important. It is particularly well suited for modelling flows over the continental shelf and slope, but remains unproven in a global coupled climate modelling context. The sigma coordinate system provides a smooth representation of the ocean bottom topography, with coordinate isolines concentrated in regions where bottom boundary layer processes are most important, they allow for a natural framework for parameterising bottom boundary layer (BBL) processes. Thermodynamic effects associated with the equation of state are well represented. The representation of the mixed layer can be less well represented using sigma coordinates than with the z-coordinates; as with z-models the representation of advection and diffusion along inclined density surface in the ocean interior is cumbersome; the sigma coordinate models have difficulty accurately representing the horizontal pressure gradient.

3.2. POLCOMS Model

The Proudman Oceanographic Laboratory Coastal-Ocean Modelling System (POLCOMS) model is a three-dimensional baroclinic model which has been developed from the Proudman Oceanographic Laboratory Three-Dimension Baroclinic B-grid model (POL3DB) (James, 1986; 1996) to incorporate sophisticated features suitable for the modelling of baroclinic processes on the shelf, on the shelf slope, and in ocean regions to allow long-term coupled ocean-shelf simulation (Holt

and James, 2001a, b). The model is formulated on the spherical polar sigma coordinate set (χ, ϕ, σ) and using Arakawa (1972) B-grid. The Piecewise Parabolic Method (PPM) scheme (Colella and Woodward, 1984; James, 1996) has been used to minimize numerical diffusion. A complete description of the model is provided by Proctor and James (1996), Holt and James (2001a, b) and from the website http://cobs.pol.ac.uk/modl/

3.2.1. Equation of motions

The 3-D incompressible, Boussinesq and hydrostatic equations, in essence a development of that of James (1986) and described by James (1996), in spherical polar coordinates with a transformed vertical coordinate, σ, are given by

$$\frac{\partial u}{\partial t} = -L(u) + \left(f + \frac{u\tan\phi}{R}\right)v - \frac{1}{R\cos\phi}\left(\frac{\partial \Phi}{\partial \chi} - \left[\frac{\partial \zeta}{\partial \chi} + \sigma\frac{\partial H}{\partial \chi}\right]b\right) - \frac{1}{\rho_0 R\cos\phi}\frac{\partial P_a}{\partial \chi} + \frac{1}{H^2}\frac{\partial}{\partial \sigma}\left(A\frac{\partial u}{\partial \sigma}\right), \quad (3.2.1)$$

$$\frac{\partial v}{\partial t} = -L(v) - \left(f + \frac{u\tan\phi}{R}\right)u - \frac{1}{R}\left(\frac{\partial \Phi}{\partial \phi} - \left[\frac{\partial \zeta}{\partial \phi} + \sigma\frac{\partial H}{\partial \phi}\right]b\right) - \frac{1}{\rho_0 R}\frac{\partial P_a}{\partial \phi} + \frac{1}{H^2}\frac{\partial}{\partial \sigma}\left(A\frac{\partial v}{\partial \sigma}\right), \quad (3.2.2)$$

$$\frac{\partial b}{\partial t} = -L(b) + \frac{1}{H^2}\frac{\partial}{\partial \sigma}\left(K\frac{\partial b}{\partial \sigma}\right), \quad (3.2.3)$$

where u, v are the positive velocity components in east (χ), north (ϕ) – axes respectively; H is total depth (=h+ζ); ζ is sea-surface elevation above mean sea level; f is the Coriolis parameter; P_a = atmospheric pressure; Φ = (total pressure P–P_a)/ρ_o+gz; b=buoyancy (=$g(\rho_o-\rho)/\rho_o$); K is coefficient of vertical diffusion; and A is the coefficient of vertical viscosity.

The vertical coordinate $\sigma = (z-\zeta)/(h+\zeta)$ and the nonlinear terms $L(a)$ are given by

$$L(a) = \frac{u}{R\cos\phi}\frac{\partial a}{\partial \chi} + \frac{v}{R}\frac{\partial a}{\partial \phi} + \Omega\frac{\partial a}{\partial \sigma}, \quad (3.2.4)$$

where

$$\Omega = -\frac{\sigma}{H}\frac{\partial \zeta}{\partial t} - (HR\cos\phi)^{-1}\left[\frac{\partial}{\partial \chi}\left(H\int_0^{\sigma} u d\sigma\right) + \frac{\partial}{\partial \phi}\left(H\cos\phi\int_0^{\sigma} v d\sigma\right)\right], \quad (3.2.5)$$

also

$$b = \frac{1}{H}\frac{\partial \Phi}{\partial \sigma},$$

so

$$\Phi = H\int_0^{\sigma} b d\sigma + g\zeta .$$

Following Holt and James (2001a), the equations of motion (3.2.1, 3.2.2, 3.2.3) are solved to allow time splitting between the barotropic and the baroclinic components. They are divided into depth varying and depth independent parts; so the eastward velocity is $u = \bar{u}[\chi,\phi,t] + u_r[\chi,\phi,\sigma,t]$; and the northward velocity is $v = \bar{v} + v_r$.

The depth-mean equations are:

$$\frac{\partial \bar{u}}{\partial t} = f\bar{v} - (R\cos\phi)^{-1}\left[g\frac{\partial \zeta}{\partial \chi} + \rho_0^{-1}\frac{\partial P_a}{\partial \chi}\right] + H^{-1}[F_S - F_B] + NLB_{\chi}, \quad (3.2.6)$$

$$\frac{\partial \bar{v}}{\partial t} = -f\bar{u} - R^{-1}\left[g\frac{\partial \zeta}{\partial \phi} + \rho_0^{-1}\frac{\partial P_a}{\partial \phi}\right] + H^{-1}[G_S - G_B] + NLB_{\phi}, \quad (3.2.7)$$

and the equations for the depth varying components are

$$\frac{\partial u_r}{\partial t} = -L(u) + fv_r + \frac{uv\tan\phi}{R} - \prod_{\chi} + D(u) - H^{-1}[F_S - F_B] - NLB_{\chi}, \quad (3.2.8)$$

$$\frac{\partial v_r}{\partial t} = -L(v) - fu_r - \frac{u^2\tan\phi}{R} - \prod_{\phi} + D(v) - H^{-1}[G_S - G_B] - NLB_{\phi}, \quad (3.2.9)$$

where R is the radius of the Earth.

The buoyancy terms are given by

$$\prod_{\chi} = (R\cos\phi)^{-1}\frac{\partial \psi}{\partial \chi}\Big|_z \quad \text{and} \quad \prod_{\varphi} = R^{-1}\frac{\partial \psi}{\partial \phi}\Big|_z . \quad (3.2.10)$$

The depth means of the nonlinear and buoyancy terms are:

$$NLB_{\chi} = \int_{-1}^{0}\left[-L(u) + \frac{uv\tan\phi}{R} - \prod_{\chi}\right]d\sigma , \quad (3.2.11)$$

$$NLB_{\phi} = \int_{-1}^{0}\left[-L(v) + \frac{u^2\tan\phi}{R} - \prod_{\phi}\right]d\sigma . \quad (3.2.12)$$

The vertical gradients of the stresses $(\tau_{z\chi}, \tau_{z\phi})/\rho$ have been replaced by a diffusion term:

$$D(a) = H^{-2}\frac{\partial}{\partial\sigma}\left(K_z\frac{\partial a}{\partial\sigma}\right), \tag{3.2.13}$$

where K_z is the eddy viscosity which will be defined in section 3.2.2.

The equation for the free surface is

$$\frac{\partial\zeta}{\partial t} = -(R\cos\phi)^{-1}\left[\frac{\partial}{\partial\chi}(H\bar{u}) + \frac{\partial}{\partial\phi}(H\cos\phi\bar{v})\right]. \tag{3.2.14}$$

The model uses slip vertical boundary conditions: the components of surface stress (F_S, G_S) are given by

$$(F_S, G_S) = C_s\frac{\rho_a}{\rho_0}(u_w, v_w)\sqrt{u_w^2 + v_w^2}\,, \tag{3.2.15}$$

Where the friction coefficient $C_s = 0.63 + 0.66\sqrt{u_w^2 + v_w^2}$ following Smith and Banke (1975); and u_w, v_w is the wind velocity at 10m. The components of bottom stress (F_B, G_B) are given by

$$(F_B, G_B) = C_B(u_B, v_B)\sqrt{u_B^2 + v_B^2}\,, \tag{3.2.16}$$

where

$$C_B = \left[\kappa^{-1}\log\left(\frac{\delta}{z_0}\right)\right]^{-2}, \qquad C_B > 0.005,$$

following Blumberg and Mellor (1987). The near bed velocity (u_B, v_B) is defined at a depth δ above the sea bed, the roughness is taken to be z_o = 0.003m; and κ = 0.41 is von Kármán's constant.

The transport equation for temperature (and salinity) is given by

$$\frac{\partial T}{\partial t} = -L(T) + D(T), \tag{3.2.17}$$

which uses the eddy diffusivity K_H (which will be defined in section 3.2.2).

3.2.2. Turbulence closure

To estimate the vertical eddy viscosity and diffusivity term in the previous section, the Mellor-Yamada-Galperin level 2.5 turbulence closure scheme (Mellor and Yamada, 1974, Galperin et al., 1988) has been employed in the POLCOMS model.

The turbulent kinetic energy density is given by:

$$\frac{\partial q^2}{\partial t} = 2K_Z M^2 - 2(K_H - \alpha K_z)N^2 - \frac{2}{B_1}\frac{q^3}{l} + D(q^2), \qquad (3.2.18)$$

where

$$M^2 = \frac{1}{H^2}\left[\left(\frac{\partial u}{\partial \sigma}\right)^2 + \left(\frac{\partial v}{\partial \sigma}\right)^2\right],$$

$$N^2 = \frac{1}{H}\frac{\partial b_0}{\partial \sigma},$$

and $B_1 = 16.6$. The term in αK_z (with $\alpha = 0.7$) is a simple representation of vertical mixing by long wavelength internal waves (Mellor, 1989); and K_z, K_H and K_q are the coefficients of the eddy viscosity, eddy diffusivity and the vertical diffusion of q^2 respectively.

There are many choices of algebraic mixing length, l, (e.g. Xing and Davis, 1996). In the POLCOMS model the Bakhmetev scale has been used (Holt and James, 1999b) and it shows reasonable results in the North Sea. In Holt and James (2001a, b) the length scale in deep water is modified so that $l = \kappa H l_o(\sigma)$, where $h \le h_c$,

$$l_o = (1+\sigma)(-\sigma)^{0.5}$$

and where $h > h_c$

$$l_o = \frac{h_c}{h}\left(1+\sigma\frac{h}{h_c}\right)\left(-\sigma\frac{h}{h_c}\right)^{0.5}, \qquad \text{for} \quad \sigma \ge \frac{-h_c}{3h},$$

$$= \frac{2\sqrt{3}}{9}\frac{h_c}{h}, \qquad \text{for} \quad \frac{-h_c}{3h} > \sigma > \frac{2h_c}{3h} - 1,$$

$$= (1+\sigma)\left(1-\frac{h}{h_c}(1+\sigma)\right)^{0.5}, \qquad \text{for} \quad \sigma \le \frac{2h_c}{3h} - 1.$$

This maintains the surface and near-bed mixing length profiles at a depth of h_c into deep water, with intermediate depths in the water column taking the maximum value at $h=h_c$. Defining the profile in this way simulates, in an arbitrary fashion, the eddy scale becoming independent of water depth in deep water and prevents l increasing without limit with h. The eddy size in stratified water is limited according to the Ozmidov length scale (for dissipation ε), $L = (\varepsilon/N^3)^{1/2}$. POLCOMS imposes a limit on l proportional to this, following Galperin et al (1988):

$$l^2 < 0.28\frac{q^2}{N^2}. \qquad (3.2.19)$$

The near-bed boundary condition arises from a steady state balance between shear and dissipation:

$$q^2\,|_{\sigma=-1} = B_1^{2/3}\sqrt{F_B^2 + G_B^2}\,,$$

whereas at the surface a balance between diffusion and dissipation is used to represent the flux of turbulence from surface wave breaking (Craig and Banner, 1994).

$$q^2\,|_{\sigma=0} = \alpha_{wave}^{2/3}\left(3\frac{B_1}{S_q}\right)^{1/3}\sqrt{F_S^2 + G_S^2}\,,$$

with $\alpha = 100$ as the wave energy factor. Note that no temporal and spatial variations of α_{wave} are included, and the vertical resolution is unable to resolve the narrow region in which this surface turbulence is dissipated, so the effects are allowed to penetrate deeper than the work of Craig and Banner (1994) would suggest.

The system is closed by

$$K_Z = S_M lq\,;\; K_H = S_H lq\,;\; K_q = S_q lq\,,$$

using the stability relations from Galperin et al. (1988)

$$S_M = \frac{0.3933 - 3.086G}{(1-34.68G)(1-6.127G)},$$
$$S_H = \frac{0.4939}{1-34.68G},$$
$$S_q = 0.2,$$

where $G = -l^2N^2/q^2$ and (3.2.19) gives $G > -0.28$. K_q is the coefficient for the vertical diffusion of q^2. In unstably stratified conditions, a convective adjustment scheme is used to mix vertically before the diffusivities are calculated (more details are described in Holt and James, 2001a, b).

3.2.3. Equation of State

In POLCOMS, the density is defined by an approximation to the full UNESCO equation of state: $\rho(T,S,p) = \rho(T,S,0) + \rho'(T,S,p)$, where T is the potential temperature (°C); S is salinity (psu), and p is the pressure relative to the sea surface; $\rho(T,S,0)$ is taken from the UNESCO equation of state and

$$\rho'(T,S,p) = 10^4 \frac{p}{c^2}\left(1 - 0.20\frac{p}{c^2}\right), \qquad (3.2.20)$$

with c = 1449.2 + 1.34 (S - 35) + 4.55 T - 0.045 T^2 + 0.00821 p + 15.0 x 10^{-9} p^2, following Mellor (1991).

The total (hydrostatic) pressure is given by

$$P = P_a + \rho_0(\psi + g\zeta - gz) + 0.002282 g Z^2, \qquad (3.2.21)$$

where P_a is the atmospheric pressure and $\psi = H\int_0^\sigma b d\sigma$; b=b_o+b' with b_o (potential buoyancy) = $g[\rho_o$-$\rho(T, S, 0)]/\rho_o$ (ρ_o=1027 kg m^{-3}); $b' = g[\overline{\rho'(Z)} - \rho']/\rho_0$; $Z = z - \zeta = \sigma H$; in POLCOMS, the initial condition gives $\overline{\rho'(Z)}$ = - 0.004564Z (Holt and James, 2001a, b).

3.3. MICOM Model

The Miami Isopycnic Coordinate Ocean Model (MICOM) of the University of Miami is a primitive equation numerical model that describes the evolution of momentum, mass, heat and salt in the ocean. The theoretical structure of the model has been described by Bleck et al. (1992). The model uses equations that have a coordinate of density in the vertical direction, and formulated on the Arakawa C-grid, and using the split-explicit numerical scheme to separately calculate the barotropic and baroclinic components of the field of prognostic variables (Langlois, 1997). The governing equations and model grid are briefly described below. The details descriptions of the model and parameters are presented in the publications of Bleck and Boundra (1981, 1986), Bleck and Smith (1990), and especially the MICOM user's manual (Langlois, 1997).

3.3.1 Governing Equations

The Miami model is a primitive equation model containing four prognostic equations including one equation for the horizontal velocity vector, a mass continuity or layer thickness tendency equation, and two conservation equations for salt and heat. The equations, written for a generalised vertical coordinates "s" (Bleck, 1978) to make them formally applicable to both the isopycnic domain and the surface mixed layer are (Bleck et al., 1992):

$$\frac{\partial V}{\partial t_s}+\nabla_s\frac{V^2}{2}+(\zeta+f)k\times V+\left(\dot{s}\frac{\partial p}{\partial s}\right)\frac{\partial V}{\partial p}+\nabla_\alpha M=-g\frac{\partial \tau}{\partial p}+\left(\frac{\partial p}{\partial s}\right)^{-1}\nabla_s\cdot\left(\upsilon\frac{\partial p}{\partial s}\nabla_s V\right), \quad (3.3.1)$$

$$\frac{\partial}{\partial t_s}\left(\frac{\partial p}{\partial s}\right)+\nabla_s\cdot\left(V\frac{\partial p}{\partial s}\right)+\frac{\partial}{\partial s}\left(\dot{s}\frac{\partial p}{\partial s}\right)=0, \quad (3.3.2)$$

$$\frac{\partial}{\partial t_s}\left(\frac{\partial p}{\partial s}T\right)+\nabla_s\cdot\left(V\frac{\partial p}{\partial s}T\right)+\frac{\partial}{\partial s}\left(\dot{s}\frac{\partial p}{\partial s}T\right)=\nabla_s\cdot\left(\upsilon\frac{\partial p}{\partial s}\nabla_s T\right)+\mathrm{H}_T, \quad (3.3.3)$$

where $V = (u, v)$ is the horizontal velocity vector components, p is pressure, T represent any one of the model's thermodynamic variables (temperature, salinity, buoyancy), $\alpha=\rho^{-1}$ is the specific volume, $\zeta=\frac{\partial v}{\partial x_s}-\frac{\partial u}{\partial y_s}$ is the relative vorticity evaluated on an s surface, $\mathrm{M} \equiv gz + p\alpha$ is the Montgomery potential, gz is the geopotential, f is the Coriolis parameter, k is the vertical unit vector, υ is a variable eddy viscosity coefficient, and τ is the wind and bottom-drag-induced shear-stress vector; $\mathrm{H_T}$ represents the sum of the diabatic source terms acting on T. Subscripts indicate which variable is held constant during partial differentiation ($\frac{\partial}{\partial t_s}, \frac{\partial}{\partial x_s}, \frac{\partial}{\partial y_s}$ denote differentiations with s held constant). Distances in x, y directions (as well as their time derivatives $\dot{x} \equiv u$ and $\dot{y} \equiv v$) are measured in the projection onto a horizontal plane, a convention that eliminates metric terms related to the slope of the s surface.

After vertical integration over a coordinate layer, bounded by two surfaces S_{top} and S_{bottom} (the ocean surface, the bottom of the mixed layer, the seafloor, and all isopycnic layer interfaces are s surfaces), the continuity equation (2) becomes a prognostic equation for the layer weight per unit area, $\Delta p = p_{bot} - p_{top}$:

$$\frac{\partial}{\partial t_s}\Delta p+\nabla_s\cdot(V\Delta p)+\left(\dot{s}\frac{\partial p}{\partial s}\right)_{bot}-\left(\dot{s}\frac{\partial p}{\partial s}\right)_{top}=0, \quad (3.3.4)$$

The expression $\dot{s}\frac{\partial p}{\partial s}$ represents the vertical mass flux, taken to be positive if in $+p$ or downward direction, across an s surface. In (3.3.4) V is a layer average.

Multiplication of (3.3.1) by $\frac{\partial p}{\partial s}$ and integration over the interval (S_{top}, S_{bot}), followed by division by $\frac{\Delta p}{\Delta s}$, changes the shear-stress term in that equation into $\frac{g}{\Delta p}(\tau_{top} - \tau_{bot})$, while the lateral momentum mixing term integrates to:

$$(\Delta p)^{-1}\nabla_s \cdot (\nu \Delta p \nabla_s V). \qquad (3.3.5)$$

All other terms in (3.3.1) retain their original form.

Wind-induced stress is assumed to be zero at the bottom of the mixed layer, which therefore must not be allowed to become shallower than the Ekman layer. Bottom stress is prorated among coordinate layers in accordance with the assumption that is linearly decreases from $-\rho C_D |V| V$ to zero over the lowest 10m of the water column. In this formula V is the velocity vector average over the lowest 10cm, and C_D=0.003.

The layer-integrated from of (3.3.3) is

$$\frac{\partial}{\partial t} T\Delta p + \nabla_s \cdot (VT\Delta p) + \left(\dot{s} \frac{\partial p}{\partial s} T \right)_{bot} - \left(\dot{s} \frac{\partial p}{\partial s} T \right)_{top} = \nabla_s \cdot (\nu \Delta p \nabla_s T) + \mathrm{H}_T \,. \qquad (3.3.6)$$

The above prognostic equations are completed by diagnostic equations including the hydrostatic equation

$$\frac{\partial M}{\partial \alpha} = p \,. \qquad (3.3.7)$$

Since the mixed layer is non-isopycnic and subject to diabatic forcing, conservation equation for thermodynamic variables are needed there. An equation of state linking temperature (T), and salinity (S) to α, and a turbulence kinetic energy balance equation yielding the depth of the mixed layer. In the MICOM model the equation advocated by Friedrich and Levitus (1972) has been used to express the variable representing the density (σ) by a polynomial function of the temperature (in ^{o}C) and of the salinity (in $^{0}/_{00}$) as follows:

$$\sigma(T,S) = (c1+c3*S+T*(c2+c5*S+T*(c4+c7*s+c6*T)))*1e\text{-}3.$$

where: S is salinity; T is temperature; c1 = -7.2169 x 10^{-2}; c2 = 4.9762 x 10^{-2}; c3=8.0560 x 10^{-1}; c4 = 7.5911 x 10^{-3}; c5 = -3.0063 x 10^{-3}; c6 = 3.5187 x 10^{-5}; and c7= 3.7297 x 10^{-3} .

3.3.2 Model grid, parameters and forcing

Variables in the MICOM model are calculated at different points on a staggered Arakawa (1972) C-grid (Figure 3.1). Depths and Montgomery function are calculated at p points, vorticity at q points, and velocity components (u and v) are calculated on their respective grid points. When calculating terms in the momentum equation, variables are averaged or differenced onto their respective u or v grid points. In the model experiment the default coefficients were used such as the diffusion velocity (cm/s) for thickness diffusion is 0.5; the diffusion velocity (cm/s) for momentum dissipation is 1.0; the diffusion velocity (cm/s) for temperature/salinity mixing is 0.5; and the nondimensional, used in deformation-dependent viscosity is 0.2. The diapycnal mixing coefficient has been set to 0.0 which does not allow the diapycnal mixing in vertical. Especially in the experiments with realistic geometry and forcing this keeps the temperature and salinity fields close to the initial state of the realistic data from the Levitus and MIT-ECCO-GODAE datasets. The initial conditions, the lateral boundary conditions and forcing will be described before each experiment in the next chapters.

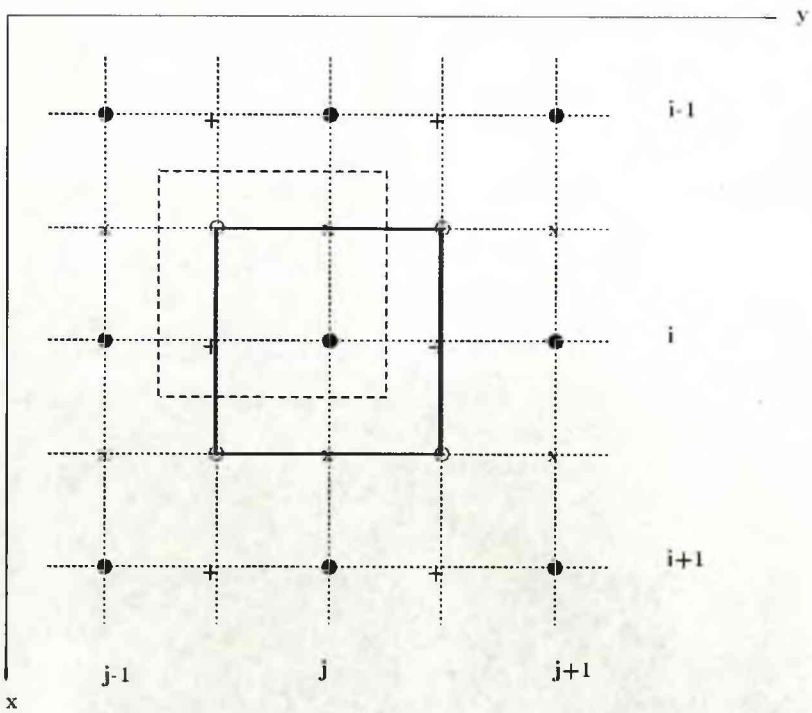

●: M, p, Δp, H, T, S points; x: u points; +: v points; o: q points

- - - - - - - - - - - - - - - - : Variables contained in array with indices i and j

———————— : Boundaries of the cell (i,j)

Figure 3.1: Distribution of the variables on an Arakawa C-grid (Langlois, 1997).

3.4. Choice of model for this project

Because the region of interest for this project has large amount of shelf-sea and extremely variable depth, it was initially decided to use the POLCOMS σ-coordinate model. However when problems with calculating the volume transport in the Throughflow became apparent it was decided to use MICOM instead as it did not suffer from these problems. The exact size of the Throughflow is an important diagnostic for computing model runs under different conditions and for comparing with other models and observations, so the diagnosed values must be reliable.

Chapter 4

RESPONSE OF AN IDEALISED MODEL TO CHANGES OF TOPOGRAPHY AND FORCING

In this Chapter the models, as described in Chapter 3, have been setup to run with different idealised wind forcing and topography in order to learn about the models, the possible flow regimes, volume transports and their responses to changes of forcing and topography. The idealised model has the benefit that it consumes relatively limited use of computer resource, but still can provide insight which will help interpret outcomes of the realistic forcing and topography model to examine the seasonal and long-term variations of the ITF and circulation in the Southeast Asian region.

4.1. Model configuration

4.1.1. Model domain

Firstly models have been run with a classical rectangular domain (referred to as blank domain or Case 4.1), which simply is a closed rectangular basin with a flat bottom at a constant depth of 4000m (Figure 4.1.a), to see whether the models can reproduce the phenomena that were known from the classical experiments of Sverdrup (1947), Stommel (1948) and Munk (1950). Secondly, models have been carried out with changes of topography which more closely resemble realistic topography of the study region (one-channel domain and two-channel domain, referred to as Case 4.2 and Case 4.3 respectively). The domain in the case of one channel is modified from the blank domain by dividing the domain into two sub-basins by placing a barrier at mid-longitude but still allowing the basins to be connected through a shallow channel of 100m depth and approximately 2000km width x 2000km long as shown in the Figure 4.1.b. The two-channel domain is based on the one-channel domain by opening a deep (4000m) channel of approximately 500km width at the southern boundary (Figure 4.1.c). Finally to examine responses of the system to changes of width and latitude of the shallow channel four more

additional domains (Figures 4.2a, 4.2b, 4.2c, 4.2d) have been used. They are hereafter referred to as Case 4.4, Case 4.5, Case 4.6 and Case 4.7 respectively.

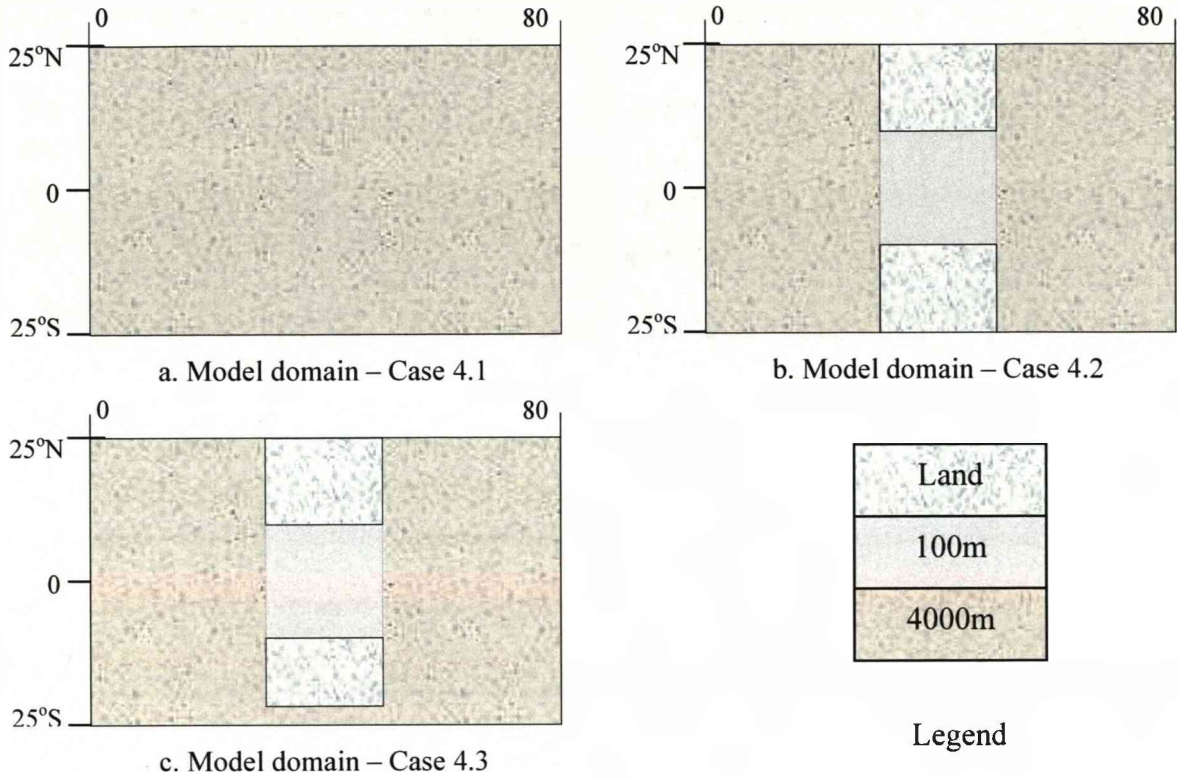

a. Model domain – Case 4.1

b. Model domain – Case 4.2

c. Model domain – Case 4.3

Figure 4.1: Illustration of the model domains – Case 4.1 to Case 4.3.

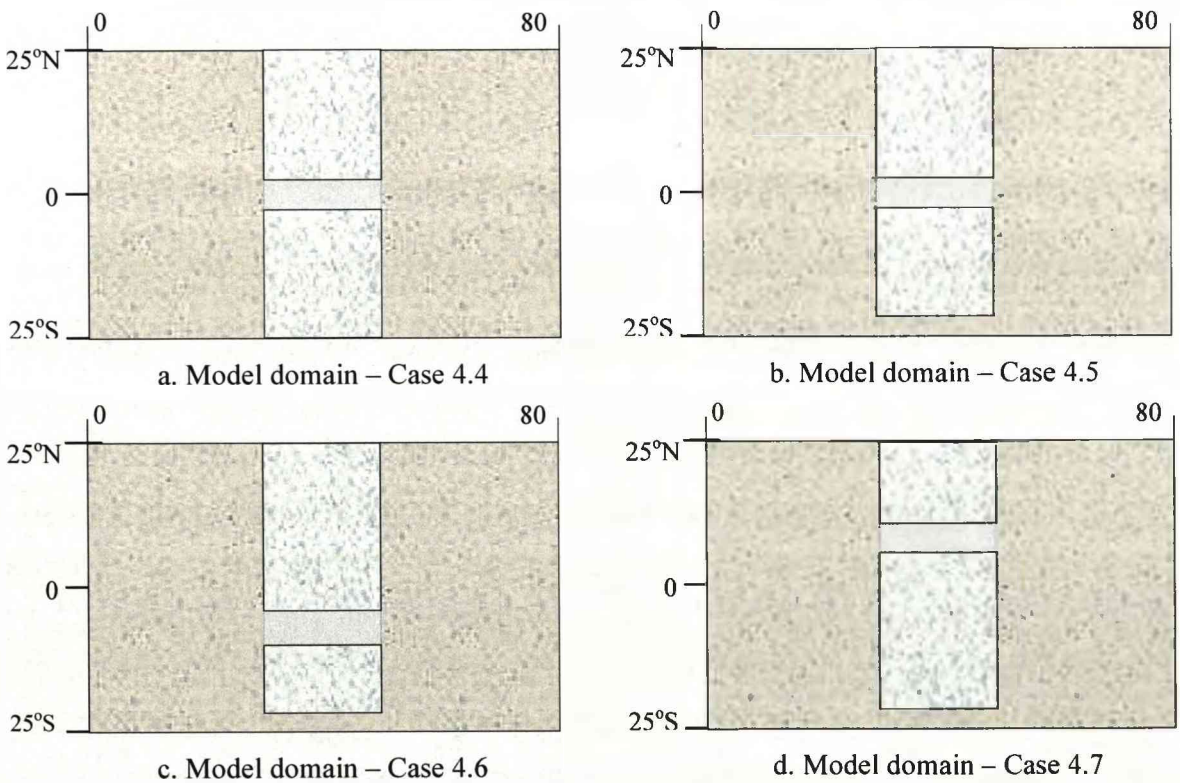

a. Model domain – Case 4.4

b. Model domain – Case 4.5

c. Model domain – Case 4.6

d. Model domain – Case 4.7

Figure 4.2: Illustration of the additional model domains (Case 4.4 - Case 4.7).

The dimension of the whole domain is about 50° latitude and 80° longitude. They were set to be symmetrical over the equator in north-south direction with the northern boundary limited at 25°N, and southern boundary at 25°S. The horizontal resolution of the model grid is 0.5 degree (dx = dy = 0.5°). The basins were set to have vertical side-wall at the eastern and western boundaries, and sloping side-walls at the two sides of the barrier (Figure 4.3).

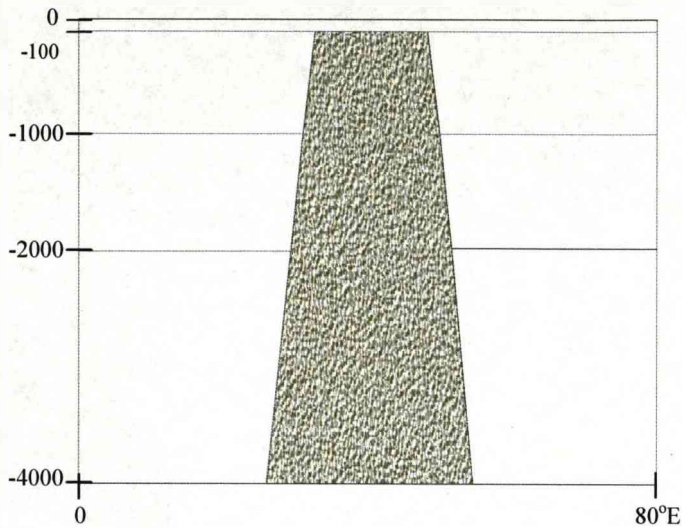

Figure 4.3: Cross section along the Equator showing initial vertical layer depths (m) of the model, cases 4.2 to 4.7 (note: the slope of the barrier has been exaggerated).

4.1.2. Model forcing

The Southeast Asia region is dominated by the monsoon wind with the reversal of the wind direction between seasons (winter and summer). Therefore in order to examine the response of the system to the change in wind forcing, different idealised zonal wind patterns have been used in the experiments, referred to as winter wind and summer wind (Figures 4.4.a, 4.4.b), the meridional wind component is set to be zero.

The winter and summer winds over the domain have been generated by the following simple sine function:

- zonal winter wind speed : $u_c = u_o * \sin(\pi * (i-1)/idm)$ (1)
- zonal summer wind speed : $u_c = -u_o * \sin(2\pi * (i-1)/idm)$ (2)

where: u_o = 10 m/s; idm is the total number of grid points in the north-south direction minus 1; i is the index of the grid point in the north-south direction.

The above zonal wind speed is converted to wind stress (dyn/cm^2) as follows:

$$\tau_x = (\rho_a * C_d * u_c * wsp) * 10.$$

where: wsp = sqrt($u_c^2 + v_c^2$) with u_c the zonal wind calculated in (1) or (2), v_c the meridional wind component ($v_c = 0$ in this research); ρ_a the air density (1.25 kg/m^3); C_d wind drag coefficient, calculated by the formula of Smith and Banke (1975):

$$C_d = (0.63 + 0.066 * wsp) * 10^{-3}.$$

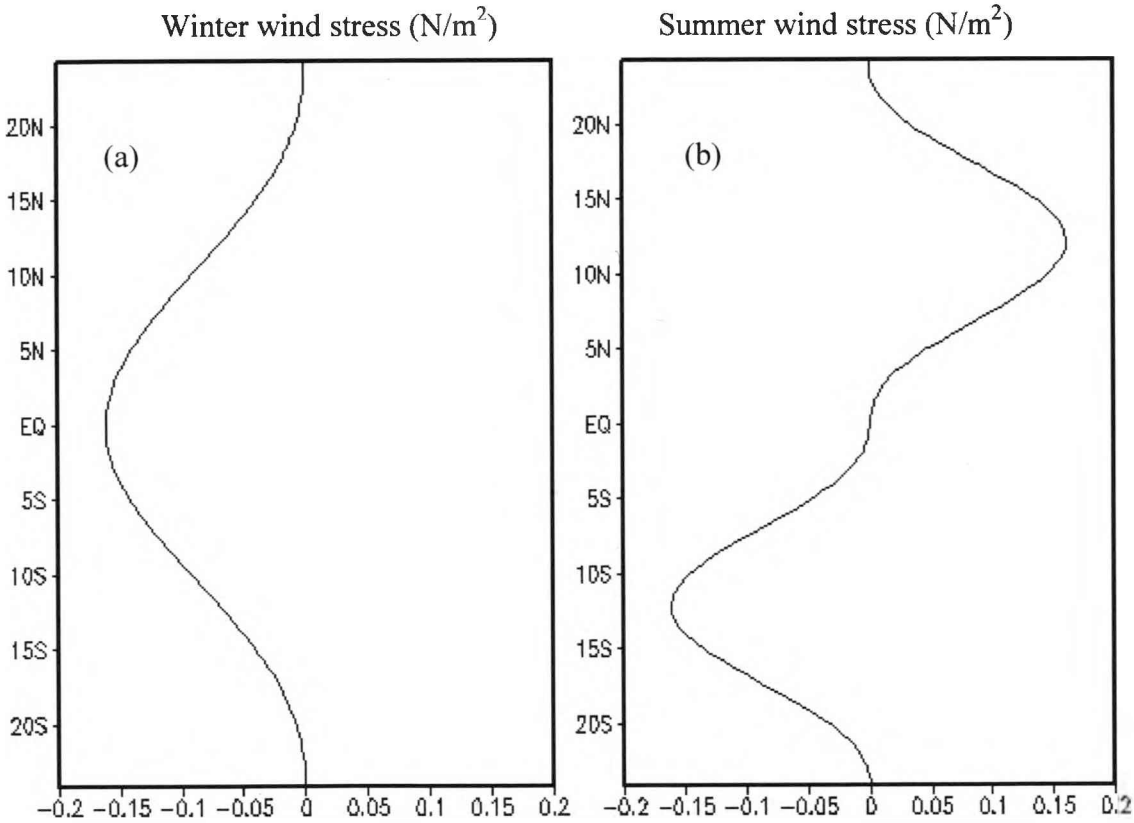

Figure 4.4: The wind stress applied in the model experiments
(a) the winter wind stress; (b) the summer wind stress.

4.1.3. Initial and lateral boundary conditions

The initial and boundary conditions for the runs using the MICOM model are as following: the initial layer depths were set to 100, 500, 2000, and 4000m with the density "sigma-t" ($\sigma_t = \rho - 1000$ where ρ is the density of seawater) of each layer being 24.0, 27.0, 27.6, and 27.8 respectively (Figure 4.3). The top surface layer (mixed layer) acts as an Ekman layer with the interface between the first two layers free to vary. At the lateral boundaries the non-slip boundary condition was applied.

The bottom friction parameter was set to 0.003. For the POLCOMS model, the numbers of vertical layer were set to 5 equal layers. Other parameters were the default which described in Chapter 3.

4.2. Model performance and its stability

The experiments with the POLCOMS model were carried on the former super computer at Manchester University and the Cluster of Proudman Oceanographic Laboratory (POL). The experiments with the MICOM model have been carried out on a Linux box at the Department of Earth and Ocean Sciences, University of Liverpool. The model experiments were set to start from rest and run up to 10 years. In all experiments the models showed a good stability after a spin-up time of about 3-4 months (POLCOMS) and 2-3 years (MICOM - Figure 4.5). It is usually difficult for basin-scale and global general circulation models to reach a state of statistical equilibrium under the applied forcing. The deep ocean requires hundreds of years to adjust, and the upper ocean requires about 50 years or so (Navy Operational Ocean Circulation and Tidal Models, 2003). Therefore with 10 years of model run as in the experiments, the deep flow is unlikely to fully come to an equilibrium state, but we can expect the barotropic flow to adjust.

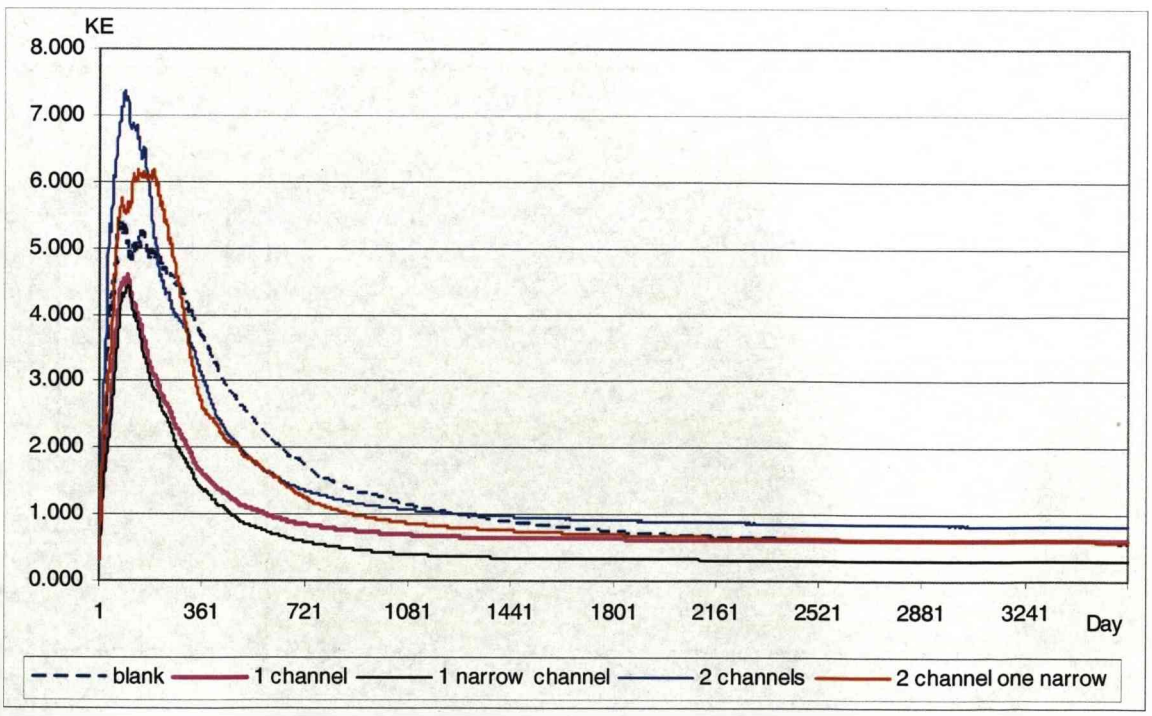

Figure 4.5: Kinetic energy of the model experiments (MICOM model).

4.3. Wind-driven circulation and volume transport

4.3.1. The Sverdrup balance

In a large scale open ocean, the temporal acceleration and advection of velocity terms are very small compared to the Coriolis acceleration (Ro=U/(fL) << 1). The Sverdrup balance for the depth-integrated meridional transport at steady state is given by neglecting bottom drag as follows:

$$\beta \int_{-H}^{0} v dz = \frac{1}{\rho}\left(\frac{\partial \tau_y^s}{\partial_x} - \frac{\partial \tau_x^s}{\partial_y}\right). \quad (4.1)$$

where β is the meridional gradient in planetary vorticity ($\beta=df/dy$), $\int_{-H}^{0} v dz$ is the depth integrated meridional velocity, H is the depth of the ocean, τ^s is the surface wind stress, the subscripts x,y denote the eastward and northward components.

The stream function of volume transport predicted for the Case 4.1 with the winter wind stress (Figure 4.4.a) using Sverdrup balance (4.1) shows two strong gyres, symmetrical about the Equator with maximum of meridional volume transport along the western boundary of about 40Sv (Figure 4.6). In the case of the summer wind stress (Figure 4.4.b), there are instead 4 symmetric gyres can be seen, each hemisphere has two gyres (Figure 4.7). This case, due to increase in the wind stress the maximum volume transport of gyres increased up to 70Sv.

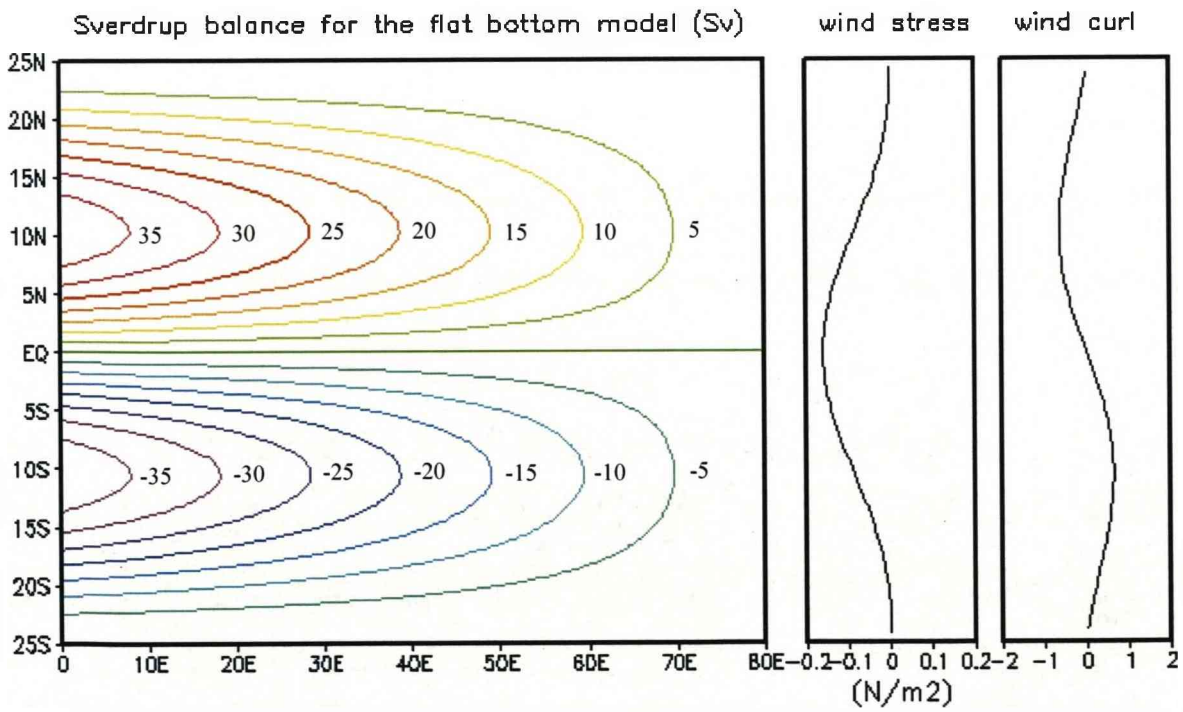

Figure 4.6: The stream function of the interior volume transport predicted by Sverdrup balance, (the winter wind stress – the contour interval is 5 Sv).

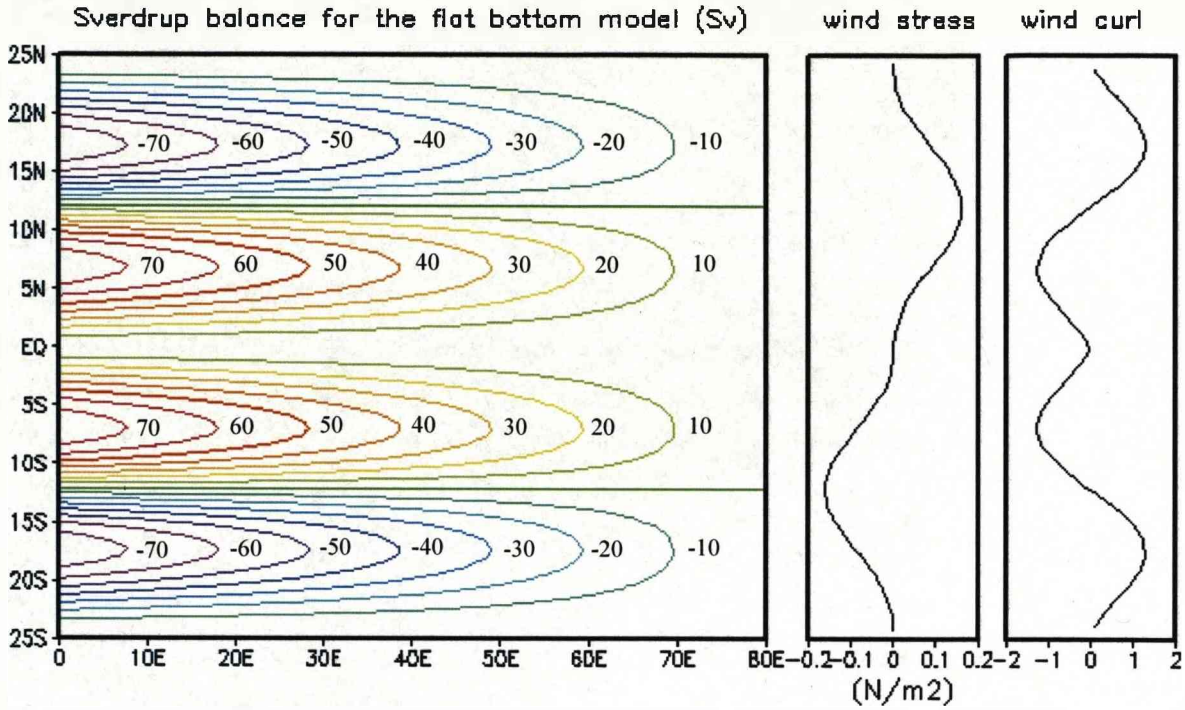

Figure 4.7: The stream function of the interior volume transport predicted by Sverdrup balance, (the summer wind stress– the contour interval is 10Sv).

4.3.2. MICOM model experiments

4.3.2.1 The classical rectangular domain (Case 4.1)

- ***The winter wind stress***

Figure 4.8 shows the circulation driven by the purely zonal winter wind stress (Figure 4.4.a). With all boundaries closed and the northern and southern boundaries limited at 25°N and 25°S respectively, the model produced two main anticyclonic gyres of the ocean circulation, anticlockwise gyre in the northern hemisphere and clockwise gyre in the southern hemisphere.

On either side of the Equator the current systems involving in a gyre including two zonal currents polewards and equatorwards of the gyre centre, and two other currents that close the gyre, the so-called western and eastern boundary currents. Among them the western boundary current is faster, narrower and deeper than the eastern boundary current. The intensification of the western boundary current along the boundary was first explained by Stommel (1948) as related to planetary vorticity or the variation of the Coriolis parameter (pseudo force) with latitude.

In the northern hemisphere, the strong western boundary current (40-50cm/s) flows polewards, from the Equator and low latitude to a higher latitude, and represents the

warm water currents such as Gulf Stream and Kuroshio systems in reality. The weaker eastern boundary current flows equatorwards, from high latitude to the Equator, represents the cold currents such as the California or Canary Currents. In the southern hemisphere these current systems are also polewards and equatorwards, the western boundary current flowing polewards from the Equator (e.g. Brazil, East Australia, Agulhas), the eastern boundary current flowing equatorwards to the Equator (e.g. Peru, Benguela, West Australia).

In terms of volume transport the results of the MICOM model closely match the Sverdrup balance in terms of location of gyres and the volume transport of the interior basin. In the northern hemisphere, in accordance with the negative wind stress curl is a clockwise gyre, centered at the maximum of the wind stress curl (12.5°N latitude) with a volume transport reaching 40 Sv. The anti-clockwise gyre present in the southern hemisphere is a result of changing of the sign of wind stress curl from negative to positive (Figure 4.9).

The stream function of the interior volume transport of both MICOM model and Sverdrup balance, plotted along a north-south cross-section at the longitude of about 10 degrees away from the western boundary, shows that the volume transport of the MICOM model matches Sverdrup balance (Figure 4.10). The comparison at locations closer to the western boundary shows a small difference between MICOM and Sverdrup (not show). An important difference between model and the Sverdrup balance is the model certainly has some friction while bottom drag is neglected in the theory of Sverdrup. This therefore can contribute to the difference between the theory and numerical model results.

- ***The summer wind stress***

The summer wind stress has been generated by setting a zonal west wind in the northern hemisphere, and a zonal east wind in the southern hemisphere (Figure 4.4.b). This makes the wind stress more intense in each hemisphere, consequently producing a higher wind stress curl compared to the winter wind stress. The change of wind forcing to the summer wind stress has significantly changed the circulation and volume transport by increasing the number of gyres and the strength of the circulation and volume transport (Figures 4.11 & 4.12).

Being driven by the summer wind stress, the circulation system is separated into four gyres, two gyres in each hemisphere. The western boundary current of gyres are strengthened in response to the increased wind stress curl with speed reaching approximately 100 cm/s and volume transport reaching 70 Sv. In each hemisphere the major dividing lines between gyres correspond to the latitude of the zero wind stress curl, which is 12.5° on either side of the equator. According to the reversal of the wind stress, the gyres in the north and south of the Equator are equivalent. As in the case of the winter wind stress, the MICOM model again shows a good agreement with Sverdrup balance in terms of the volume transport of the interior water (Figure 4.13).

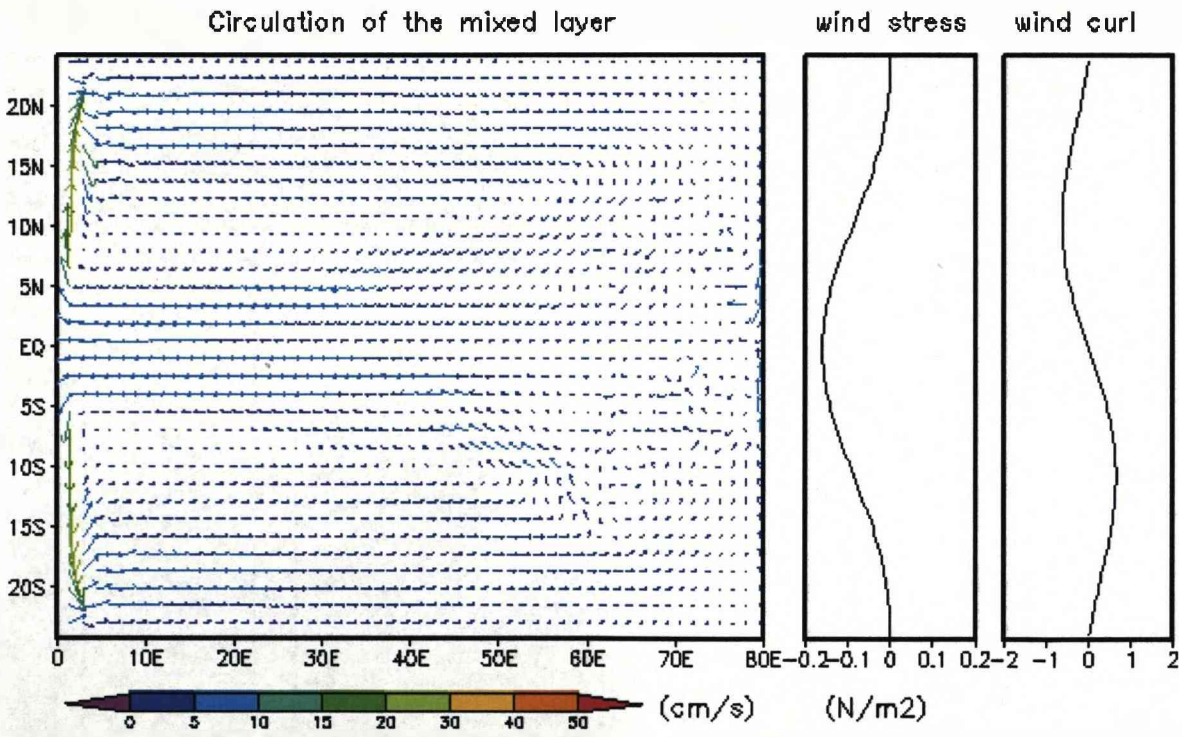

Figure 4.8. The mean circulation of the mixed layer produced by MICOM model (Case 4.1, the winter wind stress).

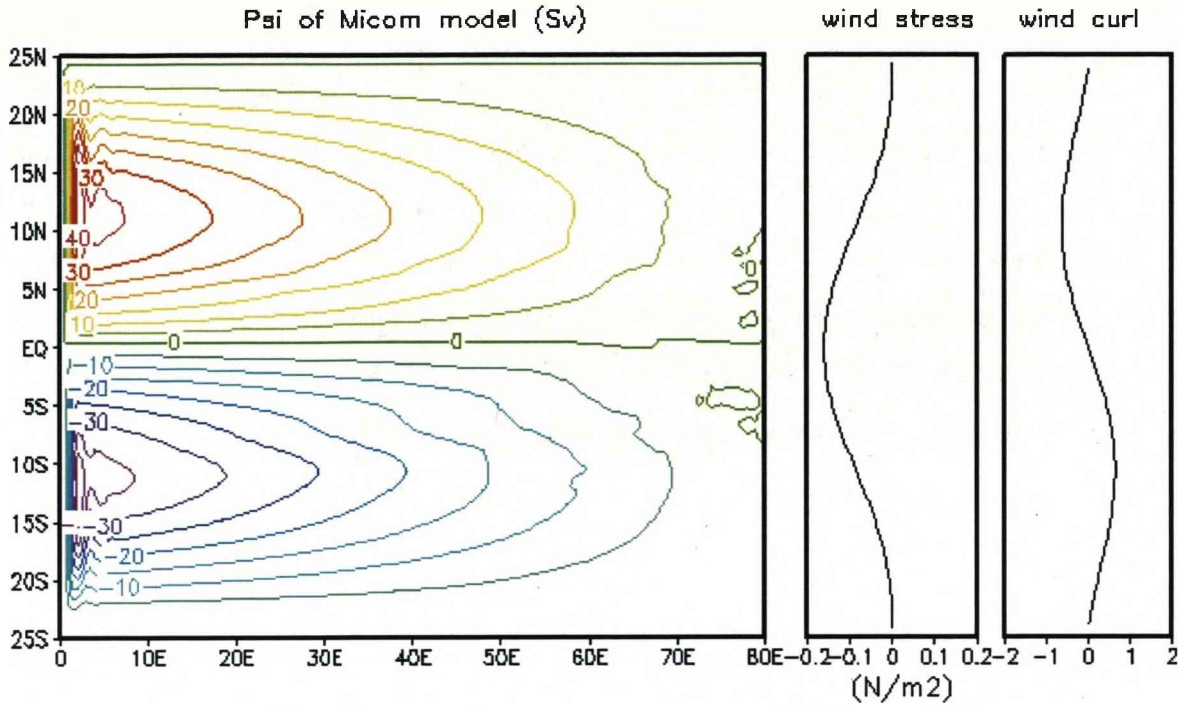

Figure 4.9. The stream function of volume transport (Case 4.1, the winter wind stress).

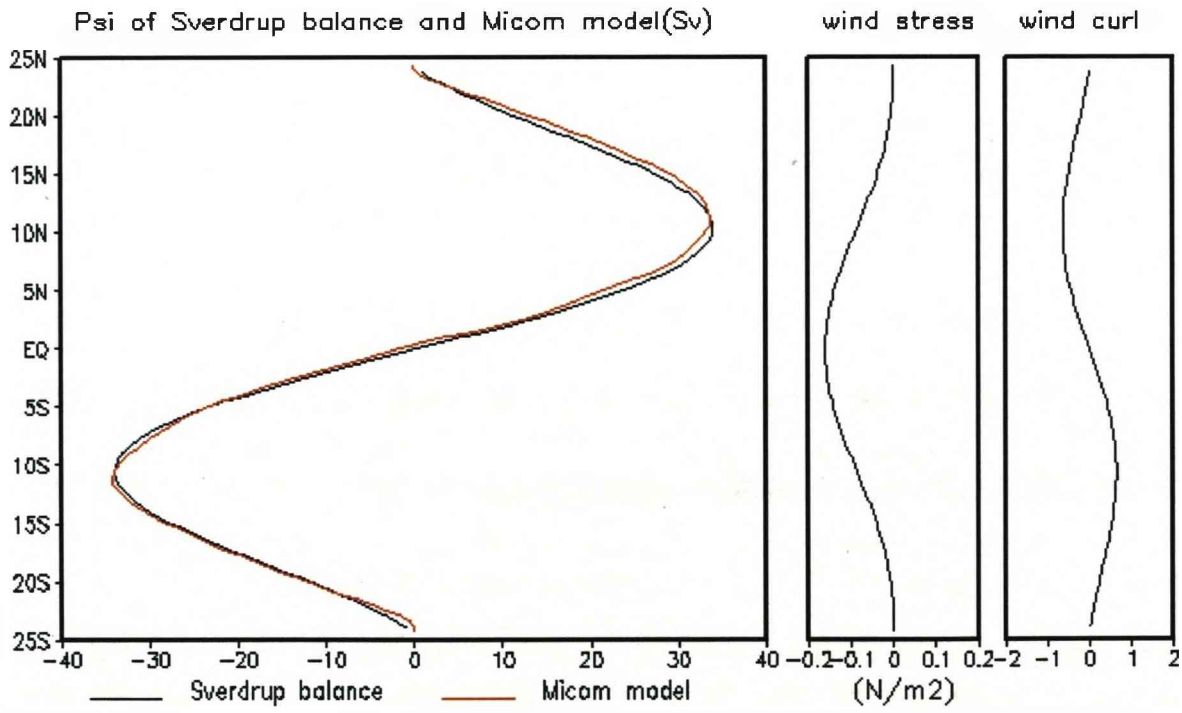

Figure 4.10. The comparison of stream function beetwen Sverdrup balance and MICOM model (Case 4.1, the winter wind stress). The location is 10° of longitude away from the western boundary.

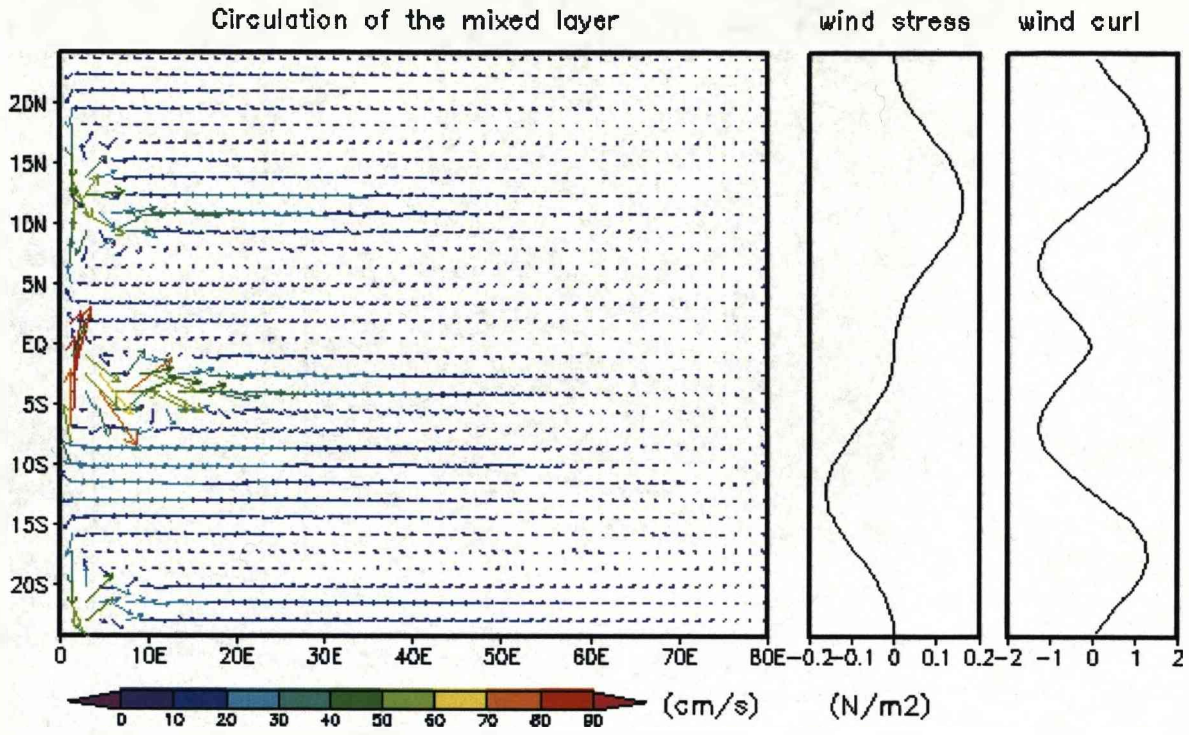

Figure 4.11. The mean circulation of the mixed layer produced by MICOM model. (Case 4.1, the summer wind stress).

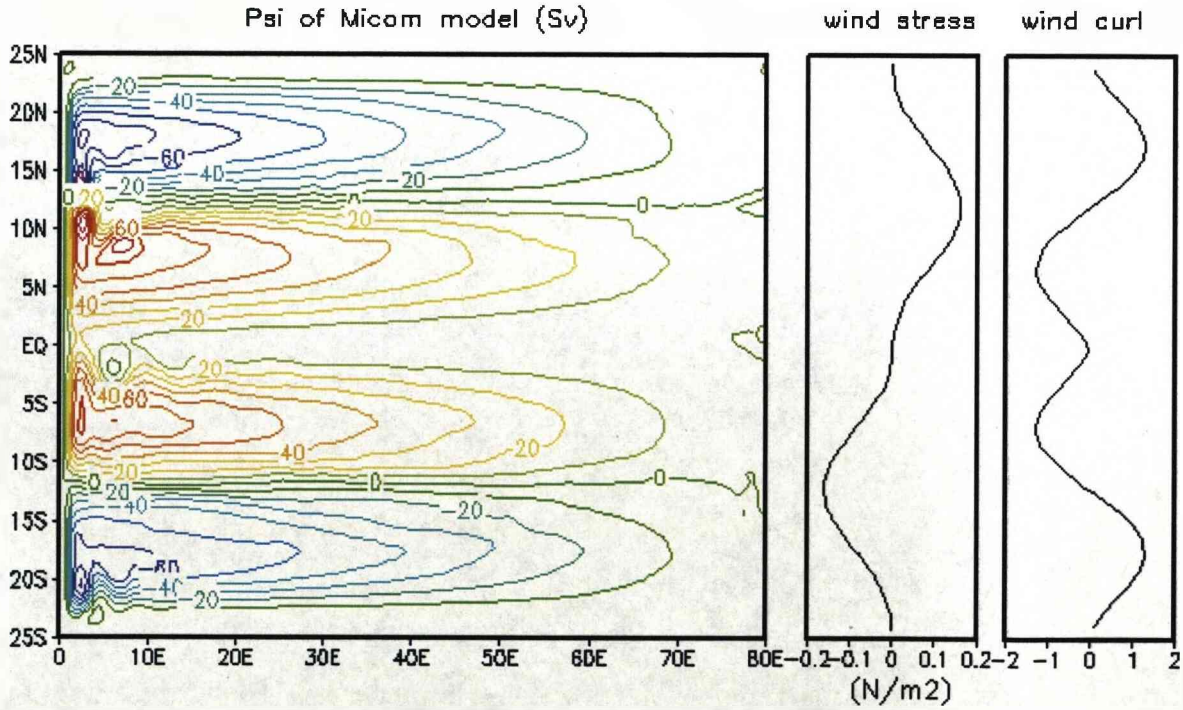

Figure 4.12. The stream function of volume transport (Case 4.1, the summer wind stress).

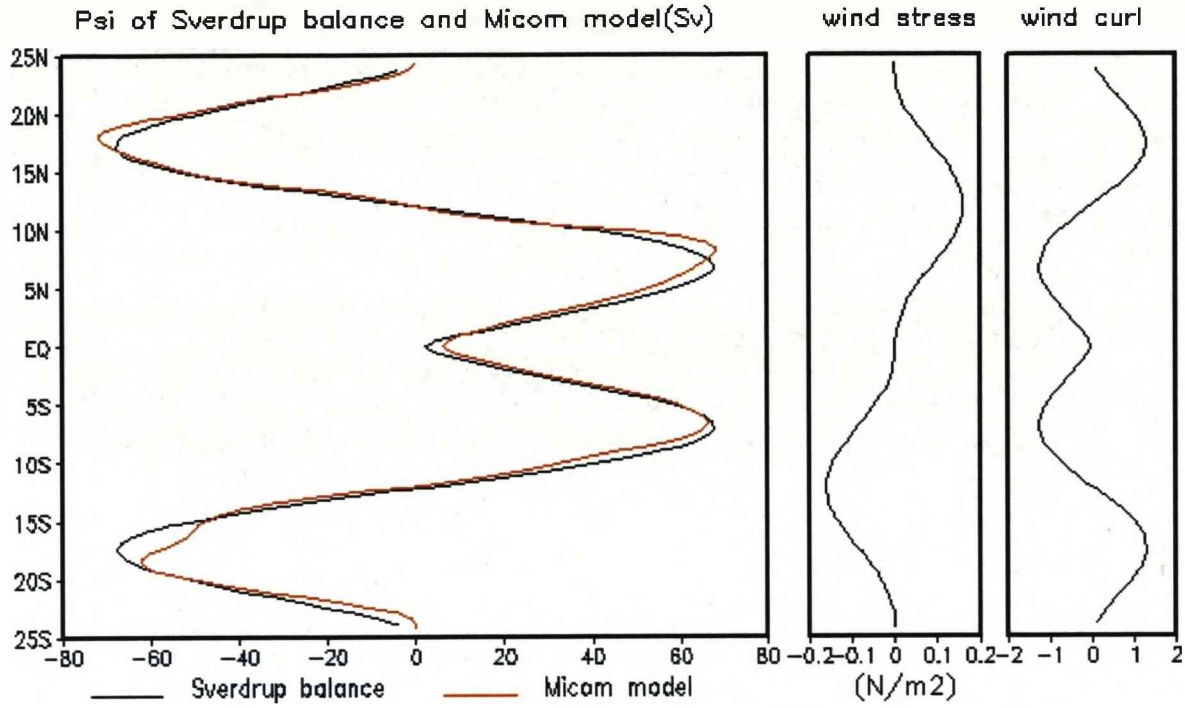

Figure 4.13. The comparison of stream function beetwen Sverdrup balance and MICOM model (Case 4.1, the summer wind stress). The location is 10° of longitude away from the western boundary.

4.3.2.2. Effect of a submerged barrier in the middle of the domain (Case 4.2)

When a barrier is submerged in the middle of the domain, it divides the whole domain into two equal sub-basins with a shorter zonal length scale. The eastern flank of the barrier acts as western boundary for the eastern basin, the western flank acts as an eastern boundary for the western basin. The submerged barrier almost blocks the movement of water between the eastern and western parts of the domain, and as a result completely changes the picture of the circulation and volume transport.

Figures 4.14 - 4.17 show the model results of Case 4.2, driven by the winter wind stress and the summer wind stress respectively. Although the sub-basins are connected through a shallow channel, the gyres almost develop within the sub-basins. The number of gyres and their strength depends on the applied wind stress. When the system was forced by the winter wind stress, there only two gyres develop in each sub-basin, but increase to four gyres when forced by the summer wind stress. Although the strength of the wind stress is kept the same as in the case of the blank domain, but with the shorter west-east length scale the strength of the western

boundary currents and volume transport are decreased. In the case of forcing by the winter wind stress, the centre of the stream function of volume transport (centre of gyre) in the western basin moves closer to the Equator and has a higher value (20 Sv) compared to the eastern basin (15 Sv). The higher meridiunal volume transport of the western basin compared to the eastern basin can be explained by the Sverdrup balance as the volume transport is integrated from the eastern boundary.

Along the shallow channel there is only barotropic flow. In the case of the winter wind stress a strong westwards current occurs along the Equator in responding to the higher strength of the westwards wind stress, the return flow from the western basin to the eastern basin appears along the northern and southern banks of the channel with smaller velocity as the strength of the wind stress in these regions is decreased (Figure 4.14) and the effect of boundary friction. In the case of the summer wind stress, the current pattern in the shallow channel is changed according to the change of the wind stress. The current along the Equator is almost zero as result of the reduction of the wind stress to nearly zero. In the northern part, a strong eastwards current occurs along the northern bank of the channel (stronger wind stress) while a weaker westwards current is present near the Equator (weak wind stress). Due to the reversal of wind stress over the Equator the situation in the southern part of the channel is in the opposing direction, a strong westwards current occurs along the southern bank of the channel, and a weaker eastwards current presents near the Equator (Figure 4.16).

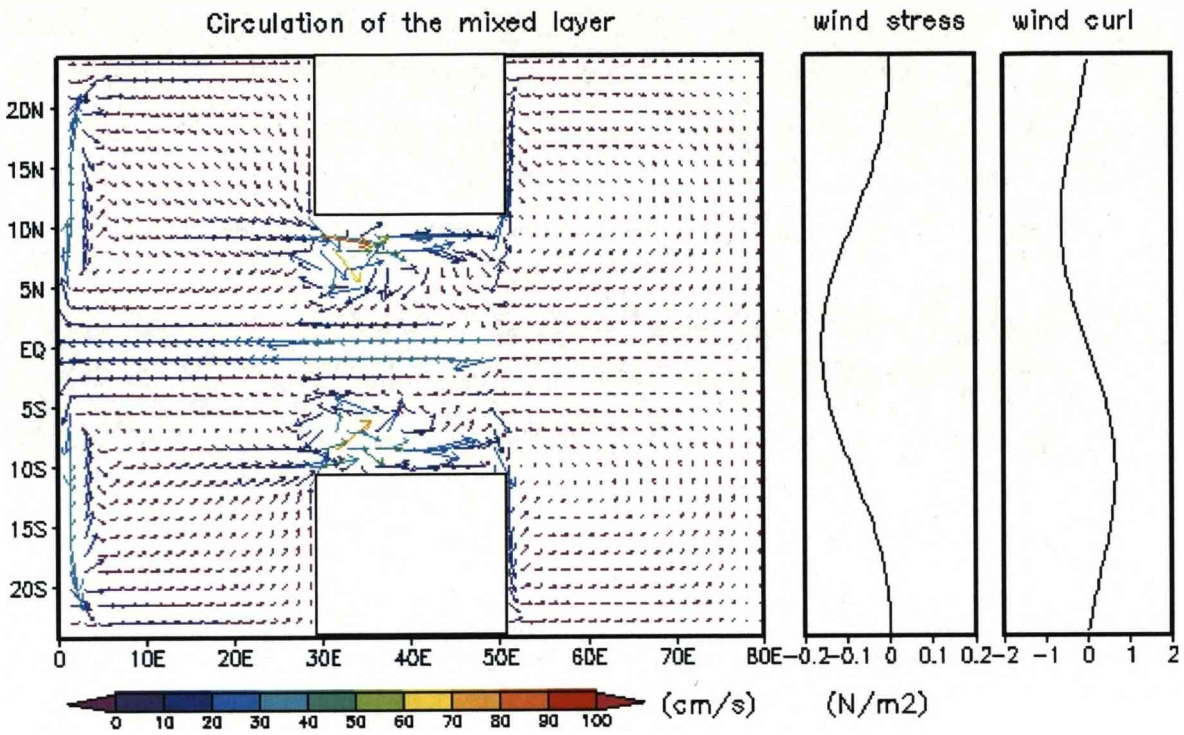

Figure 4.14. The mean circulation of the mixed layer produced by MICOM model (Case 4.2, the winter wind stress).

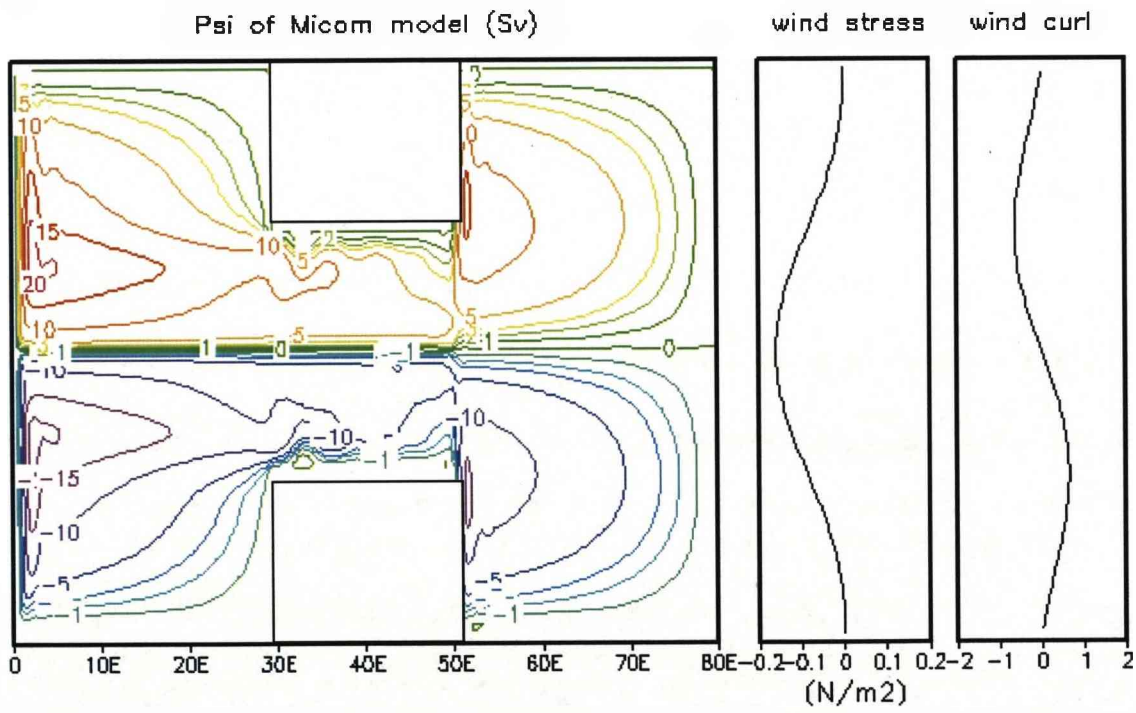

Figure 4.15. The stream function of volume transport (Case 4.2, the winter wind stress).

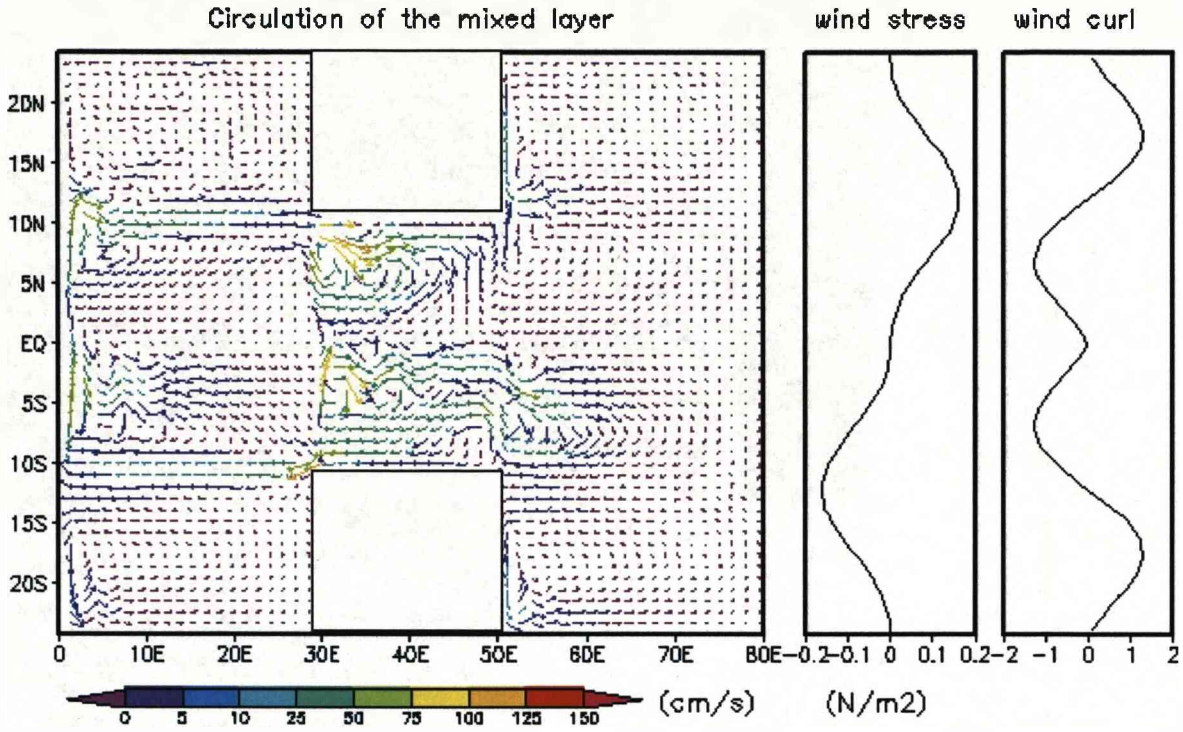

Figure 4.16. The mean circulation of the mixed layer produced by MICOM model (Case 4.2, the summer wind stress).

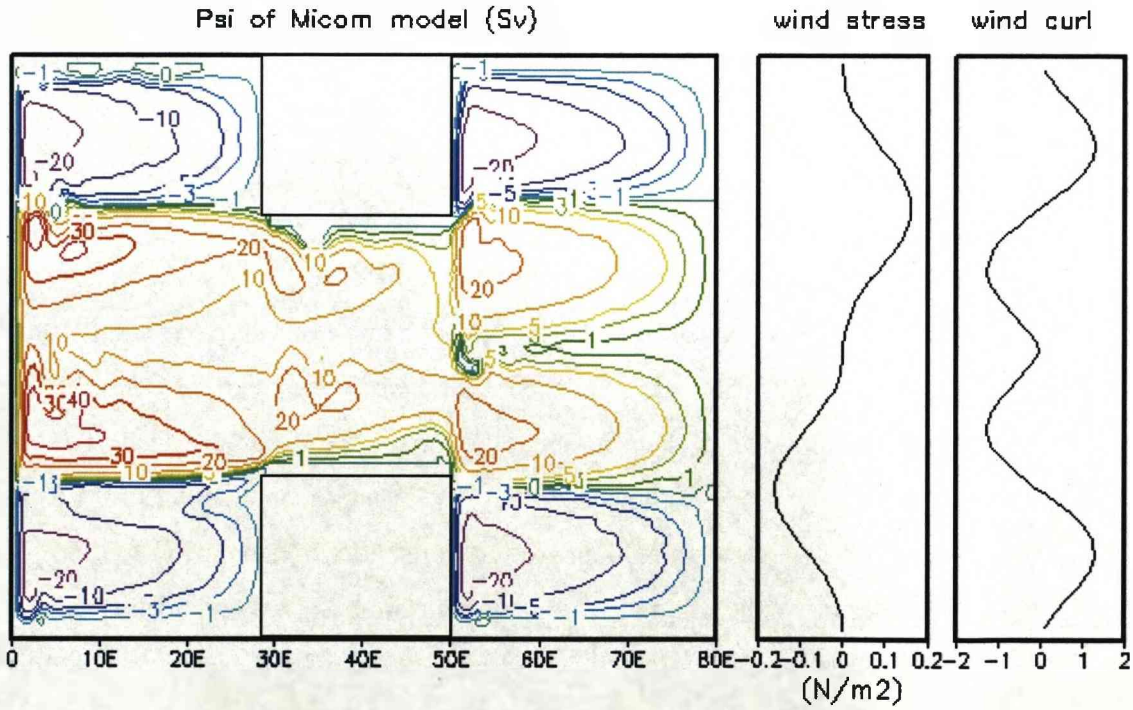

Figure 4.17. The stream function of volume transport (Case 4.2, the summer wind stress).

4.3.2.3. Effect of opening the deep channel (Case 4.3)

If the eastern basin in the one channel domain is considered as "the Pacific ocean", the western basin as "the Indian ocean" and the shallow channel represents the channels in the Southeast Asia region then opening a deep channel will allow a partial reproduction of the ACC. Unlike the Case *4.2* where water exchange between basins only occurs within a limited water depth in the shallow channel, in Case *4.3* the water exchange can take place in both the shallow and the deep channels which potentially increases the volume transport between the basins.

It can be seen from the Sverdrup balance and the previous experiments that gyres do not generally cross the line of zero wind stress curl, therefore opening the deep channel would not be expected to effect the circulation and volume transport in the northern hemisphere. The model results show that this seems to be correct for the eastern basin, but not for the western basin where the stream function of the volume transport expands southwards over the Equator (i.e. crossing the line of zero wind stress curl).

When driven by the winter wind stress, the influence of opening the deep channel on the circulation and volume transport in the southern hemisphere is very strong and clear, particularly in the western basin. The water in the western basin flowing along the southern boundary is now able to flow back to the eastern basin through the deep channel. To compensate for this amount of eastwards transport, the current velocity in the shallow channel (southern half) and the western boundary are increased (Figure 4.18), as a result of increasing the water exchange between the basins in the southern hemisphere. The stream function of the volume transport of the western basin shows a very high value along the western boundary (70-90 Sv). The total amount of westward transport through the shallow channel is about 63.5 Sv but the contribution of the southern half is about 54.3 Sv, nearly 6 times higher than the contribution of the northern half (9.2 Sv). Unlike the southern hemisphere, the opening of the deep channel does not influence the circulation in the northern hemisphere very much. The circulation and stream function of volume transport in the northern hemisphere are rather similar with the case of one channel domain in terms of pattern and strength. The volume transport of the western boundary current

is about 10-15 Sv in the eastern basin, and 15-20 Sv in the western basin (Figure 4.19).

When the driving force is the summer wind stress, the circulation pattern is rather different in comparison to the circulation in the case of winter wind stress (Figure 4.20). The flows at about 12^{o} latitudes (both northern and southern hemispheres) are strengthened, and the strong current flowing from the western basin to the eastern basin along the southern boundary in the case of winter wind stress is weakened. The change of the circulation pattern due to the change of the wind stress results in a change in the volume transport between the basins. The stream function of volume transport (Figure 4.21) shows that, in the southern hemisphere, the meridional transport along the western boundary of the western basin is strongly decreased (from ~70 Sv to ~20 Sv). In the deep channel there is also a large change in volume transport between the basins. This will be discussed more in the section 4.4.2.

4.3.2.4. Effect of change of the shallow channel's width and latitude

- **Change of shallow channel width**

Figures 4.22 - 4.24 show the models results of the one channel domain when the channel is reduced to a quarter of its original width (Case 4.4), driven by winter wind stress. When the shallow channel is narrowed it reduces the water exchange between basins, decreasing the meridional transport along the western boundary in the western basin and moving the centre of the gyres futher north and south away from the equator to the location of the maximum of the wind stress curl. In the shallow channel, a strong westward current occurs in the middle, the weaker eastwards currents occur along the northern and southern banks in responding to the strength of wind stress and boundary friction (Figure 4.23).

Figures 4.25 and 4.26 show the model results of two-channel domain where the shallow channel has been narrowed and driven by winter wind stress (Case 4.5). In the Case 4.5, there is only strong westward current in the shallow channel and weaker eastwards current in the deep channel. The meridional volume transport along the western boundaries is increased in comparison with the one narrow channel, particularly in the southern hemisphere part of the western basin.

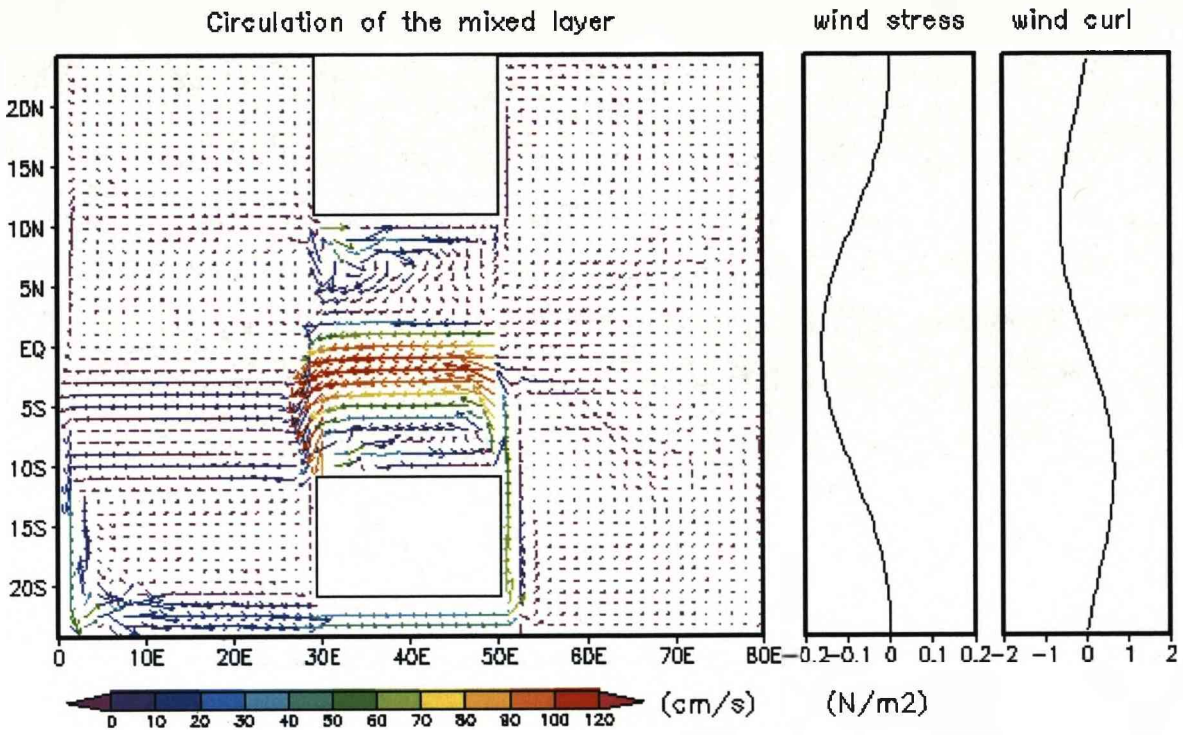

Figure 4.18. The mean circulation of the mixed layer produced by MICOM model (Case 4.3, the winter wind stress).

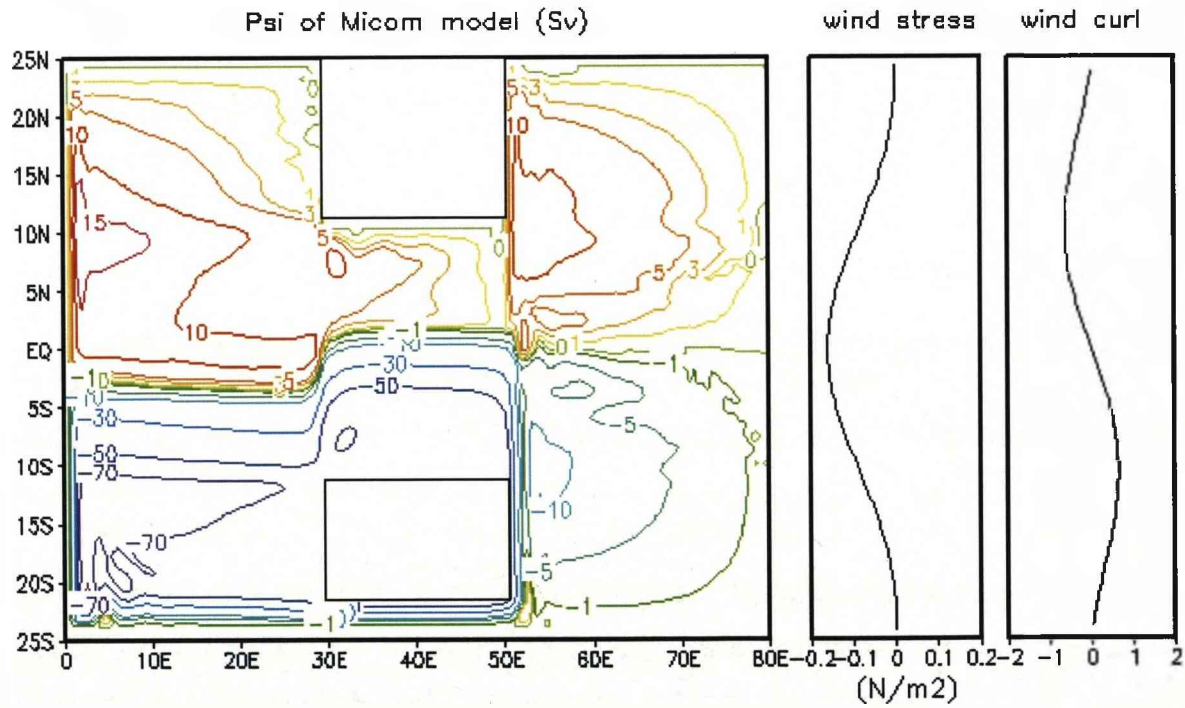

Figure 4.19. The stream function of volume transport (Case 4.3, the winter wind stress).

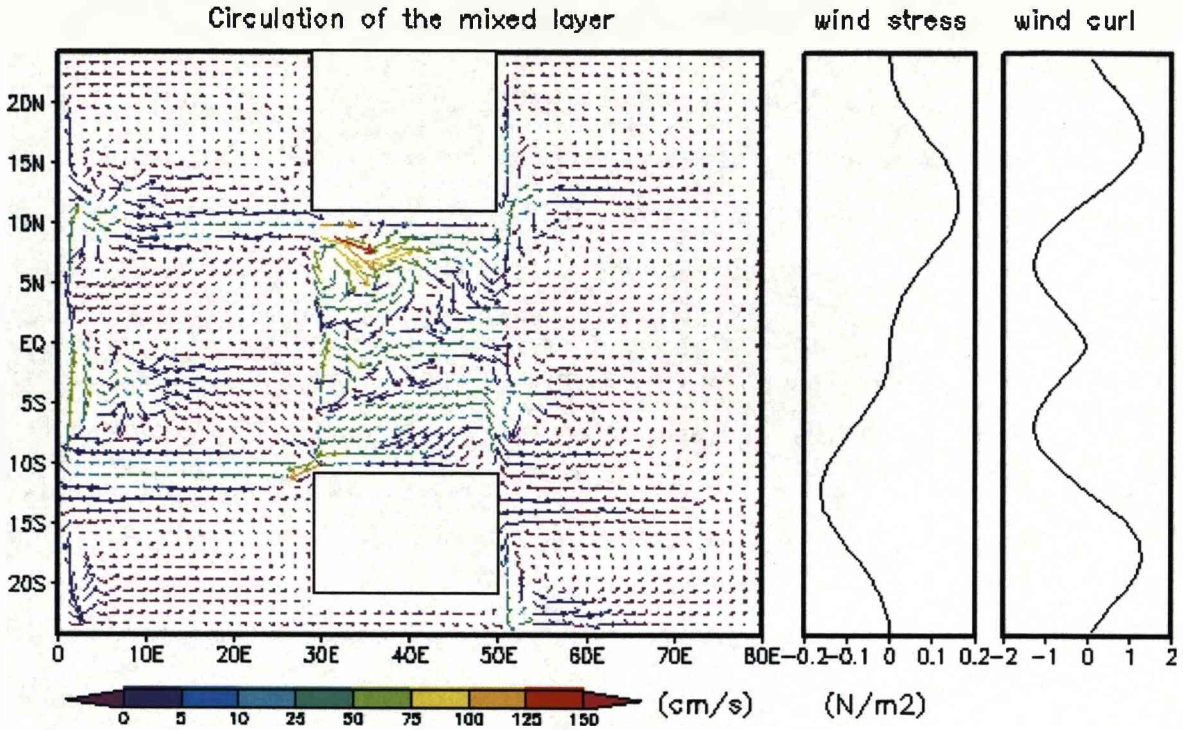

Figure 4.20. The mean circulation of the mixed layer produced by MICOM model (Case 4.3, the summer wind stress).

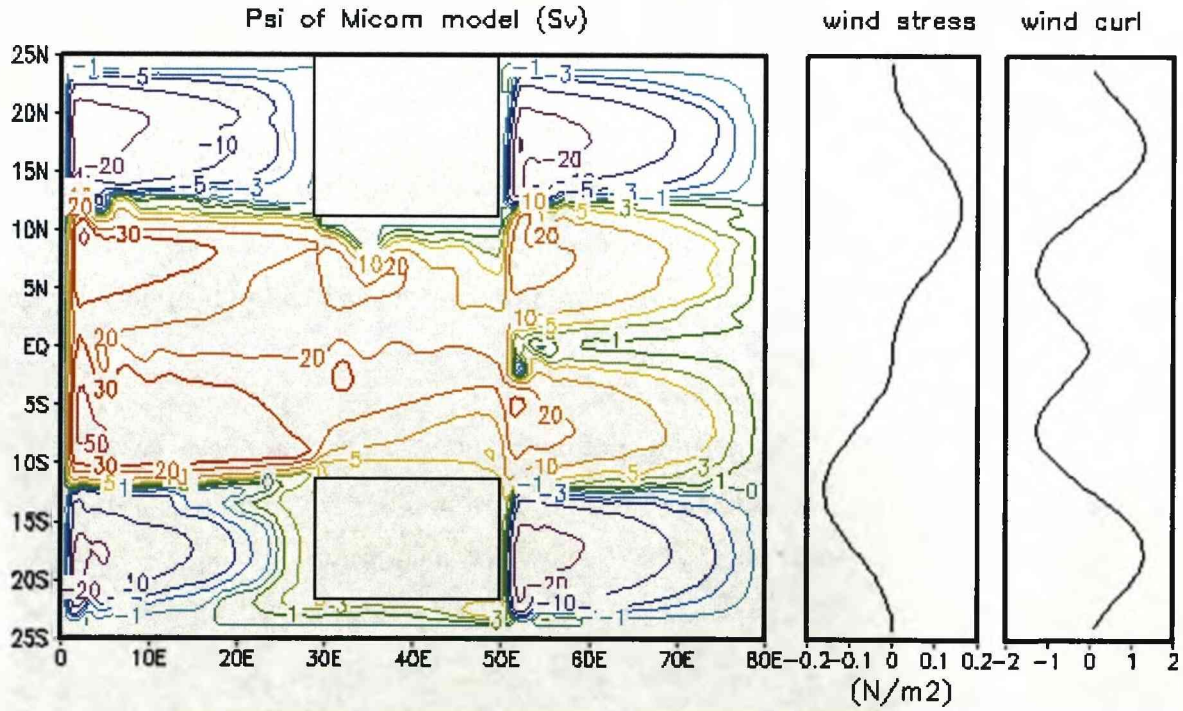

Figure 4.21. The stream function of volume transport (Case 4.3, the summer wind stress).

- **Change of the latitude of the shallow channel**

When the shallow channel is shifted south (Case 4.6), the northern hemisphere is still separated from the southern hemisphere through the line of zero wind stress curl along the Equator. The stream functions of volume transport in the north of the basins are almost identical (Figure 4.27). In the southern hemisphere the strength and pattern of the stream function of volume transport in the eastern basin is still the same, but not in the western basin. The depth-integrated stream function in the western basin has increased its strength to compensate for the amount of water flowing eastward through the deep channel. This increase is associated with the strong westward jet along 15°S (Figure 4.28).

There is only an eastward current along the deep channel, but both westwards and eastwards currents present in the shallow channel. According to the difference in the strength of the wind stress over the channel (stronger in the northern bank and weaker in the southern bank), the velocity of the westward current along the northern bank of the shallow channel is higher than the eastward current along the southern bank (Figure 4.29).

Figures 4.30, 4.32 show the model results when the shallow channel shifted north (Case 4.7). The strength of currents in the deep channel and shallow channel are similar to the previous case, only an eastward current is present in the deep channel. Westward and eastward currents both occur in the shallow channel, but this time the speed of westward current along southern boundary is higher than the eastward current along the northern boundary (Figure 4.31).

In both cases when the latitude of the shallow channel has been moved, the dividing line between northern and southern hemisphere gyres remains at the Equator where the wind stress reaches the maximum value and the curl is zero.

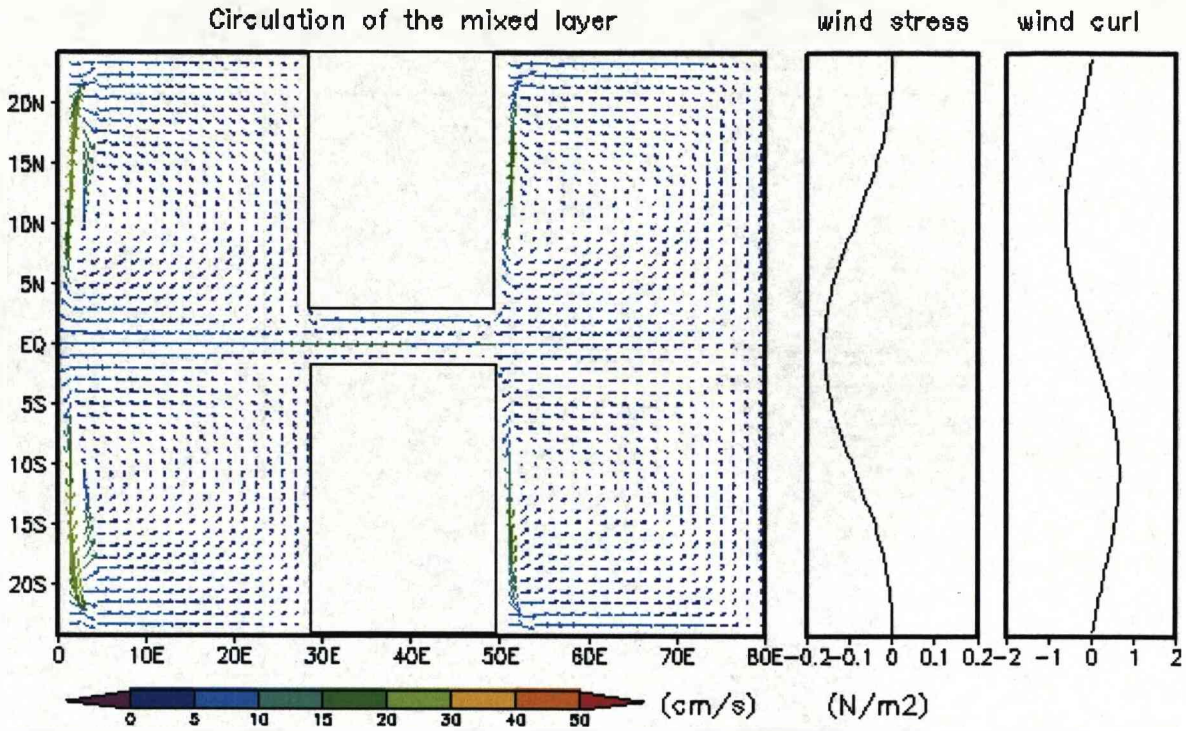

Figure 4.22. The mean circulation of the mixed layer produced by MICOM model (Case 4.4, the winter wind stress).

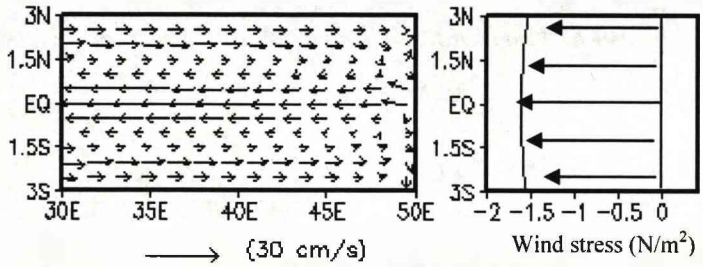

Figure 4.23: The current pattern and wind stress in the shallow channel.

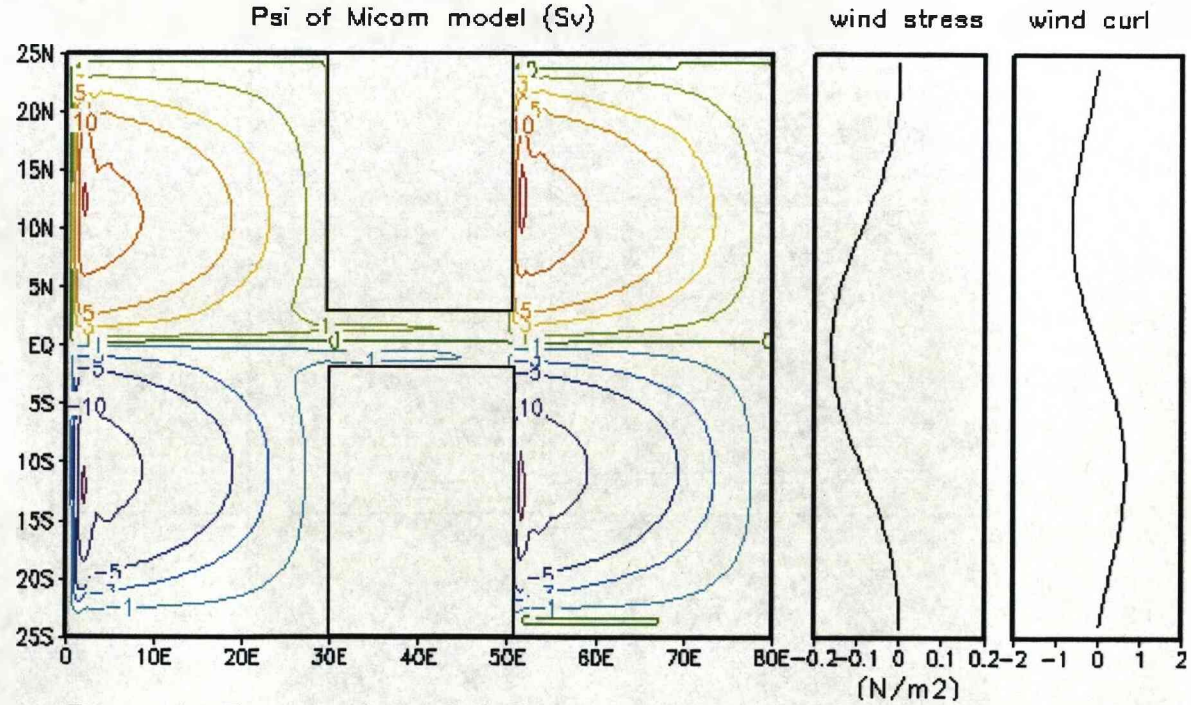

Figure 4.24. The stream function of volume transport (Case 4.4, the winter wind stress).

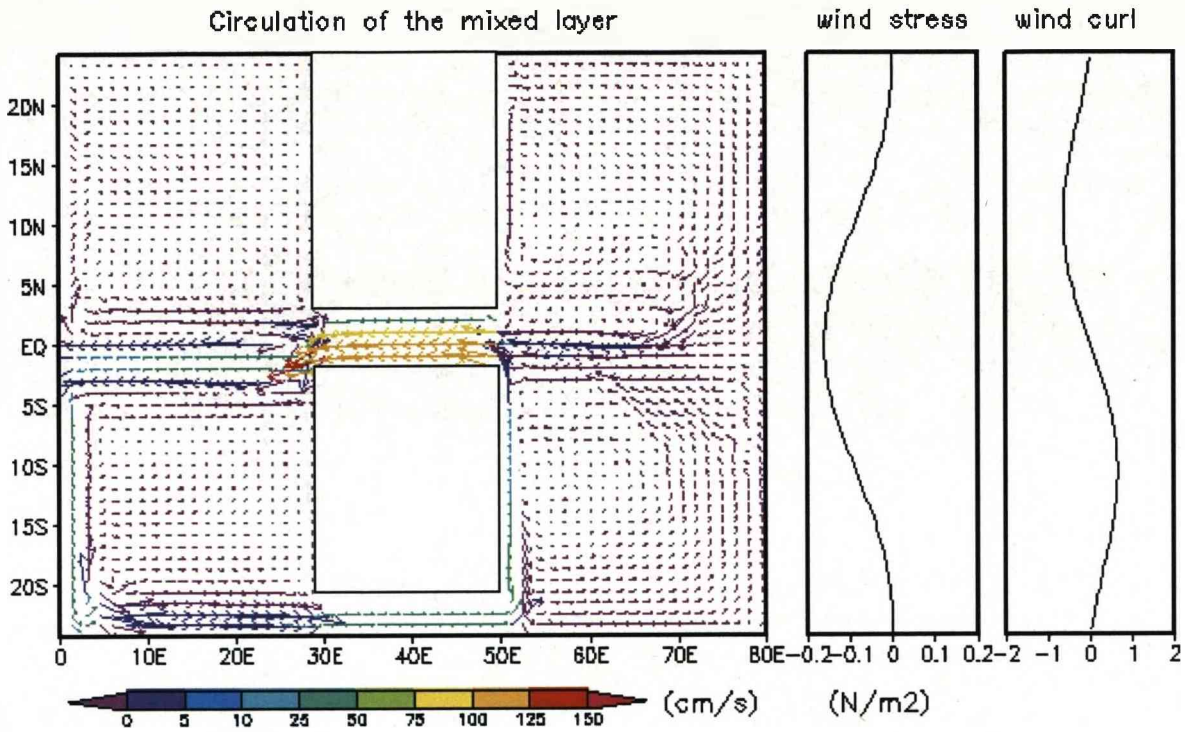

Figure 4.25. The mean circulation of the mixed layer produced by MICOM model (Case 4.5, the winter wind stress).

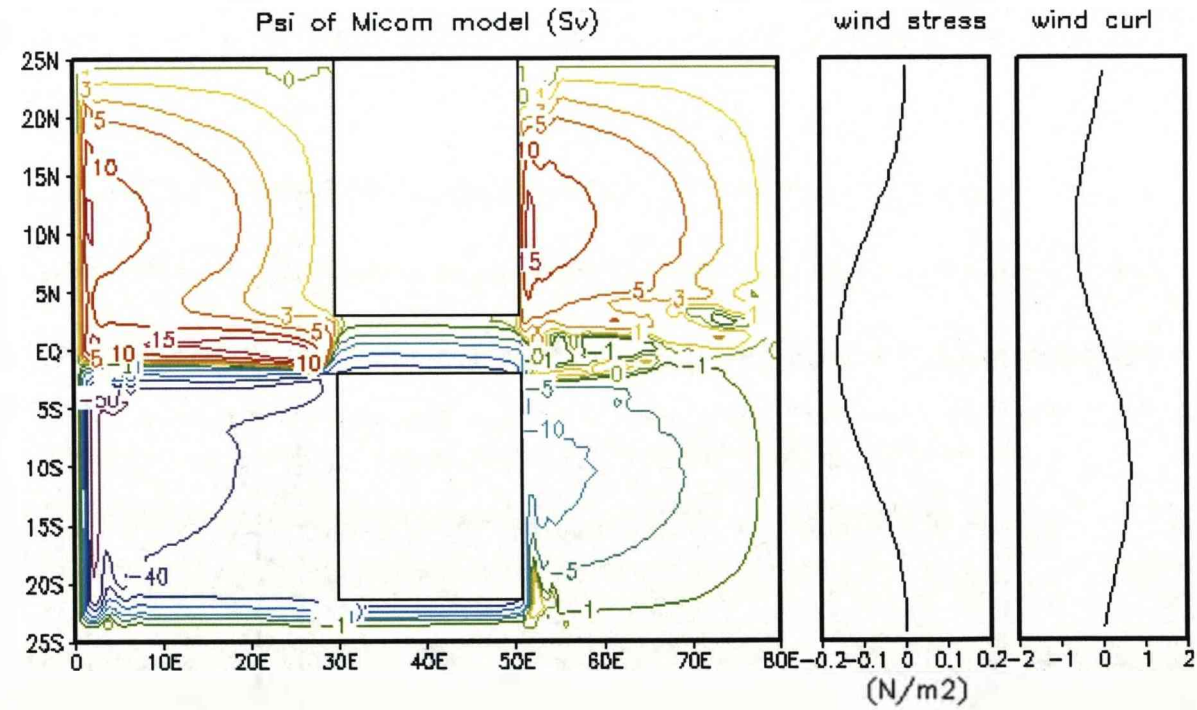

Figure 4.26. The stream function of volume transport (Case 4.5, the winter wind stress).

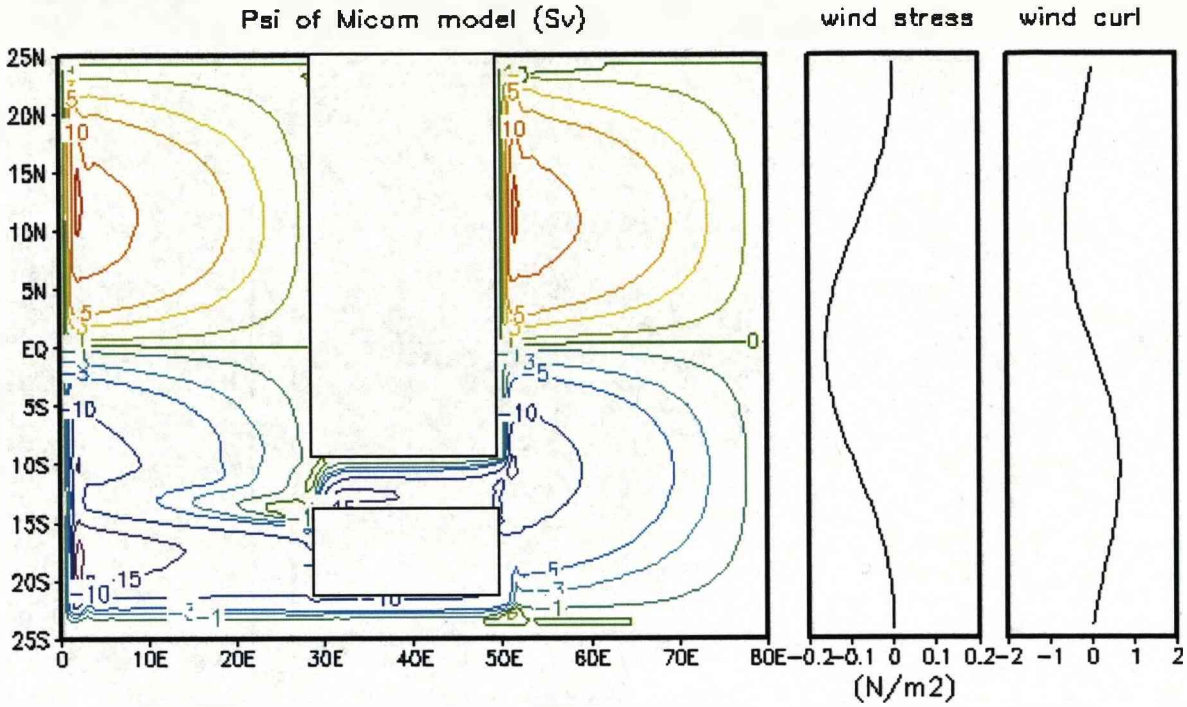

Figure 4.27. The stream function of volume transport (Case 4.6, the winter wind stress).

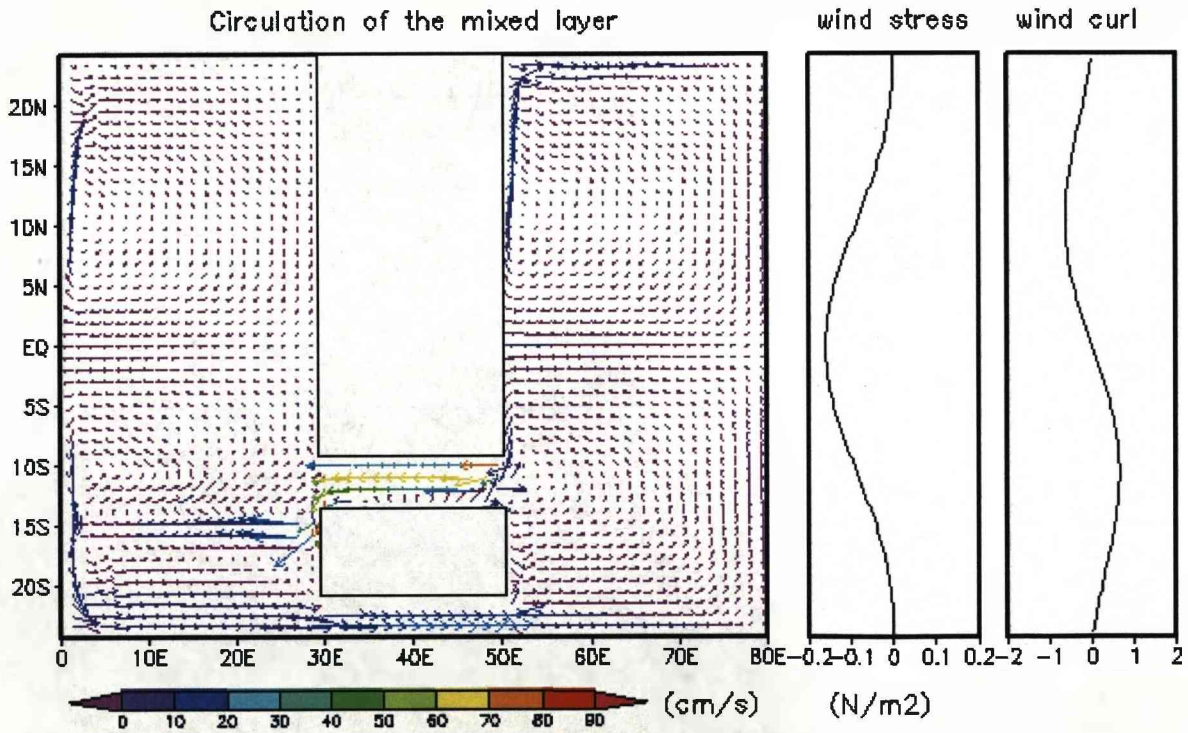

Figure 4.28. The mean circulation of the mixed layer produced by MICOM model (Case 4.6, the winter wind stress).

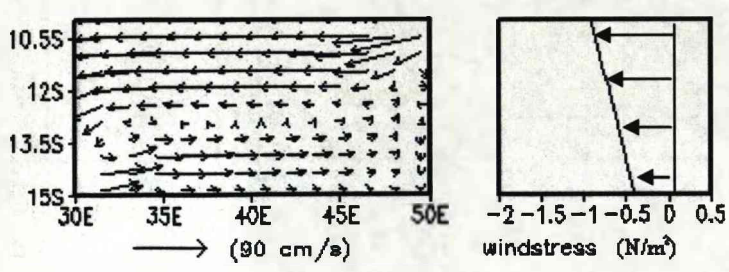

Figure 4.29: The current pattern and wind stress in the shallow channel.

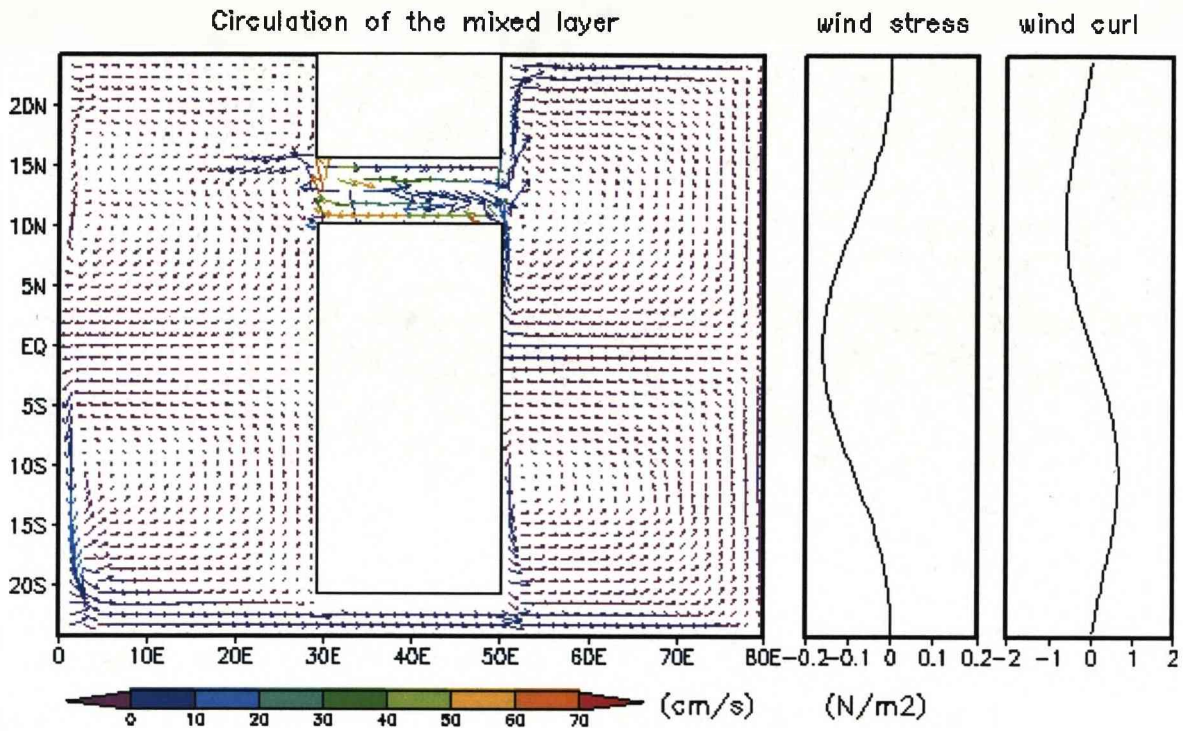

Figure 4.30. The mean circulation of the mixed layer produced by MICOM model (Case 4.7, the winter wind stress).

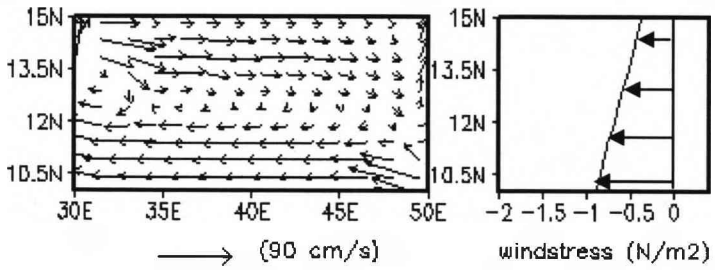

Figure 4.31: The current pattern and wind stress in the shallow channel.

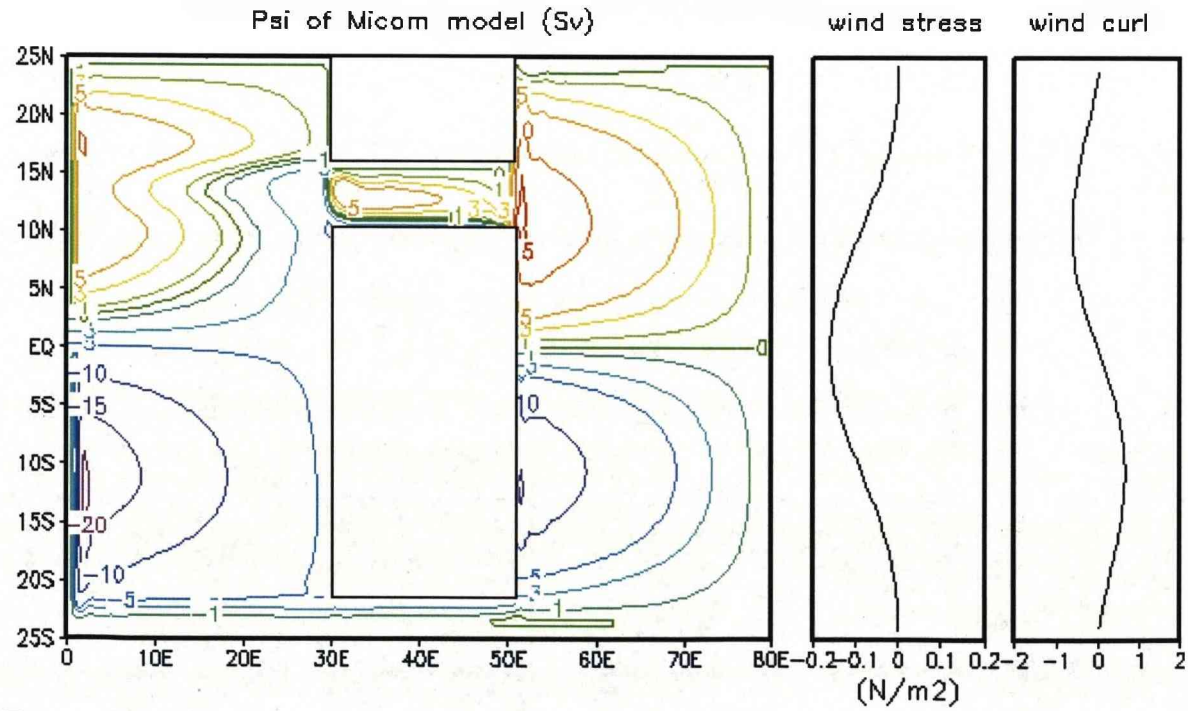

Figure 4.32. The stream function of volume transport (Case 4.7, the winter wind stress).

4.4. Volume transport between the basins and at the shallow channel

One of the main objectives of the research is modelling the water exchanges between the Pacific Ocean and the Indian Ocean through the passages in the Southeast Asia region. Understanding the water exchange between the basins, particularly in the shallow channel of the idealised model experiments, will help construction of the realistic model experiments and later understand the results of the realistic topography and wind forcing model in this complex region.

To examine the water exchange between the basins, total fluxes across meridional sections located at the middle of the domains are calculated. Table 4.1 shows the total volume transport between the basins of the idealised experiments.

4.4.1. Volume transport of Case 4.2

In Case 4.2, the water exchange between the basins occurs only at the shallow channel. A net transport between the basins is not permitted or in other words the value of the net transport needs to be zero to satisfy mass conservation.

In the case of forcing by the winter wind stress, there is only a westwards wind stress over the channel. This wind stress produces approximately 17.0 Sv of westwards volume transport from the eastern basin to the western basin through the middle of the channel reflecting the sign and strength of the wind stress. To maintain the mass conservation of the whole domain there is an equivalent amount of eastwards transport from the western basin to the eastern basin along the northern and southern banks of the channel. In the case of forcing by the summer wind stress, the northern half of the channel is driven by the eastward wind stress, while the southern half is driven by the westward wind stress. This pattern of wind stress has increased approximately 1.5 times of the water exchange between the basins (Table 4.1).

Table 4.1: The volume transport (Sv) between the basins - idealised model experiments

Domain	wind regime	westwards transport	eastwards transport	Shallow channel			Deep channel		
				westwards	eastwards	net	westwards	eastwards	net
Case 4.2 (only shallow channel)	Winter	-16.98	16.99						
	Summer	-24.72	24.75						
Case 4.3 (shallow and deep channel)	Winter	-73.56	73.57	-73.56	10.00	-63.56	0.00	63.57	63.57
	Summer	-26.97	26.86	-21.96	26.86	4.90	-9.55	4.54	-5.01
	Winter x 2	-183.06	182.94	-183.06	17.65	-165.40	0.00	165.29	165.29
	Summer x 2	-41.01	41.04	-37.49	40.45	2.96	-3.52	0.60	-2.92
Case 4.4 (only narrow channel)	Winter	-2.22	2.22						
Case 4.5 (narrow and deep channels)	Winter	-34.78	34.77	-34.78	0.00	-34.78	0.00	34.77	34.77
	Summer	-4.56	4.56	-4.10	3.67	-0.43	-0.46	0.89	0.43
Case 4.6 (narrow channel shifted south)	Winter	-14.63	14.63	-14.63	4.40	-10.23	0.00	10.23	10.23
Case 4.7 (narrow channel shifted north)	Winter	-10.51	10.52	-10.51	5.64	-4.87	0.00	4.87	4.87

Note: the negative values show westwards transport and vice versa.

4.4.2. Volume transport of Case 4.3

In Case 4.3, water exchange between the basins occurs in both the shallow and deep channels. Although a net volume transport is still not permitted between the basins, but with the presence of the deep channel a net transport in the shallow channel is likely to occur. In comparison with the one channel domain, opening the deep channel increases the water exchange between the basins (Table 4.1).

In the case of forcing by the winter wind stress, in the shallow channel there are both westward and eastward transports, but the net integrated transport over the channel is westwards, with the total amount of about 63.57Sv, equivalent to the eastward transport through the deep channel. In the case of forcing by the summer wind stress, due to the change in circulation as mentioned in the section 4.3.2.3 there are significant changes of the volume transport. In the shallow channel the westward transport is about 21.96 Sv, and the eastward transport of about 26.86 Sv giving an eastward transport for the net volume transport with the magnitude of about 4.90 Sv. In the deep channel, the eastwards transport (~ 4.54 Sv) occurs in the surface layer (mixed layer), but there is a westwards transport in all the deep layers with a magnitude of about 9.55 Sv. This led to an overall westward depth-integrated transport of 5.01 Sv (Table 4.1, Figure 4.33). These results show that the wind regimes play a very important role, and dictating the volume transport between the basins in both magnitude and direction.

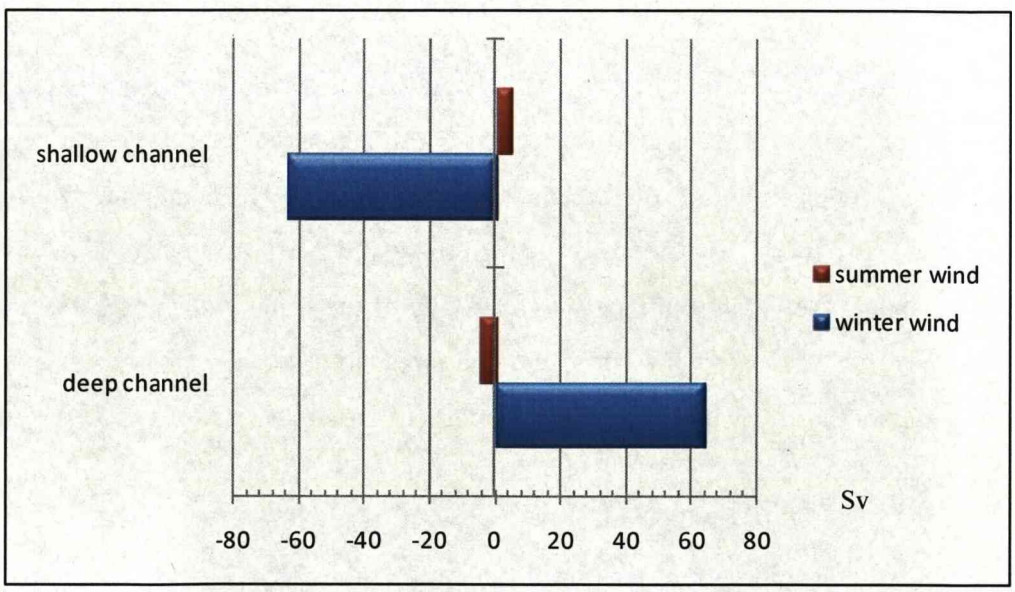

Figure 4.33: The volume transport in the channels under different wind regimes.

In order to examine the sensitivity of the volume transport to the change of the wind forcing, the strength of the wind speed over the whole domain has been doubled. When doubling the wind speed, the increase of wind stress is different between the winter and summer wind patterns. In the case of the winter wind, due to its pattern the wind stress over the shallow channel has more increase than over the deep channel. In the case of the summer wind the increase of wind stress over the deep channel is higher than that in the winter wind. The result shows that the water exchange between the basins has increased in response to the change of the wind speed, but the magnitude of the volume transport is not exactly proportional to the increase of the wind speed where doubling the wind speed results in 2.5 times an increase of the total volume transport in the winter wind, and an 1.5 times increase in the summer wind (Table 4.1). The difference can be explained as the increase of the wind stress over the channels is different between the winter and summer wind patterns.

4.4.3. Volume transport responds to changes of the shallow channel's width and latitude

4.4.3.1. Change of the channel's width

The passages in the Southeast Asia region are rather narrow. Therefore, in order to investigate the water exchange between the basins, the shallow channel of the idealised model has been narrowed by a factor of 4. This is expected to give a closer result to reality.

The result shows that in Case 4.4, when driven by the winter stress, and narrowing the channel to a quarter of its original width leads approximately to a decrease of the transport to an eighth of the exchange between the basins (Table 4.1). In Case 4.5, when the model is forced by the winter wind stress, the narrowing of the shallow channel results approximately to a halving of the water exchange between the basins, and when driven by the summer wind stress to a decrease to a sixth. In the shallow channel there is only westward transport (Figure 4.34).

4.4.3.2. Change of the channel's latitude

The winter wind stress was used to examine the effect of moving the latitude of the shallow channel. The model results are as follow:

- When shifting the shallow channel to the south (Case 4.6) and the north (Case 4.7) of the equator, the strength of wind stress over the channel is decreased. This decreases the current velocity in the channels and as a result reducing the water exchange between the basins (Table 4.1) by a factor of about 3. Shifting the shallow channel to the north (Case 4.7) produces less volume transport (70% reduction) in comparison with shifting it to the south (Case 4.6) (58% reduction).

- In the shallow channel, there are both westward and eastward volume transports, but the net integrated transport is westward here (Figure 4.34). In the deep channel, in both cases, the volume transport has an opposing eastward direction.

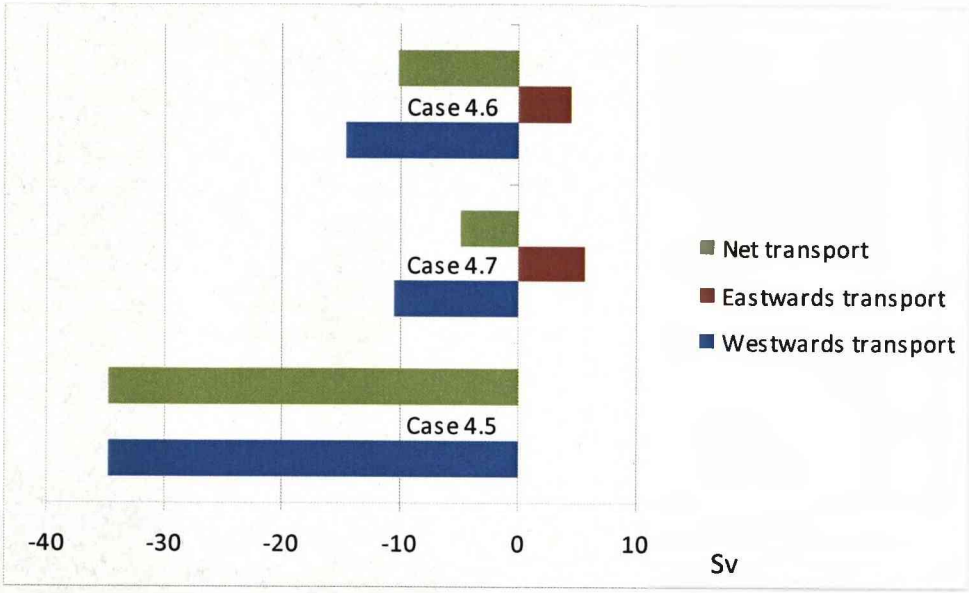

Figure 4.34: The volume transport exchange between the basins in the shallow channel when the channel's width and latitude changed.

4.5. Testing Godfrey's Island Rule (GIR) for Cases 4.3, 4.5 and 4.7

4.5.1. Godfrey's Island Rule

Godfrey's original Island Rule (Godfrey, 1989) can be summarised as following:

Imagine a closed rectangular ocean basin $0<x<L$, $0<y<B$. In the basin there is a rectangular island, $W<x<E$, $S<y<N$ (Figure 4.35). According to the Island Rule, the total transport around the island is given by

$$T_0 = \frac{\oint \tau \bullet \mathbf{ds}}{\rho_0 (f_N - f_S)}. \qquad (4.2)$$

Where: T_o is the total depth-integrated mass transport around island, τ is the time averaged wind stress, **ds** is the locus of the path of integration, ρ_o is the mean water density (10^3 kg m^{-3}), f_N *and* f_S are the values of the Coriolis parameter of the latitudes of the north and south extremities of the island.

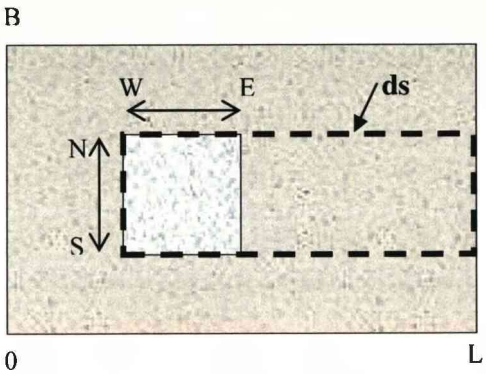

Figure 4.35: The plan view of the domain for calculation of the volume transport around an island by Godfrey's island rule

With purely zonal wind stresses:

$$T_0 = \frac{\tau_N (W - L) + \tau_S (L - W)}{\rho_0 (f_N - f_S)},$$

If $X = L - W$

$$T_0 = -\frac{(\tau_N - \tau_S) X}{\rho_0 (f_N - f_S)},$$

If we assume a β-plane

$$f = f_0 + \beta y,$$

So that

$$f_N = f_0 + \beta N$$
$$f_S = f_0 + \beta S,$$

Then

$$T_0 = -\frac{(\tau_N - \tau_S) X}{\rho_0 \beta (N - S)},$$

If $Y = N - S$

$$T_0 = -\frac{(\tau_N - \tau_S) X}{\rho_0 \beta Y}. \qquad (4.3)$$

4.5.2. Calculation of transport around an island

When using the formula 4.3 for calculating the mass transport around the island for idealised geometries (Cases 4.3, 4.5, and 4.7), we have ρ_o, β are constants, and X in all cases is unchanged. Therefore T_o only depends on the difference of the wind stress between the island extremities (τ_N-τ_S) and Y. According to the change of the geometries, the integral path varied between Cases 4.3, 4.5 and 4.7 as shown in Figures 4.36, 4.37, and 4.38. Note that in all cases the width of the deep channel is unchanged and there is only small westward wind stress over it.

As shown in the formula 4.1, the "correct" GIR uses the wind stress at the northern and southern latitude of the island extremities. However, in both winter and summer the wind stress over the deep channel varies slightly, while over the shallow channel there is a big difference, especially in the summer there is both westward and eastward wind stress in the shallow channel. Therefore we suspect that the "correct" wind stress may not give total mass transport in the channel. Thus besides calculating T_o using the "correct" GIR we have carried out further calculation with the average of wind stress over the channels (i.e. τ_N is the average wind stress over the shallow channel and τ_S is the average of wind stress over the deep channel).

The results of calculating the total depth-integrated mass transport by using GIR and the volume transport calculated by the numerical model (MICOM model) are shown in Table 4.2. It is very interesting that when using the wind stress exactly at the north and south latitudes of the island extremities (Table 4.3), the magnitude of volume transport is quite different compared to the transport calculated by the MICOM model. Especially in Case 4.3, T_0 increases while MICOM output shows a decrease. When using the average values of the wind stress over the shallow channel and deep channel (Table 4.4), the results show a rather good agreement between the two methods in terms of the magnitude of the transport and the sign.

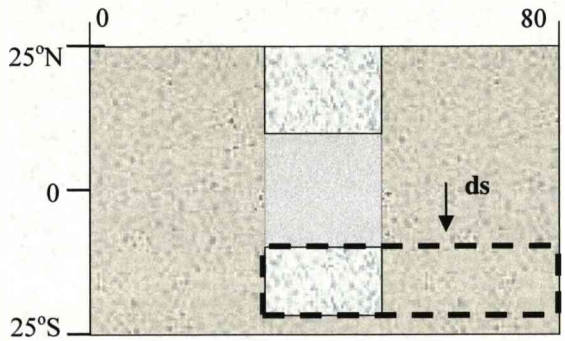

Figure 4.36: The integration path for calculation of the volume transport using GIR – Case 4.3

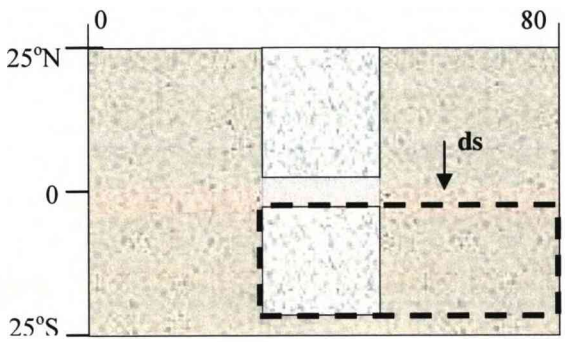

Figure 4.37: The integration path for calculation of the volume transport using GIR - Case 4.5

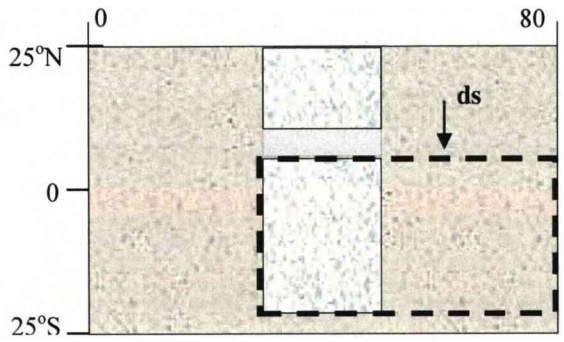

Figure 4.38: The integration path for calculation of the volume transport using GIR – Case 4.7

Table 4.2: Volume transport around island calculated by using GIR and the volume transport in the shallow channel calculated by MICOM model.

Unit: Sv

	Case 4.3		Case 4.5		Case 4.7
	Winter wind stress	Summer wind stress	Winter wind stress	Summer wind stress	Winter wind stress
T_0-GIR (c)	-37.63	-58.29	-39.70	0.00	-15.43
T_0-GIR (a)	-58.96	1.53	-41.70	0.93	-10.82
T_0- MICOM	-63.56	4.90	-34.78	-0.43	-4.87

Note:

T_0-GIR (c): volume transport around island calculated by GIR using the "correct" wind stress; T_0-GIR (a): volume transport around island calculated by GIR using the average wind stress; T_0-MICOM: volume transport in the shallow channel (calculated by MICOM model); negative values show transport from the eastern basin to the western basin and vice versa. (The GIR transport is conventionally positive anticlockwise around the island, but the sign has been changed in the Table to conform to the convention used here, namely westward ITF is negative).

Table 4.3: The wind stress at the latitudes of the north and south extremities of the island.

Unit: N/m^2

	Case 4.3		Case 4.5		Case 4.7
	Winter wind stress	Summer wind stress	Winter wind stress	Summer wind stress	Winter wind stress
North extremity (τ_N)	-0.08987	-0.14885	-0.15418	-0.01479	-0.10055
South extremity (τ_S)	-0.00331	-0.01479	-0.00331	-0.01479	-0.00331
$\tau_N - \tau_S$	-0.08656	-0.13406	-0.15087	0.00	-0.09724

Table 4.4: Average of wind stress over the shallow and deep channels.

Unit: N/m^2

	Case 4.3		Case 4.5		Case 4.7
	Winter wind stress	Summer wind stress	Winter wind stress	Summer wind stress	Winter wind stress
Shallow channel (τ_N)	-0.13641	0.00000	-0.15927	0.00000	-0.06897
Deep channel (τ_S)	-0.00080	-0.00352	-0.00080	-0.00352	-0.00080
$\tau_N - \tau_S$	-0.13561	0.00352	-0.15847	0.00352	-0.06817

Case 4.3: There is a rather large difference between the transport calculated using the "correct" GIR and the volume transport of the numerical model (MICOM model). The calculation in winter gives a much lower mass transport compared to the numerical model, and the calculation in summer gives an increase of total mass transport which is opposite to the MICOM result. The increase of the transport in summer can be explained as following: in summer, there are both westward and eastward wind stress in the shallow channel, meaning that there are both westward and eastward transport, but the wind stress used for the calculation was only the wind stress at the north extremity which is westward direction (meaning that only westward transport is taken into account). This leads to a large difference of (τ_N-τ_S), and as consequence leading to increase of T_o.

When using average wind stress over the channel, both westward and eastward of transport in the shallow channel are taken into account. Due to the balance of the wind stress, the net transport produced by wind stress in the shallow channel is zero. However due to the existence of the westward wind stress in the deep channel which producing a westward transport, an eastward transport occurs in the shallow channel to compensate the westward transport in the deep channel.

Case 4.5: There is a good agreement of volume transport calculated by GIR (both "correct" and average wind stress) and numerical model. The reason why the "correct" wind stress gives good agreement with average wind stress and numerical model can be explained as following: due to the width of the shallow channel is reduced to a quarter of its original width (Case 4.3), the magnitude of the wind stress at the north extremity is close to the average of wind stress over the channel. Therefore the transports produced by both kind of wind stress are similar.

Case 4.7: Result of calculating the mass transport around the island using the "correct" wind stress and the average wind stress is higher than that of the MICOM model. But the outcome of the average wind stress is smaller, as a result of smaller $(\tau_N-\tau_S)$, and so closer to the numerical model.

In all these Cases the deep channel is not very far south relative to the wind, so that the water in the channel is not properly driven by westerly winds. With the fact that the wind stress in the deep channel in both cases (winter and summer) does not change very much, the wind stress's patterns in the shallow channel dictate the volume transport between the basins. An important difference between the theory and the model is that the GIR theory is inviscid, i.e. there is no friction, while the model certainly has some friction. This therefore can contribute to the difference between the GIR and numerical model results.

4.6. POLCOMS model

Several model experiments with different idealised geometries and wind forcing were carried out using the POLCOMS model. In terms of circulation the model results (Figures 4.39 and 4.40) show that POLCOMS can reproduce rather well some physical phenomena such as basin scale gyres, boundary currents, equatorial current system, especially the equatorial counter current which has not been clearly seen in the experiments with MICOM model. Unfortunately, there was a problem with the conservation of the water mass which could not be resolved. The calculation of the volume transport exchange between the basins at the meridional cross-section in the middle of the domain shows that during 20 years of model run, there was always a net of volume transport from the eastern basin to the western basin, which is not consistent with volume conservation. This maybe a problem with the model itself but

it could also coming from incorrect setup of the model parameters. However, this problem in combination with the difficulty in computer resources led to the decision not to use the POLCOMS model for the experiments with realistic topography and forcing.

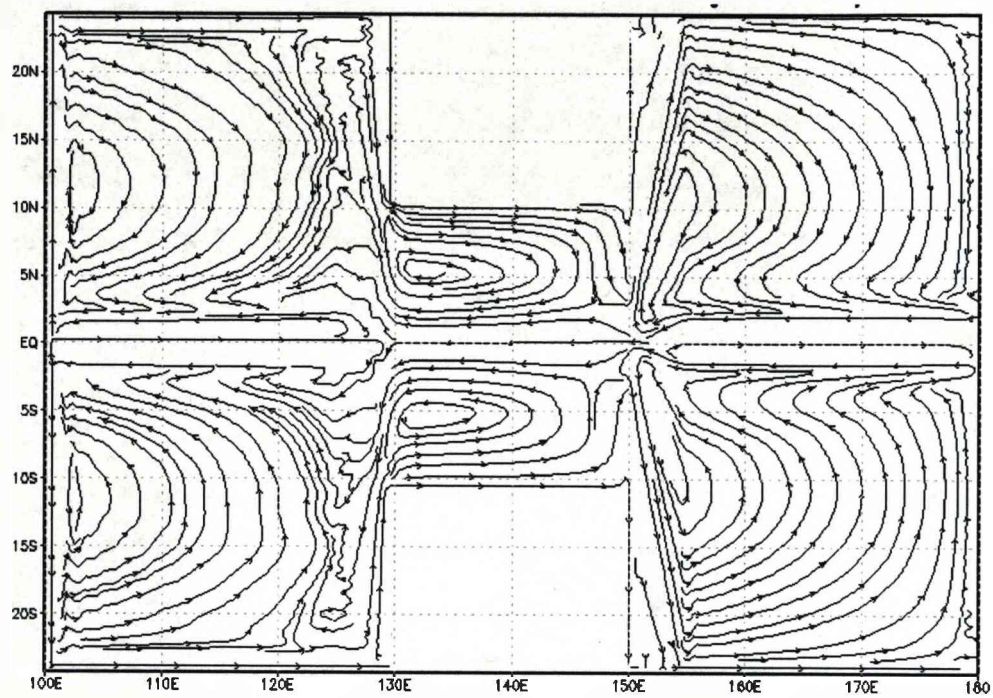

Figure 4.39. The mean velocity of circulation (streamline of velocity) of Case 4.2, POLCOMS model, forced by the winter wind stress.

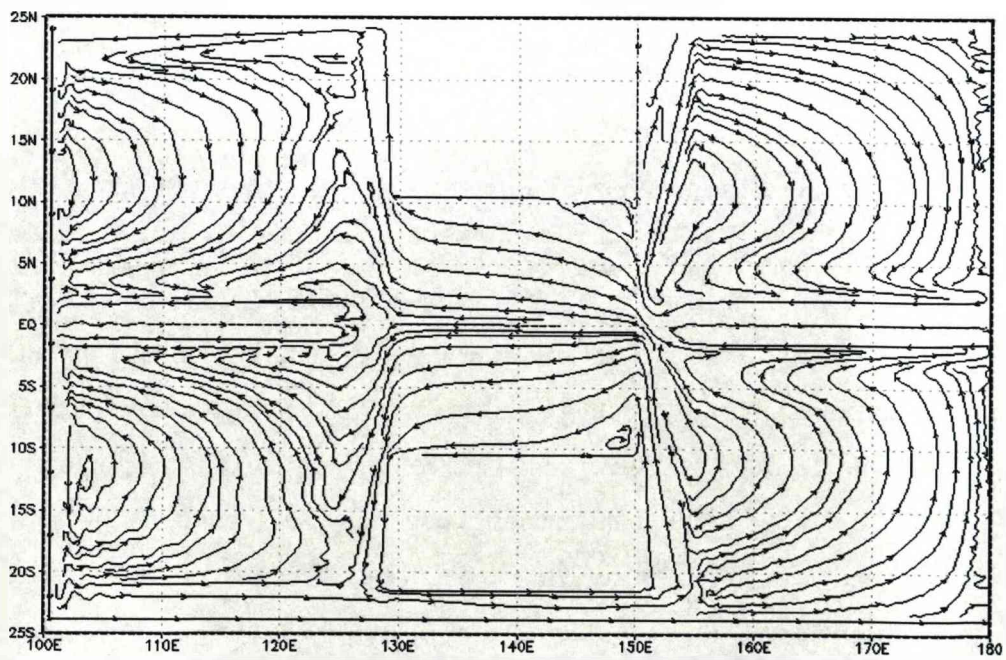

Figure 4.40. The mean velocity of circulation (streamline of velocity) of Case 4.3, POLCOMS model, forced by the winter wind stress.

4.7. Summary

In all idealised experiments, the models showed good stability after a spin-up time of about 3 years. The physical oceanographic phenomena were well reproduced; the basin scale gyres, the boundary currents, and the equatorial currents were all clearly seen. The results from the MICOM model closely match with the Sverdrup balance in terms of the location of gyres and the interior volume transport. It can also be seen from the Sverdrup balance calculation and the numerical model experiments that in each hemisphere the major dividing lines between the gyres corresponded to the latitude of the zero wind stress curl, and the gyres do not generally cross the line of zero wind stress curl.

In Case 4.2, when a barrier is submerged in the middle of the domain, it almost blocks the movement of water between the basins, and completely changes the picture of the circulation and volume transport. In this case, the gyres almost develop within the basins only, and with the shorter west-east length scale the strength of the western boundary currents and volume transport in the basins are decreased. The changes in the applied driving force (the winter wind stress or the summer wind stress) can make significant changes in the circulation and volume transport such as a change in the number of gyres, changes in the strength of the circulation and volume transport.

When a deep channel is opened (Case 4.3), the water in the western basin is able to flow back to the eastern basin through the deep channel. This has a very strong and clear influence to the circulation and volume transport between the basins, especially in the southern hemisphere. In the case of forcing by the winter wind stress, the total amount of the westward transport through the shallow channel is about 63.5 Sv but the contribution of the southern half is about 54.3 Sv, nearly 6 times higher than the contribution of the northern half (9.2 Sv). When the driving force is the summer wind stress, the meridional transport along the western boundary of the western basin is strongly decreased (from ~70 Sv to ~20 Sv). There is a little influence of opening the deep channel to the northern hemisphere. The circulation and stream function of volume transport in the northern hemisphere are rather similar to Case 4.2 in terms of the pattern and strength.

The model result shows that the volume transport between the basins is sensitive to changes in strength of the wind stress, but the magnitude of the volume transport is not exactly proportional with strength of the applied wind where doubling the wind speed results in 2.5 times an increase of the total volume transport for the winter wind, and a 1.5 times increase in the case of the summer wind.

When the shallow channel was narrowed by a factor of 4 (Case 4.4), it reduces by approximately 8 times the water exchanged between basins (driven by the winter stress). In Case 4.5, when the model is forced by the winter wind stress, narrowing of the shallow channel results approximately in a halving of the water exchanged between the basins; it is a sixth when driven by the summer wind stress. In the shallow channel there is only westward transport.

The change of the narrow channel's latitude has a strong influence on the total water exchange between the basins. When shifting the shallow channel to the south of the Equator (Case 4.6) there is 58% reduction of the volume transport. There is a 70% reduction when shifting the channel to the north (Case 4.7).

It is very interesting that the transport calculation using the "correct" GIR did not give good result compared to the MICOM model but that by changing the wind stress to the channel average the calculated transport is much more like the numerical model.

In summary the volume transport reproduced by MICOM model closely matches with the Sverdrup balance. The model results have shown that the volume transport between the basins is sensitive to the applied wind regime, the strength of the wind stress, and the topography. Although successfully reproducing the classical wind-driven flow, especially the equatorial counter current, due to problems with water mass conservation and computer resource, the POLCOMS model was not selected for the realistic topography and forcing experiments. The MICOM model was successfully setup and reproduced the circulation, volume transport and its responses to changes of topography and forcing. Therefore the MICOM model is used in the experiments with the realistic topography and forcing as presented in the next chapter.

Chapter 5

MODELLING CIRCULATION AND VOLUME TRANSPORT IN THE SOUTHEAST ASIA REGION

5.1. Introduction

In this Chapter, a series of the model experiments using realistic topography and forcing to simulate the circulation and volume transport of the throughflow between the Pacific and Indian Oceans through the Southeast Asia region will be presented. Throughout the model experiments, the variability of the Indonesian throughflow (ITF), the main driving forces of the ITF and the main characteristics of the ITF will be discussed and compared with the observations and other studies where possible. The focus of the analysis will be on the volume transport of the throughflow and its variability. The list of model run is shown in Table 5.1.

5.2. The model experiments with wind stress alone

The ITF has been a subject of investigation in numerous analytical and numerical studies. In the study of Hirst and Godfrey (1994), a depth-integrated numerical ocean model was used to test the hypothesis of the Godfrey's island rule to show that the wind stress is the governing force of the throughflow. The relationship between the wind stress and the ITF on inter-annual time-scales was further investigated in the numerical model studies of Wajsowicz (1995; 1996). The studies of Wajsowicz (1995; 1996) showed that the variability of the ITF largely correlated with wind variations. In the previous Chapter, the results of the idealised model experiments also showed that the wind stress over the domain can produce a rather high volume transport between the basins. Therefore the first model experiments with the realistic topography and forcing were carried out with wind stress as the only driving force.

Table 5.1: List of the model runs.

	Domain	Forcing	
		Wind stress	Thermal forcing (temperature & salinity)
Case 5.1	Domain 1	ECMWF	No thermal forcing.
Case 5.2	Domain 2	ECMWF	No thermal forcing.
Case 5.3	Domain 2	NCEP	No thermal forcing.
Case 5.4	Domain 2	NCEP	Annual mean temperature and salinity in the mixed layer.
Case 5.5	Domain 2	NCEP	Annual mean temperature and salinity in the mixed layer, and increase the number of vertical layers from 4 to 6.
Case 5.6	Domain 3	NCEP	5 flat layers in vertical, no thermal forcing.
Case 5.7	Domain 2	NCEP	Monthly mean temperature and salinity with 1 year of relaxation for all layers.
Case 5.8	Domain 2	No wind	No relaxation at all.
Case 5.9	Domain 2	No wind	No relaxation of mixed layer, deep layers relaxed.
Case 5.10	Domain 2	No wind	1 year relaxation for temperature and salinity.

Note:

Domain 1: partital Indian Ocean and partial Pacific Ocean.
Domain 2: whole Indian Ocean and partial Pacific Ocean.
Domain 3: whole Indian Ocean and whole Pacific Ocean.

5.2.1. The model experiment with the partial Indian Ocean (case 5.1)

5.2.1.1 Model configuration

The geographical domain of the model was chosen to cover a region from 40°N to 60°S and 80°E to 185°E, hereafter referred to as the Domain 1 (Figure 5.1). All the boundaries are closed and located rather far away from the region of interest (the Southeast Asian region) to capture the physical features of the Pacific and the Indian Oceans, and to reduce the effect of boundary conditions to the study region. The horizontal resolution of the model is 0.5° in both zonal and meridional directions. In the vertical there are 4 layers with the initial layer interface depths were set to 100, 500, 2000, 4000m, and the density "sigma-t" ($\sigma_t = \rho - 1000$ where ρ is the density of seawater) of each layer were 24.0, 27.0, 27.6, and 27.8 (kgm^{-3}) respectively. The model bathymetry is derived from the 5-min ETOPO5 topography dataset. In order to reflect the fact that the surface temperature decreases towards high latitudes and

the surface salinity has its peaks at mid-latitudes, an idealised surface temperature and salinity of the model experiment were simply set up as a combination of sine functions. The north-south distribution of the idealised salinity and temperature are shown in Figures 5.2 and 5.3, respectively.

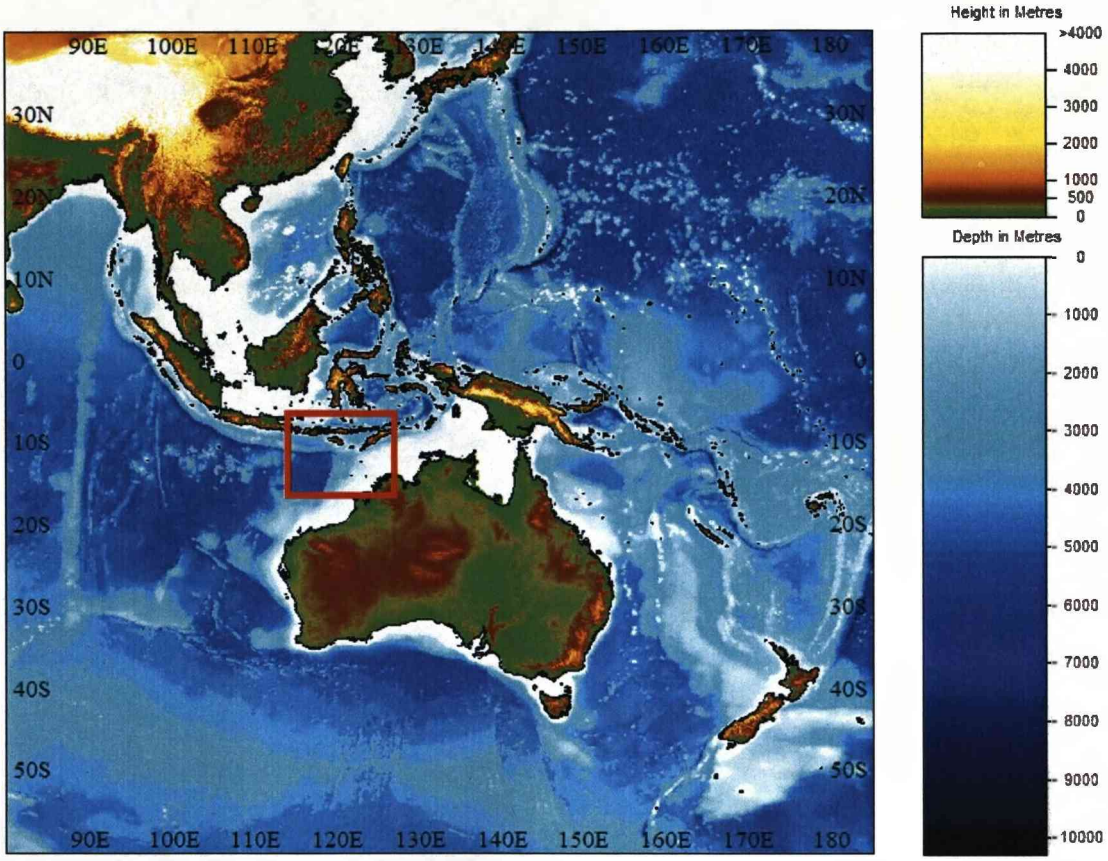

Figure 5.1: The model domain for the partial Indian and Pacific Oceans. The red rectangle shows the region covering the sections used to calculate the volume transport between the oceans. The picture is extracted from the GEBCO digital atlas, 2003.

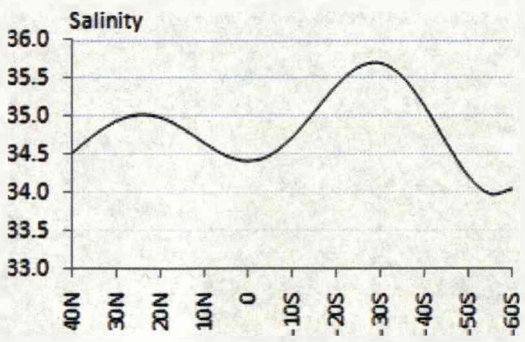

Figure 5.2: The north-south distribution of the idealised salinity.

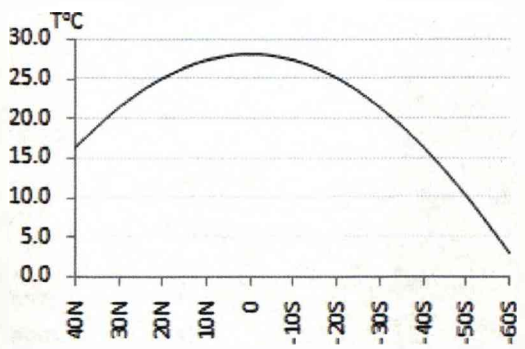

Figure 5.3: The north-south distribution of the idealised temperature.

At the lateral boundaries a non-slip boundary condition was applied. The bottom friction parameter was set equal to 0.003. In this first experiment in realistic geometry, the model was run for 50 years, starting from rest and continuously forced by the ECMWF's monthly-mean wind stress (ECMWF reanalysis ERA-15, 1979-1993) (Figures 5.4, 5.5). To estimate the volume transport between the Pacific and Indian oceans, the depth-integrated volume transports at some main passages in the Indonesian Seas were calculated, the cross-sections for calculating the transport are shown in the Figure 5.6.

5.2.1.2. Model result

The volume transport between the oceans

The horizontal volume transport through a section is defined conventionally as the integral of the flux normal to that cross-section. Table 5.2 shows the annual mean depth-integrated volume transport at the sections in the Indonesian Seas (Figure 5.6), and the total volume transport between the oceans. In comparison with the volume transport of the ITF from the observations and the volume transport estimated by numerical models (Table 2.2 – Chapter 2), the total volume transport produced by our model (5.08 Sv, transport from the Indian Ocean to the Pacific Ocean) is not consistent in either magnitude or direction. Among the sections, the volume transport at the Timor Sea section (-1.34 Sv) shows the right direction in comparison with the work of Gordon, 2001 (Figure 2.17 - Chapter 2) but smaller in term of magnitude (Table 2.3 - Chapter 2). The volume transport of the other sections is not consistent with reality.

Table 5.2: The annual-mean volume transport at the sections in the Indonesian Seas (Case 5.1).

No.	The section name	The depth-integrated volume transport (Sv)
1	Makassar Strait	2.01
2	Lombok Strait	2.99
3	Flores	0.69
4	Savu 1	1.09
5	Savu 2	1.65
6	Timor	-1.34
	Total transport	***5.08***

Note: The total transport is the summation of the volume transport from Section 2 to Section 6. Negative values show transport to the Indian Ocean, positive values show the transport to the Pacific Ocean. The annual-mean transport value was calculated for the last year of the run (the year 50).

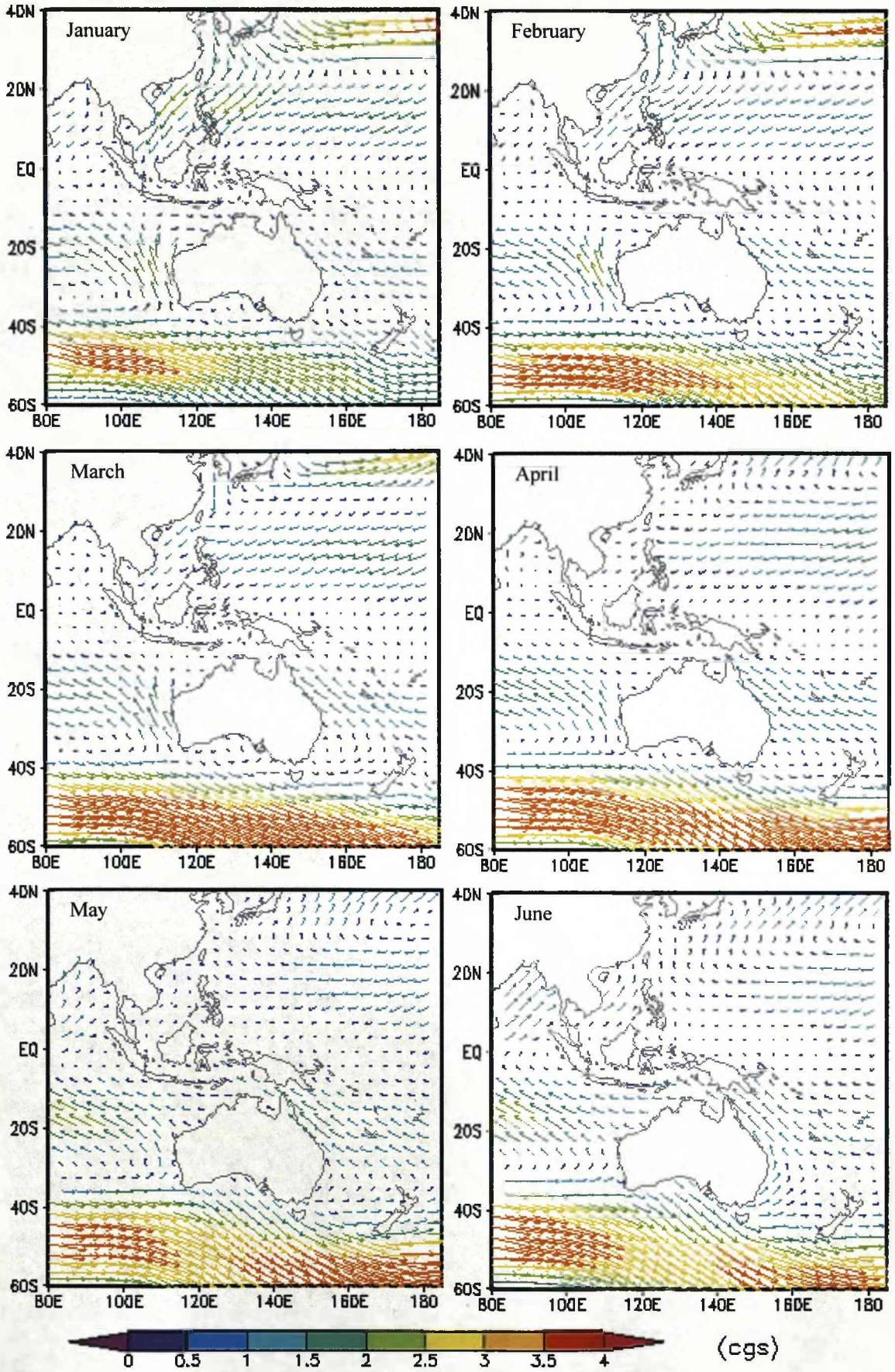

Figure 5.4: The monthly mean ECMWF's wind stress (January-June).

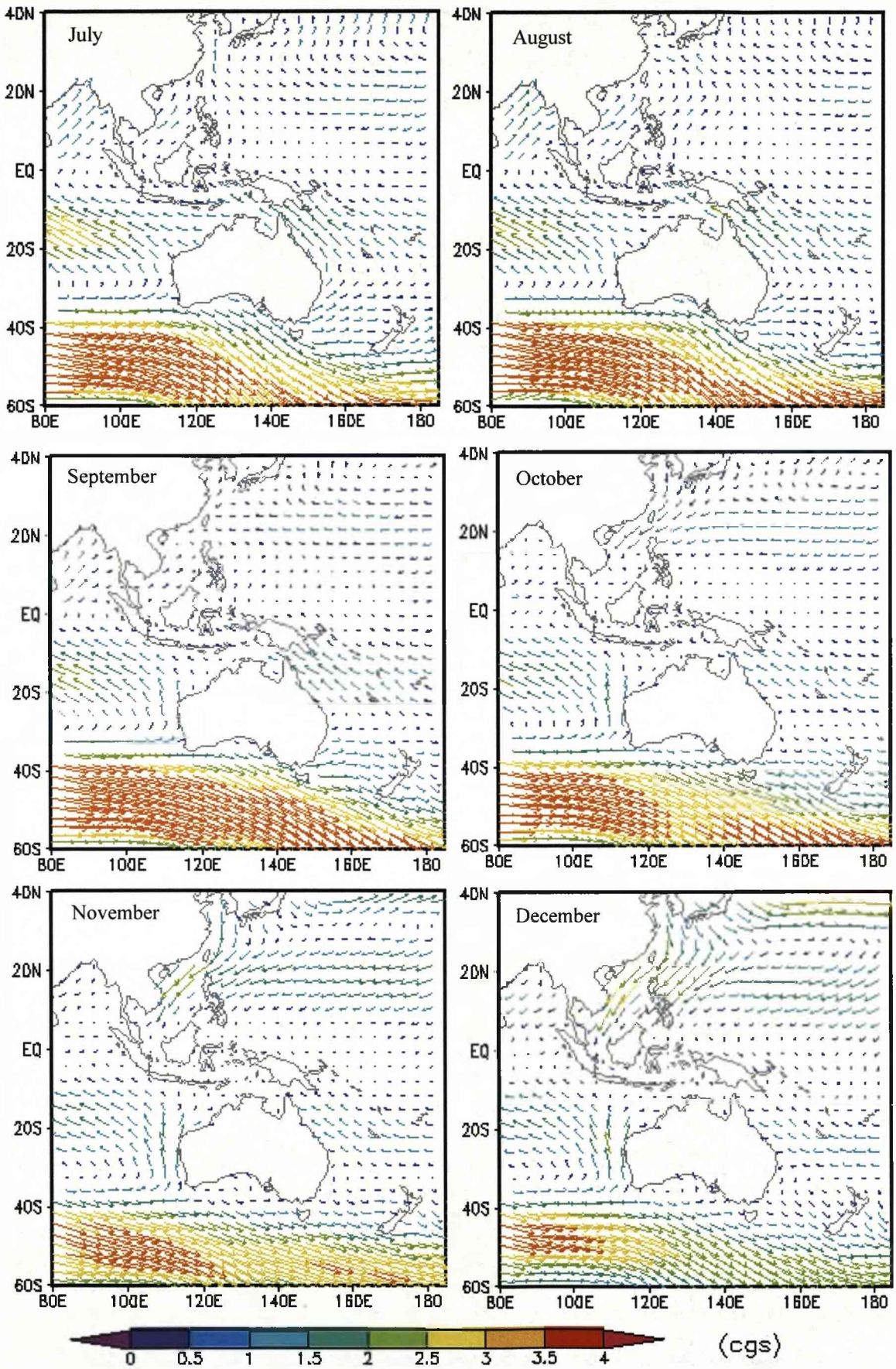

Figure 5.5: The monthly mean ECMWF's wind stress (July-December).

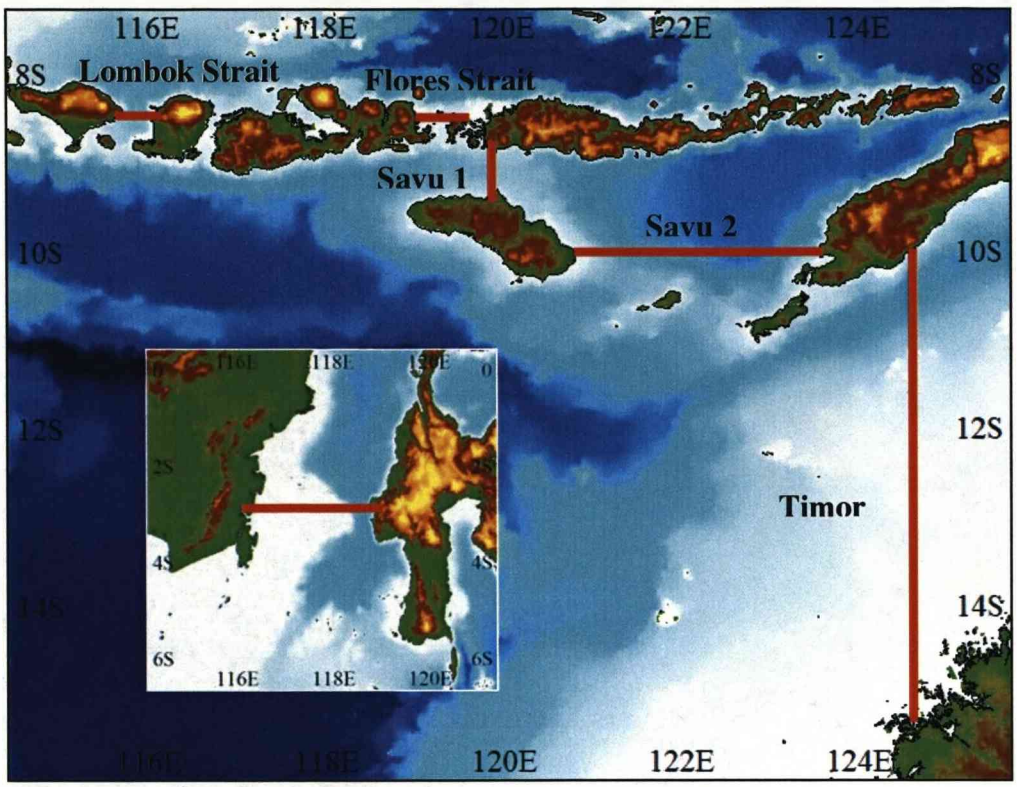

Figure 5.6: The sections for calculation of the volume transport between the oceans. The small figure shows the section at the Makassar Strait. The picture is extracted from the GEBCO digital atlas, 2003.

The mean circulation

Although the model does not reproduce the volume transport between the oceans correctly, in terms of circulation, it has reproduced rather well the ocean circulations such as the partial ACC, the north equatorial current in the Pacific ocean, the south equatorial current in the Indian Ocean, and particularly the well-known Kuroshio Current in the northern Pacific and the Leeuwin current along the northwest coast of Australia (Figure 5.7).

However, in the Indian Ocean, the model produced a strong eastward surface current along 10°S (Figure 5.7) which is in the opposite direction to reality. This strong current drives water from the Indian Ocean into the Indonesian Seas via the Lombok Strait and the Ombai Strait. After entering the Indonesian Seas the current from the Lombok Strait flows through the Makassar Strait to the Celebes Sea before entering the Pacific Ocean. The current from the Savu Sea (Ombai Strait) flows into the Banda Sea, and enter the Pacific Ocean through the Halmahera Sea. This pattern of circulation (Figure 5.8) is mostly in the opposing direction to reality and appears to be the reason for the incorrect direction of the ITF.

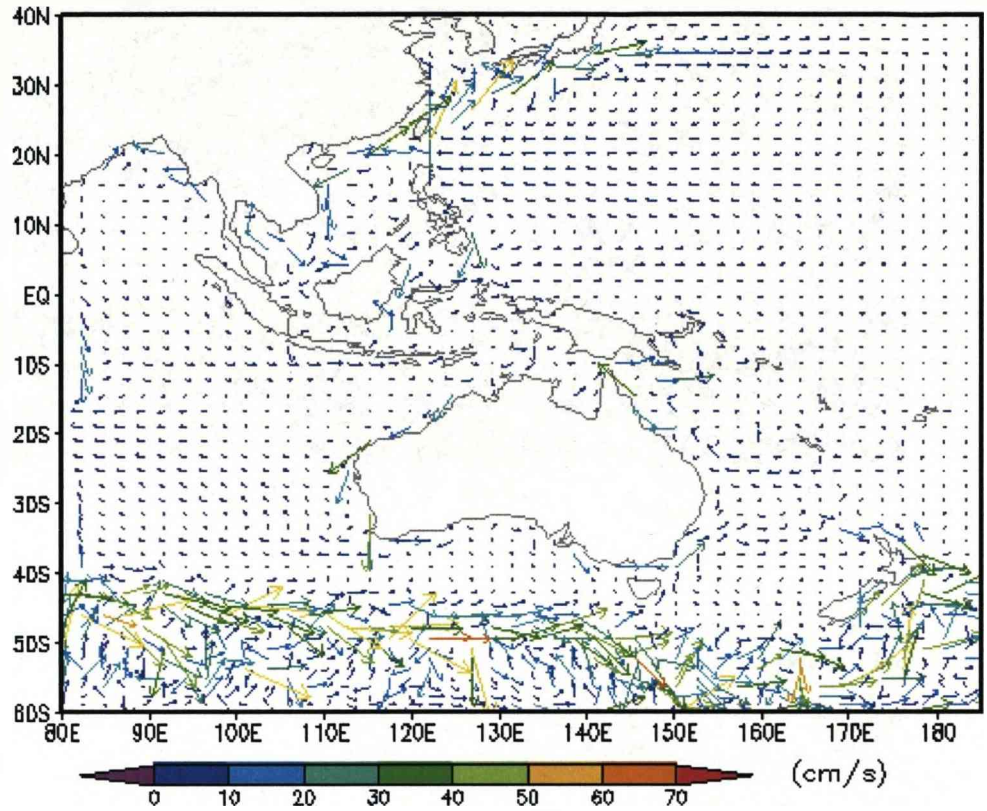

Figure 5.7: The annual-mean circulation of the last year of the run of the mixed layer. The arrows are plotted at every 5 grid-cells.

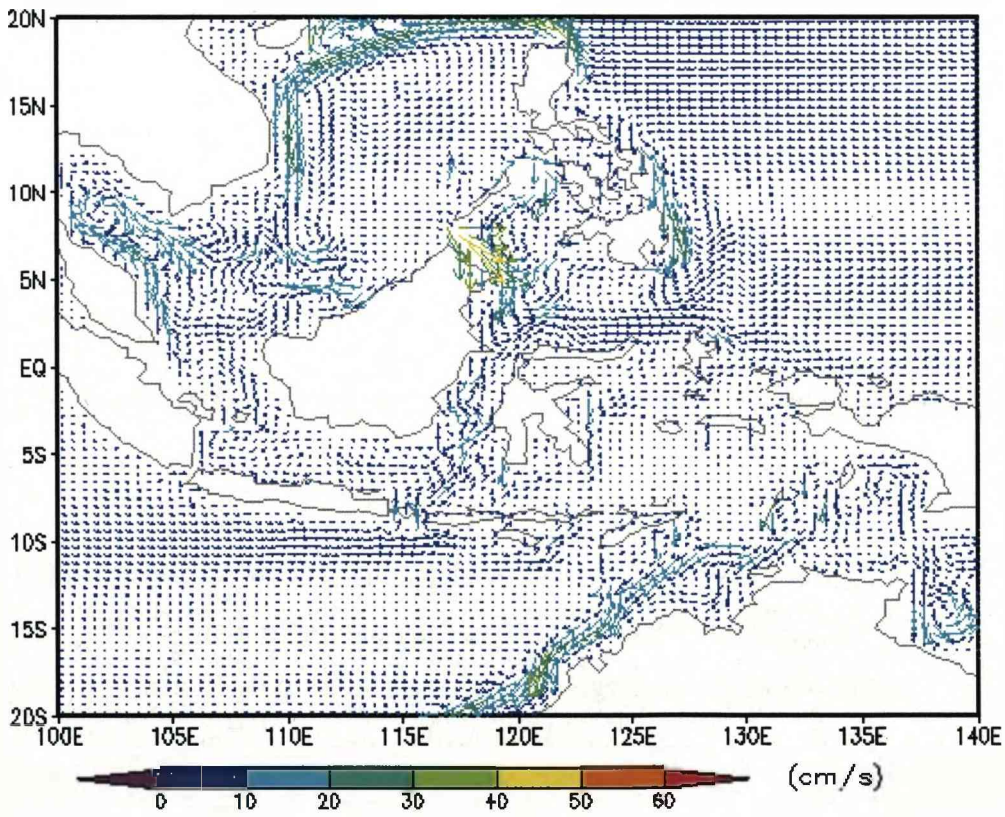

Figure 5.8: The annual-mean circulation of the last year of the run of the mixed layer in the Southeast Asia region.

5.2.2. Model experiments with the whole Indian Ocean domain (Case 5.2 - 5.5)

The result of the idealised model experiments in Chapter 2 (Case 4.2) showed that the east-west length scale of the domain influenced the circulation and the water exchange between the basins. Therefore in order to resolve the problem with the magnitude and direction of the volume transport of the ITF, the model experiments with the western boundary extended to the African coast, referred to as the Domain 2 (Figure 5.9), were carried out, referred to as Case 5.2, hoping that the monsoon circulation in the northern Indian Ocean would be properly represented. The monthly-mean ECMWF's wind stress is still the only driving force (Figures A.1, A.2, and A.3 - Appendix). The other outcome of the idealised model experiments was that the volume transport between the basins is rather sensitive to wind stress, therefore another experiment was also set up to run with the monthly-mean NCEP's wind stress (Figures A.4, A.5, and A.6 - Appendix), referred to as Case 5.3. There was a change in the model boundary where both the western and eastern boundaries were opened from 60°S to 35°S instead of being closed as in the previous experiment. This change allows water to flow into and out of the model domain to create a more realistic simulation of the ACC. The total kinetic energy (not show) of the previous model experiment (Case 5.1) showed that the model settled down rather quickly (approximately after 10 years) therefore the model experiments (Cases 5.2 & 5.3) were run for 20 years, starting from rest.

Table 5.3 shows the annual-mean depth-integrated volume transport at the sections and the total volume transport between the oceans in these two model experiments (Case 5.2 & Case 5.3). In terms of volume transport, the total volume transport produced by the NCEP's wind stress (Case 5.3) is smaller than that in the case of the ECMWF's wind stress (Case 5.2). In comparison with the previous experiment (Case 5.1), the extension of the western boundary has decreased the total volume transport from the Indian Ocean to the Pacific Ocean but it was not significant enough to resolve the problem of incorrect ITF where the ITF transport is still from the Indian Ocean to the Pacific Ocean.

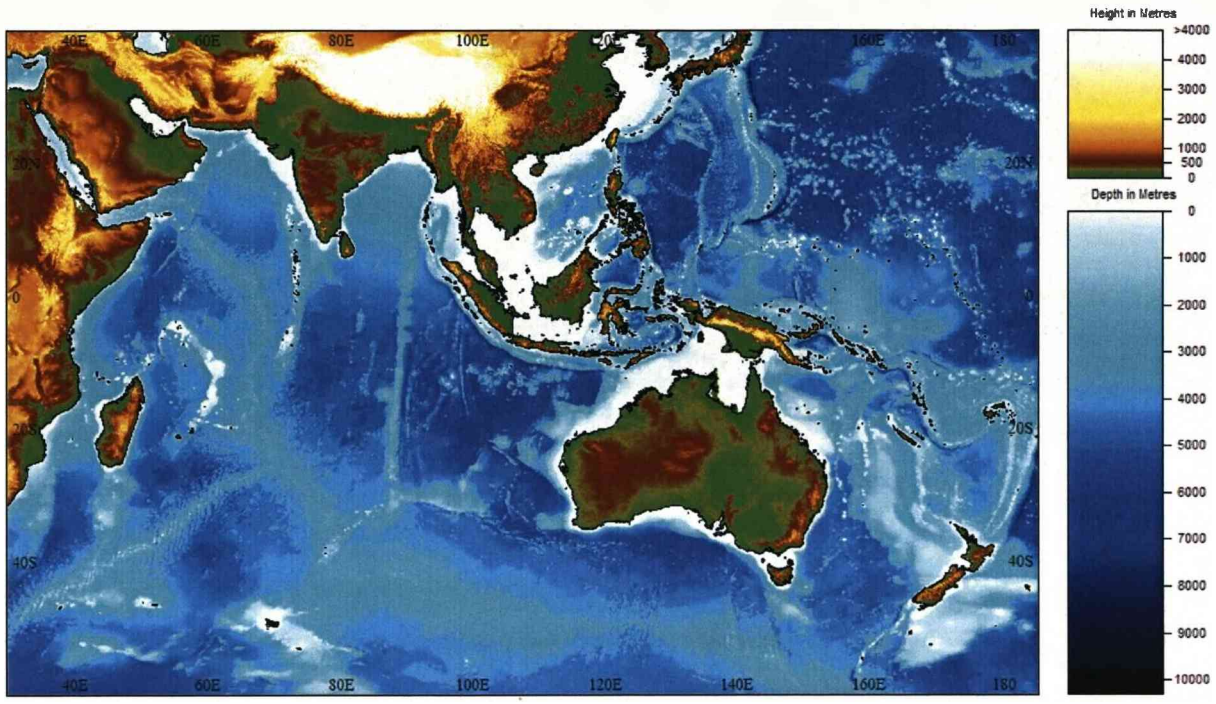

Figure 5.9: The model domain with the extended western boundary. The picture has been extracted from the GEBCO digital atlas, 2003.

Figures 5.10, 5.11 show the annual-mean circulation of the mixed layer over the whole domain and the annual-mean circulation of the Southeast Asia region (Case 5.2) respectively. The circulation reproduced in Case 5.3 (not shown) is similar to the circulation in Case 5.2. In the Pacific Ocean the circulation in Case 5.2 and Case 5.3 is similar to the circulation in Case 5.1. In the Indian Ocean, with the boundary extended to the eastern coast of Africa, the model has successfully reproduced the Somali, Mozambique, and Agulhas Currents. However the strong eastwards current along 10°S is still present and acts as one of the reason for the wrong ITF direction by driving the water from the Indian Ocean into the Indonesian Seas as mentioned in the previous section. The model has failed to reproduce the circulation in the Indonesian Seas where it is in the opposing direction to reality.

The failure in reproducing correctly the circulation in the Indonesian Seas can be explained when we look at the sea surface height between the oceans. In his works, Wrytki (1961, 1987) urged that the sea level in the western Pacific Ocean is higher than that in the eastern Indian Ocean. Consequently, it creates a pressure gradient between the oceans that drive water from the western Pacific Ocean to eastern Indian Ocean through the Indonesian Seas to form the ITF. The annual mean sea surface

height produced by the model (Figure 5.12) shows an opposing situation where the sea surface height in the eastern Indian Ocean (between Java and Australia area, where the water from the Indonesian Seas exit to the Indian Ocean in reality) is higher than that in the western Pacific Ocean (the area from the Equator to 10°N, where the water from the western Pacific ocean enter the Indonesian Seas to form the ITF in reality). Therefore water has been driven from the eastern Indian Ocean and Indonesian Seas to the western Pacific Ocean which is inconsistent with Wrytki's works and reality.

Table 5.3: The annual-mean of volume transport at the main sections in the Indonesian Seas (Cases 5.2 & 5.3).

No.	The section name	The depth-integrated volume transport (Sv)	
		Case 5.2	**Case 5.3**
1	Makassar Strait	4.05	3.59
2	Lombok Strait	2.21	2.14
3	Flores	1.64	1.42
4	Savu 1	-0.74	-0.50
5	Savu 2	0.95	0.90
6	Timor	-1.21	-2.15
	Total transport	***2.85***	***1.81***

Note: The mean value is the summation of the volume transport from Section 2 to 6. Negative values show transport to the Indian Ocean, positive values show the transport to the Pacific Ocean. The annual mean of volume transport was calculated for the last year of the runs (the year 20).

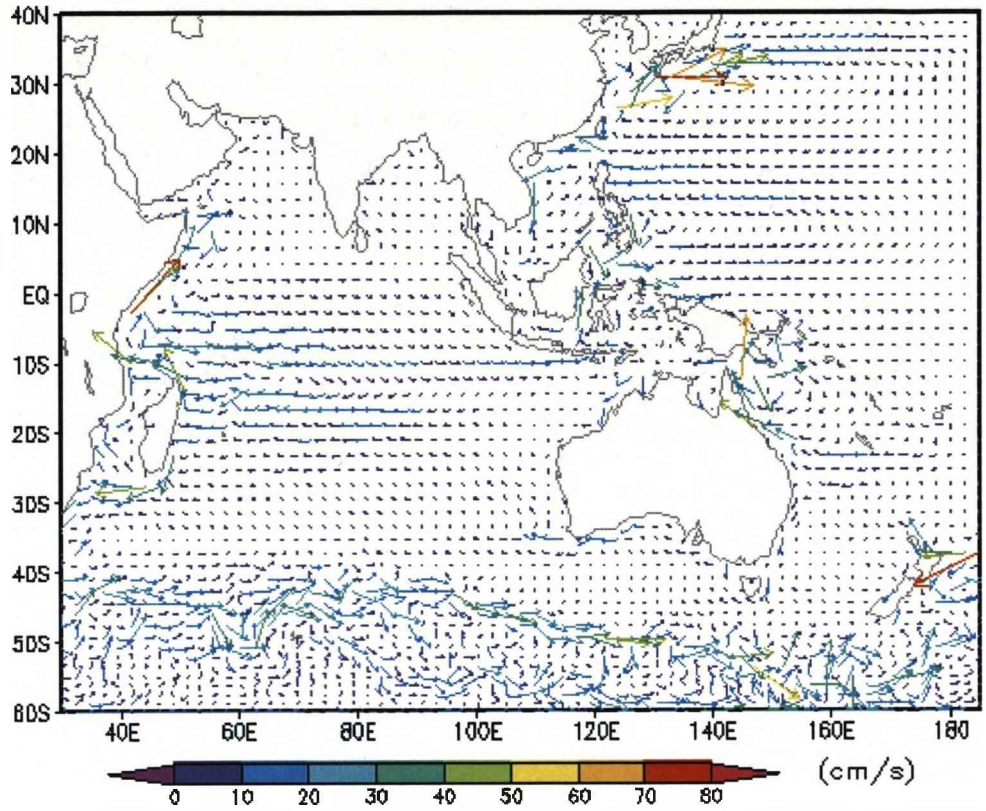

Figure 5.10. The annual-mean circulation of the mixed layer (Case 5.2). The arrows are plotted at every 5 grid-cells.

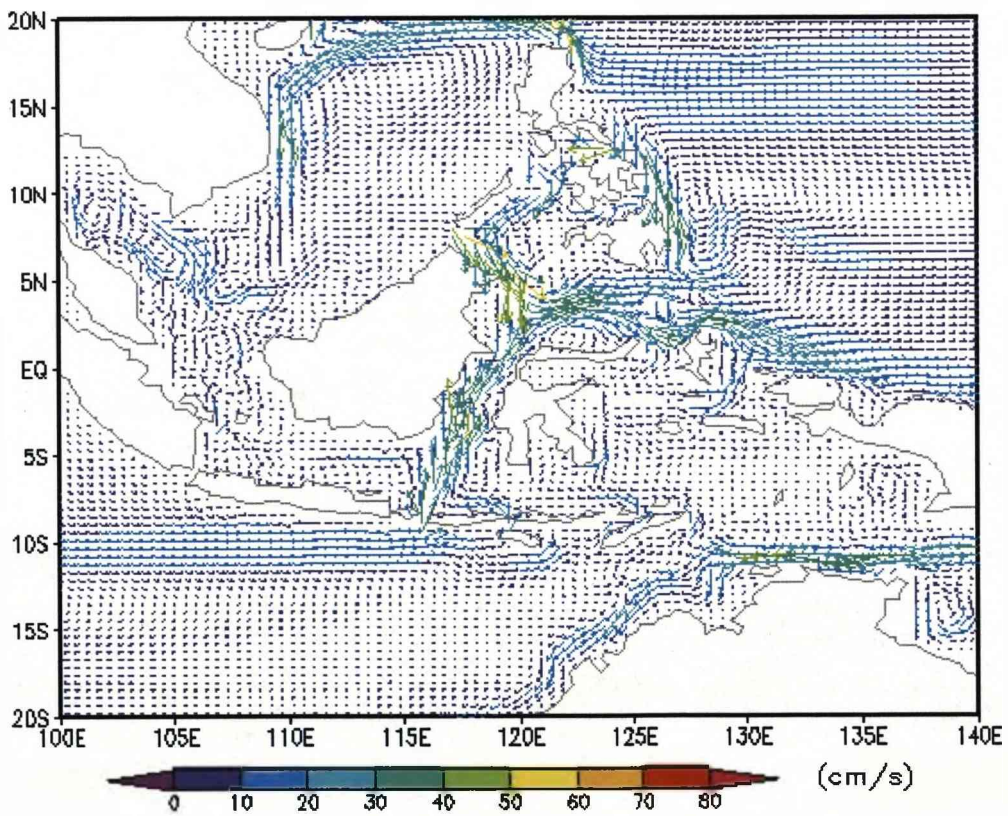

Figure 5.11: The annual-mean circulation of the mixed layer in the Southeast Asia region (Case 5.2).

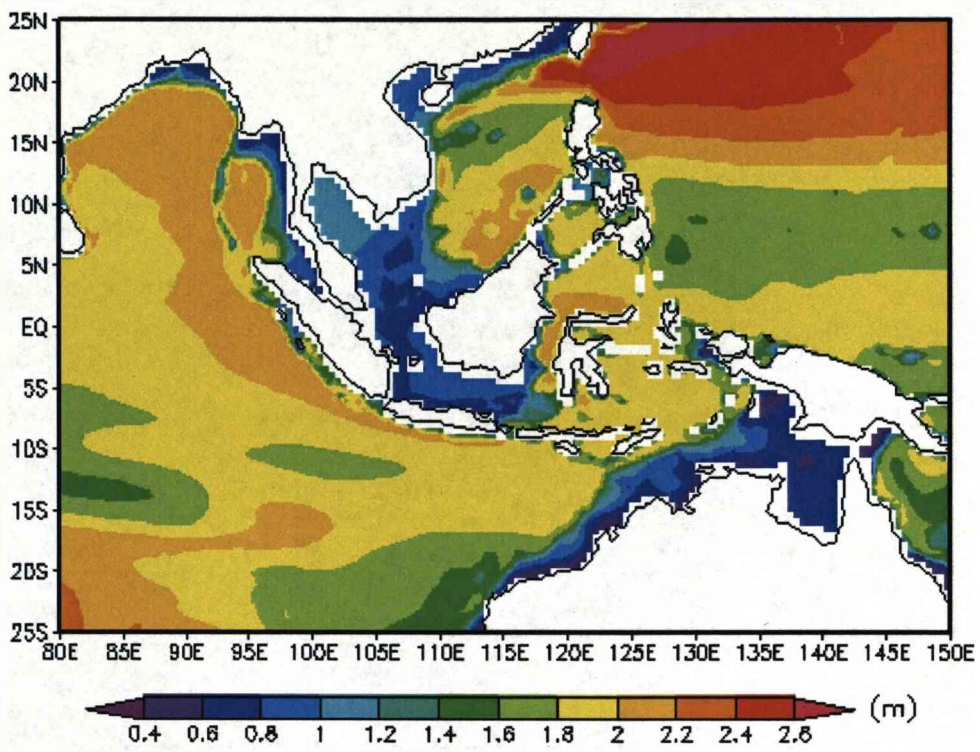

Figure 5.12: The annual-mean sea surface height of the Southeast Asia and vicinity (Case 5.3).

Two more extra model experiments were carried out with the monthly mean NCEP's wind stress and some changes in topography and forcing. The first one, referred to as Case 5.4, was carried out with the opening of the Java Strait and introducing hydrographic fields for the mixed layer. The hydrographic fields used in the experiment were the annual-mean temperature and salinity derived from the Levitus Atlas, 1998 (NODC_WOA98); In the second experiment, referred to as Case 5.5, besides using the annual-mean temperature and salinity field as Case 5.4, the number of vertical layers was increased from 4 to 6 with the corresponding density "sigma-t" of each layer was 22.4, 24.4, 26.6, 27.5, 27.74, 27.8 (kgm^{-3}) respectively. The model experiments were also run for 20 years, starting from rest. However the results show that these changes did not make a significant change to the ITF. The total volume transport in Case 5.4 and Case 5.5 is about 1.84 Sv and 1.10 Sv respectively (Table 5.4), and still from the Indian Ocean to the Pacific Ocean which is in the opposite direction to reality.

Even though the model experiments could not reproduce the ITF correctly, it is of interest to examine the seasonal variability of the monthly-mean depth-integrated volume transport between the oceans in the different experiments (Cases 5.3, 5.4,

and 5.5). Figure 5.13 shows that ignoring the incorrect value of the magnitude and direction of the annual-mean value, the model can produce a strong seasonal variation of the volume transport between the oceans through the Indonesian Seas. Despite the total volume transport of the ITF being from the Indian Ocean to the Pacific Ocean, the model result shows that from May to August, when the Southeast Asian Summer Monsoon is strongest, the wind stress can produce a small amount of total volume transport from the Pacific Ocean to the Indian Ocean.

Table 5.4: The volume transport at the sections in the Indonesian Seas (Cases 5.4 & 5.5).

No.	The section name	The depth-integrated volume transport (Sv)	
		Case 5.4	Case 5.5
1	Makassar Strait	2.76	2.34
2	Java	-0.13	-0.09
3	Lombok Strait	1.86	1.98
4	Flores	0.30	0.44
5	Savu 1	0.05	0.07
6	Savu 2	-0.31	-1.12
7	Timor	0.05	-0.18
	Total transport	***1.84***	***1.10***

Note: The mean value is the summation of the volume transport from Section 2 to 7. Negative values show transport to the Indian Ocean, positive values show the transport to the Pacific Ocean. The volume transport values were calculated at the last year of the runs (the year 20).

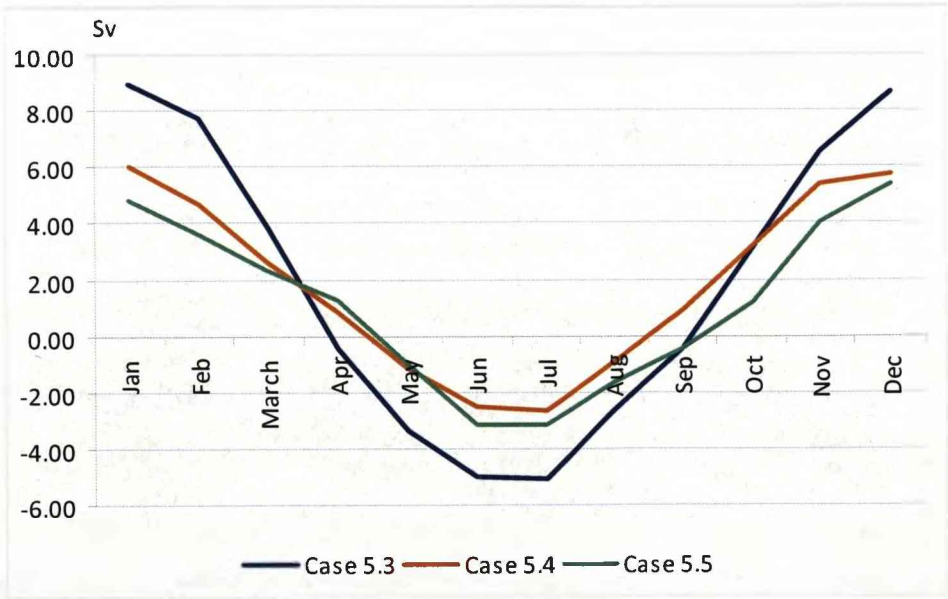

Figure 5.13: The seasonal variation of the ITF of the different experiments.

5.2.3. Model experiment with the whole Indian and Pacific Oceans domain (Case 5.6)

5.2.3.1. Model setup

The expansion of the western boundary to the eastern coast of Africa could not resolve the problem with the throughflow, therefore we next consider the fact that the Sverdrup transport accumulates from the eastern boundary, thus another experiment, referred to as Case 5.6, with the eastern boundary extended to the western coast of America, referred to as the Domain 3 (Figure 5.14), was carried out. In this experiment, the model was set up with 5 flat layers in the vertical. The initial layer interface depths were 150, 500, 1500, and 3500m and the density "sigma-t" of each layer was 2.35, 26.6, 27.5, 27.74, and 27.8 (kgm^{-3}) respectively. The driving force was the monthly-mean NCEP's wind stress (from 1952-2001), and no relaxation was used. The model was run for 20 years, starting from rest. With the above setup we will be able to see how much of the volume transport can be produced by the only wind stress over the domain.

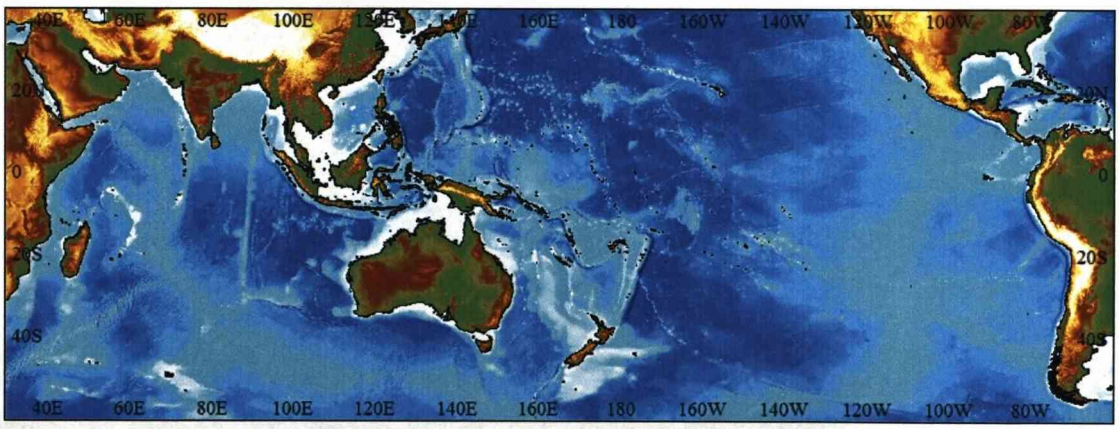

Figure 5.14: The model domain in the case of extending the eastern boundary to the western coast of America (Domain 3). The picture has been extracted from the GEBCO digital atlas, 2003.

5.2.3.2. Model result

The total kinetic energy and annual mean volume transport of the throughflow in the Indonesian Seas have been plotted from the beginning of the run to see how the model develops (Figures 5.15 and 5.16).

In general, the surface circulation in the Pacific and Indian oceans was well reproduced (Figure 5.17), especially the eastward surface jet along 10°S in the Indian

Ocean. This current system was incorrectly simulated in the previous experiment when its direction was westwards. On the smaller scale (the Southeast Asia, Indonesian Seas), the modelled surface circulation patterns (Figures 5.18 & 5.19) are in good agreement with the schematic diagrams of major currents in the region (Godfrey, 1996, Wyrtki, 1961, Tomczak and Godfrey, 2001) such as the Mindanao Eddy and Halmahera Eddy, the southward current in the South China Sea (SCS), the current system in the Celebes sea, and the throughflow in the Makassar Strait.

In terms of volume transport, the experiment result shows that when the model boundaries extended to cover the whole Indian and Pacific oceans, the wind stress produces a relatively small of annual-mean throughflow from Pacific Ocean to Indian Ocean, with the magnitude of about 1.2 Sv (averaged from year 13 to year 20 of the run). This value is close to the estimate of Wyrtki (1961), however recent estimate of the throughflow (based on both observation and numerical models) have given much higher values, as mentioned in Chapter 2.

There is a large area of high sea surface height in the eastern Pacific, which covering an area from the western coast of the Philippines to Taiwan (Figure 5.20). This is likely the cause of the intrusion of the water from the western Pacific into the SCS and producing a strong north-south current system in the SCS. This strong current system enters the Makassar Strait from the South and inhibits the southwards throughflow in the strait (Figures 5.18 & 5.19). As agreed by other studies, most of the throughflow is from the Makassar Strait therefore the current from the SCS is likely one of the reason for the decrease of the throughflow.

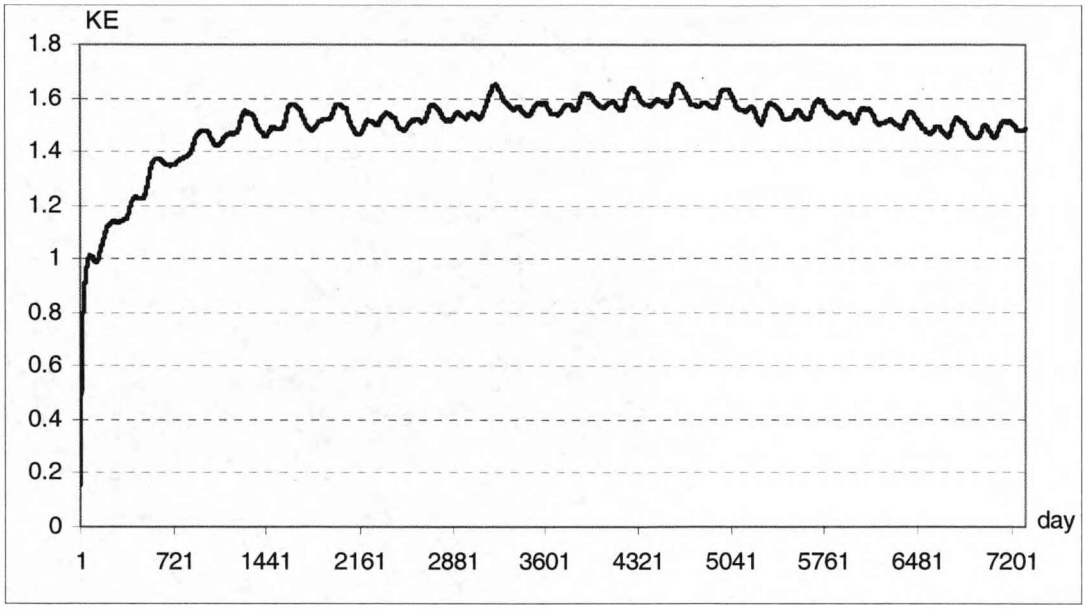

Figure 5.15: The KE of the experiment with whole Pacific and Indian Ocean. The model was run from rest to 20 years (Case 5.6).

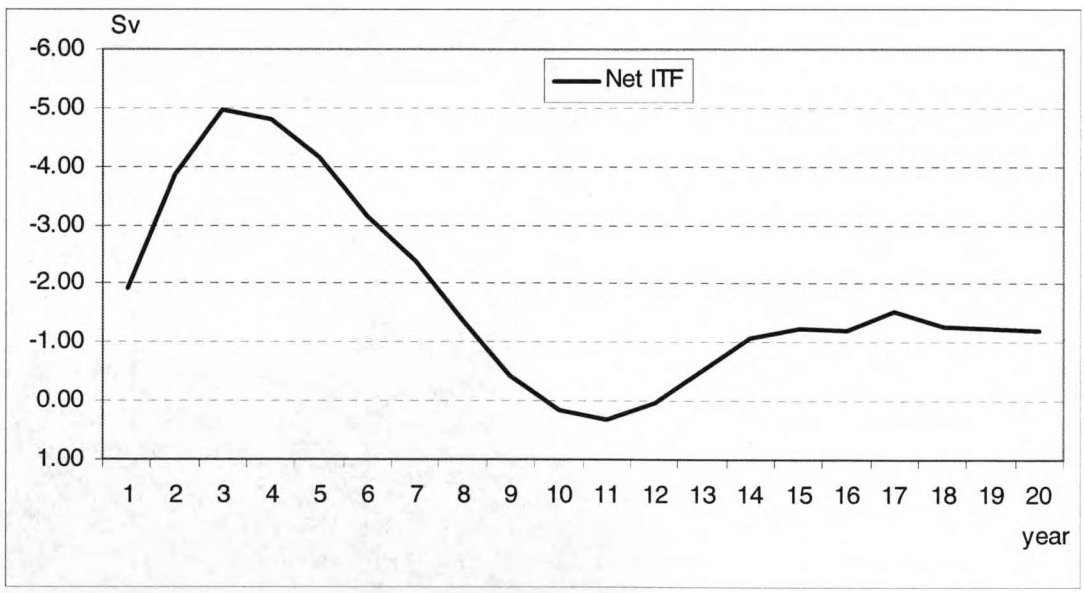

Figure 5.16: The annual mean ITF of the experiment with whole Pacific and Indian Ocean. The model was run from rest to 20 years (Case 5.6).

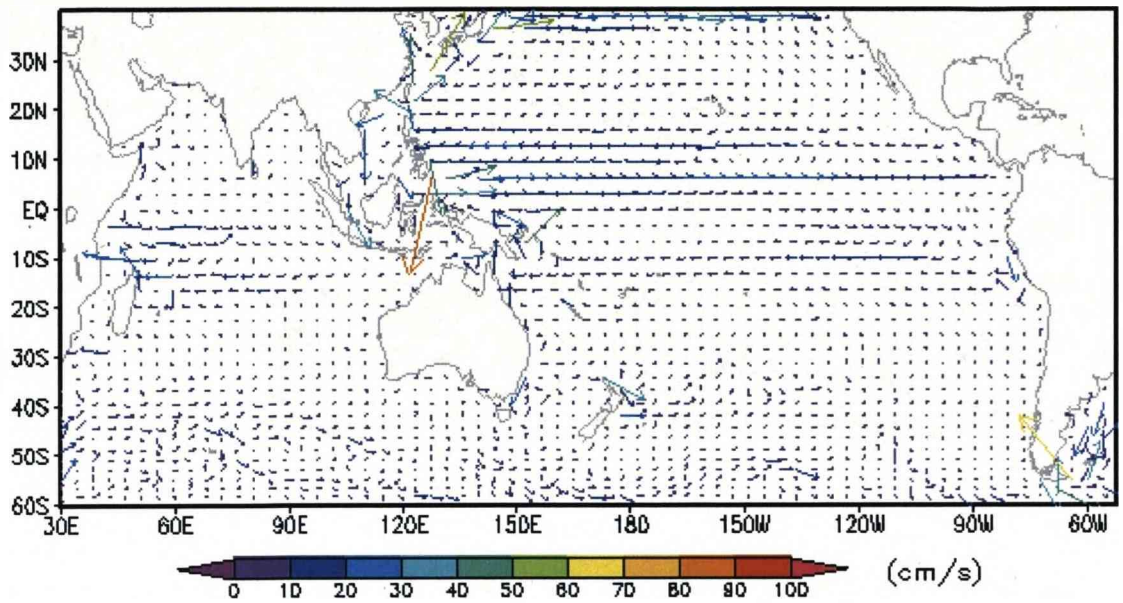

Figure 5.17: The annual-mean of wind-driven circulation of the mixed-layer. The model was setup with 5 flat-layers and forced by the NCEP's monthly-mean wind stress (1952-2001). In this plot the arrows are plotted at every 9 grid-cells in east-west dimension and every 7 grid-cells in north-south dimension (Case 5.6).

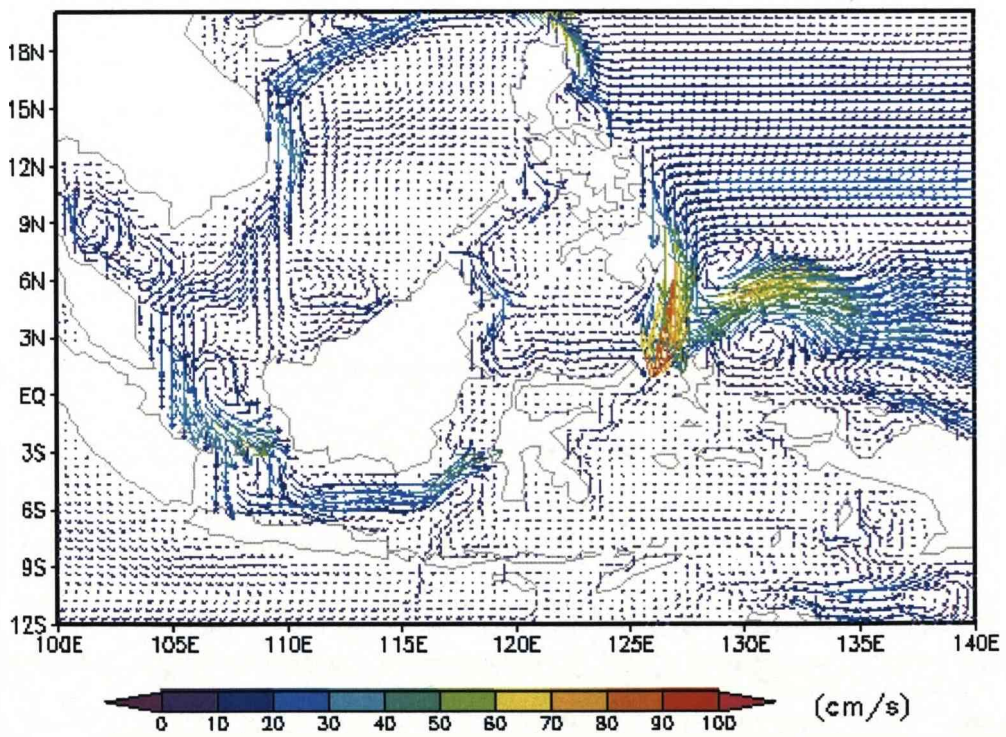

Figure 5.18: The annual-mean of wind-driven circulation of the mixed-layer in Southeast Asia. The model was setup with 5 flat-layers and forced by the NCEP's monthly-mean wind stress (1952-2001) (Case 5.6).

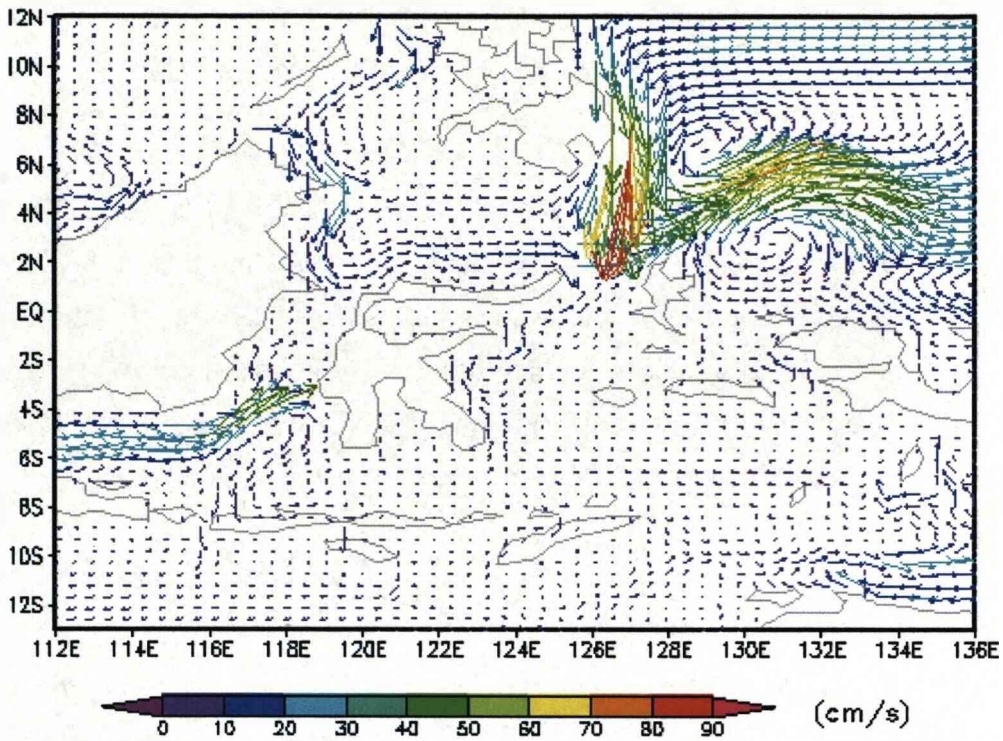

Figure 5.19: The annual-mean of wind-driven circulation of the mixed layer in the Indonesian's Seas. The model was setup with 5 flat-layers and forced by the NCEP's monthly-mean wind stress (1952-2001) (Case 5.6).

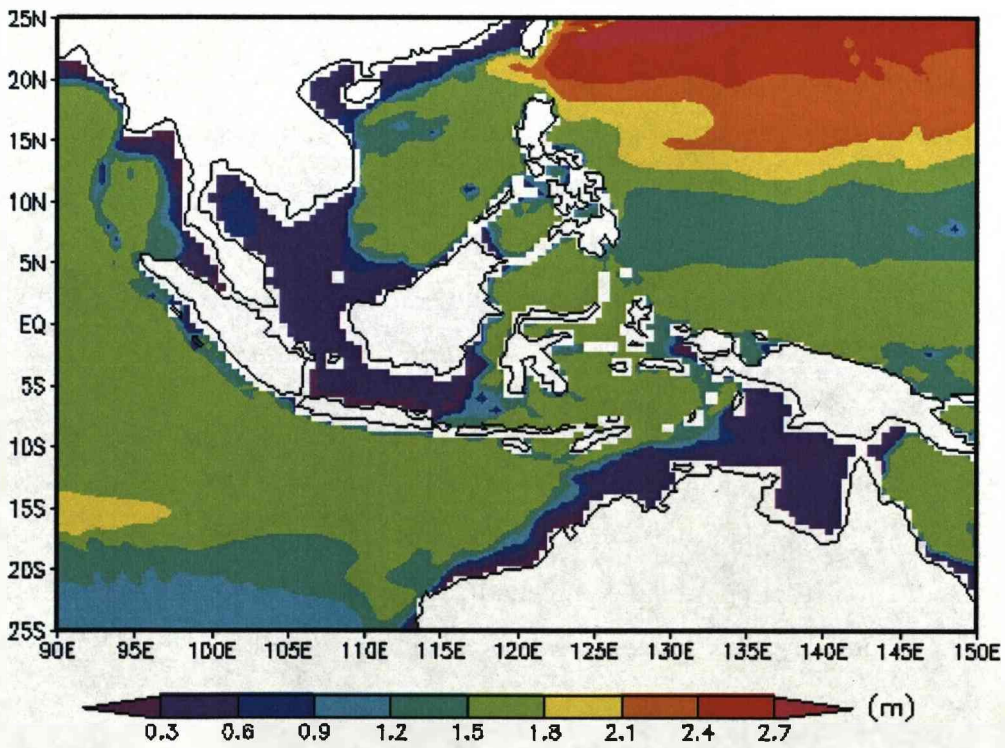

Figure 5.20: The annual-mean sea surface height of the Southeast Asia and vicinity (Case 5.6).

5.3. The model experiment with thermal forcing (Case 5.7)

The results of the model experiments with wind stress alone show that the wind stress over the domain can produces a rather strong seasonal variability of the ITF, but the annual-mean ITF transport generated by the wind stress is small compared to the recently observation and numerical model studies. In the next experiment, referred to as Case 5.7, the thermal forcing will be introduced. The thermal forcing field was generated by using the monthly-mean and annual-mean temperature and salinity fields from the Levitus Atlas, 1998 (NODC_WOA98).

5.3.1. Model setup

The model domain used in this experiment is the one which has been used in Cases 5.3, 5.4, and 5.5 (Domain 2 - Figure 5.9). The horizontal resolution of the model was 0.5^{o}. There were 6 vertical layers with the corresponding density "sigma-t" of each layer were 22.4, 24.4, 26.6, 27.5, 27.74, and 27.8 (kgm^{-3}) respectively. The initial temperature and salinity fields of these layers were derived from the annual-mean climatological Levitus Atlas, 1998 (NODC_WOA98). The monthly-mean temperature and salinity of the mixed layer were also derived from the monthly-mean Levitus Atlas, 1998 dataset. There were no explicit heat exchanges between the sea surface and atmosphere, no precipitation and evaporation, instead during the model run the salinity and temperature were relaxed with a time constant of 1 year. This relaxation will help to make these variables follow the variation of the observational data.

The model was run for 20 years, and the results of the last year will be interpreted to investigate the circulation and ITF. The model was repeatedly forced by the annual cycle of the monthly-mean NCEP's wind stress (Figures A.4 to A.6 - Appendix) and the thermal forcing (temperature and salinity relaxation). At the open boundary, cyclic boundary conditions were applied, allows water flow into and out of the model domain to reproduce the ACC.

5.3.2. Model result

5.3.2.1. The annual-mean circulation and the ITF

The surface circulation in the Indian and Pacific Oceans is strongly influenced by the wind field over the ocean surface. Especially in the northern Indian Ocean, the seasonal reversal of monsoon winds dictates seasonal change of the ocean surface current. Therefore the annual-mean circulation will not be able to represent the seasonal change of surface circulation in the northern Indian Ocean. However it will help to demonstrate and understand the tendency and overall pattern of the ocean circulation elsewhere.

Figure 5.21 shows the annual-mean circulation produced by the model. The general circulation of the oceans are well reproduced such as the Kuroshio, the NEC, the NECC in the Pacific Ocean, and the Somali Current, the westwards zonal jet, the ECC, the Agulhas in the Indian Ocean.

The annual-mean circulation of part of the western Pacific Ocean, the South China Sea (SCS) and the Indonesian Seas are shown in the Figure 5.22. In the Pacific Ocean, the NEC (10^{o}N-15^{o}N) bifurcates when approaching the Philippine coast, one branch flows northwards and the other flows southwards. Part of the northwards branch enters the SCS, the remainder continues northeastwards to form the Kuroshio Current. In the SCS, the flow from the Pacific Ocean crosses the northern part of the SCS, then flows along the east coast of Vietnam to the Java Sea. On the basin scale, this current is the western edge of the two main gyres in the SCS, the northern gyre ranges from 15^{o}N-20^{o}N and the southern gyre from 4^{o}N-8^{o}N. In the Java Sea, part of the current enters the Indian Ocean through the Java Strait, and the other joins the flow from the Makassar Strait. The southwards branch of the NEC partially enters the Celebes Sea which is the main source of the ITF, the remainder turns eastwards to feed the NECC. The combination of the NEC, southwards branch and the NECC forms the Mindanao eddy.

Within the Indonesian Seas, the current from the Pacific Ocean enters the northern Celebes Sea and flows southwards through the Makassar Strait to meet the current from the Java Sea. The combined current system partially exits to the Indian Ocean through the Lombok Strait, the remainder flows to the Flores Sea. In the Flores Sea

the current system is divided as follows: one branch flows northwards into the Molucca Sea then joins with the eastwards current from the southern Celebes Sea at northwest of the Halmahera. This combined current then enters the Pacific Ocean to feed the NECC; one branch flows into the Banda Sea; one branch exits to the Savu Sea through the Ombai Strait; and the other exits to the Indian Ocean through the Timor Sea. The last current branch rejoins the flows from the Savu Sea and Lombok Strait to form the root of the westwards zonal jet (11°S-13°S) flowing from the Indonesian Seas into the interior of the Indian Ocean (Figures 5.22 & 5.23). This zonal jet then moves directly westward across the interior Indian Ocean to the African coast. Part of the Jet turns northwards to join the well-known western boundary current in the Indian Ocean (the Somali Current), the other flowing southwards and eventually joins the Agulhas Current. As shown in the Figures 5.21, 5.22 and 5.23, the western boundary current in the Pacific Ocean, the circulation in the SCS and the Indonesian Seas seem associated with large-scale forcing over the Pacific Ocean, and the geometry of the region.

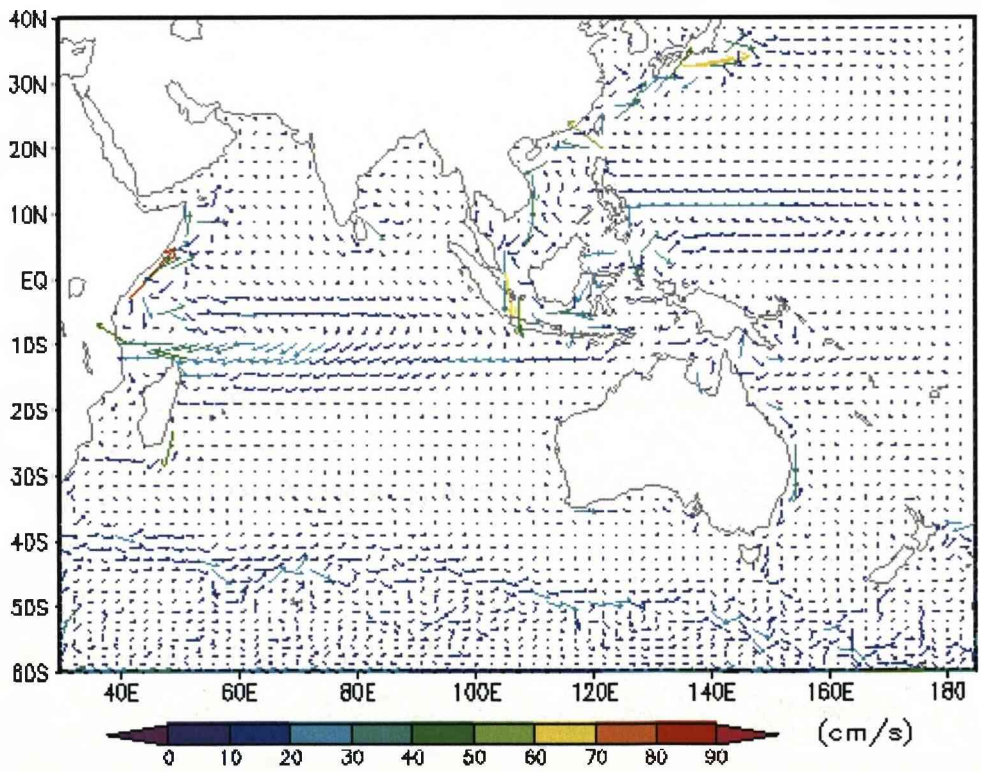

Figure 5.21: The annual-mean circulation of the mixed layer. The arrows are plotted at every 5 grid-cells.

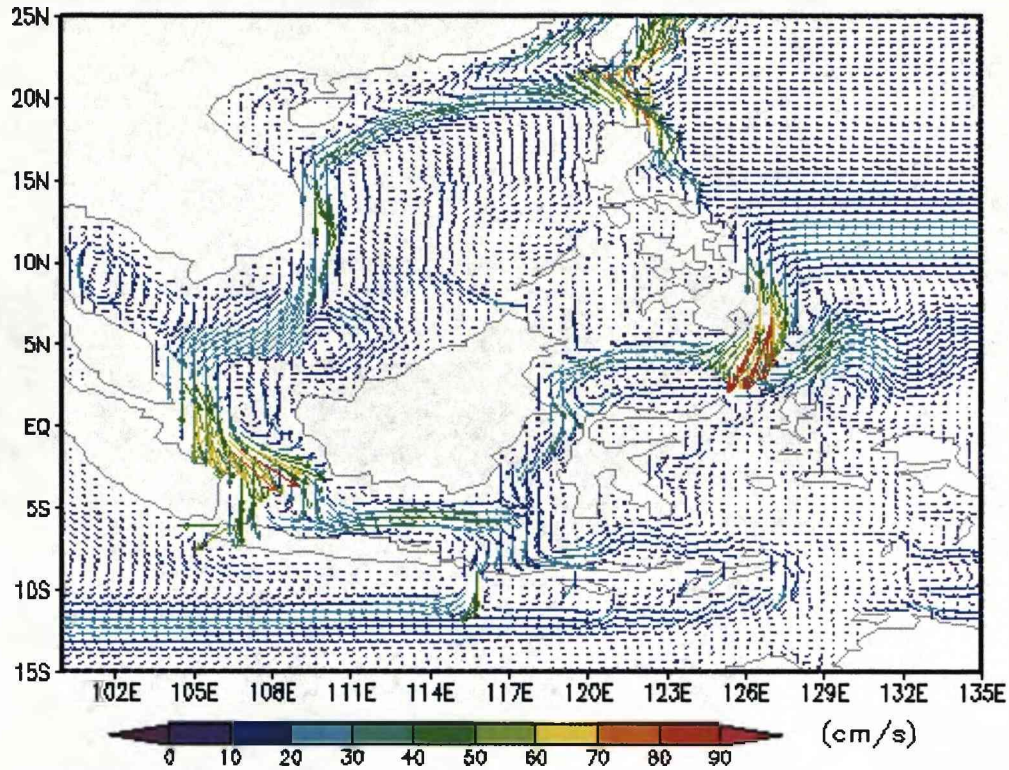

Figure 5.22: The annual-mean circulation of the mixed layer in the Southeast Asia region.

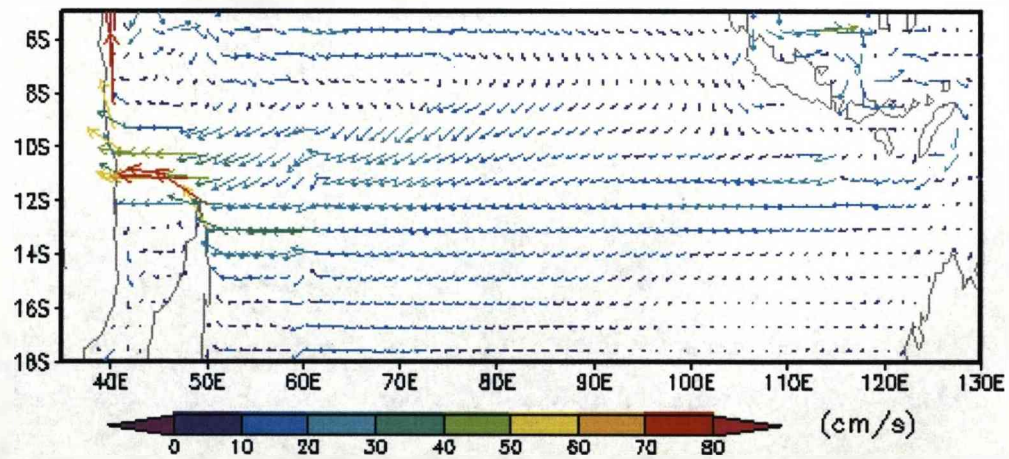

Figure 5.23: The annual-mean surface westwards jet in the Indian Ocean. The arrows are plotted at every 2 grid-cells east-west and every 3 grid-cells north-south.

The circulation over the whole model domain has been well reproduced and the volume transport between the oceans also shows a consistency with the other work. In comparison with the volume transport of the ITF of other studies (Table 2.2 – Chapter 2) the result of the experiment shows a very good agreement in both direction and magnitude. The total volume transport between the oceans is about 16.25 Sv, transport from the Pacific Ocean into the Indian Ocean, showing a very good agreement with results of other numerical calculations (Semtner and Chervin,

1988; Hirst and Godfrey, 1993; Li Wei, 2006, Humphries and Webb, 2007), and the volume transport balance between the oceans suggested by Siedler et al. (2001) (Figure 5.24). The variability of the ITF transport and volume transport at the sections will be explored more detail in the next section.

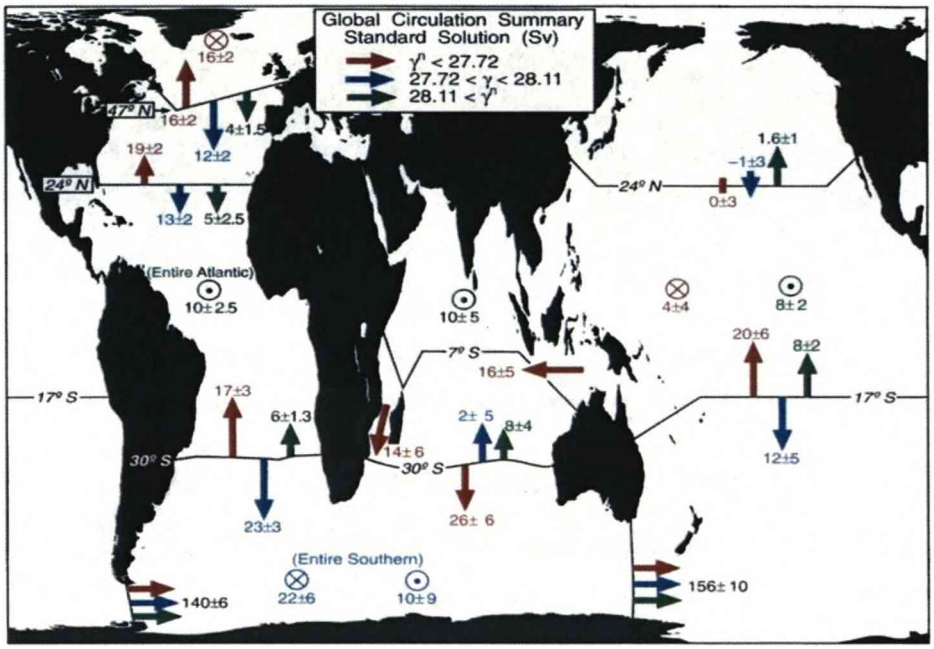

Figure 5.24: The world ocean volume transport balance (Siedler et al., 2001).

5.3.2.2. The seasonal variability of the circulation and the ITF

In the previous section the annual-mean circulation and the volume transport between the oceans have been examined. In this section, the seasonal variability of the circulation and the volume transport in the Indonesian Seas from the model results will be investigated in detail.

- ***Circulation in the Pacific and Indian Oceans***

In the Pacific Ocean, the NEC between about 8°N-20°N is directly wind-driven (Tomczak and Godfrey, 2001). It therefore responds quickly to the change of wind variation over the ocean surface. The model results show a good agreement with the work of Tomczak and Godfrey (2001). The NEC, with the core range 10°N-15°N, flows east-to-west over the year corresponding to the wind stress. The strength of the NEC varies throughout the year according to the strength of the wind field. In winter (November to April) when the trade wind is strongest, the NEC reaches its greatest strength in February and March (Figure 5.25). In summer (May to October) the

NEC's strength is weaker corresponding to the decrease of the wind strength (Figure 5.26). The NECC in the Pacific Ocean ranges between 3°N-8°N and flows west-to-east throughout the year. However the model results show that the NECC is fed by varying sources. In winter, the source of the NECC comes from the NEC and the Indonesian Seas (Figure 5.25). In summer, the NECC is fed by water from the NEC and water from the southern hemisphere, which flows northwestwards along the eastern coast of the Papua New Guinea (Figure 5.26). The well-known western boundary current in the Pacific Ocean (the Kuroshio Current) is also very well reproduced. The model results show that the Kuroshio Current is a narrow and swift current with counter currents and rings on either side. In both winter and summer, the Kuroshio Current begins from the west coast of the Philippines, flowing northeast along the Japanese coast and eventually leaves the coast around 35°N entering the interior Pacific Ocean (Figures 5.25, 5.26).

In the Indian Ocean, besides the North and South Equatorial Currents, Somali Current, the Agulhas Currents (not shown), the model has successfully reproduced the intense surface eastwards equatorial jet in the transition periods (May and October) which was first described by Wyrtki (1973) (Figure 5.27).

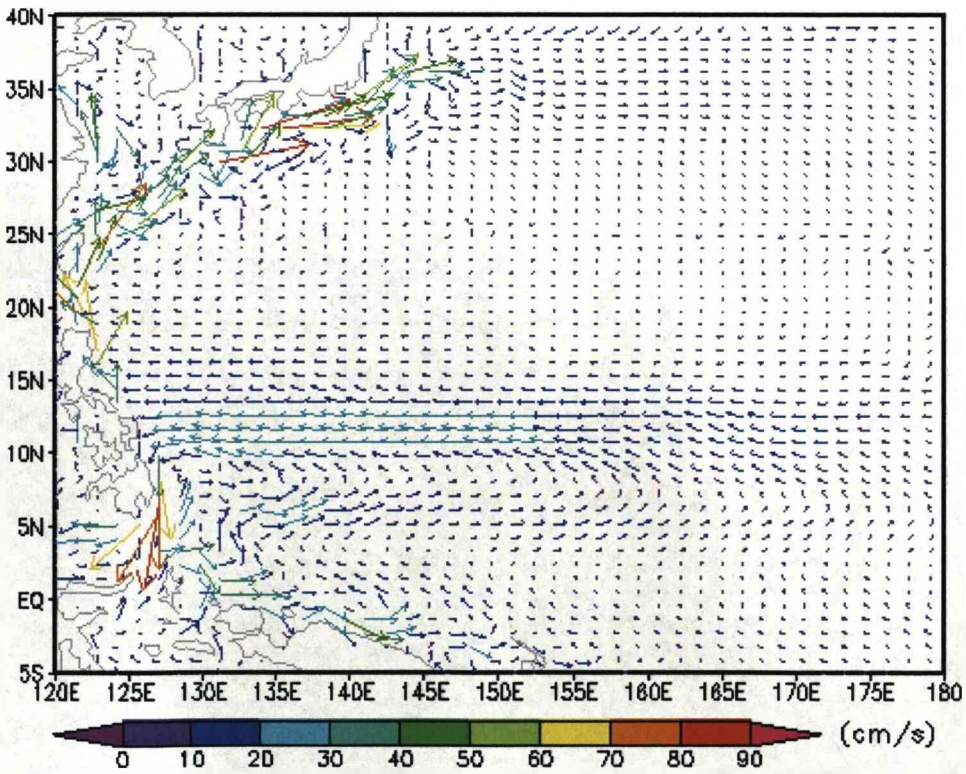

Figure 5.25: The monthly-mean surface circulation of the western Pacific Ocean in March.

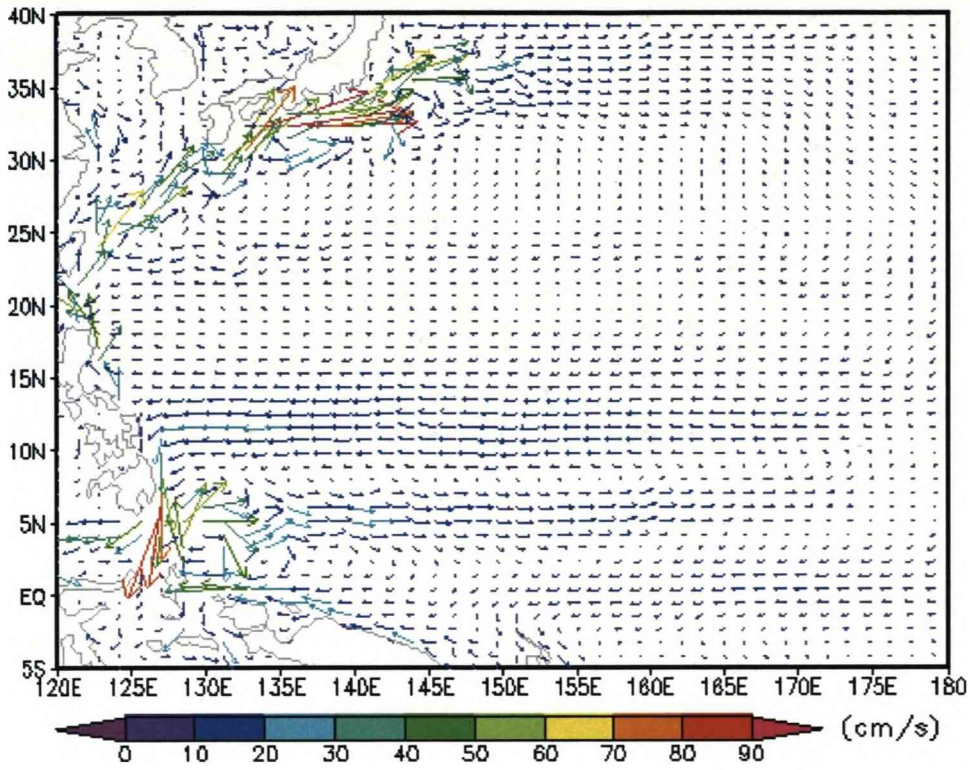

Figure 5.26: The monthly-mean surface circulation of the western Pacific Ocean in September.

- ***Circulation in the Southeast Asian waters***

The Indonesian Seas

The Indonesian region is a large and very complex area with many islands, seas and passages. In terms of circulation, since the work of Wyrtki (1961) several investigations have been caried out to explore the circulation in the region such as INSTANT and ARLINDO programmes. However these observations were mainly conducted at specific locations to serve the purpose of each study. Therefore the work of Wyrtki (1961) is still a significant reference document for the overall picture of the circulation in the Indonesian seas.

As described by Wyrtki (1961) the flow in the Makassar Strait is directed to the south throughout the year with the velocity varying according to the variability of the wind field. The barotropic circulation of the model is almost consistent with the circulation pattern of the Wyrtki atlas, but the modelled surface circulation has a significant change in winter. The seasonal variability of the surface circulation in the Indonesian Seas is described as follows:

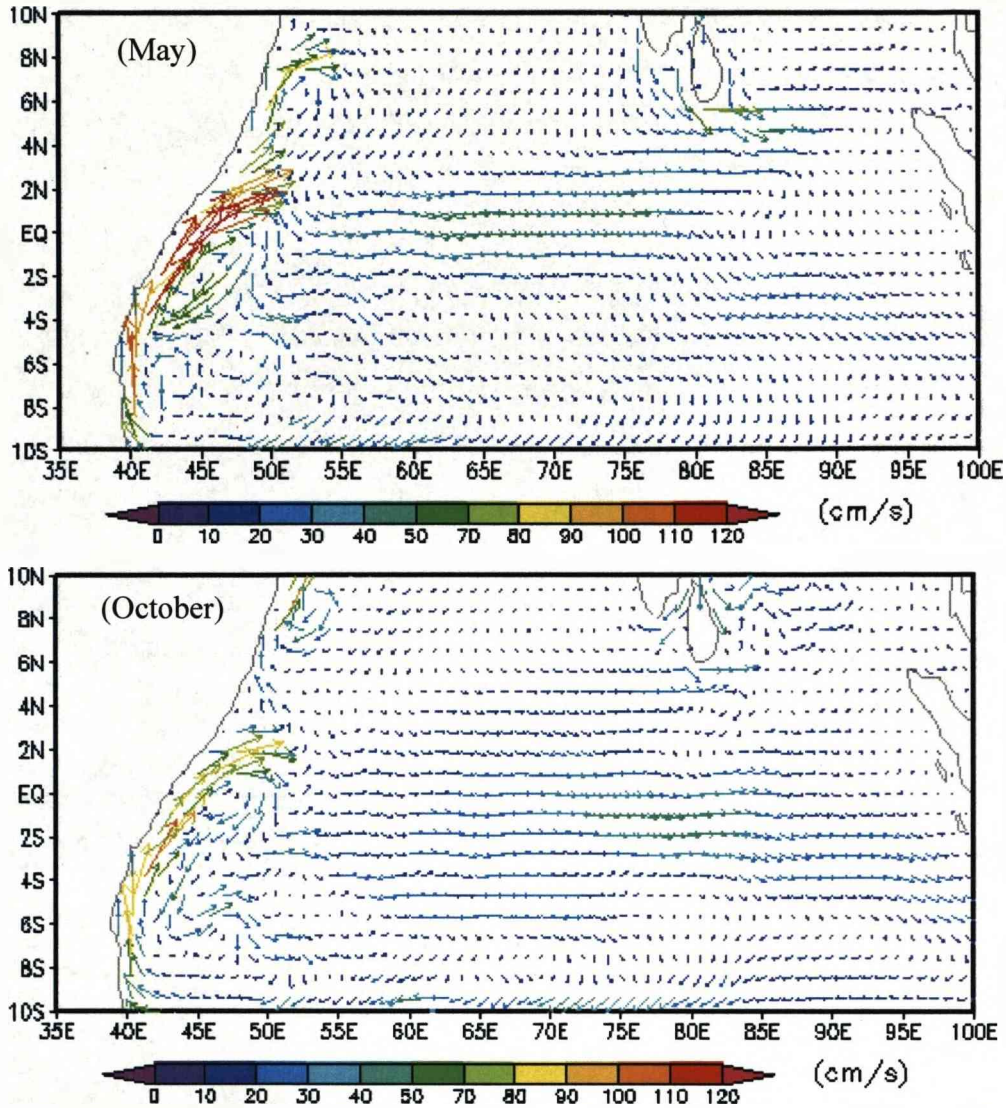

Figure 5.27: The monthly-mean surface eastwards equatorial jet in the Indian Ocean in the transition period (May and October). The arrows are plotted at every 2 grid-cells.

In winter, from November to January, when the northeast monsoon is fully developed and prevailing over the region, there is a strong surface current from the SCS flowing through the Java Sea to enter the Makassar Strait. This current flows northwards to enter the Celebes Sea, then joining with the current in the southern part of the Celebes Sea before exiting to the Pacific Ocean to feed the NECC (Figure 5.28). In summer, when the southwest monsoon inhibits water from the SCS, the Indonesian Seas are fed by water from both northern hemisphere and southern hemisphere. The water from the nothern hemisphere (NEC) enters the Indonesian Seas through the Celebes Sea then flowing through the Makassar Strait. Part of the water enters the Indian Ocean through the Lombok Strait, the rest flows to the Java

Sea and Flores Sea. The water from the southern hemisphere enters the Indonesian Seas through the Halmahera Strait, flowing into the Banda Sea and Flores Sea and eventually exits to the Indian Ocean through the Timor Sea, Ombai Strait and Flores Strait (Figure 5.29).

The Makassar Strait is one of the main pathways of the ITF from the Pacific Ocean to the Indian Ocean. The flow within the Makassar Strait is characterized by a seasonal cycle and strongly influenced by monsoonal wind changes. The minimum of the depth-integrated flow appears in December when the Java Sea and the Makassar Strait are invaded by water from the SCS. The maximum of the depth-integrated flow appears in July and August when the southwest monsoon inhibits water intrusion from the SCS to allow more water from the Pacific Ocean to enter the Celebes Sea then flowing southwards through the Makassar Strait (Figure 5.28, 5.29).

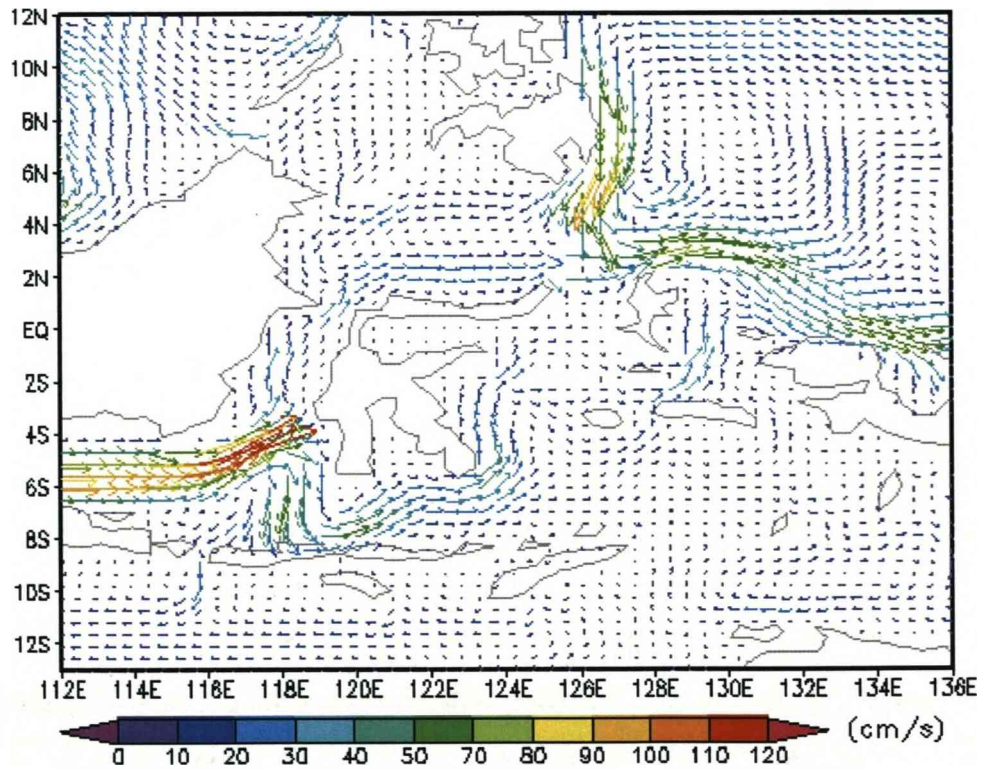

Figure 5.28: The monthly-mean surface circulation in the Indonesian Seas (December).

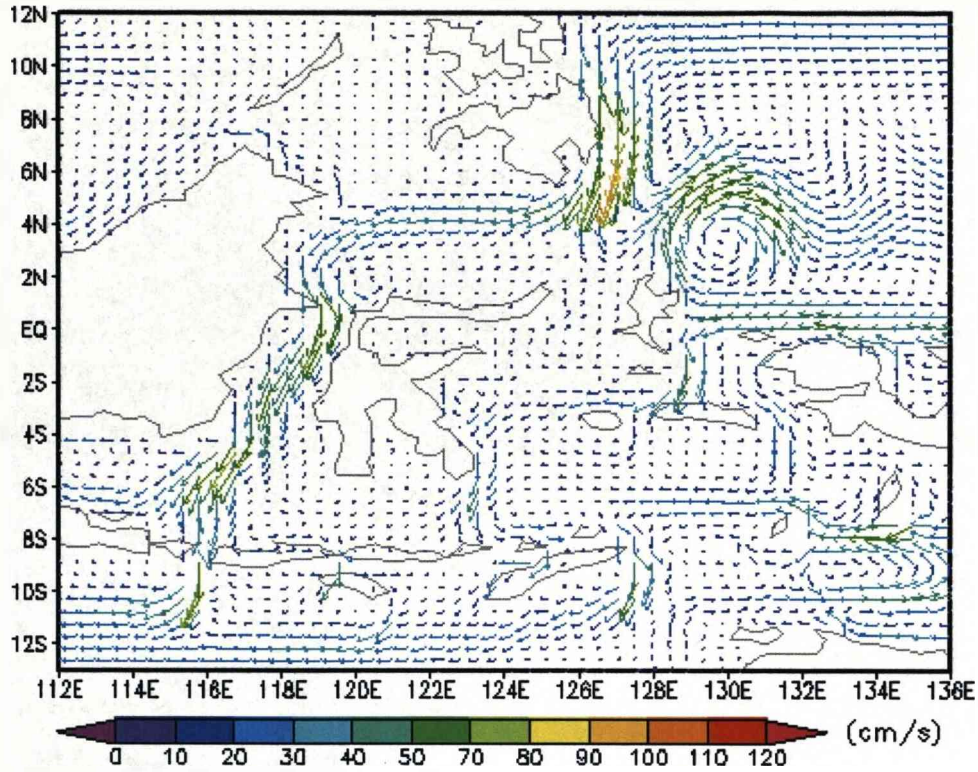

Figure 5.29: The monthly-mean surface circulation in the Indonesian Seas (July).

The South China Sea

The South China Sea is the largest marginal sea in the Southeast Asian waters. It connects in the south with the Sulu and Java Seas through a number of shallow passages and in the north with the Pacific Ocean through the deep Luzon Strait. The circulation in the South China Sea is mainly driven by the monsoons and the water intruded from the Pacific Ocean. Based on hydrographic observations, sea level records, and ship drifts, Wyrtki (1961) proposed in the first circulation atlas that the South China Sea contains basically a cyclonic gyre in winter and an anticyclonic gyre in summer, as a result of the seasonally reversing monsoon.

Figure 5.30 shows the monthly mean circulation of the mixed layer of the SCS in winter (February) and summer (August). In the winter monsoon period (November to April) the Asian high pressure system brings strong winds from the northeast. The northeast monsoon prevails over the region. The SCS is intruded by water from the Pacific Ocean through the Luzon Strait. The intense current from the Luzon Strait crosses the northern SCS, bends to southwest along the Asian continental shelf, then flowing southwards along the coast of Vietnam and eventually flows out through the

Gasper and Karimata Straits in the south. On the basin scale, there are three main gyres developed in the SCS as follows: the northern cyclonic gyre, the southern cyclonic gyre and the weaker anticyclone between the two gyres. This pattern is generally consistent with the circulation atlas proposed by Wyrtki (1961). During the summer monsoon period (May to October) the southwest monsoon prevails over the region. In the northern part of the SCS, there still exists the intense current from the Luzon Strait crossing the SCS to the coast of Vietnam as in the winter monsoon. This current combines with the northwards current flowing along the west coast of the Philippines to form the northern cyclonic gyre in the northern part of the SCS. In the southern part of the SCS, the current from the entrance of the Gulf of Thailand flowing northeast parallel to the southern coast of Vietnam in response to the southwest monsoon. At 9°N-14°N this current meets the southwards current from the northern part of the SCS. As a result the current turn eastwards, joining the current in the Sunda shelf to form the anticyclonic gyre in the southern part of the SCS.

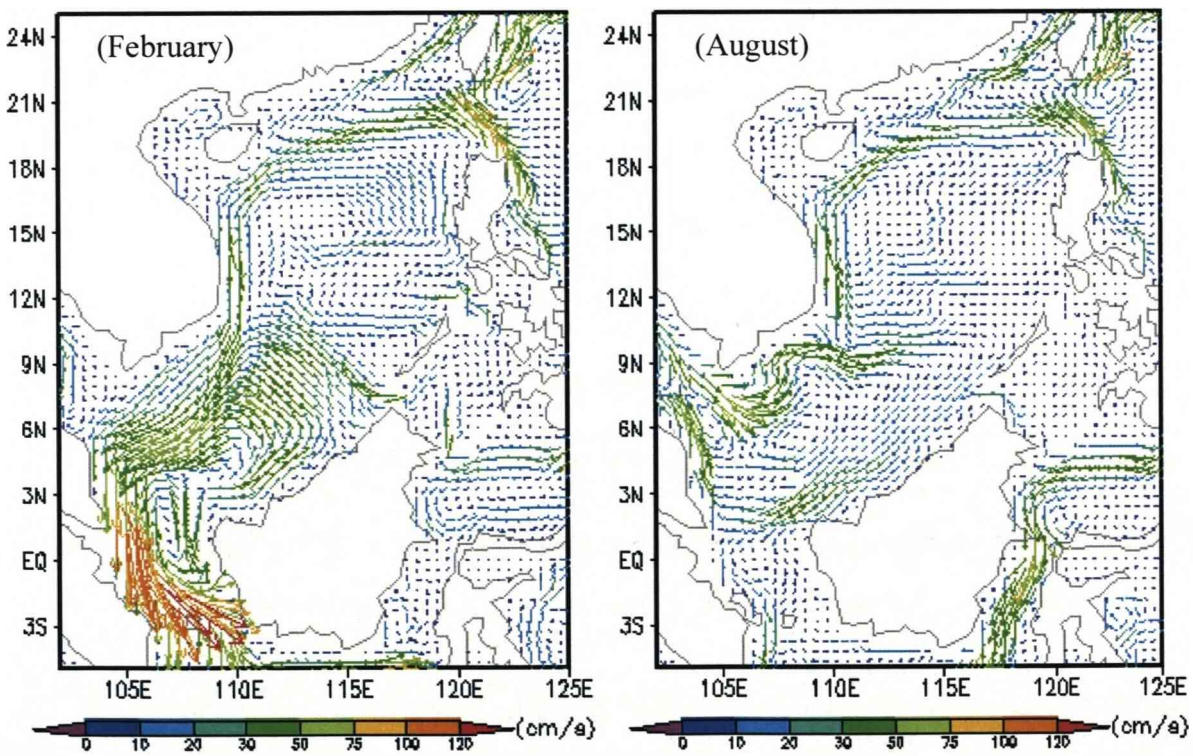

Figure 5.30: The monthly-mean circulation of the mixed layer in the South China Sea.

The existence of the intense current from the Luzon Strait to the coast of Vietnam in summer (originated from the water intrusion from the Pacific Ocean) appears inconsistent with the current pattern proposed by Wyrtki (1961) but it is consistent with the diagram of the SCS circulation proposed by Fang et al (1998) (Figure 2.12 -

Chapter 2). The appearance of this current appears to be a good explanation for the realistic phenomena of eastwards turning of the northeast current along the coast of Vietnam around 9°N-14°N which was seen in the Wyrtki Atlas but was not explained.

- ***The Indonesian Through Flow***

In other research, despite discrepancies in magnitude of the ITF, most authors report that the ITF has strong variations throughout the year. The maximum of the ITF transport appears during the summer monsoon from April to September, and the minimum of the volume transport occurs in the winter monsoon from November to January (Wyrtki, 1987; Masumoto and Yamagata, 1993; Gordon et al., 1999, 2003; Hautala et al., 1996; Potemra et al, 2007). The model result shows a good agreement with the above research. The model results (Figure 5.31 and Table 5.5) show a strong seasonal variation of the volume transport between the oceans with the minimum value of about 12.26 Sv in December, and the maximum value of about 20.28 Sv in July. This result is in good agreement with the corresponding variation of the sea surface height where the difference in monthly-mean sea surface height between the western Pacific Ocean and the eastern Indian Ocean in December is smaller than that in July (Figures 5.32 & 5.33).

The seasonal variability of the ITF appears to be governed by large–scale forcing and local wind changes related to the monsoonal cycle, and can be explained on the basis of the circulation as follows: in winter the northeast monsoon prevailing over the SCS drives a large amount of surface water from the South China Sea through the Java Sea into the Indonesian Seas (Makassar Strait, Flores Sea, Banda Sea, Molucca Sea) (Figure 5.30 - February) and inhibits the surface water flow from the Pacific Ocean to the Indian Ocean, consequently reducing the ITF transport. In summer the southwest monsoon prevails over the SCS and inhibits surface water from the SCS from entering the Indonesian seas. This allows more water from the Pacific Ocean to enter the Celebes Sea flowing southwards through the Makassar Strait and to exit to the Indian Ocean. On the other hand, during summer, there is another water source entering the Indonesian Seas from the southern hemisphere through the Halmahera Strait (Figure 5.30 - August) and as a result this leads to an increase of the water

transport from the Pacific Ocean to the Indian Ocean (increase the ITF). This explanation is consistent with the mechanism proposed by Gordon et al. (2003) on the basic of analysing ocean current and stratification data along with satellite-derived wind measurements, and has pointed out that the SCS plays an important role in the variability of the ITF.

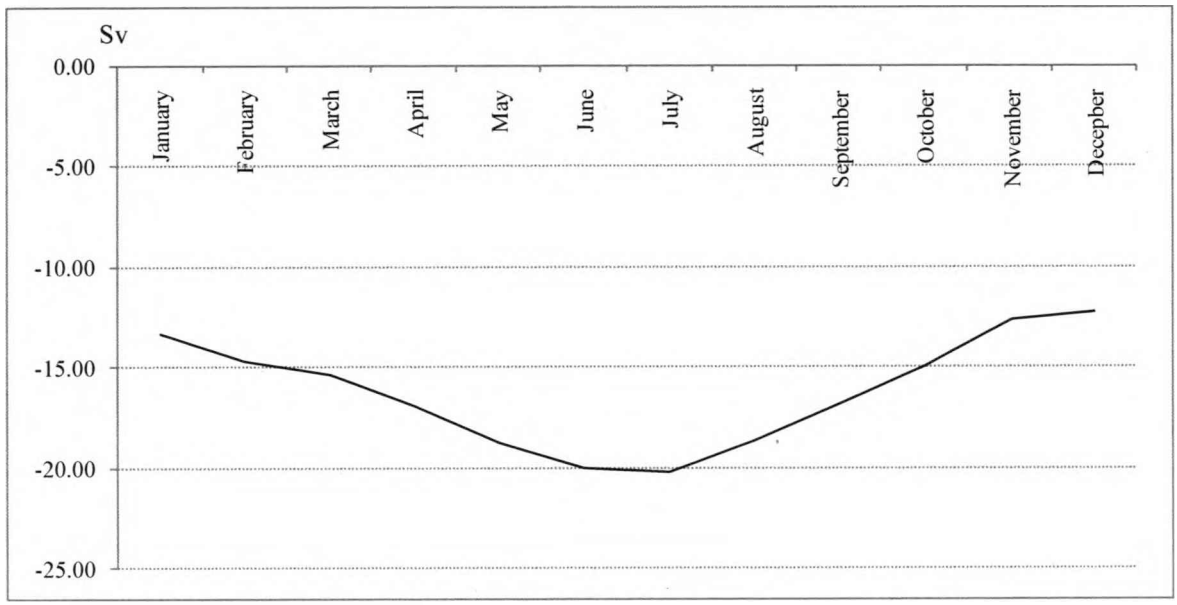

Figure 5.31: The seasonal variation of the depth-integrated volume transport between the oceans. The negative value shows the transport from the Pacific Ocean to the Indian Ocean.

Table 5.5: The monthly-mean volume transport of the ITF.

Month	The ITF (Sv)	Month	The ITF (Sv)
January	-13.31	*July*	-20.28
February	-14.72	*August*	-18.67
March	-15.4	*September*	-16.87
April	-16.94	*October*	-15.01
May	-18.86	*November*	-12.65
June	-20.04	*December*	-12.26

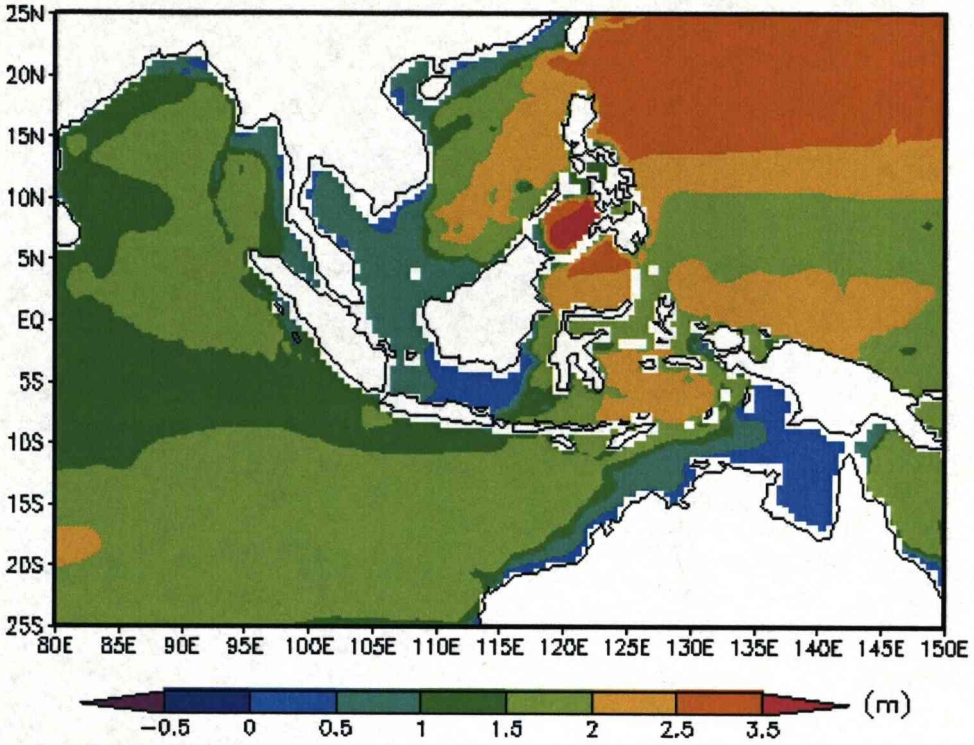

Figure 5.32: The monthly mean sea surface height in Southeast Asia and vicinity in July.

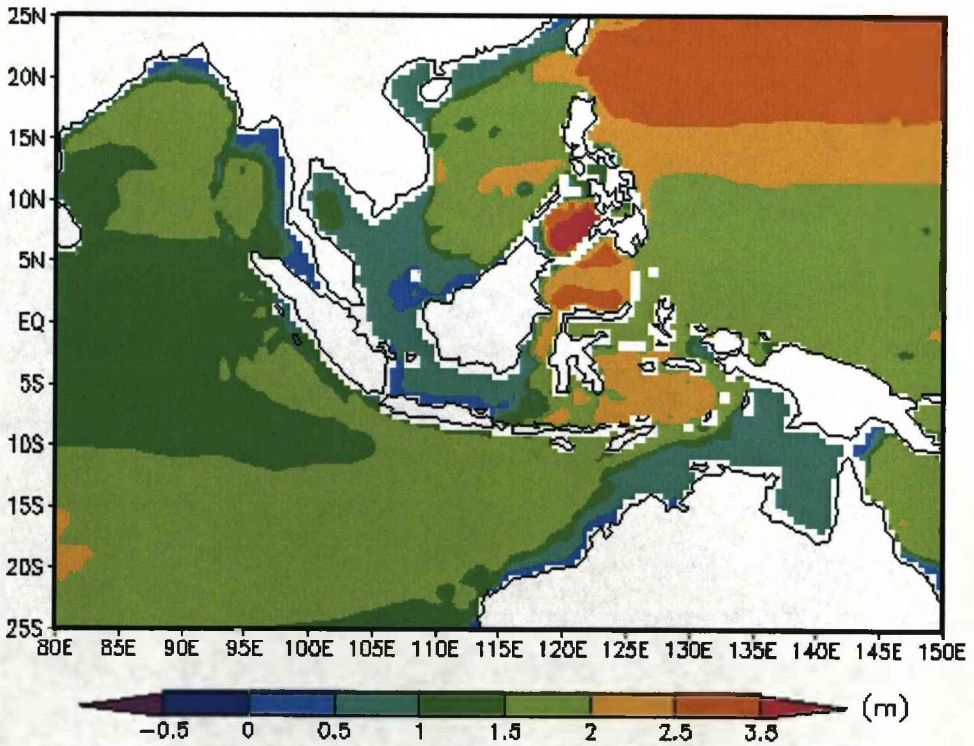

Figure 5.33: The monthly mean sea surface height in Southeast Asia and vicinity in December.

5.3.2.3. Vertical distribution of the volume transport of the ITF

The volume transport of the ITF mainly appears in the upper layer from 200m (Wyrtki, 1987) to 500m (Molcard et al, 1996). The model result shows that most of the ITF transport appears in the upper layer with the first two upper layers providing a total of over 10 Sv. The model result also show that although the mean current is strongest in the upper layer, the deeper flow carries significant part of the transport (over 6 Sv) and is in good agreement with estimation of Molcard et al (2001) based on the current meter mooring (Table 5.6).

Table 5.6: The volume transport at the sections in different layers.

	SCS	*Makassar*	*Java*	*Lombok*	*Flores*	*Ombai*	*Timor*	*The ITF*
Mixed-layer	-4.02	-1.76	-1.01	-1.60	-0.74	-0.69	-1.64	-5.69
layer 5	-0.81	-3.17	-0.13	-1.58	-0.63	-0.90	-1.21	-4.45
layer 4	0.00	-2.45	0.00	0.00	0.00	-2.28	-1.33	-3.61
layer 3	-0.01	0.04	0.00	0.00	0.00	-2.29	-0.31	-2.61
layer 2	0.00	0.00	0.00	0.00	0.00	0.00	0.00	0.00
Bottom	-0.01	0.09	0.00	0.00	0.00	0.00	0.10	0.10
Sum	***-4.85***	***-7.25***	***-1.14***	***-3.18***	***-1.37***	***-6.16***	***-4.39***	***-16.26***

Note: The ITF is the summation of the volume transport from the last 5 sections. Negative values show transport to the Indian Ocean, positive values show the transport to the Pacific Ocean.

5.3.2.4. Volume transport at the main passages

With the model set up and tailored to the geometry of the study region, it is of interest to examine not only the total volume transport between the oceans but also the volume transport at the individual sections in the Indonesian Seas.

The calculation of the volume transport in the model takes place at the Java Strait, Lombok Strait, Flores Strait, Ombai Strait and the Timor Sea. The Java, Lombok and Flores Straits are rather narrow straits. Only the Lombok Strait is deep (250-300m) and is known as the main outflow of the ITF from the Makassar Strait, the other two are rather shallow and could be closed or opened depending on the study (numerical model study); in this experiment they are all opened. However the horizontal resolution of the model is 0.5 degree so the volume transport at these straits maybe exaggerated. In other studies, most authors agree that the bulk of the ITF passes through the Makassar Strait, and the volume transport contribution from the South China Sea is often ignored when estimating the magnitude of the ITF transport.

However Fang (2005) suggested a rather high value (3.9 Sv) of volume transport from the South China Sea to the Indonesian Seas. Therefore besides the sections for calculation of the volume transport between the oceans, volume transports have been calculated at three more sections (the Makassar Strait, South China Sea and ACC) with the purpose of having an overall picture of the volume transport in the region.

The volume transports through the main passages are given in Table 5.7 and Figure 5.34. The throughflow from the Makassar Strait to the Indian Ocean is considered to be flowing directly through the Lombok Strait (Sprintall et al., 2000). The volume transport through the Lombok Strait in the model is higher than the transport calculated by Murray and Arief (1988) based on January 1985 to March 1986 current meter mooring data (3.18 Sv compared to 1.7 Sv). The possible reason for the overestimated transport at the Lombok Strait is this narrow (approximately 18 km width) and shallow (250–300m) passage has been widened to 50.0 km due to the horizontal resolution of the model. The seasonal variability in the Lombok Strait shows the high peak of throughflow during the summer monsoon (June to September) and low peak during the winter monsoon (November to January). This model result is consistent with the results derived from the CTD and pressure gauge measurement (Murray and Arief, 1988; Hautala et al., 2001).

The most significant part of the ITF flowing into the Indian Ocean is through the Ombai Strait with the magnitude of volume transport reaching 6.17 Sv. This value is slightly higher than the values proposed by Hautala et al (2001); Molcard et al (2001): 4.5–5.0 Sv and Sprintall et al. (2004): 4.5 Sv. The seasonal variation of the volume transport shows it is strongest from April to July with maximum of 8.36 Sv in May. The weakest transport appears from August to December with minimum of 5.10 Sv in September.

The modelled volume transport at the Timor Strait is about 4.39 Sv, which is smaller than the suggested value of Creswell et al (1993) : 7.0 Sv, but is in very good agreement with Molcard et al. (1994) : 4.5 Sv; (1996) : 4.3 Sv and Sprintall et al. (2004) : 4.3 Sv. The seasonal variation of the throughflow in the Timor Sea has the same phase with the throughflow in the Ombai Strait. The strongest transport of the throughflow occurs in May (6.16 Sv), weakest transport occurs in December (2.65 Sv).

The main focus location of other research on the ITF is in the Makassar Strait which is considered as the major passage of the ITF. The recent mooring measurements in the Makassar Strait (ARLINDO 1993-1994, 1996-1998, 1998-2007; INSTANT 2003-2006) provided a good description of the throughflow dynamics within the passage. The initial result of ARLINDO has shown an average southwards transport within the Makassar Strait of 9.3 Sv with a range of about 2.5 Sv. The model result shows the transport at the Makassar Strait is about 7.26 Sv which is slightly smaller than the value of ARLINDO. In terms of seasonal variation, the ITF at the Makassar Strait shows a very strong variability with the difference between maximum transport in July (10.92 Sv) and minimum transport in December (2.04) of about 8.88 Sv. The high variation of the volume transport in the Makassar Strait is in opposite phase to the volume transport from the SCS. The minimum volume transport from SCS appears in June (0.55 Sv), and the maximum is in December (10.52 Sv) (Figure 5.34). The discrepancy in phase of the volume transport between the Makassar Strait and the SCS can be explained as a result of the difference of current regime between them which is very much related to the monsoonal wind fields over the region.

The Java and Flores Straits are two narrow and shallow passages. The contributions to the total ITF transport of these two passages are 1.15 Sv and 1.37 Sv respectively. However the actual magnitude is possibly smaller than that because, as mentioned before, these two straits have been widened due to the horizontal resolution of the model. The model stop at 60°S (the southern boundary) and is not primarily designed to model the ACC where transport is about 147±10 Sv south of Australia (Rintoul et al. 2001). The volume transport of the ACC produced by the model is about 90.58 Sv with the maximum from April to October and the minimum from November to March.

Figure 5.34 shows that the Java, Lombok and Flores Straits almost have the same phase of throughflow variability. The maximum of the transport occurs in July and August which is a 2 months lag in comparison with the Ombai Strait and the Timor Strait. The discrepancy in phase of the volume transport between the sections could be explained as the Indonesian Seas are fed from the difference sources at different time in the year which is associated with the large-scale and local forcing of the wind fields, and the geometry of the region.

Table 5.7: The monthly-mean variation of the volume transport at the sections (Sv).

	ACC	SCS	Makassar	Java	Lombok	Flores	Ombai	Timor
January	75.27	-10.36	-3.00	-1.11	-2.66	-0.39	-5.99	-3.15
February	80.16	-8.03	-5.20	-1.11	-3.05	-0.73	-5.99	-3.83
March	86.58	-5.29	-7.76	-1.10	-3.08	-1.21	-5.82	-4.18
April	91.79	-2.18	-9.29	-1.09	-2.41	-1.34	-6.98	-5.12
May	95.90	-0.80	-9.68	-0.93	-1.98	-1.44	-8.36	-6.16
June	100.39	-0.55	-10.32	-1.19	-3.52	-1.95	-7.38	-6.00
July	103.39	-0.82	-10.92	-1.54	-4.39	-2.35	-6.33	-5.68
August	103.54	-1.85	-10.37	-1.68	-4.38	-2.29	-5.48	-4.85
September	100.55	-3.67	-8.80	-1.44	-4.05	-2.04	-5.10	-4.24
October	91.93	-5.70	-6.36	-1.00	-3.27	-1.43	-5.45	-3.85
November	81.86	-8.32	-3.42	-0.70	-2.73	-0.79	-5.52	-2.91
December	75.63	-10.52	-2.04	-0.89	-2.63	-0.44	-5.65	-2.65
Mean value	***90.58***	***-4.84***	***-7.26***	***-1.15***	***-3.18***	***-1.37***	***-6.17***	***-4.39***

Note: The negative values show transport to the Indian Ocean, the positive values show the transport to the Pacific Ocean.

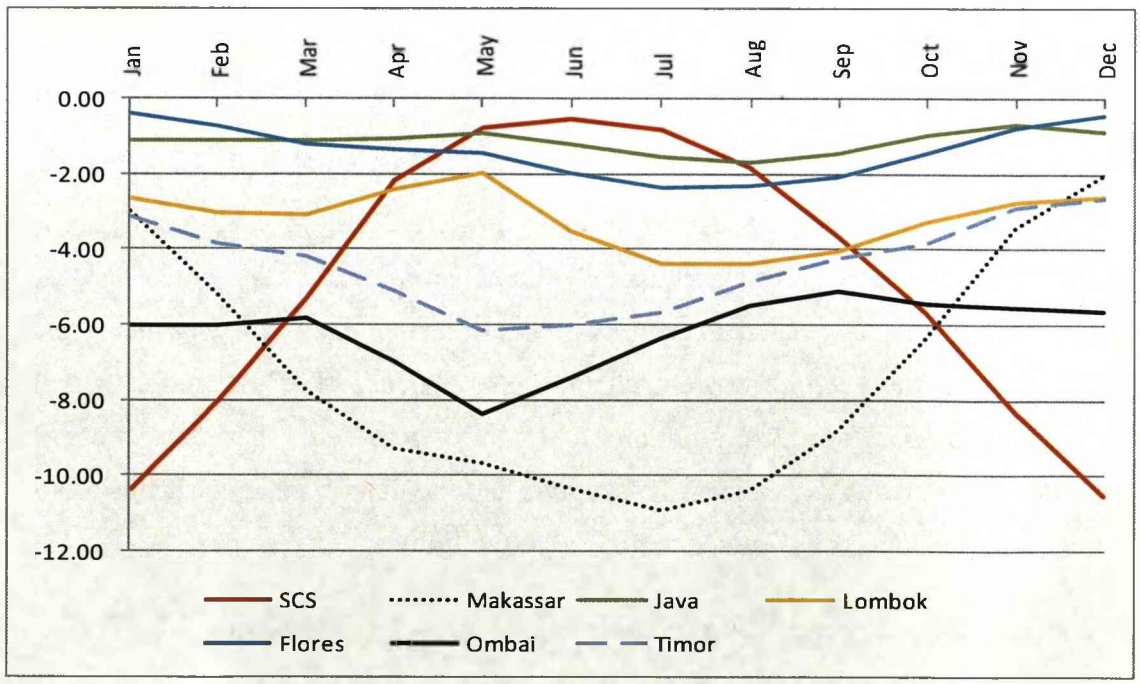

Figure 5.34: The seasonal variability of the ITF at the main passages in the Indonesian Seas.

5.4. Spin-down experiments (Case 5.8, 5.9)

Two spin-down experiments were carried out in order to examine the role of the hydrographical fields (the temperature and salinity) on the volume transport of the throughflow between the oceans. These two experiments were based on Case 5.7 experiment. They are hereafter referred to as Case 5.8 or spin-down 1 (No wind, no relaxation at all), and Case 5.9 or spin-down 2 (No wind, the deep ocean relaxed, no surface relaxation). The model experiments were run for 20 years, starting from rest. The total kinetic energy and volume transport through the Indonesian Seas were calculated and plotted as shown in Figures 5.35 & 5.36 (Case 5.8), Figures 5.37 & 5.38 (Case 5.9).

Case 5.8: The model run settled down rather quick with the total kinetic energy does not changing much after approximately 10 years (Figure 5.35). With no relaxation and no wind stress applied, meaning no driving force, there was a gradual decrease of the volume transport from Pacific to Indian Ocean from about 22 Sv initially to near zero in year 12 (Figure 5.36). This experiment showed that the setting with the initial density fields to climatology (the salinity and temperature fields derived from the Levitus Atlas, 1998 (NODC_WOA98)) created a pressure gradient between the oceans which drives water from the Pacific to Indian Ocean.

Case 5.9: In this case the total kinetic energy shows that the model settled down faster than Case 5.8, just after approximately 2 years compared to 10 years in Case 5.8 (Figure 5.37). This might be explained as that in this case, the deep ocean is already relaxed and therefore the adjustment mainly happens in the mixed layer. With the deep ocean relaxed the volume transport from Pacific to Indian Ocean decreased from 22 Sv initially to 15 Sv in year 2 and then remained stable around this value (Figure 5.38). This shows that the deep ocean contributes a large amount to the total volume transport of the throughflow.

These two experiments have proved that the stratification of the salinity and temperature in the Pacific and Indian Oceans can produce a strong Indonesian Throughflow (ITF).

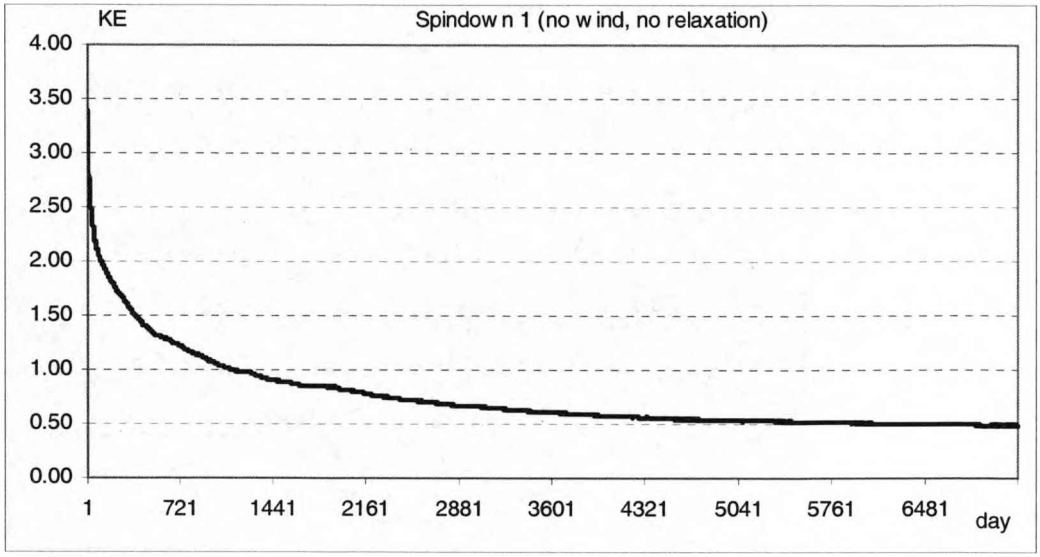

Figure 5.35: The KE of the spin-down 1 scenario (no wind, no relaxation). The model was run from rest to 20 years.

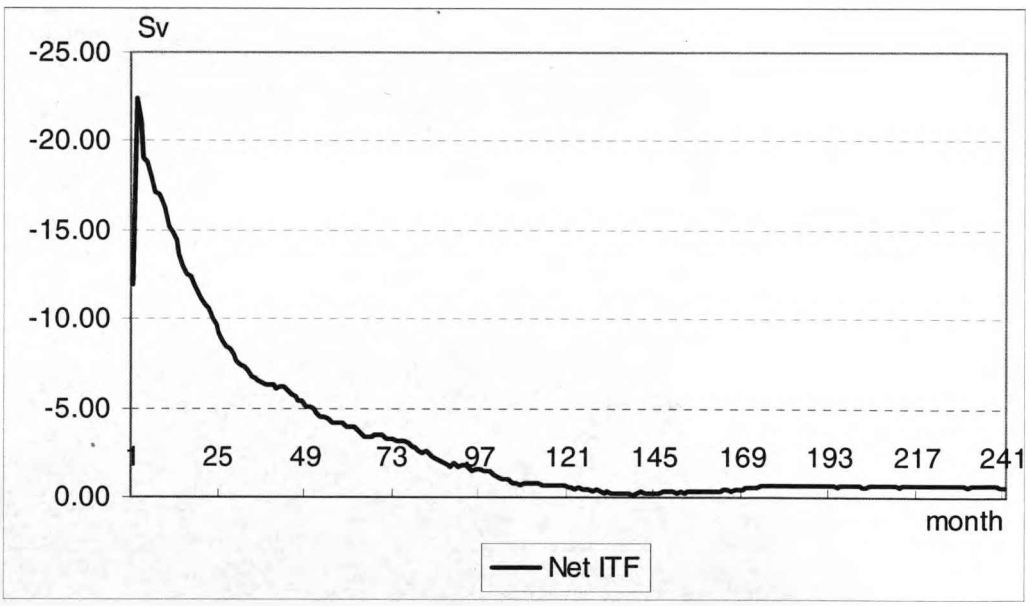

Figure 5.36: The ITF of the spin-down 1 scenario (no wind, no relaxation). The model was run from rest to 20 years.

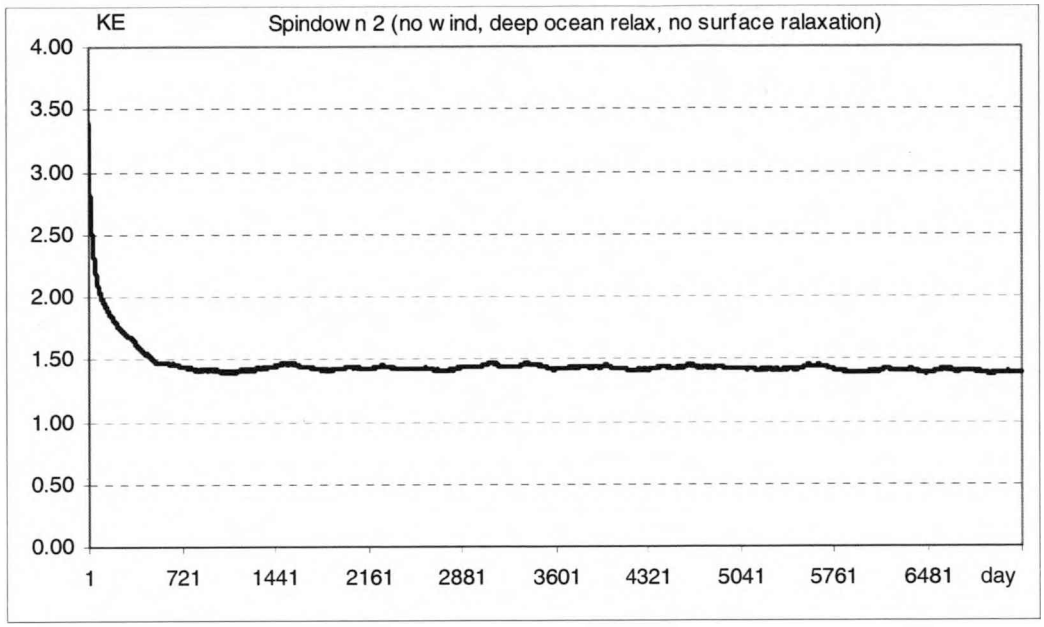

Figure 5.37: The KE of the spin-down 2 scenario. The model was run from rest to 20 years (no wind, deep ocean relax, no surface relaxation).

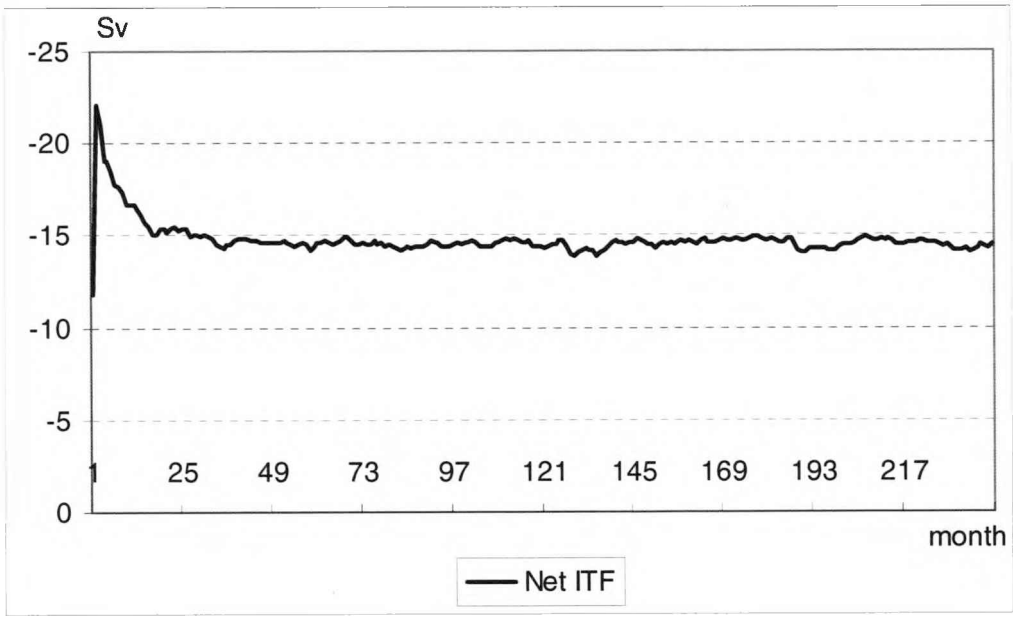

Figure 5.38: The ITF of the spin-down 2 scenario. The model was run from rest to 20 years (no wind, deep ocean relax, no surface relaxation).

5.5. The density driven flow and the ITF (Case 5.10)

Throughout the experiments, it is shown that the ITF transport generated by the wind forcing is rather small compared to recent observational and numerical studies. Therefore an experiment, referred to as Case 5.10, with no wind forcing has been

carried out to examine the ITF under thermal forcing conditions alone (the wind stress is switched off but the monthly-mean temperature and salinity fields derived from Levitus Atlas, 1998 are still applied and relaxed as in Case 5.7).

The annual-mean barotropic flow and the mixed layer flow which are driven by thermal forcing alone are shown in the Figure 5.39 and Figure 5.40 respectively. The annual-mean barotropic flow shows a strong current in the southern part of the SCS flowing into the Java Sea. This current joins with southwards flow in the Makassar Strait before exiting to the Indian Ocean (Figure 5.39) via Lombok Strait. The mixed layer throughflow is characterised by an intense and rather strong current (40-50 cm/s) from the Pacific Ocean to the Celebes Sea and flowing southwards through the Makassar Strait to join with the current from the SCS. This throughflow partially exits to the Indian Ocean through the Lombok Strait, the remainder enters the Flores Sea (exit to the Indian Ocean through the Flores Strait) and southern Banda Sea (exit to the Savu Sea through the Ombai Strait) and eventually flows out of the Indonesian Seas through the Timor Sea to form the westwards zonal jet in the Indian Ocean at latitudes 10°S-13°S (Figure 5.40).

The model results show a small seasonal variability of the volume transport; with the magnitude of the annual-mean volume transport of about 15.06 Sv. The annual-mean transport at the main passages is almost similar to Case 5.7 (Table 5.8). This result suggests that the wind forcing does not significantly change the volume transport but influences its variability. It also shows that the density gradient between the oceans is sufficient to control the surface flow. The results suggest that both wind and density forcing need to be taken into account to correctly simulate the ITF and its seasonal variation.

Table 5.8: The annual-mean volume transport at the main passages produced by the thermal forcing alone.

ACC	SCS	Makassar	Java	Lombok	Flores	Ombai	Timor	The ITF
54.64	-3.47	-7.62	-1.12	-3.20	-1.48	-5.66	-3.60	-15.06

Note: The ITF transport is the summation of the volume transport from the Java, Lombok, Flores, Ombai and Timor sections. Negative values show transport to the Indian Ocean.

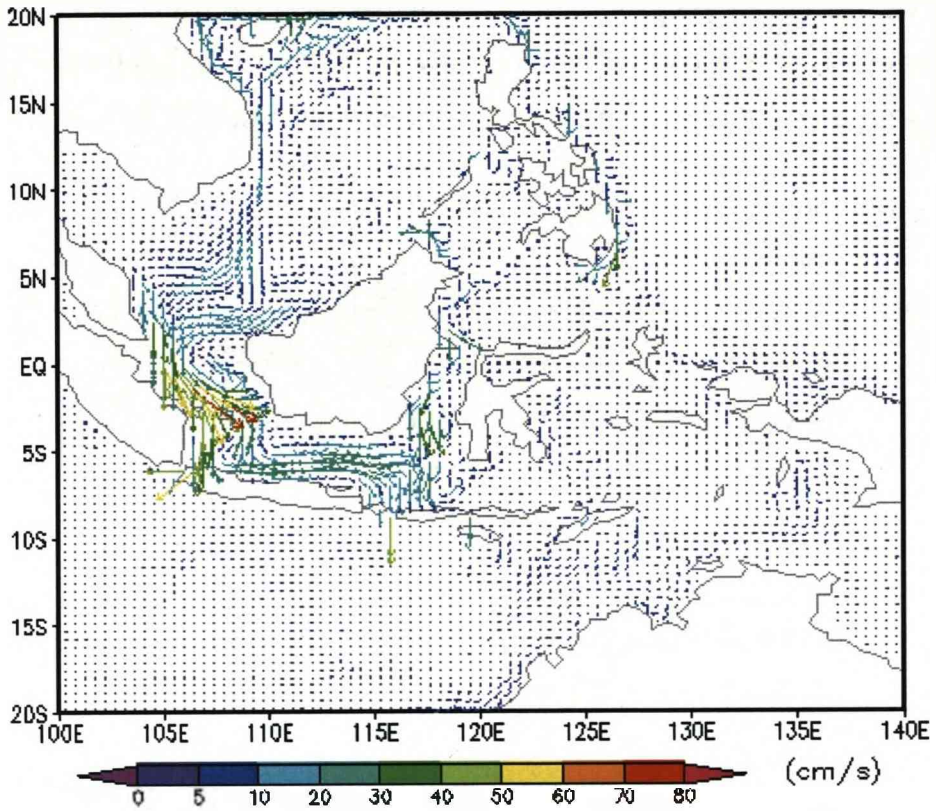

Figure 5.39: The annual-mean barotropic circulation in the Southeast Asia region (no wind forcing).

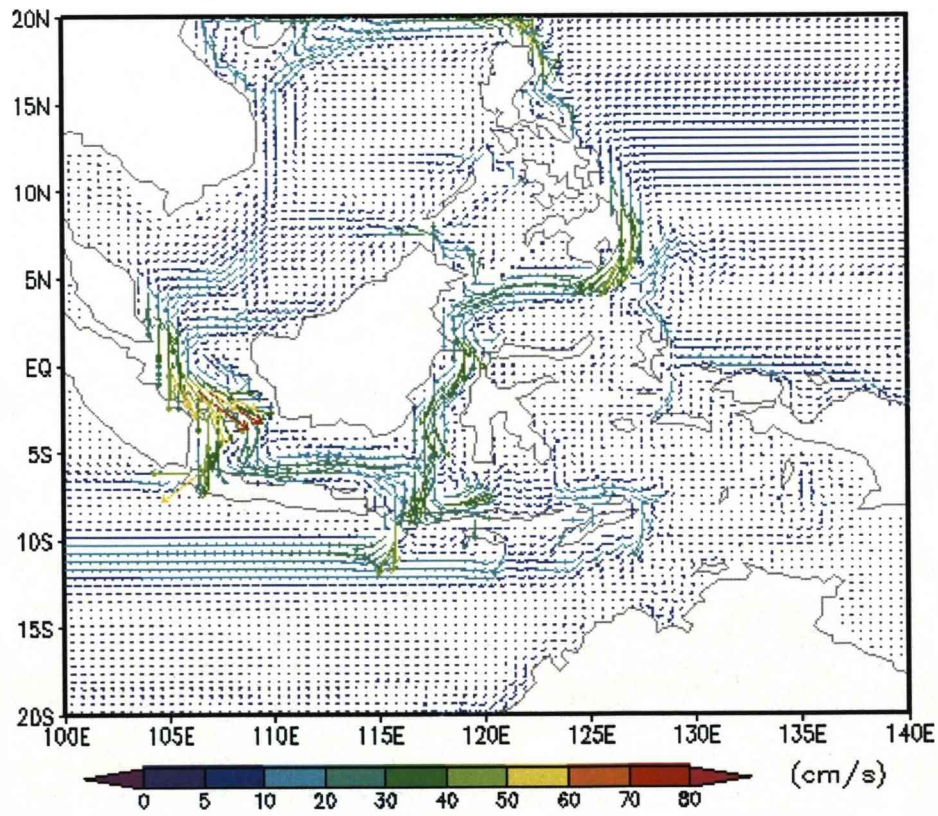

Figure 5.40: The annual-mean circulation of the mixed layer in the Southeast Asia region (no wind forcing).

5.6. Summary

Despite the model experiments with idealised topography and wind forcing in the previous Chapter showing that the idealised wind forcing can produce a rather high volume transport between the basins, the experiments with the realistic wind forcing and topography have pointed out that the wind forcing alone over the ocean surface can produce a rather high seasonal variation of the volume transport between the oceans but it only produces a rather small ITF transport compared to recent observational and numerical studies.

The experiment with both thermal and wind forcing gives a total annual-mean volume transport from the Pacific Ocean to the Indian Ocean of about 16.25 Sv, and shows a strong seasonal variation with the minimum transport of about 12.26 Sv in December, and the maximum transport of about 20.28 Sv in July. The Makassar Strait contributes approximately 50% of the total ITF transport and the SCS plays a significant role in the variability of the ITF. The model result shows that during certain periods of the year, the ITF source is only from the northern hemisphere and at other time it is from both northern and southern hemispheres. In the vertical, most of the volume transport of the throughflow appears in the upper layer with the first two upper layers contributing a total of over 10 Sv (62%). The deep layers also contribute a significant amount (over 6 Sv) to the volume transport of the throughflow. The model result is in very good agreement with the observations and other numerical studies.

The spin-down experiments have proved that the stratification of the salinity and temperature in the Pacific and Indian Oceans can produce a strong Indonesian Throughflow (ITF). The experiment with the thermal forcing only (no wind forcing) showing that the density gradient between the oceans is sufficient to control the throughflow, especially in the upper layer.

The model has also successfully reproduced ocean circulation features such as the well-known Kuroshio, equatorial current system in the Pacific Ocean, and the Somali, the Agulhas, the equatorial current system and westwards zonal jet and especially the intense surface eastwards equatorial jet in the transition period in the

Indian Ocean. The western boundary current in the Pacific Ocean, the circulation in the SCS and the Indonesian Seas seem related to large-scale forcing over the Pacific Ocean, and the geometry of the region.

Throughout the model experiments, the main driving forces of the ITF are the wind stress and the thermal forcing. The wind stress over the ocean surface produced a relatively small amount of the ITF transport compared to the observation and other numerical studies but it is responsible for the seasonal variability of the ITF. Therefore both the wind and thermal forcing need to be taken into account to correctly simulate the ITF and its seasonal variation.

The model limitations are that there were no sea-air interactions, no heat exchanges between sea and atmosphere. The eastern boundary did not cover the whole Pacific Ocean therefore could not fully reproduce large-scale processes in the Pacific Ocean.

Chapter 6

THE ITF RESPONSE TO EXTREME CLIMATIC CONDITIONS

6.1. Introduction

The early theoretical work of Wyrtki (1987) and Clarke and Liu (1994) hinted at a relationship between the ITF and ENSO. They suggested that the volume transport of the ITF would be reduced (enhanced) during El Niño (La Niña) events. The hypothesis was based on the change in the Pacific trade winds during ENSO events and the associated responses of the sea level of the western Pacific and eastern Indian Ocean. Other work (Meyer, 1996) showed that the depth integrated transport between Australia and Java, computed from observational data (temperature and salinity data) was enhanced during the La Niña event of 1988/1989 and reduced during the El Niño of the early 1990s.

However in more recent studies (England and Huang, 2005; Sprintall et al, 2004) a major part of the inter-annual variation in ITF appears to be independent of ENSO, and there are several years in which the ITF transport does not appear to match ENSO variation. Potemra and Schneider (2007) suggested that the discrepancy between ENSO and the ITF variability may be explained by the observed estimates being based on a geostrophic calculation while the actual flow maybe ageostrophic; the calculation relies on a level of no motion that may not be accurate; the inter-annual forcing may act differently on different vertical layers of the ITF; and it may be the case that inter-annual variations of the ITF are caused by something other than, or in combination with, ENSO.

Since the beginning of the 20th century, the average global surface temperature has increased (Wainwright et al., 2008). The IPCC predicts global temperature change of 1.4 - 5.8K due to global warming from 1990-2100 (IPCC, 2001). It is therefore of

interest to examine the change of the ITF transport under the conditions of global warming.

In this Chapter, model experiments are reported which were carried out to examine the long term change of the ITF transport, the ITF transport in ENSO events, and ITF transport under the idealised global warming conditions. Based on the model result the correlation analysis was also implemented to determine the strength of the relationship between the ITF transport and ENSO.

6.2. Interannual variability of the ITF

6.2.1. Model setup

In order to examine the interannual variability of the volume transport of the ITF, it needs to be run over several years to allow significant fluctuation from the mean values. Therefore the model was run for 20 years, restarting from the previous 20-year model run in the previous chapter (Case 5.7). The model was forced by the monthly-mean time series (from 1982 to 2001) of the wind stress, temperature and salinity derived from the MIT-ECCO-GODAE dataset. This data set is a contribution of the Consortium for Estimating the Circulation and Climate of the Ocean (ECCO) funded by the National Oceanographic Partnership Program. The volume transport of the ITF was calculated at the same sections as in Case 5.7. This model experiment is hereafter referred to as Case 6.1.

6.2.2. Model result

The ITF transport produced by the MIT-ECCO-GODAE dataset appears to match with the ITF transport produced by the Levitus Atlas, 1998 dataset in Case 5.7, with the annual-mean volume transport of about 16.06 Sv (Table 6.1). The ITF transport produced by the monthly-mean time series (from 1982 to 2001) of the wind stress, temperature and salinity fields of the MIT-ECCO-GODAE dataset is almost the same the ITF transport produced by the monthly-mean fields of the Levitus Atlas, 1998 suggesting that these two datasets are in good agreement, and the monthly-mean data of the Levitus Atlas, 1998 can be used to simulate the ITF transport.

The result in Table 6.1 shows that, in the vertical, the total volume transport of the ITF mainly occurs in the upper layer with the first two layers contributing of about 10.02 Sv, accounting for more than 62 % of the total mean ITF transport. The deep layers at the Ombai Strait and Timor Strait also contribute a rather large amount to the total volume transport (6.15 Sv – 38%), suggesting that the deep layers play an important role in the volume transport between the Pacific and Indian oceans through the Indonesian seas. This result is in good agreement with the result of Cases 5.7 & 5.9.

In terms of inter-annual variability we can see from Figure 6.1 and the corresponding El Niños, La Niñas from 1982-2001 in Table 6.2 that there is a clear link between ENSO events and the time series of the annual-mean transport of ITF where the annual-mean volume transport of the ITF reduced in the El Niños and enhanced in the La Niñas. Figure 6.1 also shows that the annual-mean volume transport of the ITF showing an increasing trend from 1982 to 2001, however this is more likely a model drift rather than a realistic increase of the ITF transport. In order to clarify whether it is a realistic increasing trend of the ITF transport or just a model drift, the model run with a variety of different start dates could be the solution.

Table 6.1: The annual-mean volume transport of the ITF at the sections, and at the different layers (Sv).

	ACC	**SCS**	**Makassar**	**Java**	**Lomb**	**Flores**	**Ombai**	**Timor**	**ITF**
Mixed layer	32.84	-4.02	-1.69	-0.88	-1.40	-0.64	-0.68	-1.92	-5.51
layer 5	0.00	-0.87	-3.03	-0.10	-1.62	-0.68	-0.89	-1.22	-4.51
layer 4	-2.02	0.00	-2.42	0.00	0.00	0.00	-2.25	-1.30	-3.55
layer 3	25.78	0.00	0.04	0.00	0.00	0.00	-2.25	-0.35	-2.60
layer 2	10.59	0.00	0.00	0.00	0.00	0.00	-0.01	0.01	0.00
Bottom	20.70	0.00	0.09	0.00	0.00	0.00	0.00	0.11	0.11
Sum	***87.89***	***-4.89***	***-7.01***	***-0.98***	***-3.02***	***-1.32***	***-6.08***	***-4.67***	***-16.06***

Note: The volume transport of the ITF (last column) is the summation of the Java, Lombok, Flores, Ombai, and Timor sections only.

Table 6.2: Cold and warm ENSO episodes by season.
(http://www.cpc.noaa.gov/products/analysis_monitoring/ensostuff/ensoyears.ERSST.v2.shtml)

Year	JAN	FEB	MAR	APR	MAY	JUN	JUL	AUG	SEP	OCT	NOV	DEC
1982	0.0	0.1	0.2	0.4	0.6	0.7	0.8	1.0	1.5	1.9	2.2	2.3
1983	2.3	2.0	1.6	1.2	1.0	0.6	0.2	-0.2	-0.5	-0.8	-0.9	-0.8
1984	-0.5	-0.3	-0.2	-0.4	-0.5	-0.5	-0.3	-0.2	-0.3	-0.6	-1.0	-1.1
1985	-1.0	-0.8	-0.8	-0.8	-0.7	-0.5	-0.4	-0.4	-0.4	-0.3	-0.2	-0.3
1986	-0.4	-0.4	-0.3	-0.2	-0.1	0.0	0.2	0.5	0.7	0.9	1.1	1.2
1987	1.3	1.2	1.1	1.0	1.0	1.2	1.5	1.6	1.6	1.5	1.3	1.1
1988	0.8	0.5	0.1	-0.3	-0.8	-1.2	-1.2	-1.1	-1.3	-1.6	-1.9	-1.9
1989	-1.7	-1.5	-1.1	-0.9	-0.6	-0.4	-0.3	-0.3	-0.3	-0.3	-0.2	-0.1
1990	0.1	0.2	0.3	0.3	0.3	0.3	0.3	0.4	0.3	0.3	0.3	0.4
1991	0.5	0.4	0.4	0.4	0.6	0.8	0.9	0.9	0.8	1.0	1.4	1.7
1992	1.8	1.7	1.6	1.4	1.1	0.8	0.4	0.2	-0.1	-0.1	0.0	0.1
1993	0.3	0.4	0.6	0.8	0.8	0.7	0.5	0.4	0.4	0.3	0.2	0.2
1994	0.2	0.3	0.4	0.5	0.6	0.6	0.6	0.6	0.7	0.9	1.2	1.3
1995	1.2	0.9	0.7	0.4	0.2	0.1	0.0	-0.3	-0.5	-0.6	-0.7	-0.8
1996	-0.8	-0.7	-0.5	-0.3	-0.2	-0.2	-0.1	-0.2	-0.2	-0.2	-0.3	-0.4
1997	-0.4	-0.3	0.0	0.4	0.9	1.4	1.7	2.0	2.3	2.4	2.5	2.5
1998	2.4	2.0	1.4	1.1	0.4	-0.1	-0.8	-1.0	-1.1	-1.1	-1.3	-1.5
1999	-1.6	-1.2	-0.9	-0.7	-0.8	-0.8	-0.9	-0.9	-1.0	-1.2	-1.4	-1.6
2000	-1.6	-1.5	-1.1	-0.9	-0.7	-0.6	-0.4	-0.3	-0.4	-0.5	-0.7	-0.7
2001	-0.7	-0.5	-0.4	-0.2	-0.1	0.1	0.2	0.1	0.0	-0.1	-0.2	-0.2
2002	-0.1	0.1	0.3	0.4	0.7	0.8	0.9	0.9	1.1	1.3	1.5	1.3
2003	1.1	0.8	0.6	0.1	-0.1	0.0	0.3	0.4	0.5	0.5	0.6	0.5
2004	0.4	0.2	0.2	0.2	0.3	0.4	0.7	0.8	0.9	0.9	0.9	0.8
2005	0.6	0.5	0.3	0.4	0.5	0.3	0.2	0.0	0.0	-0.2	-0.4	-0.7
2006	-0.8	-0.7	-0.4	-0.2	0.0	0.1	0.3	0.4	0.7	0.9	1.1	1.1
2007	0.8	0.3	0.1	-0.1								

Note: (Warm (red) and cold (blue) episodes based on a threshold of +/- 0.5°C for the Oceanic Niño Index (ONI) [3 month running mean of ERSST.v2 SST anomalies in the Niño 3.4 region (5°N-5°S, 120°-170°W)], based on the 1971-2000 base period. For historical purposes cold and warm episodes (blue and red numbers) are defined when the threshold is met for a minimum of 5 consecutive over-lapping seasons).

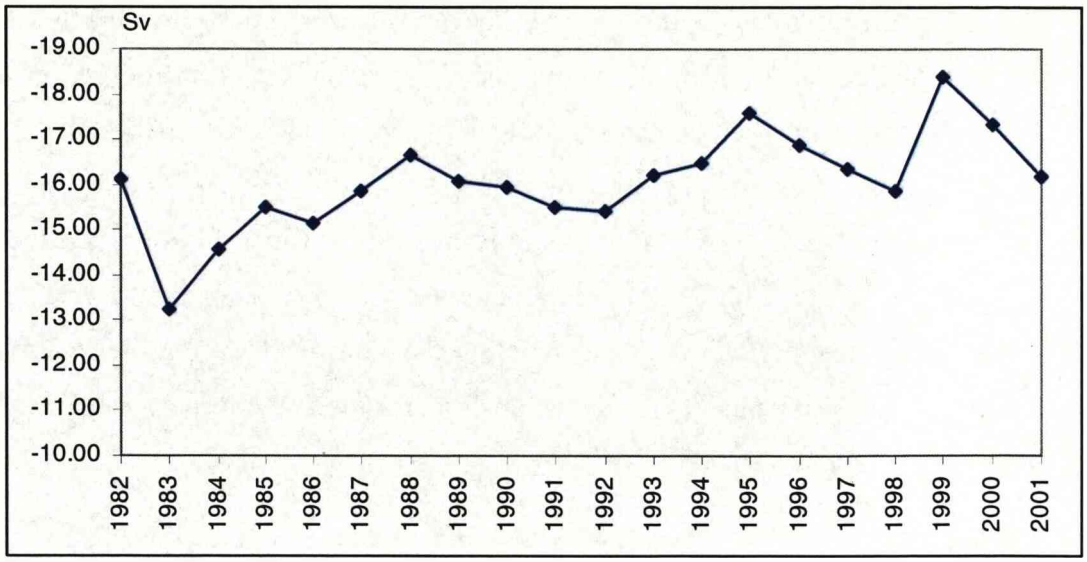

Figure 6.1: The inter-annual variability of the total volume transport of the ITF from 1982-2001. The model was forced by monthly-mean time-series of MIT-ECCO-GODAE data set.

In order to determine the strength of the relationship between the ITF and ENSO using the output from the numerical models, the MICOM model and the OCCAM 1/12 degree global ocean model (the volume transport of the ITF of the OCCAM model was provided by David Stevens, University of East Anglia, *personal communication*), and the ONI index. The most widely used correlation coefficient (Pearson's correlation coefficient - r) has been calculated. The formula for calculating Pearson's correlation coefficient is as following:

$$r = \frac{\sum\left[\left(x-\bar{x}\right)\left(y-\bar{y}\right)\right]}{\sqrt{\sum\left(x-\bar{x}\right)^2 \sum\left(y-\bar{y}\right)^2}}$$

where x, y are the samples.

To test the significance of the relationship, the statistic t was calculated using the formula:

$$t = r\sqrt{\frac{n-2}{1-r^2}}$$

where r is Pearson's correlation coefficient, and n is the number of samples. The t statistic then will be used with a t-table (two-tailed test) to find out the confidence level of the relationship.

Due to the difference in time periods between the model outputs (the MICOM model from the period of 1982-2001, and the OCCAM model from the period of 1989-2001), the correlation analysis were mainly carried out for the period of 1989-2001. The analysis for the whole period of 1982-2001 was the analysis for the MICOM model result which will be used to examine the relationship between the annual-mean of the ITF with ENSO events, and relationship between the mean ITF transport and the strong ENSO events only (ENSO events which have the ONI indexes higher than 1.0). The results of correlation analysis for the ITF transport and the ONI index are shown in Tables 6.3, 6.4 and 6.5.

The time-series of the monthly-mean volume transport of the ITF (Figure 6.2) shows a strong seasonal variability of the ITF transport. However as showed in Tables 6.3 & 6.4, in terms of the monthly-mean scale, based on the calculation of 156 samples (156 months) both outcome of the MICOM and OCCAM models show a very weak relationship between the ITF transport and ENSO with the correlation coefficients of about 0.11 (80% of confidence level) and 0.27 (99% of confidence level) respectively. In terms of the annual-mean scale there only 13 samples (13 years, 1989-2001) which were used for the correlation analysis. The result shows that there was a rather strong relationship between the annual-mean of ITF transport and ENSO. The correlation coefficient between the MICOM model outcome and the ONI index is 0.63 with the confidence level of 0.025 (97.5 % of confidence), and the OCCAM model outcome is about 0.89 and the confidence level of 0.01 (99% of confidence) (Tables 6.3 & 6.4, Figure 6.3). The analysis for the period of 1982-2001 with the outcome of the MICOM model (Table 6.5) shows a weaker relationship with the correlation coefficient of about 0.35 (80% of confidence level) which is similar to the result of England and Huang (2005).

Further correlation analysis between the ITF transport of the MICOM model and the ONI index in the strong ENSO events shows a very high correlation, if the annual mean value of the ONI index higher than 1.0 (6 strongest ENSO events from 1982-2001) then the correlation coefficient is about 0.89 with 97.5% of confidence (Table 6.5, Figure 6.4). The result of correlation analysis for the OCCAM model result for the period of 1989-2001 (5 ENSO events) also shows a strong relationship between the ITF and the ENSO events with the correlation coefficient of 0.89 with the significance level of about 0.05 (95% of confidence) (Table 6.4).

With the rather high correlation coefficients of the both numerical models, we can say in confidence that, in terms of annual-mean scale there was a strong relationship between ITF and ENSO during the period 1989-2001. The reason why the OCCAM model output shows stronger relationship between ITF and ENSO can be explained by the OCCAM 1/12° being a global ocean model with very high resolution, therefore it can capture fully the large scale effects of the ENSO on the ITF. Meanwhile the MICOM model, due to some constrains with computer resources, was configured to run mainly for the Southeast Asia region (a regional model).

Table 6.3: Correlation coefficient between ITF (MICOM model 0.5°) and ONI index (Data series: 1/1989-12/2001).

	N	Correlation coefficient (r)	t	Confidence level (p)
Monthly mean ITF	156	0.11	1.41	0.2 (80 %)
Annual mean ITF	13	0.63	2.72	0.025 (97.5%)

Table 6.4: Correlation coefficient between ITF (OCCAM model 1/12°) and ONI index (Data series: 1/1989-12/2001).

	N	Correlation coefficient (r)	t	Confidence level (p)
Monthly mean ITF	156	0.27	3.42	0.01 (99%)
Annual mean ITF	13	0.85	5.42	0.01 (99%)
ENSO events (1989-2001)	5	0.89	3.46	0.05 (95%)

Note: The ENSO events from 1989 to 2001 were the El Niño (1991-1992), El Niño (1994-1995), La Niña (1995-1996), El Niño (1997-1998), and La Niña (1998-2000).

Table 6.5: Correlation coefficient between ITF (MICOM model 0.5°) and ONI index (Data series: 1/1982-12/2001).

	N	Correlation coefficient (r)	t	Confidence level (p)
Annual mean ITF for the whole 1982-2001 period	20	0.35	1.58	0.2 (80%)
Strong ENSO events (ONI index higher than 1.0)	6	0.89	3.96	0.025 (97.5%)

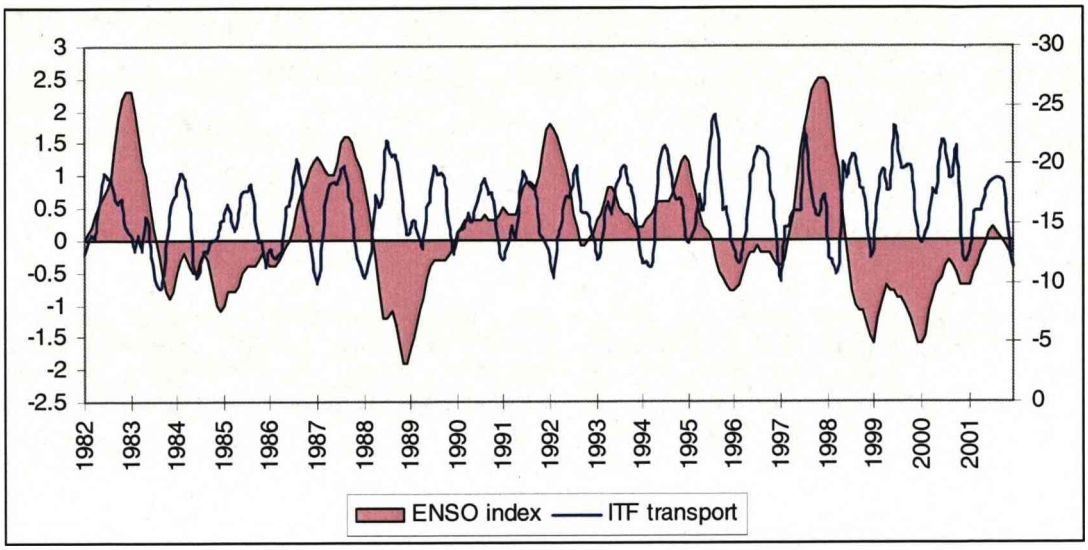

Figure 6.2: The monthly-mean volume transport of the ITF and the ENSO index (1982-2001).

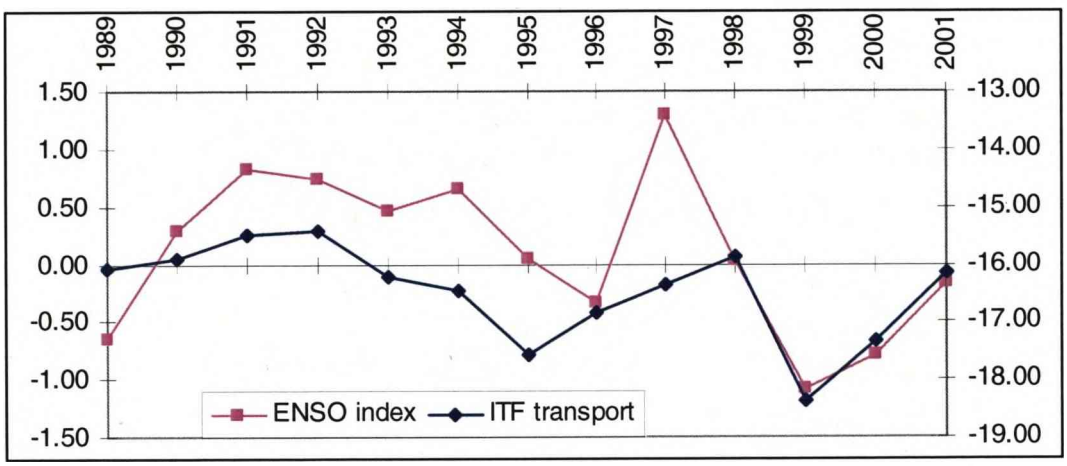

Figure 6.3: The annual mean volume transport of the ITF and the ENSO index (1987-2001).

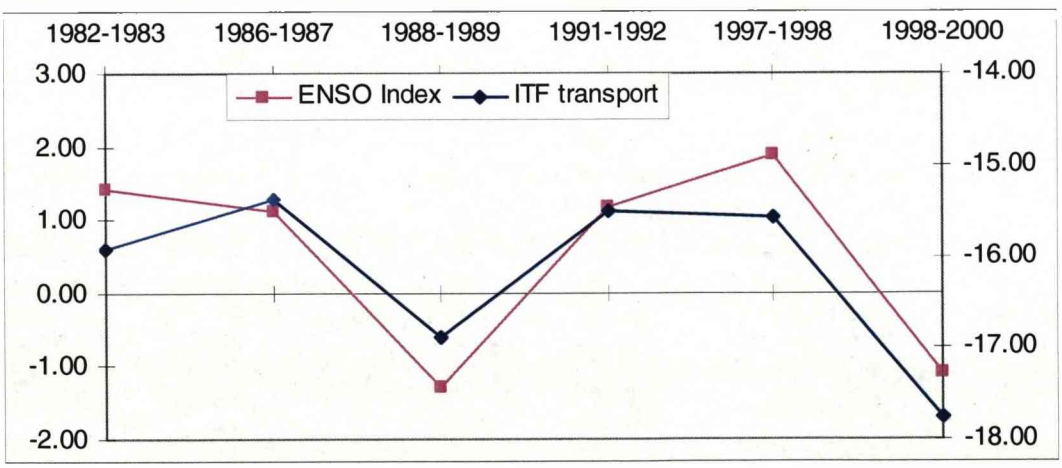

Figure 6.4: The volume transport of the ITF and the 6 strongest ENSO events (the index is higher than 1.0.

6.3. The ITF in the strongest ENSO events

6.3.1. Model setup

The ENSO events which have been chosen to examine the volume transport of the ITF are the four strongest ENSO events during the period of 1982-2007, including El Niños 1982-1983 & 1997-1998, and La Niñas 1988-1989 & 1998-2000. They are hereafter referred to as El Niño 1982, El Niño 1997, La Niña 1988 and La Niña 1999 respectively. These ENSO events have been chosen based on the *Oceanic Niño Index (ONI)*, ERSST Version 2 which was produced by NOAA/National Weather Service, National Center for Environmental Prediction, Climate Prediction Center (Table 6.2 and Figure 6.5).

The result of the experiments in Chapter 5 (Cases 5.7 & 5.9) and Case 6.1 (this chapter) shows that despite the deep layer contributing a rather large amount of the volume transport between the oceans, most of the volume transport of the ITF appears in the upper ocean. Therefore when setting up the present model experiment, the temperature and salinity of the deep layer was still the climatological Levitus Atlas, 1998 data as in Case 5.7 but the wind stress and the temperature and salinity fields of the mixed layer are replaced by the monthly-mean data derived from the MIT-ECCO-GODAE dataset.

The model was run for 5 years, restarting from the 20^{th} year of the model run of Case 5.7, and forced repeatedly by an annual cycle of the monthly-mean wind stress and the temperature and salinity fields. For the El Niño event 1982-1983, the ONI index showing that the El Niño event extended from May 1982 to June 1983 (the index is higher than 0.5) therefore, in order to create one year of input data which covered the ENSO event but also started from January for the model run, we have used the data of the early months of the year 1983 (from January to May) to replace the data of those months of the year 1982. This method was applied to the other events with the corresponding adjustment to the starting months of the ENSO events.

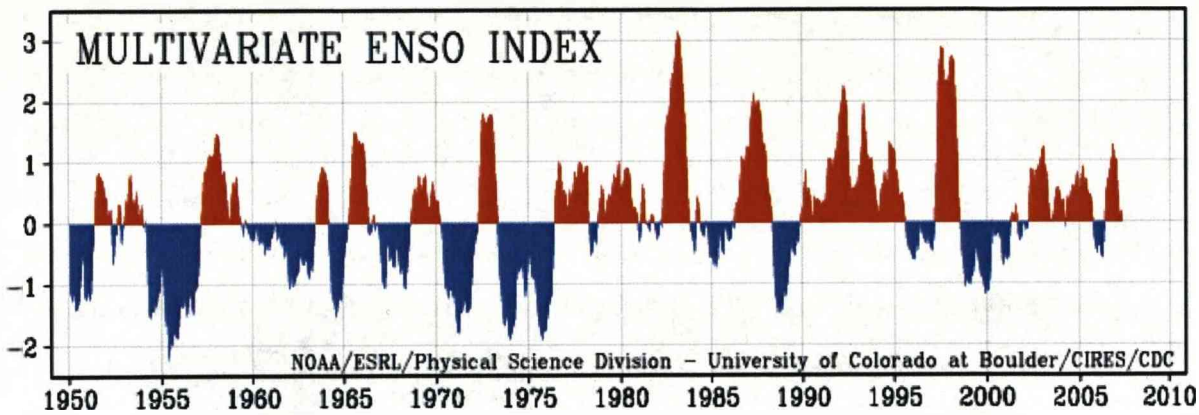

Figure 6.5: The illustration of the ENSO events. (http://www.cdc.noaa.gov/people/klaus.wolter/MEI/mei.html).

6.3.2. Model result

In an El Niño event the surface temperature of the western Pacific Ocean decreases (suggesting a reduced ITF as the hypothesis of Wyrtki, 1987), and in a La Niña event the surface temperature increases (suggesting an enhanced ITF). The model experiment results showing that the variability of the ITF transport (Figures 6.6 and 6.7) is almost identical during the 5 model years, suggesting that the model responds very well to the change of the driving forces. In the case of the El Niño 1982-1983, even though the annual mean value of the total volume transport of the ITF is higher than that in Case 5.7, the ITF transport has rather small amplitude of seasonal variability compared to Case 5.7 and the El Niño event 1997. In the La Niña condition the total volume transport of the ITF is shifted with both the maximum (minimum) values are higher than the maximum (minimum) of Case 5.7.

In the El Niño events, the ITF volume transport shows a complicated variability compared to the La Niña events. During the El Niño event 1997, the volume transport shows two maxima (January and June) and two minima (May and December). In El Niño 1982, the volume transport shows a more complicated variation with a fluctuation between months; there is one maximum of volume transport in July and two minima of volume transport in March and November. In the La Niña events, the ITF transport variability is rather smooth and matches with the ITF transport in Case 5.7. However the phase of the maximum values of the transport has shifted. The maximum transport in the case of the La Niña event 1988 occurs one month earlier (June), and it is two months earlier in the La Niña 1999 (May).

The model results of the four strongest ENSO events show that in all cases there is enhancement of the ITF transport compared to the volume transport in Case 5.7 (considered to as the normal condition). Among the four ENSO events, the total volume transport of the ITF in the case of the La Niña event 1999 is highest (Table 6.6 and Figure 6.8). All four most extreme cases have bigger ITF transport than the long-term mean (16.06 Sv, Case 6.1) plus confidence limits (0.49) and so are significantly outside the usual interannual variability. The enhancement of the total volume transport of the ITF in the El Niño events disagrees with the hypothesis of Wyrtki (1987), Clarke and Liu (1994), and the observation of Mayer (1996). However as suggested by Potemra and Schneider (2007) the enhancement of the total ITF transport in the El Niño events could be explained as wind patterns that do not adhere to the typical ENSO conditions, or it could be that flow in the deep layer is playing the role. Based on our model experiments the later one is likely the case as we can see from Cases 5.7, 5.9, and 6.1 the deep layers contributes a large amount to the total volume transport between the oceans.

Table 6.6: The annual mean volume transport of the ITF in the typical ENSO events (Sv) at different layers.

	El Niño 1982	***La Niña 1988***	***El Niño 1997***	***La Niña 1999***	***ITF (Case 5.7)***
Mixed-layer	-6.41	-5.74	-6.79	-6.68	-5.69
Layer 5	-4.58	-4.77	-5.35	-5.01	-4.45
Layer 4	-3.36	-3.84	-2.99	-3.57	-3.61
Layer 3	-2.57	-2.70	-2.05	-2.41	-2.61
Layer 2	0.00	0.00	0.00	0.00	0.00
Bottom Layer	0.11	0.10	0.11	0.11	0.10
Total transport	***-16.80***	***-16.94***	***-17.07***	***-17.56***	***-16.26***

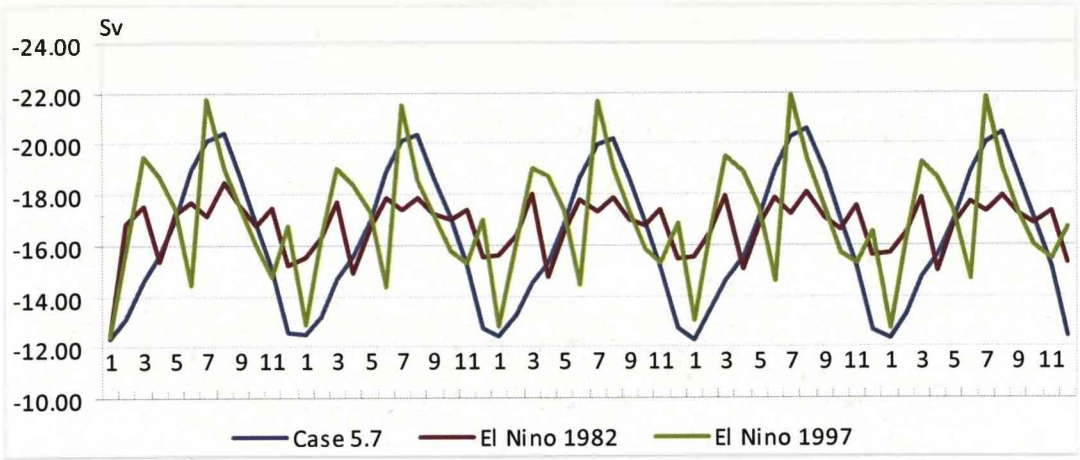

Figure 6.6: Comparison between the volume transport of the ITF in the El Niño events conditions and volume transport produced by the monthly mean (Sv).

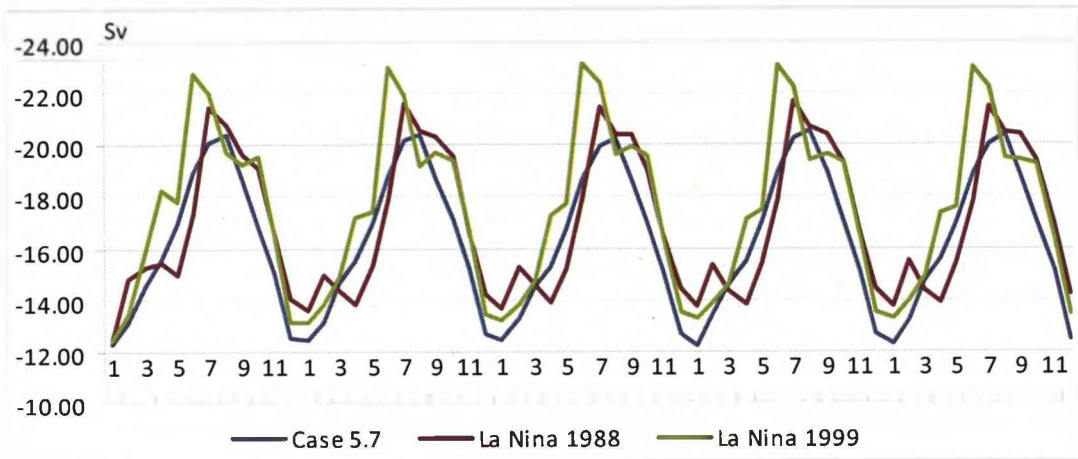

Figure 6.7: Comparison between the volume transport of the ITF in the La Niña events conditions and volume transport produced by the monthly mean (Sv).

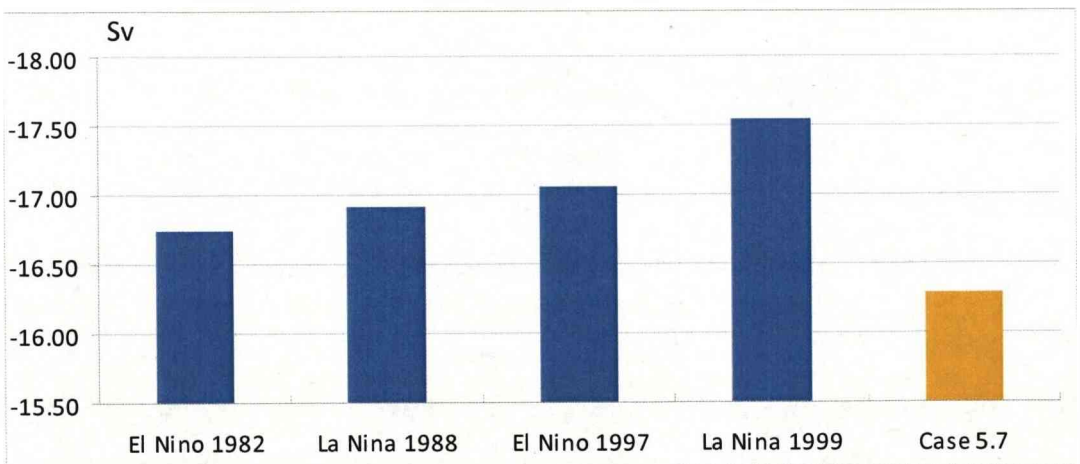

Figure 6.8: The volume transport of the ITF in the typical ENSO events (Sv).

6.4. The ITF response to global warming

6.4.1. Model setup

Numerical model predictions for global warming to the year 2100 relative to global average temperature in the year 2000 show an average increase of ocean water temperature of about 2.9 K, ranges from 2.0 K to 3.8 K (Table 6.7 and Figure 6.9). The two final model runs was carried out to examine the influence of the idealised global warming condition on the ITF transport. The sea surface temperature (SST) field was derived by increasing the realistic temperature field from the MIT-ECCO-GODAE dataset which has been used in the previous experiments (Case 6.1). The salinity field and wind forcing over the surface were kept unchanged. In the first experiment (referred to as GW1), we assume that both the Pacific Ocean and the Indian Ocean have the same increase in the SST. In order to see what might happen to the ITF transport if the SST in the Pacific Ocean increases more than the SST in the Indian Ocean, a second experiment (referred to as GW2) is performed with the SST in the Pacific Ocean increased by 3.5 K and the SST in the Indian Ocean increased by 2.5 K. The water of the SCS is considered as originated from the Pacific Ocean, therefore when increasing the SST, the Pacific Ocean and Indian Ocean are simply separated by a thick red line as showed in the Figure 6.10.

Table 6.7: Temperature increase from 2000 to 2100 (K).

Model	Total	Land	Ocean
CCSR/NIES	4.7	7.0	3.8
CCCma	4.0	5.0	3.6
CSIRO	3.8	4.9	3.4
Hadley Centre	3.7	5.5	3.0
GFDL	3.3	4.2	3.0
MPI-M	3.0	4.6	2.4
NCAR PCM	2.3	3.1	2.0
NCAR CSM	2.2	2.7	2.0
Mean	**3.4**	**4.6**	**2.9**

(Robert A. Rohde, 2007)

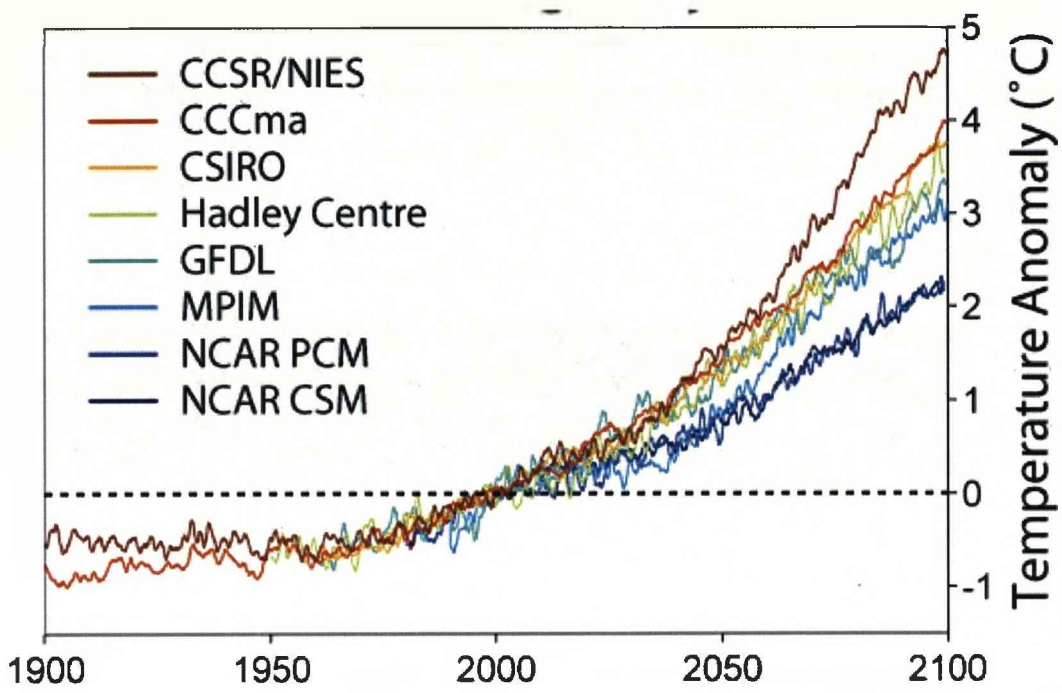

Figure 6.9: The predicted temperature to the year 2100 (Robert A. Rohde, 2007).

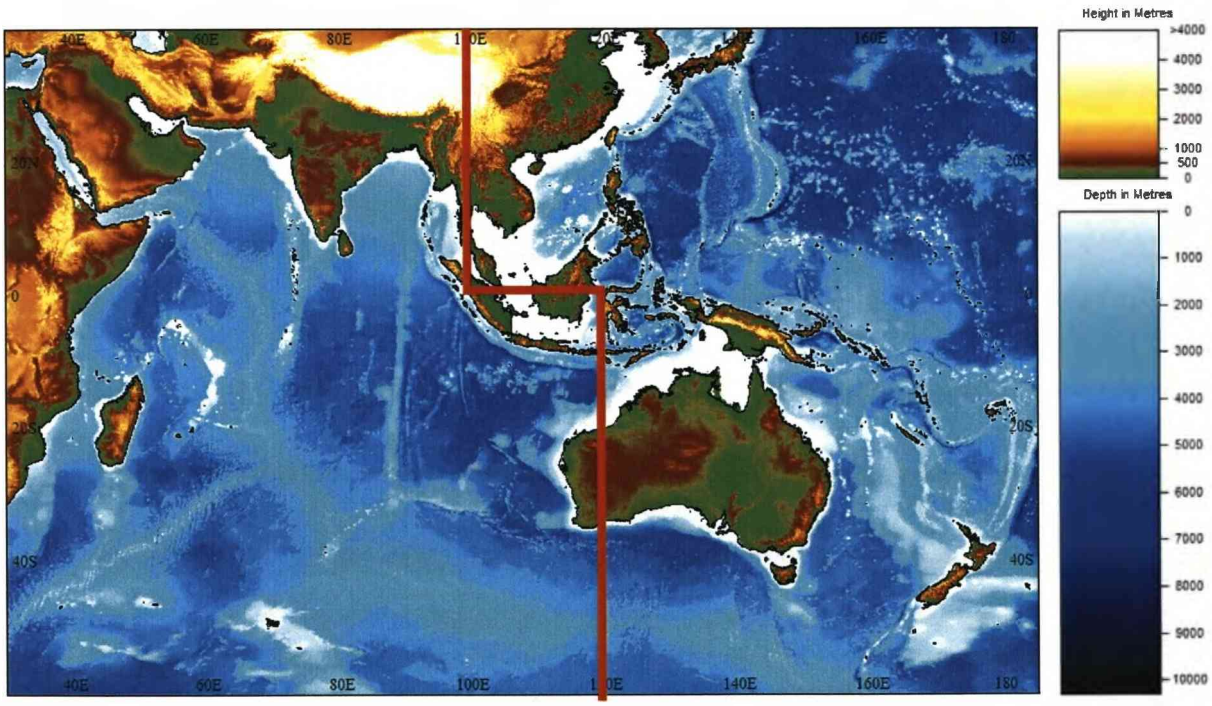

Figure 6.10: The line for SST increase in the case GW2.

6.4.2. Model result

The annual mean transports of the ITF in cases GW1 and GW2 are -15.57 Sv and -15.48 Sv respectively, slightly smaller than in Case 6.1 (Table 6.8). In terms of the

monthly-mean transport, the variation of the ITF transport in cases GW1 and GW2 is almost identical to each other and to Case 6.1 (Figure 6.11).

It is interesting to note that in case GW2 the SST of the Pacific Ocean is 1.0 K higher than that in the Indian Ocean. This would be expected to inflate the sea surface height in the Pacific Ocean while lowering the sea surface height in the Indian Ocean, and as a result would increase the volume transport of the ITF. However the model result shows that it occurs in the opposing manner, meaning a decrease, where the ITF transport in Case GW2 is slightly smaller than the ITF transport in Case 6.1. This unexpected behaviour of the ITF transport could be a result of the influence of the change of ACC or due to the local change in the Indonesian Seas where the 1K step change could induce a jet.

The result suggests that the increase in SST has made changes to the ITF transport but is not significant, and thus the relationship between the ITF transport and the idealised global warming is not as strong as might be expected and maybe associated with other processes which have not been captured in the model due to the time scale, resolution, or other details of the model.

Table 6.8: The annual mean volume transport of the ITF under idealised global warming condition.

	Case 6.1	**GW1**	**GW2**
Mixed layer	-5.51	-5.49	-5.25
Layer 5	-4.51	-4.44	-4.49
Layer 4	-3.55	-3.37	-3.41
Layer 3	-2.60	-2.38	-2.44
Layer 2	0.00	0.00	0.00
Bottom	0.11	0.11	0.11
Summary	***-16.06***	***-15.57***	***-15.48***

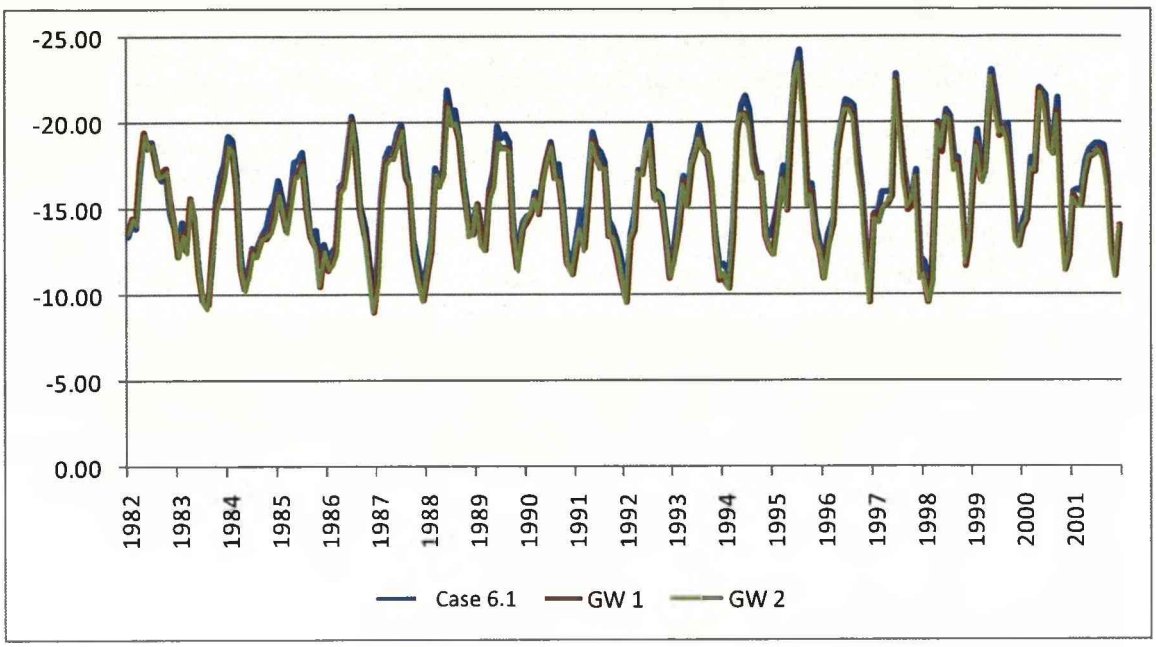

Figure 6.11: The monthly-mean ITF transport reproduced by the linear increase of the SST.

6.5 Summary

The annual mean volume transport of the ITF produced by the monthly-mean time series MIT-ECCO-GODAE dataset (from1982-2001) is about 16.06 Sv. The total volume transport of the ITF mainly occurs in the upper layer with the first two layers contributing of about 10.02 Sv (62 % of the total mean ITF transport). The deep layers play an important role in the volume transport between the oceans with the transport of the deep layers in the Ombai and Timor Straits contributing a total volume transport of 6.15 Sv (38%).

The monthly-mean time series volume transport of the ITF (from1982-2001) shows a strong seasonal variability of the ITF transport. However the correlation analysis for both the MICOM and OCCAM 1/12 model output show a very weak relationship with ENSO events where the correlation coefficients of about 0.11 (80% of confidence level) and 0.27 (99% of confidence level) respectively.

In terms of the annual-mean scale there is a clear link between ENSO and the ITF transport where the ITF volume transport reduced in the El Niños and enhanced in the La Niñas. The correlation coefficient between the annual-mean ITF transport

produced by the MICOM and OCCAM 1/12 models and the ONI index is 0.63 (97.5 % of confidence) and 0.89 (99% of confidence) respectively. The analysis for the whole period (from 1982-2001) of the MICOM model shows a weaker relationship with the correlation coefficient of about 0.35 (80% of confidence level) which is similar to the result of England and Huang (2005). Further correlation analysis between the ITF transport of MICOM model and the 6 strongest ENSO events from 1982-2001 shows a very high correlation with a correlation coefficient of about 0.89 (97.5% of confidence).

The model results show that there is only enhancement of the ITF transport in the four strongest ENSO events (during the period of 1982-2001). The enhancement of the total volume transport of the ITF in the El Niño events disagrees with the hypothesis of Wyrtki (1987), Clarke and Liu (1994), and the observation of Mayer (1996). This could be explained if the wind patterns do not adhere to the typical ENSO conditions, or it could be that the deep layer is playing a role as the model experiments (Cases 5.7, 5.9, and 6.1) show that the deep layers contribute a large amount to the total volume transport between the oceans.

The experiments with idealised global warming conditions (linear increase of the surface layer temperature) show that the increase of the surface temperature decreases the volume transport between the oceans but the changes are not significant. It suggests that global warming seems to make a little change to the volume transport of the ITF. However the experiments were only a test with an idealised condition therefore the result should be considered preliminary.

Chapter 7

DISCUSSION AND CONCLUSION

In all the idealised experiments the models performed reliably and reproduced rather well the physical phenomena such as the basin scale gyres, boundary currents and equatorial currents. The volume transport reproduced by the MICOM model closely matches the Sverdrup balance in terms of the location of gyres and interior transport. The model results show that the volume transport between the basins is sensitive to the applied wind stress regime, the strength of the wind stress, and the topography, in particular the size of the domain, number of channels and the width and latitude of the shallow channel. The result of applying Godfrey's Island Rule to calculate the volume transport for the idealised geometries and wind stress showed that the "correct" Island Rule did not give good result compared to the MICOM model but that by changing the wind stress to the channel average the calculated transport is much more like the numerical model.

Although the POLCOMS model successfully reproduced the classical wind-driven flow, especially the equatorial counter current, due to technical problems with water mass conservation and computer resources the model was not selected for the realistic topography and forcing experiments. The MICOM model was successfully set up and reproduced the circulation, volume transport and its responses to change of topography and forcing, and therefore it was used in the experiments with the realistic topography and forcing.

The MICOM model was successfully set up and tailored to the complex topography of the Southeast Asia region. The ocean circulation features in the western Pacific and Indian Oceans were successfully reproduced. The model results also show that the western boundary current in the Pacific Ocean, the circulation in the South China

Sea, and the Indonesian Seas seem related to large-scale forcing over the Pacific Ocean, and the geometry of the region.

Studies of the ITF using Godfrey's Island Rule (Godfrey, 1989; Hirst and Godfrey, 1994; Wajsowicz, 1995&1996) suggested that wind stress is the governing force of the throughflow. The results of the idealised model experiments presented in this thesis also showed that the wind stress over the domain can generate a significant volume transport between the basins. However the model experiments in realistic geometries with the wind stress alone indicated that, while the wind forcing over the ocean surface could produce a rather high seasonal variation of the volume transport between the oceans, it only produced a rather small mean ITF transport compared to the recent observational and numerical studies.

The experiment with both thermal and wind forcing gave the total annual-mean volume transport from the Pacific Ocean into the Indian Ocean of about 16.25 Sv, and showed a strong seasonal variation, with the minimum transport of about 12.26 Sv in December, and the maximum transport of about 20.28 Sv in July, which is in very good agreement with the observations and other numerical studies.

The model result suggests that the main driving forces of the ITF are the wind stress and the thermal forcing. Among them the thermal forcing is certainly dominant. This was confirmed by the spin-down experiments and the experiment with the thermal forcing only where the density gradient between the oceans was sufficient to control the throughflow and producing a significant amount of volume transport from the Pacific Ocean to the Indian Ocean which is consistent with the result of Andersson and Stigebrandt (2005). The wind stress over the ocean surface produced a relatively small amount of the ITF transport compared to the observations and other numerical studies but it is responsible for the seasonal variability of the ITF. Therefore both the wind and thermal forcing need to be taken into account in order to correctly simulate the ITF and its seasonal variability.

The volume transport in the South China Sea (SCS) is often ignored when estimating the magnitude of the ITF transport. However, the model results show a significant

contribution of the SCS to the volume transport of the ITF, which is consistent with the suggestion of Fang (2005). As described in the Chapter 5, at certain seasons, depending on the monsoon winds over the region, the SCS also can enhance or reduce the volume transport of the ITF. Therefore the SCS plays a significant role in the ITF transport and its variability.

In certain seasons, the ITF source is only from the northern hemisphere, and at other seasons it is from both the northern and southern hemispheres.

The Makassar Strait contributes approximately 50% of the total ITF transport. In the vertical, the model results showed that most of the volume transport of the throughflow appears in the upper layer with the first two upper layers contributing a total of over 10 Sv. However, the deep layers also contribute a significant amount, over 6 Sv, to the volume transport of the throughflow.

The monthly-mean time series volume transport of the ITF (from 1982-2001) shows strong seasonal variability. However the correlation analysis for both the MICOM and the OCCAM 1/12° models output show a very weak relationship with ENSO. In terms of the annual-mean there is a clear link between ENSO and the ITF transport where the ITF volume transport is reduced in the El Niños and enhanced in the La Niñas. The correlation analysis also showed a strong relationship between the annual-mean ITF transport produced by the MICOM and OCCAM 1/12° models and the ONI index with the correlation coefficient of about 0.63 (97.5 % confidence) and 0.89 (99% confidence) respectively. Further correlation analysis between the ITF transport of the MICOM model and the 6 strongest ENSO events from 1982-2001 shows a very significant correlation with the correlation coefficient is about 0.89 (97.5% confidence).

The model results show that there is only enhancement of the ITF transport in the four strongest ENSO events (during the period of 1982-2001). The enhancement of the total volume transport of the ITF in the El Niño events disagrees with the hypothesis of Wyrtki (1987), Clarke and Liu (1994), and the observation of Mayer (1996) but it could be explained if the wind patterns do not adhere to the typical

ENSO conditions, or it could be that the deep layer is playing a role; the model experiments show that the deep layers contribute a significant amount to the total volume transport between the oceans.

The experiments with idealised global warming conditions (linear increase of the surface layer temperature) show that an increase of the surface temperature decreases the volume transport between the oceans but the changes are not significant. It suggests that global warming seems to make a little change to the volume transport of the ITF. However the experiment was only a test with an idealised condition therefore the result should be considered to as preliminary.

Despite successfully reproducing the circulation and volume transport between the oceans the model still has limitations such as no sea-air interactions. The eastern boundary did not cover the whole Pacific Ocean therefore was not be able to fully reproduce large-scale processes in the Pacific Ocean. The widening of the Java, Lombok and Flores Straits due to the horizontal resolution of the model may exaggerate the volume transport at these Straits. There was no tidal forcing involved in the experiments, therefore the model could not represent the features that are caused by tides. These limitations can be suggestions for further work in the future.

APPENDIX

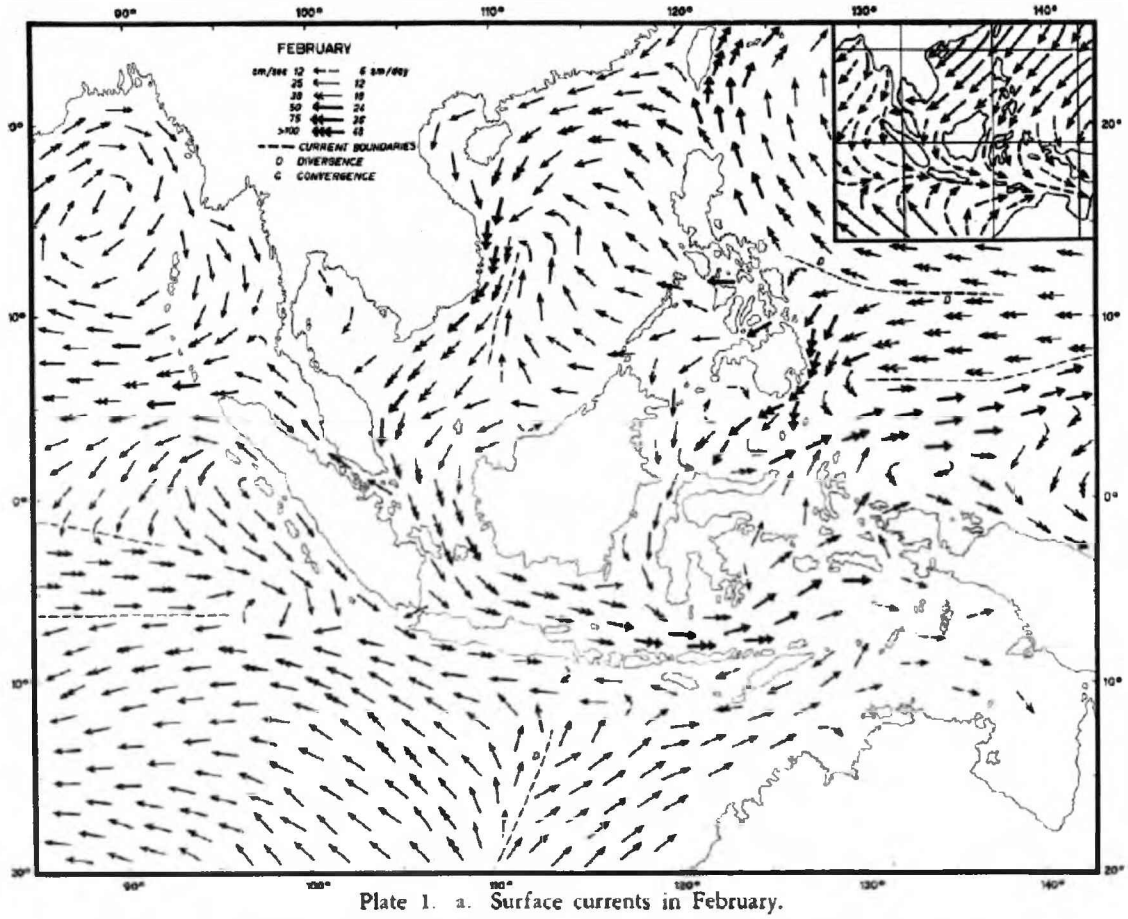

Plate 1. a. Surface currents in February.

b. Transports of surface circulation in million m^3/sec. + upwelling, o sinking.

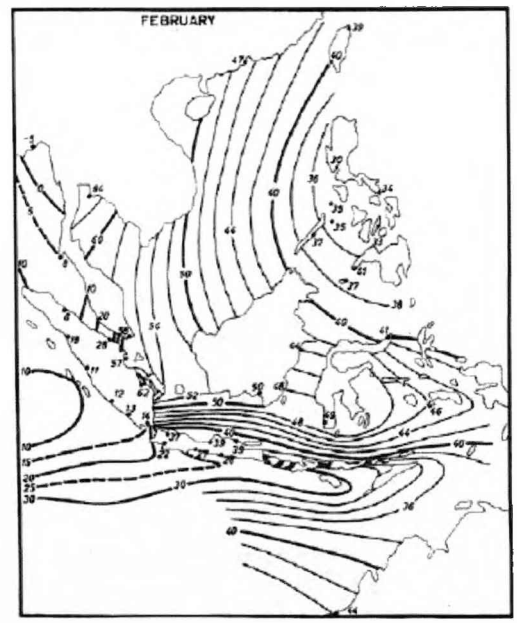

c. Topography of sea level in cm.

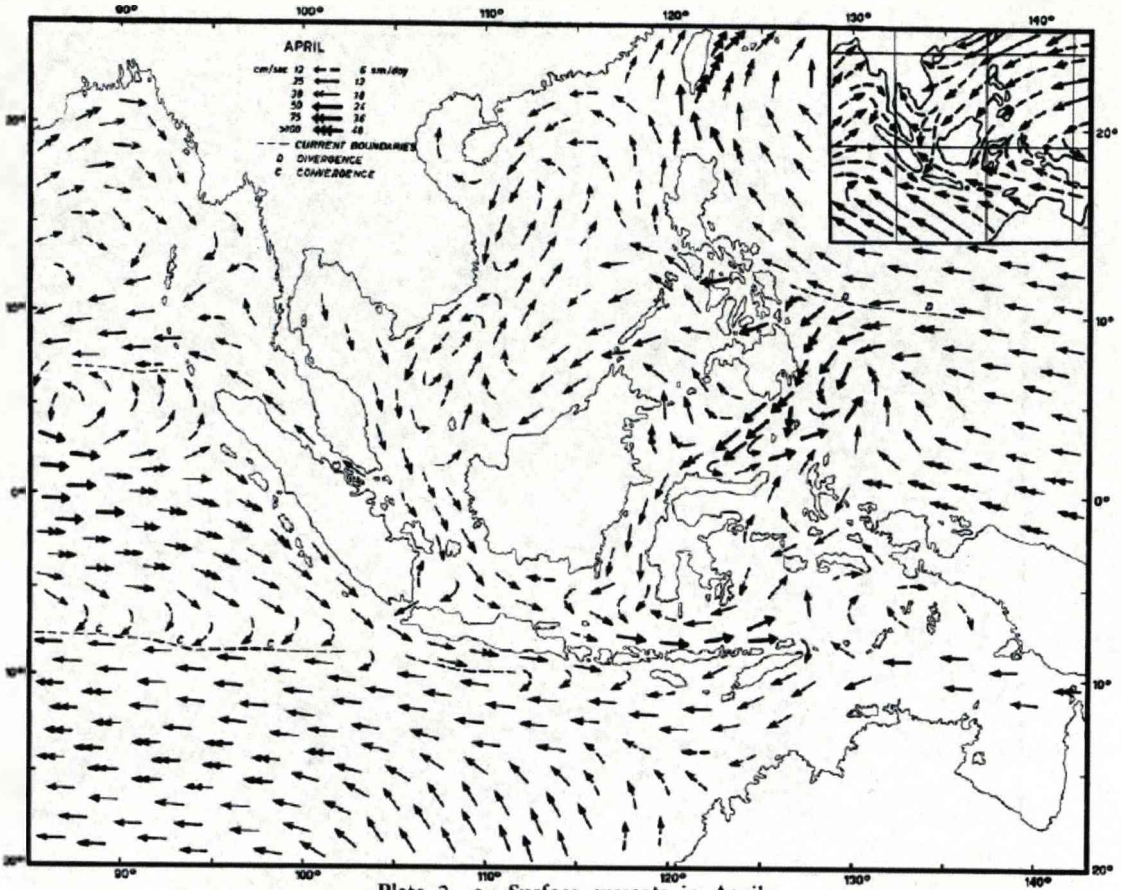

Plate 2. a. Surface currents in April.

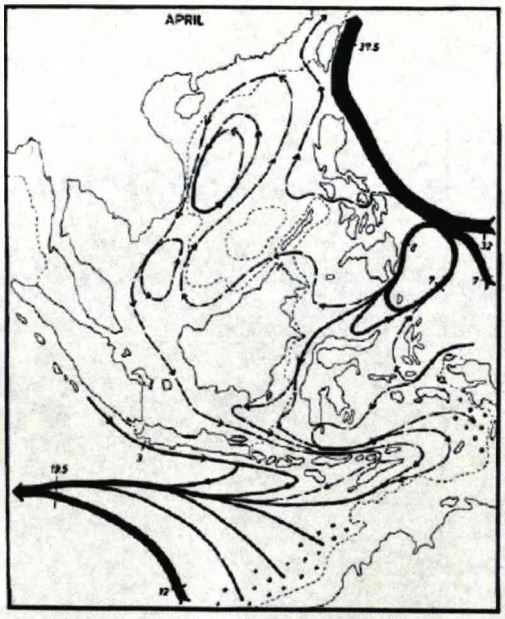

b. Transports of surface circulation in million m^3/sec. + upwelling, o sinking.

c. Topography of sea level in cm.

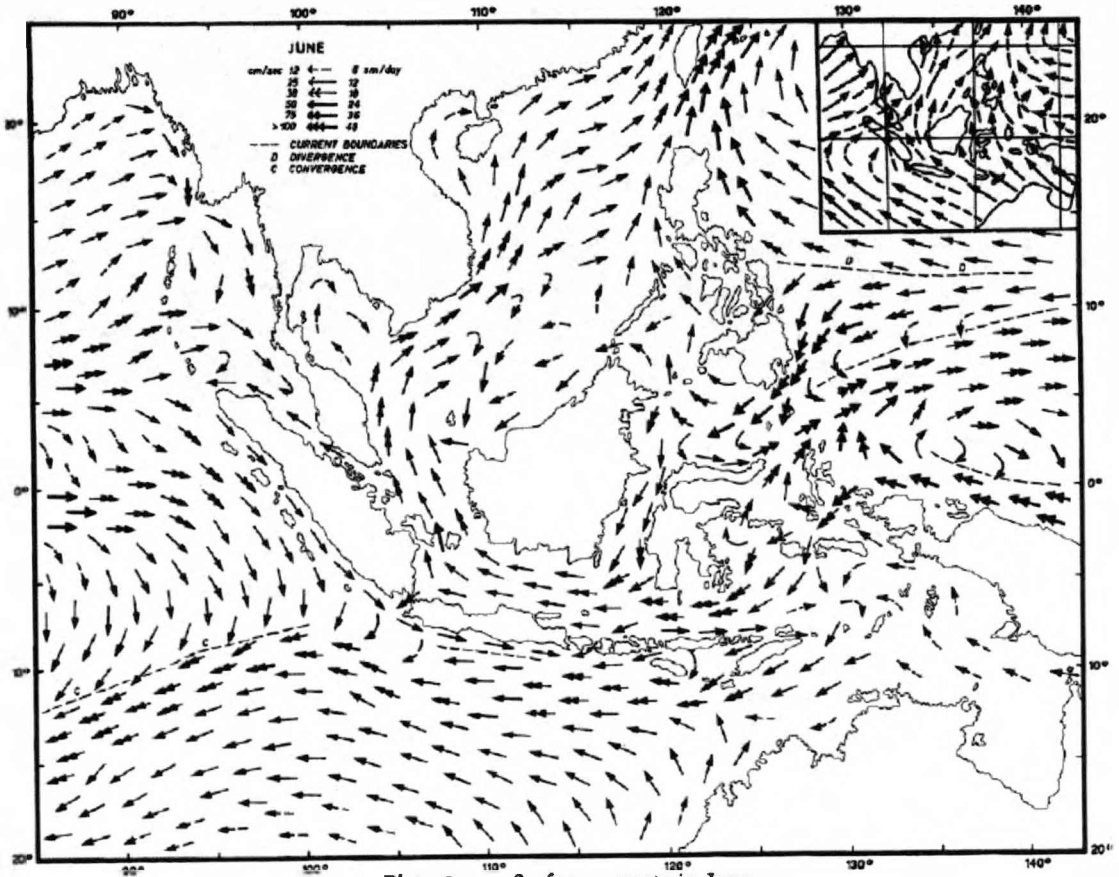

Plate 3. a. Surface currents in June.

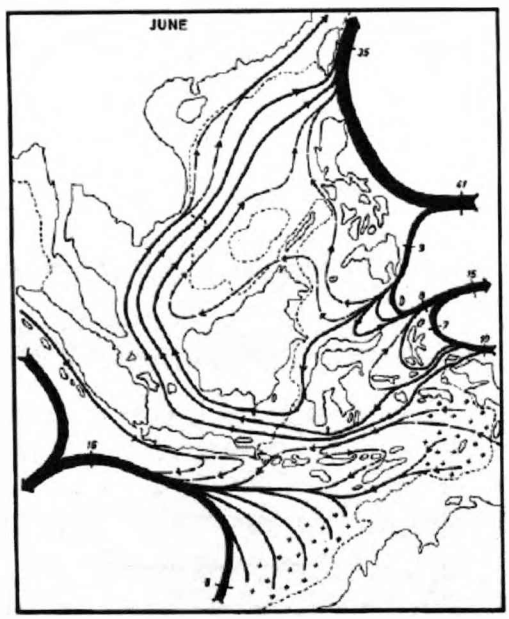

b. Transports of surface circulation in million m^3/sec. + upwelling, o sinking.

c. Topography of sea level in cm.

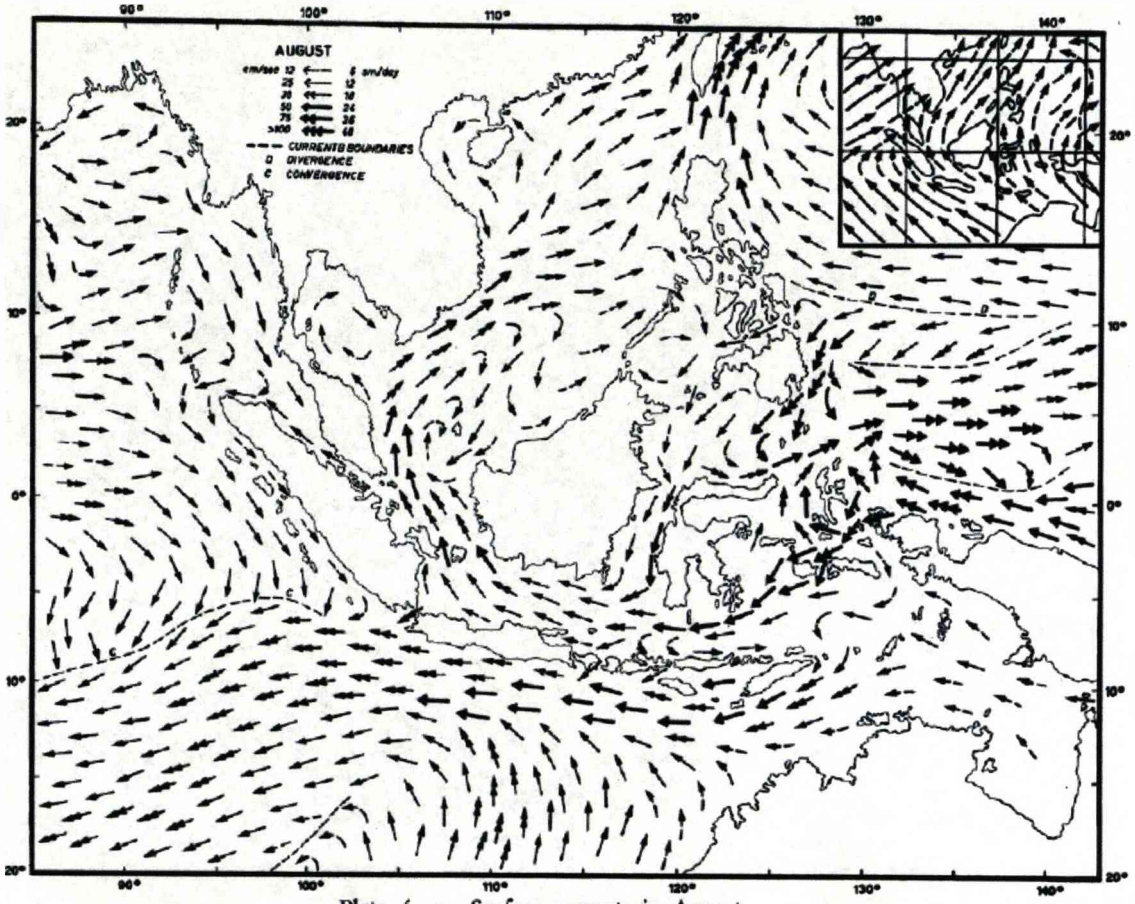

Plate 4. a. Surface currents in August.

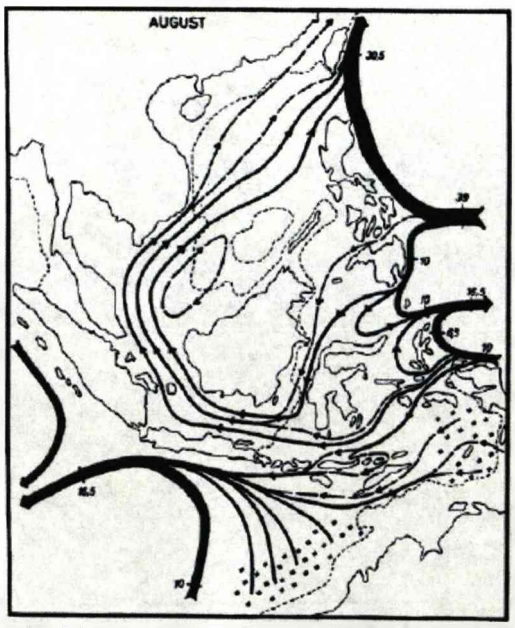

b. Transports of surface circulation in million m^3/sec. + upwelling, o sinking.

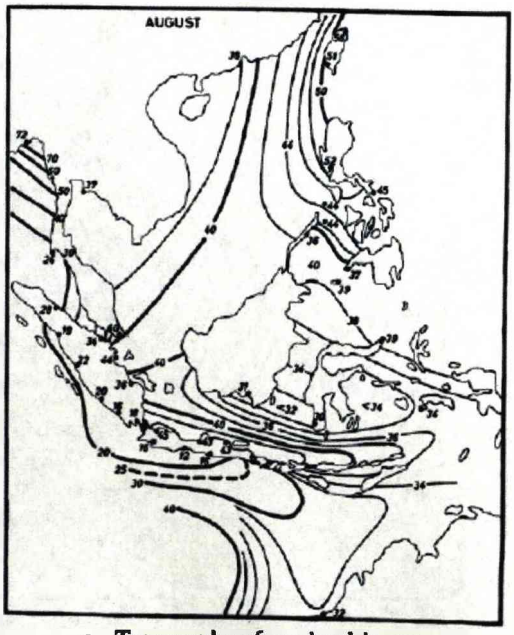

c. Topography of sea level in cm.

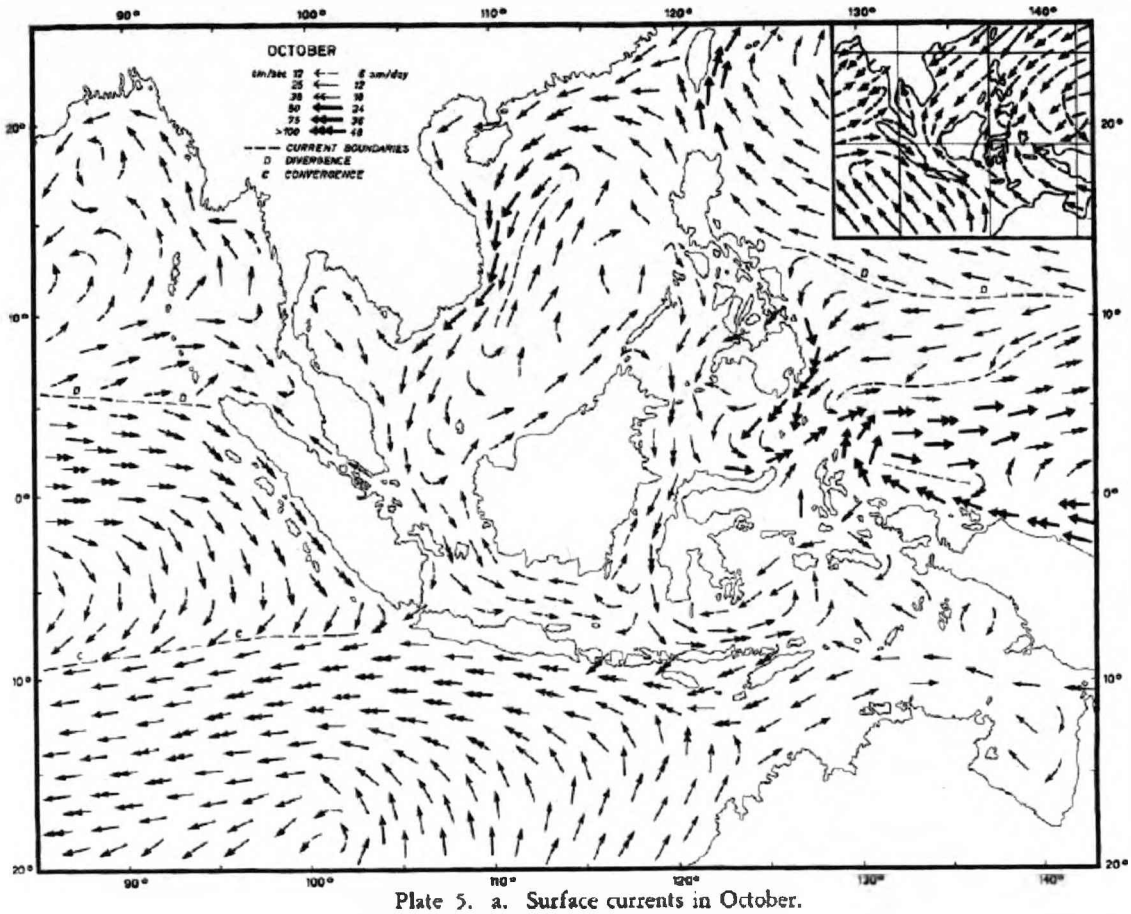

Plate 5. a. Surface currents in October.

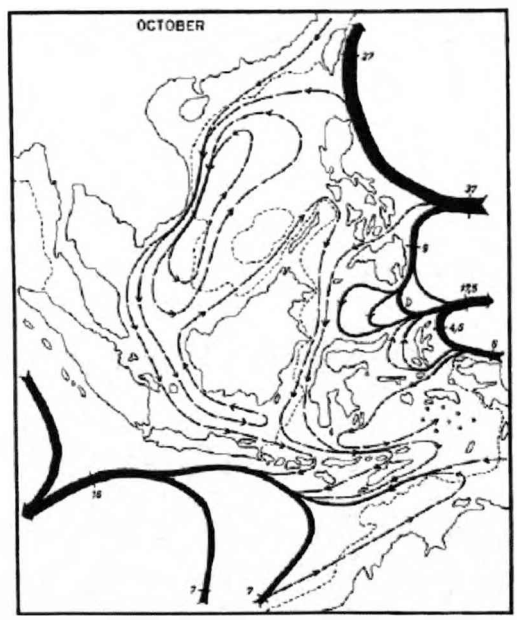

b. Transports of surface circulation in million m^3/sec. + upwelling, o sinking.

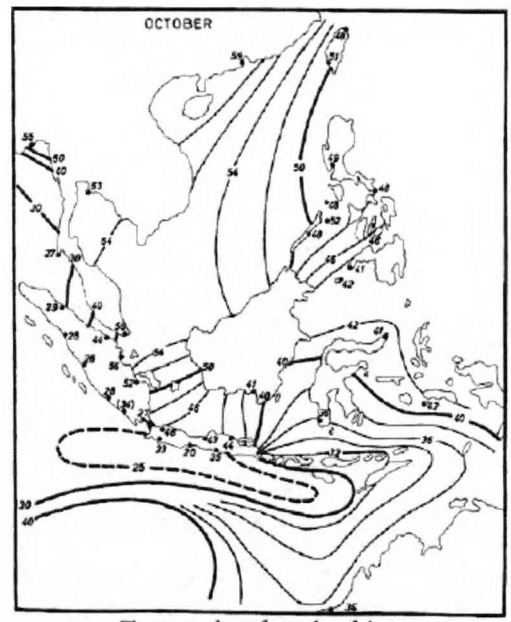

c. Topography of sea level in cm.

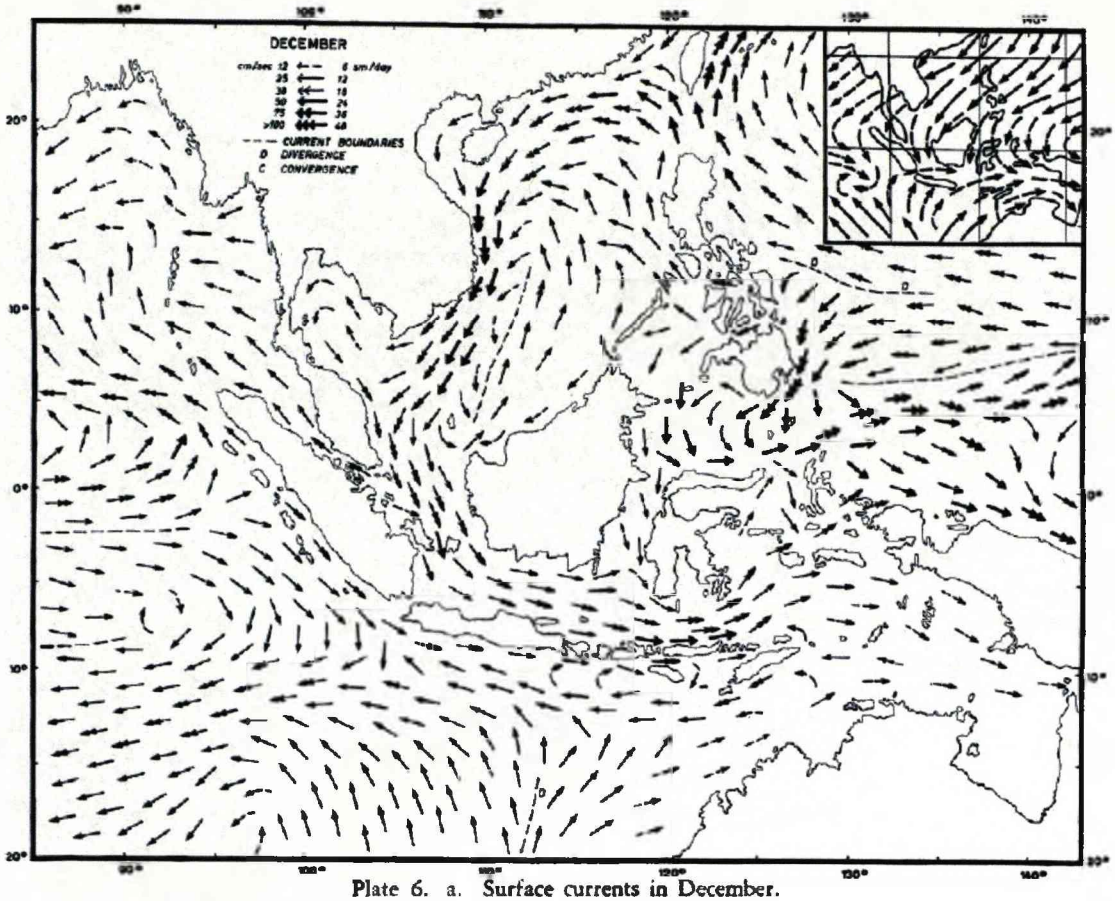

Plate 6. a. Surface currents in December.

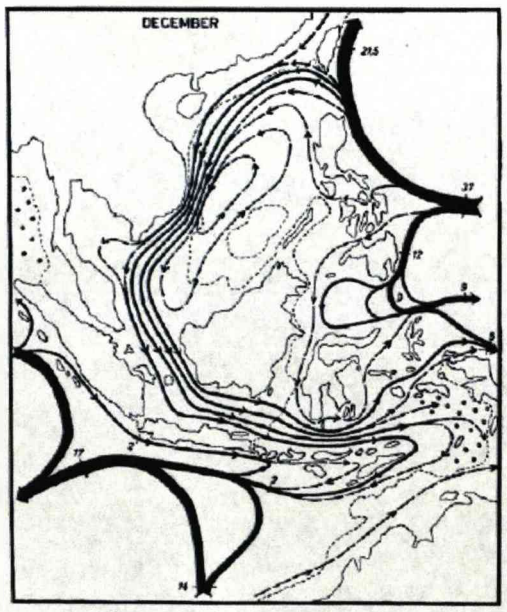

b. Transports of surface circulation in million m^3/sec. + upwelling, o sinking.

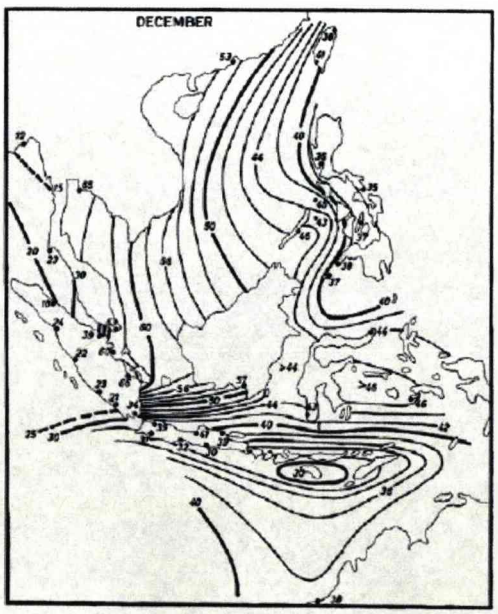

c. Topography of sea level in cm.

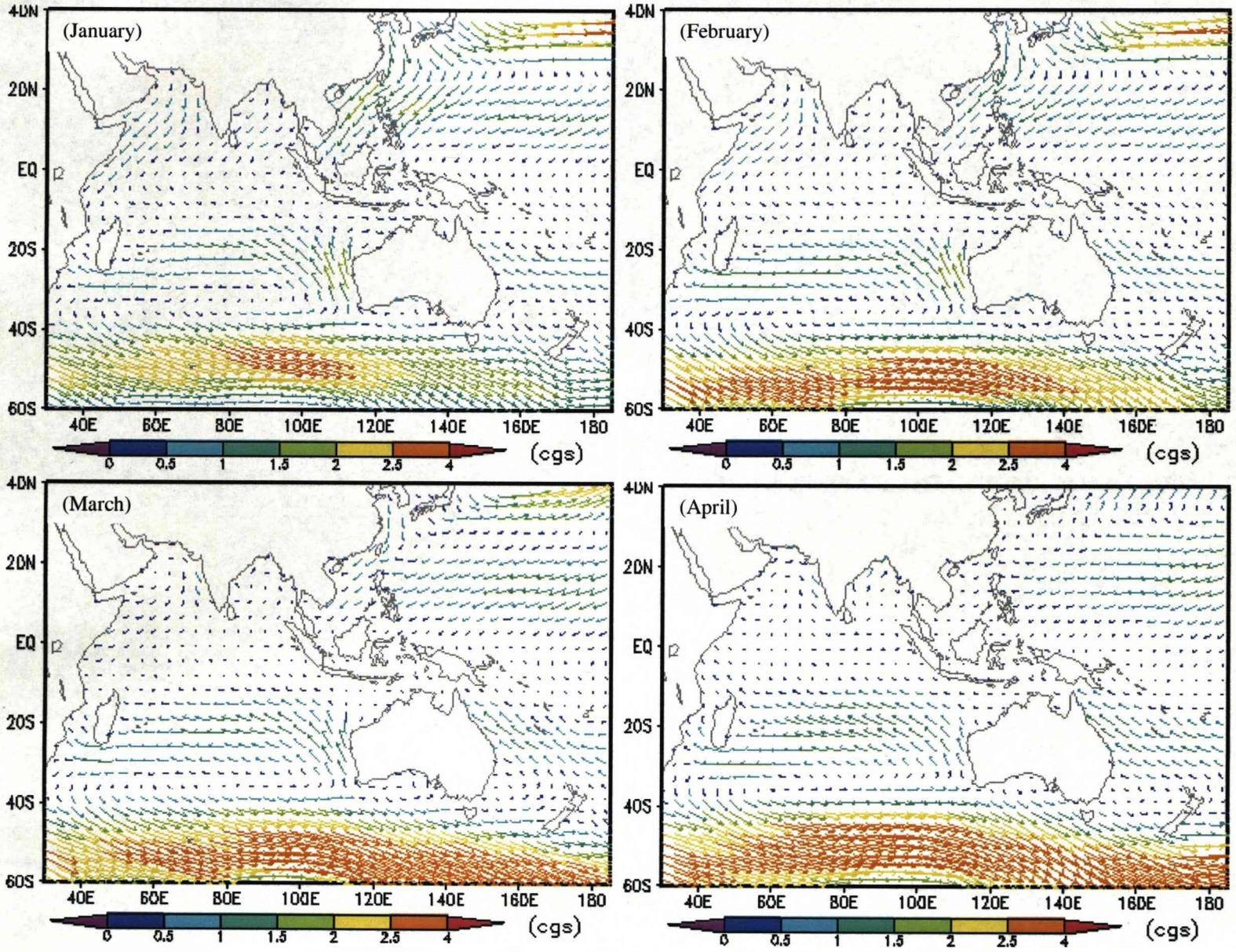

Figure A.1: The monthly mean ECMWF's wind stress (January-April).

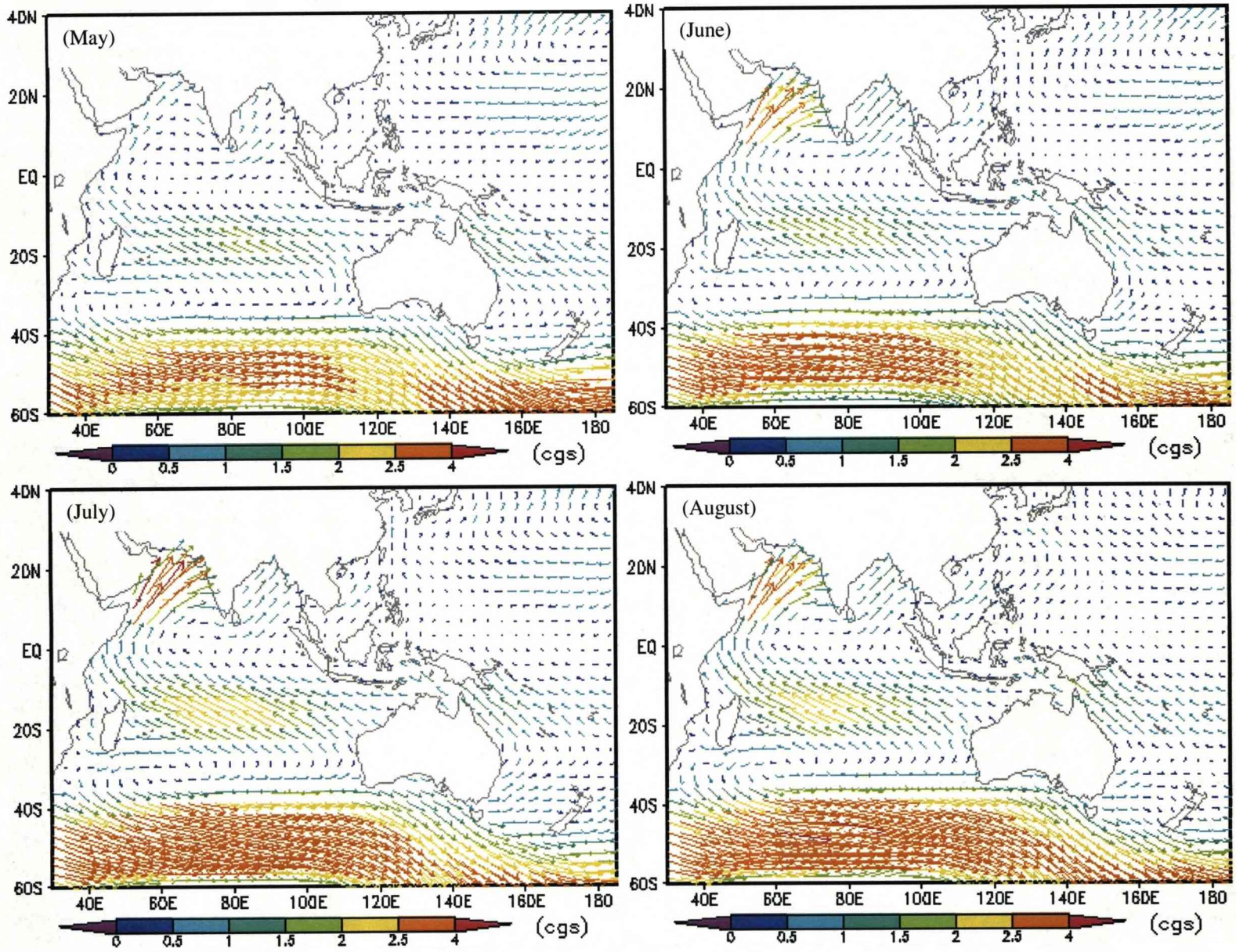

Figure A.2: The monthly mean ECMWF's wind stress (May-August).

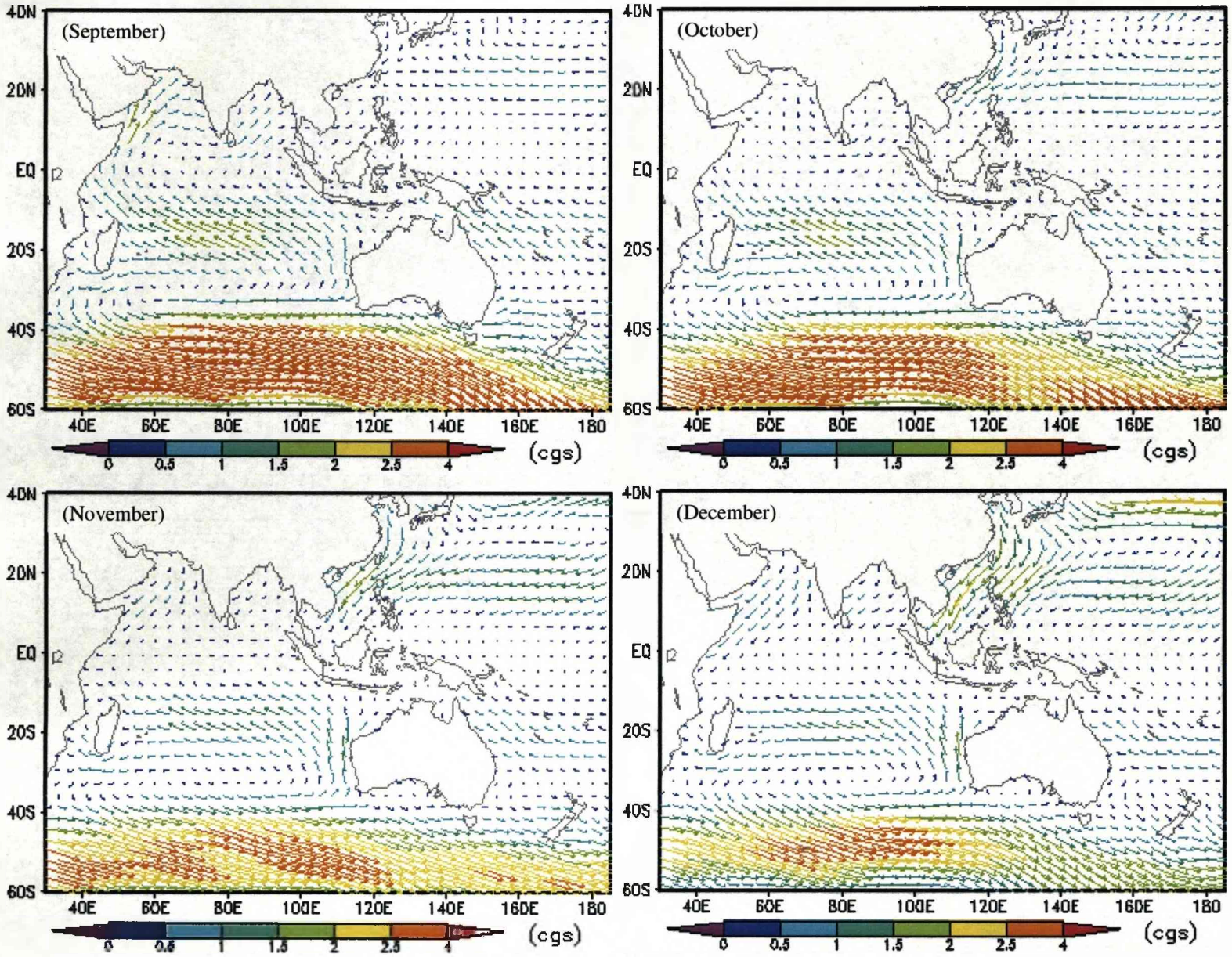

Figure A.3: The monthly mean ECMWF's wind stress (September-December).

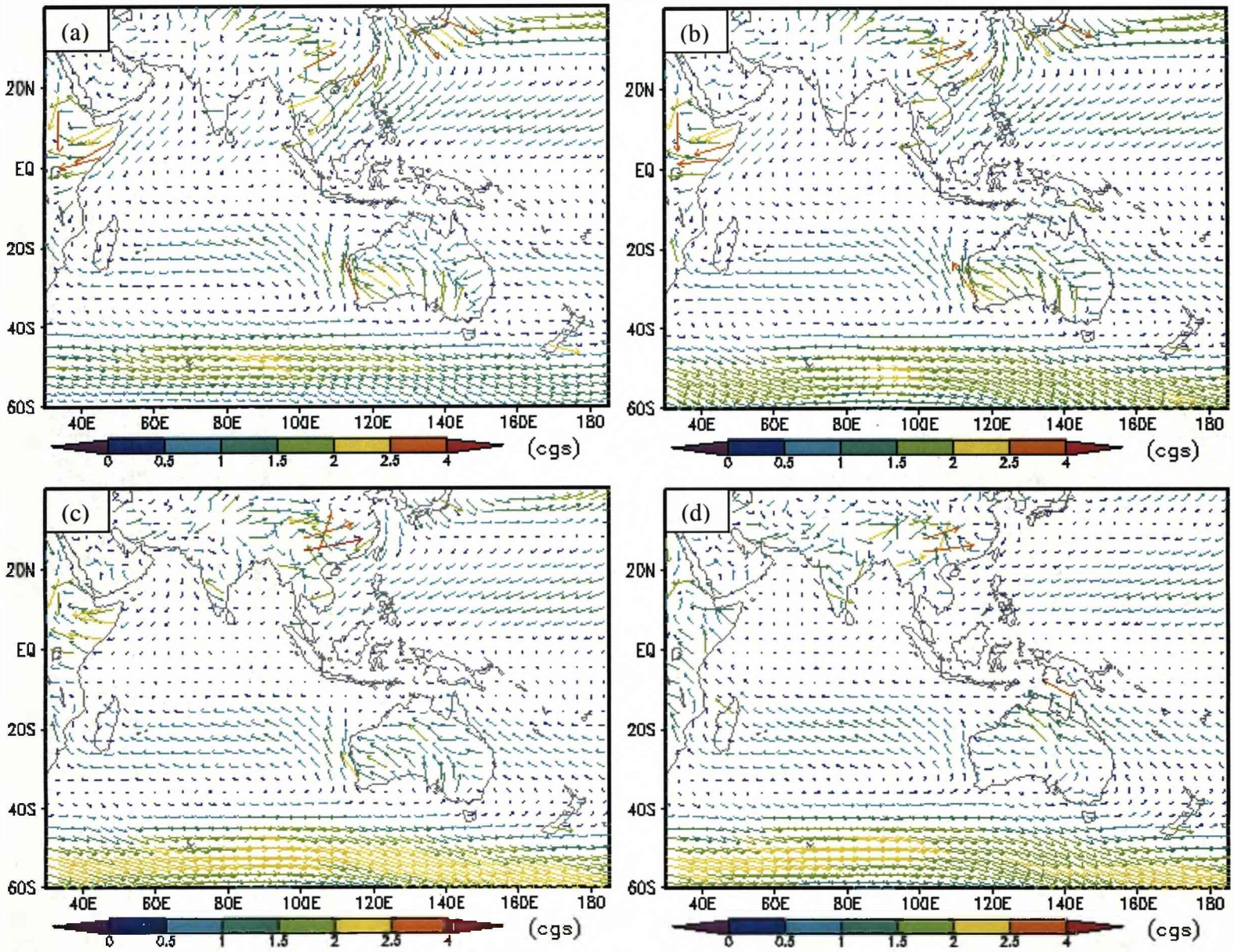

Figure A.4: The monthly-mean NCEP's wind stress from January to April (a-January; b-February; c-March; d-April).

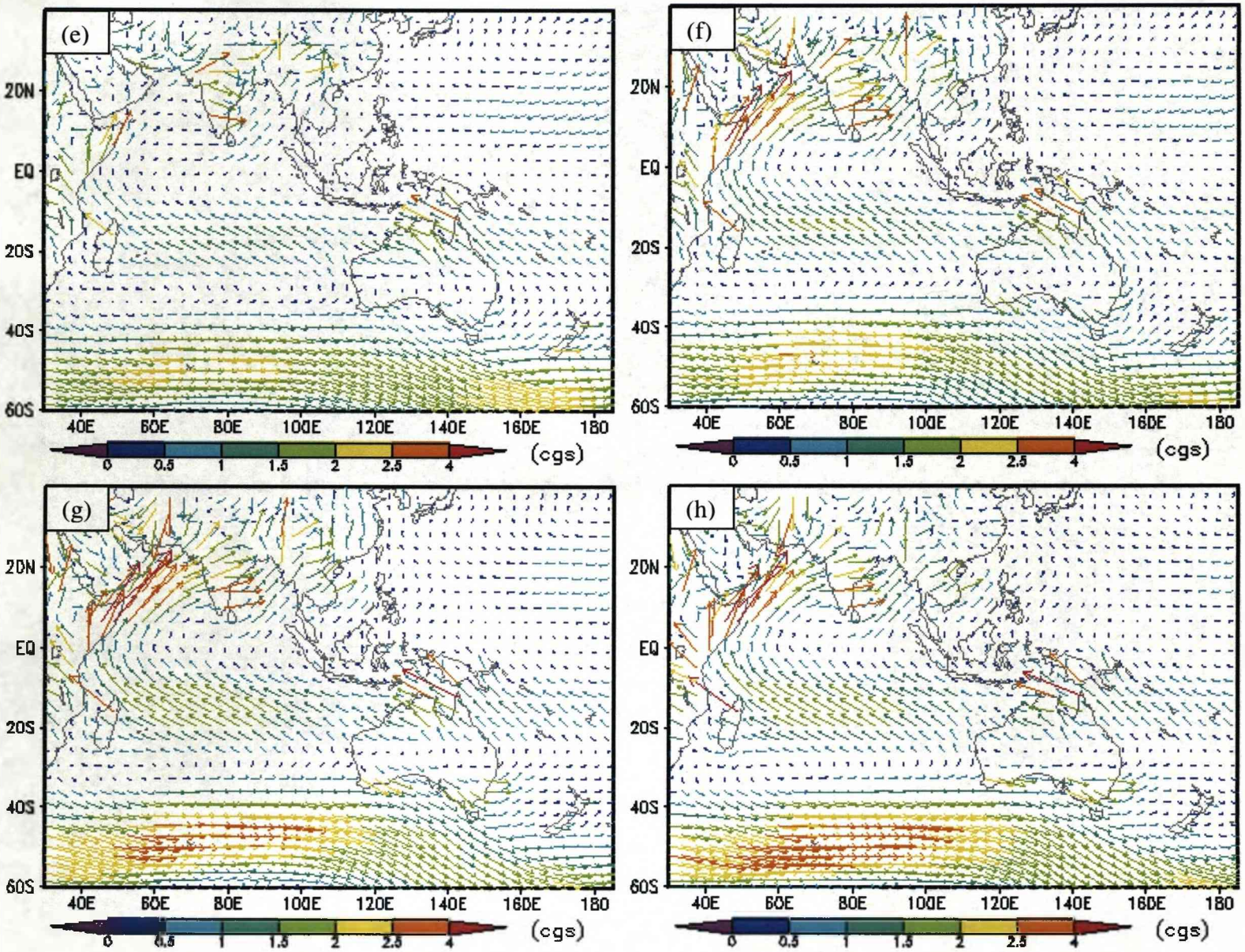

Figure A.5: The monthly-mean NCEP's wind stress from May to August (e-May; f-June; g-July; h-August).

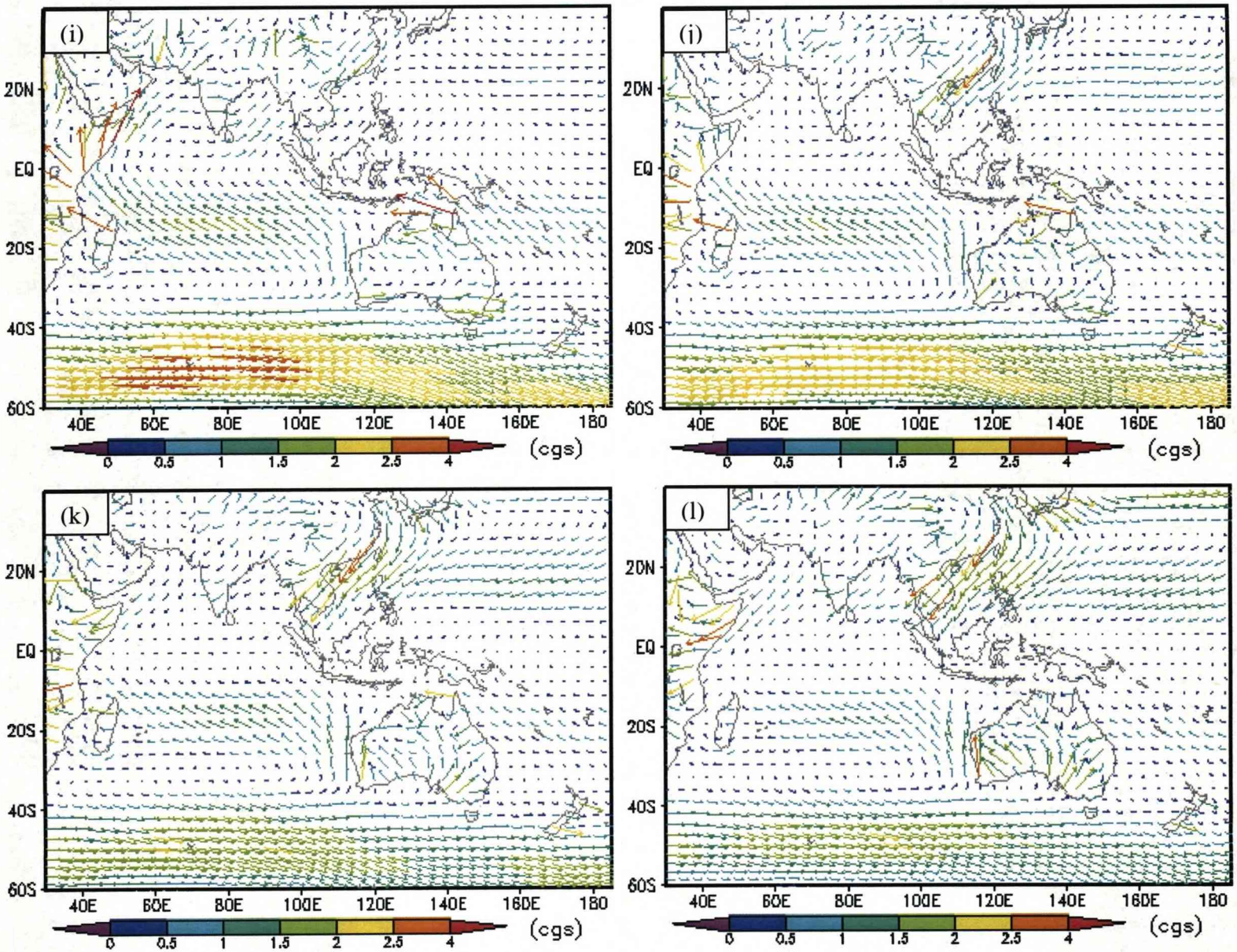

Figure A.6: The monthly-mean NCEP's wind stress from September to December (i-September; j-October; k-November; d-December).

REFERENCES

Abarbanel H. D. I and Young W. R., 1987: *General circulation of the Ocean.* Springer-Verlag New York Inc.

ACIA, 2007: *ACIA graphic, graphic set 1.* Obtained from the website: http://amap.no/acia/.

Andersson, H. C. and A. Stigebrandt 2005: *Regulation of the Indonesian throughflow by baroclinic draining of the North Australian Basin.* Deep-Sea Research, Part I. 52 2214–2233. Elsevier Ltd.

Arakawa, A., 1972: *Design of the UCLA general circulation model.* Tech. Report No. 7, Department of Meteorology, University of California, Los Angeles, 116 pp.

Argo, 2007: *A Global Array of Temperature/salinity Profiling Floats.* Obtained from the website: http://www.argo.ucsd.edu/index.html.

Arief, D., S. P. Murray 1996: *Low-frequency fluctuations in the Indonesian Throughflow through Lombok Strait.* Journal of Geophysical Research, 101(C5) 12455-12464.

ASEAN-JAPAN Centre 2004: Obtained from the website: http://www.asean.or.jp/eng/general/base/glance2004.html.

Bingham, F. M., Lukas, R., 1994: *The Southward Intrusion of North Pacific Intermediate Water along the Mindanao Coast.* Journal of Physical Oceanography, 24, 141-154.

Bleck, R., 1978: *Finite-difference equations in generalized vertical coordinates.* Part I: Total energy conservation. Contribution to Atmospheric Physics, 51, 360-372.

Bleck, R., and D. B. Boudra, 1981: *Initial testing of a numerical ocean circulation model using a hybrid (quasi-isopycnic) vertical coordinate.* Journal of Physical Oceanography, 11, 755-770.

Bleck, R., and D. B. Boudra, 1986: *Wind-driven spin up in eddy-resolving ocean models formulated in isopycnic and isobaric coordinates.* Journal of Geophysical Research, 91, 7611-7621.

Bleck, R., and L. T. Smith, 1990: *A wind-driven isopycnic coordinate model of the North and Equatorial Atlantic Ocean. 1: Model development and supporting experiments.* Journal of Geophysical Research, 95, 3273-3285.

Bleck, R. C Rooth D Hu and L Smith, 1992: *Salinity-Driven Thermo-cline Transients in a Wind- and Thermohaline- Forced Isopycnic Coordinate Model of the North Atlantic.* Journal of Physical Oceanography, 22, 1486-1505.

Blumberg A.F. and G.L. Mellor 1987: *A description of a three-dimensional coastal ocean model.* Pp. 1-16 in ``Three Dimensional Coastal Ocean Models", ed. N.S. Heaps, American Geophysical Union, Washington, DC.

Bogdanov K. T. and Moroz V. V., 1995: *Thermohaline structure and water circulation in the South China Sea.* Oceanology, Vol 34, No 6.

Broebecker W.,S., 1991: *The Great Ocean Conveyor.* Oceanography, Vol 4, No.2, 79-89.

Bryan, K., A. 1969: *Numerical Method for the Study of the Circulation of the World Ocean.* Journal of Computational Physics, 4(3):347-376.

Chao S.Y., Shaw P. T., Wu S. Y., 1996: *Deep water ventilation in the South China Sea.* Deep Sea Research I. Vol. 43, No. 4, pp. 445466.

Chu C. P. et al., 1999: *Dynamical Mechanisms for the South China Sea Seasonal Circulation and Thermohaline Variabilities.* Journal of Physical Oceanography. Vol. 29, 2971-2989.

Clarke, A.J. and X. Liu, 1993: *Observations and dynamics of semiannual and annual sea levels near the eastern equatorial Indian Ocean boundary.* Journal of Physical Oceanography. Vol. 23, 386-399.

Clarke, A.J. and X. Liu, 1994: *Inter-annual sea level in the northern and eastern Indian Ocean.* Journal of Physical Oceanography. Vol 24, 1224-1235.

Clivar, 1998: *Asian-Australian Monsoon, AGCM inter-comparison project.* Obtained from the website: http://climate.snu.ac.kr/clivar/index.htm.

Colella P. and Woodward P.R., 1984: *The piecewise parabolic method (PPM) for gas-dynamical simulations.* Journal of Computational Physics 54:174-201.

Craig P.D. and M.L. Banner 1994: *Modelling wave-enhanced turbulence in the ocean surface layer.* Journal of Physical Oceanography 24:2546-2559.

Cresswell, G., A. Frische, J. Peterson and Quadfasel, D.R, 1993: *Circulation in the Timor Sea.* Journal of Geophysical Research, vol. 98 (C8). p. 7742-7748.

CSIRO, 2001: *The Leeuwin Current – life of the West. The facts: CSIRO marine research – understanding ours oceans.* a fact sheet provided by CSIRO, the Commonwealth Scientific and Industrial Research Organization, describes the Leeuwin Current and its influence on Western Australia.

Dale, W. L., 1956: *Wind and drift currents in the South China Sea.* The Malaysian Journal of Tropical Geography, 8, 1-31.

Doron N., 1996: *What control the origin of the Indonesian throughflow?* Journal of Geophysical Research, 101, 12,301-12,314.

England, M.H., and F. Huang, 2005: *On the inter-annual variability of the Indonesian Throughflow and its linkage with ENSO*. Journal of Climate, 18, 1435-1444.

Fang et al., 1998: *A survey of studies on the South China Sea upper ocean circulation.* Acta Oceanographica Taiwanica, 37(1), 1–16.

Fang G. et al., 2005: *A note on the South China Sea shallow inter-ocean circulation.* Advances in Atmospheric Sciences, vol. 22, no. 6, 946–954.

Ffield, A., A. Gordon, 1992: *Vertical mixing in the Indonesian thermocline*. Journal of Physical Oceanography, vol.22. pp. 184-195.

Fieux, M., C. André, P. Delecluse, A.G. Ilahude, A. Kartavtseff, F. Mantisi, R. Molcard and J.C. Swallow, 1994: *Measurements within the Pacific-Indian oceans throughflow region*. Deep Sea Research, vol. 41. No. 7, p. 1091-1130.

Fine R. A., 1985: *Direct evidence using tritium data for the Throughflow from the Pacific into the Indian Ocean.* Nature 315, 478–480.

Friedrich, H., and S Levitus, 1972: *An approximation to the equation of state for sea water, suitable for numerical ocean models*. Journal of Physical Oceanography. 2, 514-517.

Fu, L., 1986: *Mass, heat and freshwater fluxes in the south Indian Ocean*. Journal of Physical Oceanography, 16, 1683–1693.

Galperin B., L.H. Kantha, S. Hassid and A. Rosati, 1988: *A quasi-equilibrium turbulent energy model for geophysical flows*. Journal of Atmospheric Sciences 45:55-62.

Gan, J., H. Li, E. N. Curchitser, and D. B. Haidvogel, 2006: *Modeling South China Sea circulation: Response to seasonal forcing regimes*. Journal of Geophysical Research, 111, C06034, doi:10.1029/2005JC003298.

Gill A., E., 1982: *Atmosphere-Ocean Dynamic*. Academic Press, INC.

Godfrey, J. S., 1989: *A Sverdrup model of the depth-integrated flow for the world ocean allowing for island circulation.* Geophysics Astrophysics Fluid Dynamic, 45, 89-112.

Godfrey, J. S., 1996: *The effect of the Indonesian Throughflow on ocean circulation and heat exchange with the atmosphere: A review.* Journal of Geophysical Research, 101, 12.217-12.237.

Godfrey, J. S., and Golding, T. J., 1981: *The Sverdrup relation in the Indian Ocean, and the effect of Pacific-Indian Ocean throughflow on Indian Ocean circulation and on the East Australian Current*, Journal of Physical Oceanography. vol. 11, p711-p779.

Gordon, A., L., 1986: *Inter-ocean exchange of thermocline waters.* Journal of Geophysical Research, 91C, 5037-5046.

Gordon, A.L. and R. Fine, 1996: *Pathways of water between the Pacific and Indian oceans in the Indonesian seas.* Nature 379(6561): 146-149.

Gordon, A. L. and R. D. Susanto, 2001: *Banda Sea Surface Layer Divergence.* Ocean Dynamics, 52, (1), 2-10.

Gordon, A., L., Susanto R., D. Vranes K, 2003: *Cool Indonesian throughflow as a consequence of restricted surface layer flow.* Letters to Nature, vol. 425.

Gordon, A.L., McClean, J.L., 1999: *Thermohaline stratification of the Indonesian Sea: model and observations.* Journal of Physical Oceanography, 29(2), 198-216.

Gordon, A.L.., Susanto, R.D., Ffield, A., 1999: *Throughflow within Makassar Strait.* Geophysical Research Letters, 26(21), 3325-3328.

Gordon, A. L., 2001: *Inter-ocean Exchange. In: "Ocean Circulation and Climate"*, G. Siedler, J.Church and J. Gould (eds.), Academic Press.

Gordon, A. L., Susanto, R. D., & Vranes, K., 2003: *Cool Indonesian throughflow as a consequence of restricted surface layer flow.* Nature, 425, 824-828.

Griffies, S.M., Boning, C., Bryan, F.O., Chassignet, E.P., Gerdes, R., Hasumi, H., Hirst, A., Treguier, A-M. and Webb, D. 2000: *Developments in ocean climate modelling.* Ocean Modelling, 2, (3/4), 123-192.

Haidvogel D.B. and A. Beckmann., 1999: *Numerical Ocean Circulation Modeling.* London, Imperial College Press.

Haidvogel D.B., and A. Beckmann., 1998: *Numerical models of the coastal ocean. In The Sea.* Volume 10. Edited by K. H. Brink and A. R. Robinson. 457–482. New York: John Wiley and Sons, Inc.

Hautala, S., J. Reid and N. Bray, 1996: *The distribution and mixing of Pacific water masses in the Indonesian Seas.* Journal of Geophysical Research, 101(C5):12375-12389.

Hautala, S. L., J. Sprintall, J. T. Potemra, J. C. Chong, W. Pandoe, N. Bray, and A. G. Ilahude, 2001: *Velocity structure and transport of the Indonesian Throughflow in the major straits restricting flow into the Indian Ocean.* Journal of Geophysical Research, 106(C9), 19,527–19,546.

Hirst, A.C. and J.S. Godfrey, 1993: *The role of Indonesian throughflow in a global ocean GCM.* Journal of Physical Oceanography, vol. 23. p. 1057-1086.

Hirst, A.C. and J.S. Godfrey, 1994: *The response to a sudden change in Indonesian throughflow in a global ocean GCM.* Journal of Physical Oceanography, vol. 24. pp. 1895-1910.

Holt J.T. and I.D. James 1999b: *A simulation of the southern North Sea in comparison with measurements from the North Sea Project. Part 2: Suspended particulate matter.* Continental Shelf Research, 19:1617-1642.

Holt J.T. and I.D. James. 2001a: *An s co-ordinate density evolving model of the northwest European continental shelf. 1, Model description and density structure.* Journal of Geophysical Research, 106:14015-14034.

Holt J.T., and I.D. James. 2001b: *An s co-ordinate density evolving model of the northwest European continental shelf. 2, Seasonal currents and tides.* Journal of Geophysical Research, 106:14035-14053.

Humphries and Webb, 2007: *On the Indonesian throughflow in the OCCAM ¼ degree ocean model.* Ocean Sci. Discuss., 4, 325-370.

IPCC 2001: *Climate Change 2001: The Scientific Basis*, in: Contribution of Working Group I to the Third Assessment Report of the Intergovernmental Panel on Climate Change, edited by: Houghton, J. T., Ding, Y., Griggs, D. J., Noguer, M., van de Linden, P. J., Dai, X., Mashell, K., and Johnson, C. A., Cambridge University Press, Cambridge, UK and New York, USA, 1–16, 105–164, 503–504, 567–568, 2001a.

Irwin P. G., 1968: *Monsoon Asia.* Jacaranda Press PTY. Ltd.

James, I.D., 1986: *A front-resolving sigma coordinate sea model with a simple hybrid advection scheme.* Applied Mathematical Modelling 10, 87-92.

James, I.D., 1996: *Advection schemes for shelf sea models.* Journal of Marine Systems 8, 237-254.

JAXA, 2004: *Movement of the Kuroshio Current.* Obtained form the website: http://www.eorc.jaxa.jp/en/imgdata/topics/2004/tp040611.html.

Kantha L., H., and Clayson C., A., 2000: *Numerical Models of Oceans and Oceanic Processes.* Academic Press.

Kindle, J. C., H. E. Hurlburt, and E. J. Metzger, 1989: *On the seasonal and inter-annual variability of the Pacific to Indian Ocean throughflow.* Proc. Western Pacific Int. Meeting and Workshop on TOGA COARE, Noumea, New Caledonia, 355–365.

Knauss J., A., 1997: *Introduction to physical oceanography.* Second edition. Prentice-Hall, Inc.

Langlois, G., 1997: *Miami Isopycnic coordinate ocean model (MICOM)* – user's manual. Agence de Dévelopments en Hydrodynamique et Océanographie, Côtière, France, 2.6a edition. Translated from French by D Brydon, R Bleck and S Dean.

Li Wei et al., 2006: *ITF in a coupled GCM and its inter-annual variability related to ENSO and IOD*. Acta Oceanologica Sinica, vol.25 No.1 P.32-47.

Ilahude, A. G., A. L. Gordon, 1996: *Themocline stratification within the Indonesian Seas*. Journal of Geophysical Research, 101(C5) 12401-12409.

Lukas, R., E. Firing, P. Hacker, P. L. Richardson, C. A. Collins, R. A. Fine, R. Gammon, 1991: *Observations of the Mindanao Current during the Western Equatorial Pacific Ocean Circulation Study*. Journal of Geophysical Research, 96, 7089-7104.

Masumoto, Y., and T., Yamagata, 1993: *Simulated seasonal circulation in the Indonesian Seas*. Journal of Geophysical Research, vol 98. No. C7. 12501-12509.

Masumoto, Y., and T., Yamagata, 1996: *Seasonal variation of the Indonesian throughflow in a general ocean circulation model*. Journal of Geophysical Research, 101, 12,287-12,293.

Mellor G.L. and T. Yamada 1974: *A Hierarchy of Turbulence Closure Models for Planetary Boundary Layers*. Journal of Atmospheric Sciences 31:1791-1806.

Mellor G.L. 1989: *Retrospective on oceanic boundary layer modelling and second moment closure*. Pp. 251-271 in "The Parameterisation of Small Scale Processes. Proceedings of the Aha Hulikoa Hawaiian Winter Workshop", ed. D. Henderson and P. Müller, University of Hawaii, Manoa.

Mellor G.L. 1991: *An equation of state for numerical models of oceans and estuaries.* Journal of Atmospheric and Oceanic Technology 8:609-611.

Meyers, G., R.J. Bailey and A.P. Worby, 1995: *Geostrophic transport of Indonesian throughflow*. Deep Sea Research, vol. 42. No. 7, p. 1163-1174.

Meyers, G., 1996: *Variation of the Indonesian throughflow and the El Niño-Southern Oscillation*. Journal of Geophysical Research, vol. 101. No. C5, p. 12 255-12 263.

Metzger, E. J. and H. Hurlburt., 1996: *Coupled dynamics of the South China Sea, the Sulu Sea and the Pacific Ocean*. Journal of Geophysical Research, 101 (C5), 12331-12352.

Molcard, R., A.G. Ilahude, M. Fieux, J.C. Swallow, and J. Banjarnahor, 1994: *Low frequency variability of the currents in Indonesian Channels (Savu-Roti M1 and Roti-Ashmore Reef M2)*. Deep Sea Research, 41, 1643-1662.

Molcard, R., M. Fieux, and A.G. Ilahude, 1996: *The Indo-Pacific throughflow in the Timor Passage*. Journal of Geophysical Research, 101 (C5), 12411-12420.

Molcard, R., M. Fieux, and F. Syamsudin, 2001: *The Throughflow within Ombai Strait*. Deep-sea Res., I, 48, 1237-1253.

Munk W.H., 1950: *On the wind-driven ocean circulation.* Journal of Meteorology 7 (2): 79–93.

Murray, S. P., and D. Arief, 1988: *Throughflow into the Indian Ocean through the Lombok Strait. January 1985-January 1986.* Nature, 333, 444-447.

Murray, S.P., D. Arief, J.C. Kindle, and H.E. Hurlburt, 1989: *Characteristics of circulation in an Indonesian Archipelago Strait from hydrography, current measurements and modeling results.* NATO Advanced Research Workshop on the Physical Oceanography of Sea Straits, Les Arcs, Kluwer Academic Publishers.

NAS, 2000: *El Niño and La Niña: Tracing the Dance of Ocean and Atmosphere.* Obtained from the website: http://www7.nationalacademies.org/opus/elnino.html

NASA, 2003: *El Nino - and What is the Southern Oscillation Anyway?!.* Obtained from the website: http://kids.earth.nasa.gov/archive/nino/intro.html.

NASA, 2007: *Ocean motion and surface current.* Obtained from the website: http://oceanmotion.org/html/background/wind-driven-surface.htm.

Navy Operational Ocean Circulation and Tidal Models, 2003: *Model initialization and spin-up.* Obtained from the website: http://iodeweb5.vliz.be/oceanteacher/resources/other/NOMModeling/modeling/initial.html.

Netherlands Meteorological Institute, 1936: *Oceanographic and meteorological observations in the China Seas and in the western part of the North Pacific Ocean.* No. 115.

Netherlands Meteorological Institute, 1949: *Sea areas around Australia.* Oceanographic and Meteorological data. No. 124.

Netherlands Meteorological Institute, 1952: *Indian Ocean, general current circulation.* No. 125.

NOAA, 2005: *Warm (El Nino/ southern oscillation – ENSO) episodes in the tropic Pacific.* Obtained from the National weather service/Climate prediction centre website:http://www.cpc.ncep.noaa.gov/products/analysis_monitoring/impacts/warm_impacts.shtml.

NOAA, 2007: *NOAA El Nino page.* Obtained from the website: http://www.elnino.noaa.gov/

NODC_WOA98 *data provided by the NOAA/OAR/ESRL PSD, Boulder, Colorado, USA, from their web site at* http://www.cdc.noaa.gov/.

Nof, D., 1996: *What controls the origin of the Indonesian throughflow?* Journal of Geophysical Research, vol. 101, No. C5, 12301-12314.

Open University, 2002: *Ocean circulation.* Second edition, Butterworth-Heinemann Ltd.

Pedlosky J., 1987: *Geophysical fluid dynamics.* Second edition, Springer–Verlag New York.

Pedlosky J., 1996: *Ocean Circulation Theory.* Berlin: Springer–Verlag.

PhysicalGeography.net., 2007: *Fundamentals of physical geography.* Obtained from the website: http://www.physicalgeography.net/fundamentals/8q.html.

Pickard G. L. and Emery W. J., 1990: *Descriptive physical oceanography: An introduction.* 5th (SI) edition, Pergamon press.

Piola R. A. and Gordon A., L., 1984: *Pacific and Indian Ocean upper-layer salinity budget.* Journal of Physical Oceanography, vol. 14, 747-753.

Potemra, J. T., 1999: *Seasonal variations of the Pacific to Indian Ocean throughflow.* Journal of Physical Oceanography, 29, 2930–2944.

Potemra, T., J, Susan L. Hautala, and Janet Sprintall, 2003: *Vertical structure of Indonesian throughflow in a large-scale model.* Deep Sea Research. II, 50 (12/13), 2143-2161.

Potemra T., J and Sneider N., 2007: *Inter-annual variation of the Indonesian throughflow.* Journal of Geophysical Research, 112, C05035.

Proctor R. and I.D. James 1996: *A fine-resolution 3D model of the southern North Sea.* Journal of Marine Systems 8:285-295.

Qu T. D., 2000: *Upper-layer circulation in the South China Sea.* Journal of Physical Oceanography. Vol. 30.

Rintoul, S. R., and S. Sokolov, 2001: *Baroclinic transport variability of the Antarctic Circumpolar Current south of Australia (WOCE repeat section SR3).* Journal of Geophysical Research, 106(C2), 2815–2832.

Robert A. Rohde, 2007: Obtained from the website: http://www.globalwarmingart.com/wiki/Image:Global_Warming_Predictions_png).

Shaw, P. T. and S. Y. Chao, 1994: *Surface circulation in the South China Sea.* Deep Sea Research, 41, 1663-1683.

Semtner J, A, and Chervin M., R., 1988: *A simulation of the global ocean circulation with resolved eddies.* Journal of Geophysical Research, vol. 93, No. C12, 15502-15522.

Siedler G., Church J., and Gould J., 2001: *Ocean Circulation and Climate: Observing and Modeling the Global Ocean.* Academic Press: San Diego, San Francisco, New York, Boston, London, Sydney, Tokyo.

Schneider, N. and T.P. Barnett, 1997: *Indonesian Throughflow in a coupled general circulation model.* Journal of Geophysical Research, vol.102, No.C6, p.12341-12358.

Schneider, N., 1998: *The Indonesian Throughflow and the global climate system.* Journal of Climate, vol.11, p.676-689.

Smith S.D. and E.G. Banke 1975: *Variation of the sea surface drag coefficient with wind speed.* Quarterly Journal of the Royal Meteorological Society 101:665-673.

Sparrow, M., Chapman, P. and Gould, J. (eds.) (2005): *The World Ocean Circulation Experiment (WOCE) Hydrographic Atlas Series.* Southampton, UK, International WOCE Project Office.

Sprintall, J., A. L. Gordon, R. Murtugudde and R. D. Susanto, 2000: *A semiannual Indian Ocean forced Kelvin wave observed in the Indonesian seas in May 1997.* Journal of Geophysical Research, 105, 17217-17230.

Sprintall J., Wijffels S., Gordon A. L., et al., 2004: *INSTANT: A new international array to measure the Indonesian Throughflow.* EOS, Transactions, American Geophysical Union, vol 85, no 39.

Stewart R., H., 2006: *Introduction to physical oceanography.* The online version at the website: http://oceanworld.tamu.edu/resources/ocng_textbook/contents.html.

Stommel H., 1948: *The westward intensification of wind-driven ocean currents.* Transactions of the American Geophysical Union 29 (2): 202–206.

Susanto, R. D., and A. L. Gordon 2005: *Velocity and transport of the Makassar Strait throughflow.* Journal of Geophysical Research, 110, C01005, doi:10.1029/2004JC002425.

Sverdrup H.U., 1947: *Wind-driven currents in a baroclinic ocean: with application to the equatorial currents of the eastern Pacific.* Proceedings of the National Academy of Sciences 33 (11): 318–326.

TAO, 2007: *The Tropical Atmosphere Ocean project.* Obtained from the website: http://www.pmel.noaa.gov/tao/

Tomczak M. and Godfrey J., S., 2001: *Regional oceanography.* The online version at the website: http://www.cmima.csic.es/mirror/mattom/regoc/index.html.

Toole, J., M., E. Zou, and R., C., Millard, 1988: *On the circulation of the upper waters in the western equatorial pacific.* Deep Sea Research, Part A, 35, 1451-1482.

Toole, J. M. &Warren, B. A., 1993: *A hydrographic section across the subtropical South Indian Ocean.* Deep Sea Research, I 40, 1973–2019.

United States Navy Hydrographic Office, 1944: *Current charts, Southwestern Pacific Ocean.* H. O. No. 10058.

United States Navy Hydrographic Office, 1950: *Atlas of surface current, Indian Ocean.* H. O. No. 566.

United States Weather Bureau, 1938: *Atlas of climatic charts of the oceans.* W. B. No. 1247.

van Aken, H. M, J. Punjanan and S. Saimima, 1988: *Physical aspects of the flushing of the East Indonesian basins.* Neth. J. Sea Res. 22, 315-339.

van Aken H., M, 2007: *The Oceanic Thermohaline Circulation: An Introduction.* Springer Sciences + Bussiness Media, LLC.

Vranes, K., and A., L. Gordon, 2005: *Comparison of Indonesian Throughflow transport observations, Makassar Strait to eastern Indian Ocean.* Geophysical Research Letter, 32, L10606.

Wainwright, L., G. Meyers, S. Wijffels, and L. Pigot, 2008: *Change in the Indonesian Throughflow with the climatic shift of 1976/77.* Geophys. Res. Lett., 35, L03604, doi:10.1029/2007GL031911.

Wang et al. 2003: *Advances in Studying Oceanic Circulation from Hydrographic Data with Applications in the South China Sea.* Advances in Atmospheric Sciences, vol. 20, No. 6, 2003, pp. 914–920.

Wajsowicz, R.C., 1993a: *A simple model of the Indonesian throughflow and its composition.* Journal of Physical Oceanography, vol. 23. No.12, p.2683-2703.

Wajsowicz, R.C., 1993b: *The Circulation of the depth-integrated flow around an island with application to the Indonesian throughflow.* Journal of Physical Oceanography, vol. 23. No.7, p.1470-1484.

Wajsowicz, R.C., 1994: *A relationship between inter-annual variations in the South Pacific wind stress curl and the Indonesian throughflow, and the West Pacific warm water pool.* Journal of Physical Oceanography, vol. 24. No.10, p.2180-2187.

Wajsowicz, R.C., 1995: *The response of the Indo-Pacific throughflow to inter-annual variations in the Pacific wind stress. Part1: Idealized geometry and variations.* Journal of Physical Oceanography, vol. 25. No.8, p.1805-1826.

Wajsowicz, R.C., 1996: *The response of the Indo-Pacific Throughflow to inter-annual variations in the Pacific wind stress. Part II: Realistic geometry and ECMWF wind stress anomalies for 1985-89.* Journal of Physical Oceanography, 26(12), 2589-2610.

Wajsowicz, R.C., and E. K. Schneider, 2001: *The Indonesian throughflow's effect on global climate determined from the COLA coupled climate system.* Journal of Climate, 14, 3029-3042.

Wajsowicz, R. C., Gordon, A. L., Ffield, A., Susanto D. R., 2003: *Estimating transport in Makassar Strait.* Deep-Sea Research II, 50, 2163-2181.

Warren B., A., and Wunsch C., 1981: *Evolution of physical oceanography: scientific surveys in honor of Henry Stommel.* edited by Bruce A. Warren and Carl Wunsch. MIT Press, Cambridge (Mass.).

WOCE, 2002: *The World Ocean Circulation Experiment.* Obtained from the website: http://www.soc.soton.ac.uk/OTHERS/woceipo/ipo.html.

Wijffels, S. E., R. W. Schmitt, H. Bryden, and A. Stigebrand, 1992: *Transport of freshwater by the ocean.* Journal of Physical Oceanography, 22, 155– 162.

Wu C. R. et al. 1998: *Seasonal and Inter-annual Variations in the Velocity Field of the South China Sea.* Journal of Oceanography, vol. 54, pp. 361 to 372.

Wunsch C. et al. 1983: *Mass, heat, salt and nutrient fluxes in the South Pacific Ocean.* Journal of Physical Oceanography, vol. 13, 725-753.

Wunsch C. 2002: *What is the thermohaline circulation?* Science 298(5596): 1179–1180.

WW2010, 1998: *El Niño - a warm current of water.* University of Illinois. Obtained from the website: http://ww2010.atmos.uiuc.edu/(Gh)/guides/mtr/eln/def.rxml.

Wyrtki K., 1961: *Physical oceanography of the Southeast Asian Waters, NAGA Report 2.* Scripps Institute of Oceanography, LaJolla, California.

Wyrtki K., 1987: *Indonesian throughflow and the associated pressure gradient.* Journal of Geophysical Research, 92, 12,941-12,946.

Wyrtki, K., 1973: *An equatorial jet in the Indian Ocean.* Science 181, 262-264.

Yamagata, T., K. Mizuno, and Y., Masumoto, 1996: *Seasonal variation in the equatorial Indian ocean and their impact on Lombok throughflow.* Journal of Geophysical Research, 101, 12465-12,473.

Xing J. and A.M. Davies 1996: *The influence of mixing length formulation and stratification on tidal currents in shallow seas.* Estuarine, Coastal and Shelf Science 42:417-456.